

5-2018

## Algorithmic Advances to Increase the Fidelity Of Conceptual Hypersonic Mission Design

Harish Saranathan  
*Purdue University*

Follow this and additional works at: [https://docs.lib.purdue.edu/open\\_access\\_dissertations](https://docs.lib.purdue.edu/open_access_dissertations)

---

### Recommended Citation

Saranathan, Harish, "Algorithmic Advances to Increase the Fidelity Of Conceptual Hypersonic Mission Design" (2018). *Open Access Dissertations*. 1820.  
[https://docs.lib.purdue.edu/open\\_access\\_dissertations/1820](https://docs.lib.purdue.edu/open_access_dissertations/1820)

This document has been made available through Purdue e-Pubs, a service of the Purdue University Libraries.  
Please contact [epubs@purdue.edu](mailto:epubs@purdue.edu) for additional information.

ALGORITHMIC ADVANCES TO INCREASE THE FIDELITY OF  
CONCEPTUAL HYPERSONIC MISSION DESIGN

A Dissertation

Submitted to the Faculty

of

Purdue University

by

Harish Saranathan

In Partial Fulfillment of the

Requirements for the Degree

of

Doctor of Philosophy

May 2018

Purdue University

West Lafayette, Indiana



**THE PURDUE UNIVERSITY GRADUATE SCHOOL**  
**STATEMENT OF DISSERTATION APPROVAL**

Dr. Michael J. Grant, Chair

School of Aeronautics and Astronautics

Dr. Alina Alexeenko

School of Aeronautics and Astronautics

Dr. James M. Longuski

School of Aeronautics and Astronautics

Dr. Christopher D. Karlgaard

Analytical Mechanics Associates, Inc.

**Approved by:**

Dr. Weinong Chen

Aeronautics and Astronautics Associate Head for Graduate Education

*To my parents, Jayasree and Saranathan.*

*To my sister, Maya.*

*It is their continued support and motivation since my formative years  
that have enabled me to pursue the dream of flight.*

## ACKNOWLEDGMENTS

I would first like to thank my advisor, Prof. Michael J. Grant. It has been a great privilege working with you. It is your continued confidence in me, your motivation and guidance that has enabled my smooth transition into aerospace engineering and subsequent growth to the point where I am able to make substantial contributions to the field. I also thank you for your complete trust in me in every situation during my time in graduate school. I thoroughly enjoyed our interactions during research meetings, classroom interactions, conferences and other meetings.

I would also like to thank Prof. James M. Longuski for his valuable insights in the field of dynamics. I learned a lot from your classes and your professionalism. I also thank my other committee members, Dr. Christopher C. Karlgaard and Prof. Alina Alexeenko for their valuable insights into the contributions of my dissertation. I would also like to acknowledge Prof. Sarag J. Saikia for being a mentor during the early phase of my graduate school, when he was still a graduate student.

I would like to thank the Office of the Dean, College of Engineering, Purdue University, for funding a substantial portion of my graduate school. My duties as a graduate student assistant enabled me to expand my professional network. I would specifically like to acknowledge Dr. Audeen W. Fentiman for her general guidance and advice that extended beyond my graduate assistantship. I would also like to acknowledge all the coworkers in the Dean's office for their continued words of motivation. I would also like to thank Sandia National Laboratories for funding part of my doctoral work. I would also like to acknowledge the School of Aeronautics and Astronautics at Purdue University for funding me briefly as a teaching assistant and enabling me to gain some teaching experience.

I consider myself fortunate to have great lab mates in the Rapid Design of Systems Laboratory. They have always provided stimulating insights into my research work.

I will always remember our unique combined sense of humor and all our “Fiesta” trips for lunch. I would specifically like to acknowledge Thomas Antony (alias Macman), Kshitij Mall (alias Mallman), Zhenbo Wang (alias Shockwave King), Justin Mansell, Joseph Williams, Sean Nolan and Michael Sparapany (who has macaroni with spaghetti) for their “next level” ness.

Finally, I would like to thank my family. I am the person today because of their constant nurturing during my formative years. It is their love and support that continue to motivate me to pursue my dreams.

## TABLE OF CONTENTS

	Page
LIST OF TABLES . . . . .	xi
LIST OF FIGURES . . . . .	xiii
ABBREVIATIONS . . . . .	xvii
NOMENCLATURE . . . . .	xix
ABSTRACT . . . . .	xxvi
1 INTRODUCTION . . . . .	1
1.1 Motivation . . . . .	1
1.1.1 The Necessity for Capturing the Coupling Between Ablative Shape Change and Trajectory . . . . .	2
1.1.2 Advantage of Incorporating Rigid Body Dynamics Into Con- ceptual Mission Design . . . . .	3
1.1.3 The Need for Employing Indirect Methods to Design highly Coupled Multi-Phase Trajectories . . . . .	4
1.1.4 Unified Framework for Increased Fidelity of Conceptual Hyper- sonic Mission Design . . . . .	6
1.2 Summary . . . . .	6
2 LITERATURE REVIEW . . . . .	9
2.1 The State-of-the-Art Conceptual hypersonic Mission Design Process . .	9
2.2 Prior Work Related to Capturing the Coupling Between Ablative Shape Change and Trajectory . . . . .	10
2.3 Prior Work Related to Incorporating Rigid Body Dynamics Into Con- ceptual Mission Design . . . . .	13
2.4 Prior Work Related to the Design of Multi-Phase Trajectories . . . . .	15
2.5 Summary . . . . .	18
3 POINT-MASS FLIGHT DYNAMICS . . . . .	19
4 AERODYNAMICS . . . . .	23
4.1 Introduction . . . . .	23
4.2 Steady Flow: Modified Newtonian Flow Theory . . . . .	23
4.3 Unsteady Flow: Piston Theory . . . . .	27
4.4 Panel Methods . . . . .	29
4.4.1 Approximation of the Vehicle Geometry using Flat Panels . . .	29
4.4.2 Computation of Aerodynamic Force and Moment for Each Panel	31



	Page
4.4.3 Validation of the Panel Methods . . . . .	34
4.5 Computation of Lift, Drag and Moment Coefficients . . . . .	39
4.6 Summary . . . . .	42
5 TRAJECTORY OPTIMIZATION USING INDIRECT METHODS . . . . .	43
5.1 Introduction . . . . .	43
5.1.1 Direct Methods of Trajectory Optimization and Their Key Limitations . . . . .	44
5.1.2 The Need for Indirect Methods of Trajectory Optimization . . . . .	45
5.2 Indirect Methods - The Necessary Conditions of Optimality . . . . .	46
5.2.1 Unconstrained Trajectory Optimization Problems . . . . .	46
5.2.2 Constrained Trajectory Optimization Problems . . . . .	47
5.3 Numerical Solution to the Two-Point Boundary Value Problem . . . . .	54
5.3.1 Initial Value Methods . . . . .	54
5.3.2 Finite Difference Methods . . . . .	55
5.3.3 The Continuation Method . . . . .	57
5.4 Necessary Conditions of Optimality for Multi-Phase Systems . . . . .	59
5.5 Summary . . . . .	60
6 INTEGRATION OF ABLATIVE SHAPE CHANGE INTO CONCEPTUAL HYPERSONIC MISSION DESIGN . . . . .	61
6.1 Introduction . . . . .	61
6.2 3-Dimensional Heat-Rate Model . . . . .	61
6.2.1 Generation of Equivalent Axisymmetric Body . . . . .	62
6.2.2 Axisymmetric Heating Analysis . . . . .	63
6.2.3 Validation of Heat-Rate Model . . . . .	66
6.3 Ablation of Thermal Protection System . . . . .	70
6.3.1 Modeling Ablation using Heat of Ablation . . . . .	70
6.3.2 Validation of the Ablation Model . . . . .	72
6.3.3 Modeling Arbitrary Vehicle Geometry . . . . .	75
6.4 Integration of Ablation Model into Equations of Motion . . . . .	81
6.5 Results . . . . .	84
6.5.1 Propagation of Equations of Motion . . . . .	85
6.5.2 Trajectory Optimization of a Hypersonic Vehicle Subject to Non-Axisymmetric Ablation . . . . .	88
6.5.3 Trajectory Optimization of an Axisymmetrically Ablating Hypersonic Vehicle Subject to Inequality Constraint on Altitude . . . . .	92
6.5.4 Trade Studies for Designing New Thermal Protection System Materials . . . . .	95
6.6 Summary . . . . .	100
7 INCORPORATION OF RIGID BODY DYNAMICS INTO TRAJECTORY DESIGN . . . . .	103
7.1 Introduction . . . . .	103

	Page
7.2 Flight Dynamics Model . . . . .	103
7.3 Numerical Stiffness . . . . .	109
7.4 Results . . . . .	114
7.4.1 Single-Stage Launch to Circular Orbit . . . . .	114
7.4.2 Glide Trajectory of a Slender Hypersonic Vehicle . . . . .	120
7.5 Summary . . . . .	127
8 SIMPLIFICATION OF TRAJECTORY OPTIMIZATION OF MULTI-PHASE SYSTEMS . . . . .	129
8.1 Introduction . . . . .	129
8.2 The Relaxed Autonomously Switched Hybrid System (RASHS) Approach . . . . .	130
8.3 Results . . . . .	133
8.3.1 Atlas V 411 Launch to Circular Orbit . . . . .	133
8.3.2 Mars Entry, Descent, and Landing . . . . .	140
8.3.3 Multi-Body Example: Boost-Glide Weapon System . . . . .	149
8.4 Summary . . . . .	158
9 UNIFIED CONCEPTUAL HYPERSONIC MISSION DESIGN FRAME- WORK . . . . .	161
9.1 Introduction . . . . .	161
9.2 Two-Stage Launch to Circular Orbit . . . . .	161
9.3 Integration of Ablation With Rigid Body Dynamics . . . . .	166
9.4 Rigid Boost-Glide Weapon System Trajectory with Spent Stage Con- straints . . . . .	170
9.5 Summary . . . . .	178
10 SUMMARY AND FUTURE WORK . . . . .	181
10.1 Summary of Contributions . . . . .	181
10.1.1 Incorporation of Ablative Shape Change into Conceptual Hy- personic Mission Design . . . . .	182
10.1.2 Incorporation of Rigid Body Dynamics into Trajectory Design . . . . .	183
10.1.3 Simplification of Trajectory Optimization of Multi-Phase Syst- ems . . . . .	184
10.1.4 Unified Conceptual Hypersonic Mission Design Framework . . . . .	185
10.2 Future Work . . . . .	185
10.2.1 Incorporation of Ablative Shape Change into Conceptual Hy- personic Mission Design . . . . .	187
10.2.2 Incorporation of Rigid Body Dynamics into Trajectory Design . . . . .	189
10.2.3 Simplification of Trajectory Optimization of Multi-Phase Syst- ems . . . . .	190
REFERENCES . . . . .	192

	Page
A TRADITIONAL APPROACH TO INDIRECT CONSTRAINED TRAJECTORY OPTIMIZATION . . . . .	205
B TRAJECTORY OPTIMIZATION OF AN AXISYMMETRICALLY AB- LATING HYPERSONIC VEHICLE SUBJECT TO EQUALITY CONSTRAINT ON ALTITUDE . . . . .	209
C POTENTIAL MODIFICATION TO RASHS TO ENABLE THE EXPLICIT ENFORCEMENT OF FLIGHT PHASE SEQUENCE . . . . .	217
D PUBLICATIONS RESULTING FROM THE DOCTORAL PROGRAM . .	221
VITA . . . . .	224

## LIST OF TABLES

Table	Page
4.1 Freestream conditions for validation of panel methods. . . . .	35
6.1 Flow condition for each case. . . . .	67
6.2 Points constituting the 2-D curve representing the initial hemisphere. . . .	73
6.3 Points over which the NURBS surface interpolation is performed (units in meters). . . . .	80
6.4 Points defining initial geometry (units in meters). . . . .	85
6.5 Initial vehicle states for the propagation of the equations of motion. . . .	86
6.6 Initial conditions for the glide trajectory. . . . .	88
6.7 Points defining initial geometry (units in meters). . . . .	89
6.8 Initial and terminal constraints. . . . .	94
6.9 Conditions at booster burnout. . . . .	97
6.10 Properties of subsystems. . . . .	97
7.1 Initial and final conditions for the single-stage launch trajectory. . . . .	114
7.2 Initial and final conditions for the glide trajectory. . . . .	123
8.1 Launch vehicle characteristics. . . . .	134
8.2 Initial and final conditions for the Atlas V launch trajectory. . . . .	135
8.3 EDL vehicle mass and aerodynamic properties. . . . .	141
8.4 Initial and final conditions for the EDL trajectory. . . . .	142
8.5 “ON” conditions for each phase of flight. . . . .	144
8.6 End-point boundary conditions on states. . . . .	150
8.7 Mass properties of the boost-glide system. . . . .	151
8.8 “ON” conditions for each phase of flight. . . . .	153
9.1 Initial and final conditions on the booster states. . . . .	174
9.2 Initial and final conditions of the glide vehicle states. . . . .	174

Table	Page
B.1 Initial conditions for the trajectory arc with the altitude constraint. . . .	210
B.2 Initial and terminal conditions for the unconstrained trajectory arc. . . .	210
B.3 Initial conditions for the trajectory arc with the altitude constraint corresponding to case 2. . . . .	213
B.4 Initial and terminal conditions for the unconstrained trajectory arc corresponding to case 2. . . . .	213

## LIST OF FIGURES

Figure	Page
1.1 Illustration of the significance of explicitly capturing the coupling between the ablation of TPS and the flight dynamics of slender hypersonic vehicles used in military applications. . . . .	3
1.2 Illustration of reduction in terminal velocity resulting from modeling the vehicle as a rigid body. . . . .	4
1.3 Illustration of the influence of impact constraints of the spent boost stage on mission performance. . . . .	5
2.1 Illustration of the sequential iterative conceptual design approach. . . . .	9
2.2 Illustration of variation of trim angle-of-attack with evolution of vehicle geometry. . . . .	13
3.1 Relationship between coordinate frames. . . . .	21
4.1 Illustration of Modified Newtonian flow. . . . .	25
4.2 Illustration of unsteady flow analysis using piston theory. . . . .	27
4.3 Representation of a smooth hemisphere using flat panels. . . . .	31
4.4 Illustration of triangular and quadrilateral panels along with centroid and unit inward-pointing normal vector. . . . .	32
4.5 Illustration of the cone geometry used in validation of the panel method. . . . .	35
4.6 Illustration of validation of the panel methods. . . . .	39
4.7 Relationship between wind and body frames. . . . .	40
5.1 Illustration of a sigmoid function. . . . .	50
5.2 Illustration of an exponential function. . . . .	51
5.3 Illustration of finite difference methods to solve the TPBVP. . . . .	55
5.4 Illustration of the continuation process. . . . .	58
6.1 Illustration of generation of meridians and corresponding equivalent axisymmetric bodies. . . . .	63
6.2 Case 1 - Heating along axisymmetric 15 deg. sphere-cone and comparison with results presented by Bopp et al. [106]. . . . .	68

Figure	Page
6.3 Case 2 - Centerline heating distribution on 15 deg. sphere-cone at 20 deg. angle-of-attack and comparison with results presented by Bopp et al. [106].	69
6.4 Validation of ablation model. Since the ablation is axisymmetric, only the top portion of the hemisphere as seen from the side is shown. . . . .	74
6.5 Illustration of NURBS surface interpolation (source: Piegl and Tiller [116], modified). . . . .	76
6.6 Example NURBS surface interpolation. . . . .	79
6.7 Vehicle composed of two additional volumes with different densities. . . . .	84
6.8 Comparison of trajectories and vehicle geometry with and without ablation. The initial vehicle geometry and states are defined in Tables 6.4 and 6.5 respectively. The downrange is seen to be reduced by about 14 percent when ablation is accounted for. . . . .	87
6.9 Trajectory optimization of a hypersonic glide vehicle subject to non-axisymmetric ablation to minimize TOF. The states and glide vehicle geometry at booster separation are defined in Tables 6.6 and 6.7 respectively. . . . .	91
6.10 Comparison of maximum final velocity trajectories with altitude constraints, calculated with and without TPS ablation. The glide vehicle states and geometry at booster separation and the desired final states are defined in Table 6.8. The final velocity of the ablating vehicle is reduced by more than 60 percent. . . . .	96
6.11 Influence of increasing the heat of ablation of the TPS on the trajectory. $Q_*$ is varied from 2 MJ/kg to 10 MJ/kg, while $\rho_{TPS}$ is held at 800 kg/m <sup>3</sup> . . . . .	98
6.12 Influence of increasing the TPS density on the trajectory. $\rho_{TPS}$ is varied from 800 kg/m <sup>3</sup> to 1,500 kg/m <sup>3</sup> , while $Q_*$ is held at 2 MJ/kg. . . . .	99
7.1 Illustration of translational state variables. . . . .	104
7.2 Illustration of rotational state variables. . . . .	105
7.3 Illustration of loss in angular momentum in the products of combustion. . . . .	107
7.4 Comparison of variation in pitch rate evolution when the loss in angular momentum resulting from the ejection of combustion products is accounted for and neglected. . . . .	109
7.5 Hypothetical vehicle used in the illustration of numerical stiffness. . . . .	110
7.6 Illustration of numerical stiffness. . . . .	111
7.7 Washout filter added in the feedback path from the pitch rate to the elevon inputs. . . . .	112

Figure	Page
7.8 Damped oscillations in the presence of the washout filter, resulting in reduced numerical stiffness. . . . .	113
7.9 Launch vehicle geometry. . . . .	117
7.10 Minimum time single-stage ascent to circular equatorial orbit. The desired initial and final states are defined in Table 7.1, and the launch vehicle geometry is illustrated in Figure 7.9. . . . .	119
7.11 Vehicle configuration. . . . .	121
7.12 Elevon cross section. . . . .	122
7.13 Comparison of maximum final velocity trajectories of a hypothetical hypersonic glide vehicle calculated using rigid body and point-mass flight dynamics. The vehicle geometry and configuration at booster separation are illustrated in Figures 7.11 and 7.12. The vehicle states at booster separation and the desired final states are defined in Table 7.2. . . . .	124
7.14 Increasing elevon span from 1.6 m to 2.1 m has a negative impact on mission performance. . . . .	125
7.15 Increasing elevon chord length from 0.4 m to 0.8 m improves mission performance. . . . .	126
7.16 Moving the warhead back from 2.5 m to 2.37 m (measured from the base of the fuselage and along the roll axis) improves mission performance. . .	126
8.1 Minimum-time ascent trajectory of Atlas V 411 to equatorial circular orbit. The flight phases and the corresponding vehicle configuration are defined in Table 8.1, and the desired initial and final vehicle states are defined in Table 8.2. . . . .	138
8.2 Histories of control, co-states, and Hamiltonian. . . . .	139
8.3 Optimal Mars EDL trajectory of an MSL-like vehicle. The flight phases and the vehicle configuration are described in Table 8.3, and the desired initial and final vehicle states are defined in Table 8.4. The stagnation-point heat load is minimized until powered descent, and the thrust is minimized during powered descent. . . . .	147
8.4 Longitude and latitude co-state histories. . . . .	148
8.5 Velocity and altitude co-state histories. . . . .	149
8.6 Maximum final velocity, minimum time boost-glide trajectory with constraints on the impact location of the spent booster. The desired initial and final states of the booster and the glide vehicle are defined in Table 8.6, and their properties are defined in Table 8.7. . . . .	155



Figure	Page
8.7 Control histories. . . . .	156
8.8 Histories of co-states and Hamiltonian. . . . .	156
8.9 Mission trade study of a hypothetical boost-glide weapon system. Constraining the spent booster to impact closer to the launch site negatively impacts mission performance, wherein the impact velocity of the glide vehicle is reduced, and its TOF is increased. . . . .	158
9.1 Illustration of the launch vehicle stack. . . . .	163
9.2 Illustration of each stage of the two-stage launch vehicle. . . . .	164
9.3 Illustration of the minimum time ascent trajectory of a two-stage launch vehicle to equatorial circular orbit. The vehicle configuration is illustrated in Figures 9.1 and 9.2, and the desired initial and final vehicle states are defined in Section 7.4.1, Table 7.1. . . . .	165
9.4 Comparison of the maximum final velocity glide trajectories of a rigid hypothetical hypersonic glide vehicle, with and without an ablative TPS. The vehicle geometry and configuration at booster separation are illustrated in Section 7.4.2, Figures 7.11 and 7.12. The vehicle states at booster separation and the desired final states are defined in Section 7.4.2, Table 7.2. . . . .	169
9.5 Illustration of the vehicle configuration at launch. . . . .	171
9.6 Booster cross section. . . . .	172
9.7 Booster configuration. . . . .	173
9.8 Illustration of the minimum time trajectory of a hypothetical rigid boost glide weapon system with constraints on the impact location of the spent booster. The glide vehicle is protected by an ablative TPS, and its initial geometry is illustrated in Section 7.4.2, Figures 7.11 and 7.12. The boost-glide stack at launch is illustrated in Figure 9.5, and the booster configuration is illustrated in Figures 9.6 and 9.7. The desired initial and final states of the booster and the glide vehicle are defined in Tables 9.1 and 9.2 respectively. . . . .	177
9.9 Illustration of initial and final geometry of the glide vehicle. . . . .	178
B.1 Results of trajectory optimization of an axisymmetrically ablating hypersonic glide vehicle subject to equality constraint on altitude and high initial velocity. . . . .	212
B.2 Results of trajectory optimization of an axisymmetrically ablating hypersonic glide vehicle subject to equality constraint on altitude and low initial velocity. . . . .	214

## ABBREVIATIONS

APCP	ammonium perchlorate composite propellant
BL	boundary layer
BVP	boundary value problem
CFD	computational fluid dynamics
CM	center of mass
DAE	differential-algebraic equation
DOF	degree-of-freedom
EAB	equivalent axisymmetric body
EDL	entry, descent, and landing
GPU	graphics processing unit
HIAD	hypersonic inflatable aerodynamic decelerator
IVM	initial value method
IVP	initial value problem
LOS	line-of-sight
LOx	liquid oxygen
MDO	multidisciplinary design optimization
MINIVER	miniature version
MPBVP	multi-point boundary value problem
MSL	mars science laboratory
NURBS	non-uniform rational basis spline
OML	outer mold line
RASHS	relaxed autonomously switched hybrid system
RP-1	rocket propellant-1
SQP	sequential quadratic programming
SST	shear stress transport

SSTO	single stage to orbit
TPBVP	two-point boundary value problem
TPS	thermal protection system
2-D	two dimensional
3-D	three dimensional

## NOMENCLATURE

$A$	area, $\text{m}^2$
$a$	speed of sound or pole of washout filter, $\text{m/s}$ or $\text{rad/s}$
$b_r$	solid propellant grain burn rate, $\text{m/s}$
$\mathbf{C}$	path constraint vector or knot vector corresponding to $c$ direction of NURBS surface
$C$	scalar path constraint or washout filter
$C_D$	drag coefficient
$C_L$	lift coefficient
$CM$	moment coefficient
$C_p$	pressure coefficient
$c$	inequality path constraint that is a function of control only
$c$	first parameter representing a surface
$c_p$	heat capacity at constant pressure, $\text{J/K}$
$c_v$	heat capacity at constant volume, $\text{J/K}$
$\mathbf{D}$	knot vector corresponding to $d$ direction of NURBS surface
$D$	drag force magnitude, $\text{N}$
$d$	inequality path constraint that is a function of both control and states
$d$	second parameter representing a surface
$e$	state introduced by washout filter
$\mathbf{F}$	force vector, $\text{N}$
$\mathcal{F}$	augmented system dynamics with generic states and control
$F$	force, $\text{N}$
$\mathbf{f}$	system dynamics
$f$	cartesian equation of surface

<b>G</b>	vector field
$g$	function that defines switching condition for flight-phase transition or acceleration due to gravity of Earth, nd or m/s <sup>2</sup>
<b>H</b>	Hamiltonian
$H$	mean curvature, m
$H$	scale height of exponential atmosphere, m
$\mathcal{H}$	inertial angular momentum, kg-m <sup>2</sup> /s
$h$	enthalpy, J/kg
$h$	altitude or vertical dimension or time step, m or s
$\hbar$	scaled altitude
$\bar{\mathbf{I}}$	inertia tensor, kg-m <sup>2</sup>
$I$	inertia tensor element, kg-m <sup>2</sup>
$I_{sp}$	specific impulse, s
$J$	cost functional
$K$	gain of washout filter or weights for cost functional
$k$	empirical constant for heat-rate computation, J-s <sup>2</sup> -kg <sup>-0.5</sup> -m <sup>-3</sup>
$L$	lift force magnitude, N
$L/D$	lift-to-drag ratio
$\mathcal{L}$	Lagrangian
$l$	reference length or length of geometry, m
<b>M</b>	moment vector, N-m
$M$	moment or Mach number or scaled mass, N-m or nd
$\mathcal{M}$	fictitious Mach number
$m$	mass, kg
$\dot{m}$	mass flow rate, kg/s
$N$	basis function of NURBS surface
<b>n</b>	inward-pointing normal vector
$\hat{\mathbf{n}}$	inward-pointing unit normal vector
<b>P</b>	position vector of a point on the vehicle surface, m

$Pr$	Prandtl number
$p$	pressure, Pa
$Q$	stagnation-point heat-load, J/m <sup>2</sup>
$Q_*$	heat of ablation, J/kg
$\dot{q}$	heat-rate, W/m <sup>2</sup>
$R$	specific gas constant, J·kg <sup>-1</sup> ·K <sup>-1</sup>
$R$	radius of planet, m
$Re$	Reynolds number
$\mathbf{r}$	inertial position vector or position vector of launch vehicle components or residual vector, m or mixed units
$r$	axisymmetric radius or distance from center of mass or propellant grain radius, m
$\mathbf{S}$	parametric equation of surface or trajectory
$S$	reference area, m <sup>2</sup>
$\dot{s}$	surface recession rate of TPS, m/s
$s$	slope parameter of saturation/sigmoid function or streamwise distance or independent variable in Laplace domain, nd or m or rad/s
$T$	thrust magnitude, N
$T$	temperature, K
$t$	time, s
$\mathbf{U}$	control vector
$u$	generic control variable related to inequality constraint in states only or unit step function
$V$	volume or scaled atmospheric-relative velocity, m <sup>3</sup> or nd
$v$	atmospheric-relative velocity, m/s
$\mathbf{v}$	atmospheric-relative velocity vector, m/s
$\hat{\mathbf{v}}$	unit velocity vector
$\mathbf{W}$	control point of NURBS surface

$w$	generic control variable related to inequality constraint in states and control
$\mathbf{X}$	state vector
$\hat{\mathbf{X}}, \hat{\mathbf{Y}}, \hat{\mathbf{Z}}$	inertial unit vectors
$\hat{\mathbf{X}}_G, \hat{\mathbf{Y}}_G, \hat{\mathbf{Z}}_G$	unit vectors defining the planet-fixed, planet-centered frame
$\hat{\mathbf{x}}, \hat{\mathbf{y}}, \hat{\mathbf{z}}$	unit vectors defining a generic coordinate frame
$\hat{\mathbf{x}}_W, \hat{\mathbf{y}}_W, \hat{\mathbf{z}}_W$	unit vectors defining the wind frame
$\hat{\mathbf{x}}_B, \hat{\mathbf{y}}_B, \hat{\mathbf{z}}_B$	unit vectors defining the body frame
$x, y, z$	coordinates of a point on the vehicle surface, m
$\alpha$	angle-of-attack, rad
$\beta$	pressure gradient parameter
$\gamma$	atmospheric-relative flight-path-angle or specific heat ratio, rad or nd
$\Delta A$	area of panel, m <sup>2</sup>
$\delta$	cone half angle or deflection angle, rad
$\epsilon$	emissivity
$\epsilon$	density ratio across the normal portion of a shock or weights for generic control
$\zeta$	measure of slope of tanh function
$\eta$	transpiration coefficient
$\Theta$	pitch angle, rad
$\theta$	momentum boundary layer thickness, m
$\theta$	longitude, rad
$\kappa$	local surface inclination with respect to freestream, rad
$\boldsymbol{\lambda}$	co-state vector
$\lambda$	co-state
$\boldsymbol{\mu}$	Lagrange multiplier vector for path constraints
$\mu$	dynamic viscosity, kg-m <sup>-1</sup> -s <sup>-1</sup>

$\mu$	standard gravitational parameter or Lagrange multiplier for path constraints, $\text{m}^3/\text{s}^2$ or mixed units
$\nu$	Lagrange multiplier for inequality constraint in states and control
$\xi$	generic state variable or streamwise coordinate or switching function
$\Pi$	Lagrange multiplier vector for interior boundary conditions in multi-phase trajectories
$\rho$	density, $\text{kg}/\text{m}^3$
$\sigma$	Stefan-Boltzmann constant, $\text{W}\cdot\text{m}^{-2}\cdot\text{K}^{-4}$
$\sigma$	bank angle, rad
$\tau$	nondimensional time
$\Phi$	terminal cost
$\phi$	latitude or saturation function for inequality constraint in states and control, rad or mixed units
$\chi$	angle between inward-pointing surface normal and freestream vector, rad
$\Psi$	boundary condition vector
$\psi$	heading angle or saturation function for inequality constraint in states only, rad or variable units
$\Omega$	planetary angular velocity vector, rad/s
$\Omega$	planetary angular velocity, rad/s
$\omega$	vehicular angular velocity vector, rad/s
$\omega$	pitch rate, rad/s

### Subscripts

<i>AERO</i>	aerodynamic
<i>AFT</i>	rear section of vehicle
<i>aw</i>	adiabatic wall
<i>B</i>	base of geometry or body frame or burn



$b$	booster burnout
$C$	centroid of panel or control surface
$CM$	center of mass
$command$	property corresponding to a commanded value
$cond$	conduction
$conv$	convection
$cw$	cold wall
$EAB$	equivalent axisymmetric body
$e$	edge
$F$	fuel
$f$	quantity measured at final time
GRAIN	property corresponding to solid propellant grain
$h$	scaled altitude
INERT	property corresponding to the inert structure
$L$	lower bound or left
LOx	property corresponding to liquid oxygen
$max$	maximum
$M$	scaled mass
$N$	normal or nose
$NURBS$	non-uniform rational basis spline
$O$	origin
$P$	property at parachute deployment
PAY	property corresponding to the payload
$PDI$	property at powered descent
$R$	right
ROD	rod section of propellant grain
RP-1	property corresponding to RP-1 propellant
$r$	property based on recovery enthalpy
$rerad$	re-radiation

$t$	total
$T$	nozzle
$TPS$	thermal protection system
TUBE	tube section of propellant grain
$trans$	transpiration
$U$	upper bound
$V$	vehicle or scaled atmospheric-relative velocity
$vap$	vaporization
$w$	wall
$x, y, z$	quantity corresponding to $x$ , $y$ and $z$ axes respectively
$\gamma$	atmospheric-relative flight-path-angle
$\epsilon$	property defined at $s_\epsilon$
$\Theta$	pitch angle
$\theta$	momentum boundary layer
$\theta$	longitude
$\xi$	generic state variable
$\phi$	latitude
$\psi$	heading angle
$\omega$	pitch rate
0	initial or surface or stagnation point
2	downstream of normal portion of the shock
3D	three dimensional
$\infty$	freestream

### Superscripts

$i$	inertial
—	lower bound of inequality path constraint
+	upper bound of inequality path constraint
*	property based on reference enthalpy

## ABSTRACT

Saranathan, Harish PhD, Purdue University, May 2018. Algorithmic Advances to Increase the Fidelity Of Conceptual Hypersonic Mission Design. Major Professor: Michael J. Grant.

The contributions of this dissertation increase the fidelity of conceptual hypersonic mission design through the following innovations: 1) the introduction of coupling between the effects of ablation of the thermal protection system (TPS) and flight dynamics, 2) the introduction of rigid body dynamics into trajectory design, and 3) simplifying the design of hypersonic missions that involve multiple phases of flight. These contributions are combined into a unified conceptual mission design framework, which is in turn applicable to slender hypersonic vehicles with ablative TPS. Such vehicles are employed in military applications, wherein speed and terminal energy are of critical importance.

The fundamental observation that results from these contributions is the substantial reduction in the maximum terminal energy that is achievable when compared to the state-of-the art conceptual design process. Additionally, the control history that is required to follow the maximum terminal energy trajectory is also significantly altered, which will in turn bear consequence on the design of the control actuators.

The other important accomplishment of this dissertation is the demonstration of the ability to solve these class of problems using indirect methods. Despite being built on a strong foundation of the calculus of variations, the state-of-the-art entirely neglects indirect methods because of the challenge associated with solving the resulting boundary value problem (BVP) in a system of differential-algebraic equations (DAEs). Instead, it employs direct methods, wherein the optimality of the calculated trajectory is not guaranteed. The ability to employ indirect methods to solve for optimal trajectories that are comprised of multiple phases of flight while

also accounting for the effects of ablation of the TPS and rigid body dynamics is a substantial advancement in the state-of-the-art.



# 1. INTRODUCTION

The research presented in this dissertation increases the fidelity of conceptual hypersonic mission design via three key contributions: 1) incorporation of ablative shape change into conceptual hypersonic mission design, 2) incorporation of rigid body dynamics into trajectory design, and 3) simplification of trajectory optimization of multi-phase systems. These contributions are integrated into a single design framework, and are relevant to slender hypersonic systems with an ablative thermal protection system (TPS) used in military applications.

## 1.1 Motivation

*Speed is the new stealth. -Al Romig [1]*

The slender hypersonic vehicles employed in military applications are typically designed to fly at very high velocities to offer several tactical advantages such as the lack of warning time and the immunity to interception. These key benefits have prompted the Skunk Works’ engineering and advanced systems vice president, Dr. Alton D. Romig, to remark that “speed is the new stealth” [1]. Additionally, these vehicles are designed to surprise and distract the adversary to ensure a decisive blow [2]. Consequently, alongside stealth, “speed” has been identified as one of the factors that provide an element of surprise [3]. The additional advantage of possessing high velocity is the increased terminal kinetic energy, which in turn leads to a higher destruction capability.

The state-of-the-art conceptual hypersonic mission design for such high-speed systems is a large segregated sequential iterative root-solving process that typically involves vehicle shape design, followed by aerodynamic performance characterization (which involves the generation of large look-up tables) and trajectory design [4]. The

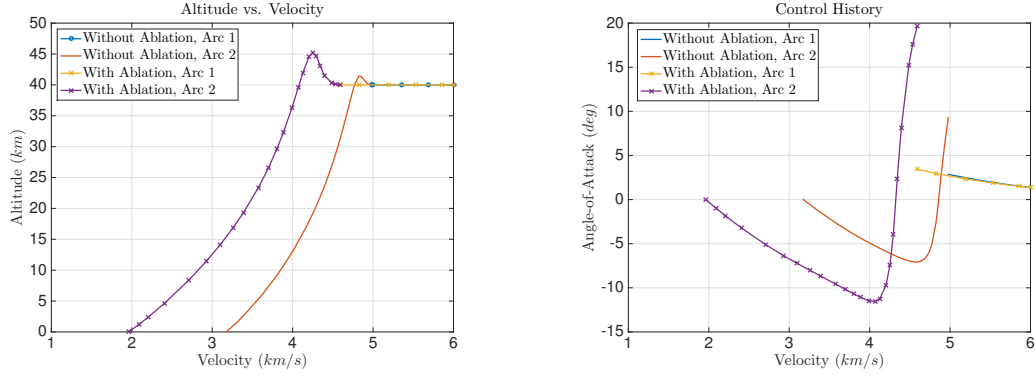
trajectory is often optimized to maximize the terminal velocity to increase the destruction capability of the vehicle, and to minimize the time-of-flight (TOF) to reduce the warning time. Although this design approach has been widely employed, it has several limitations.

### **1.1.1 The Necessity for Capturing the Coupling Between Ablative Shape Change and Trajectory**

One of the fundamental limitations of the state-of-the-art design approach is its inability to explicitly capture the coupling between the effects of ablation of the TPS and the flight dynamics. While not very critical in planetary entry missions wherein the shape change effected by ablation is not dramatic, it is an important consideration when designing missions for slender hypersonic vehicles used in military applications, which is the primary focus of this dissertation.

Since these vehicles are required to be designed with the ability to fly at very high hypersonic speeds, they encounter substantial aerothermal heating, leading to increased ablation of the TPS, which in turn significantly alters the geometry and mass properties, thereby dramatically impacting the mission performance. For example, the maximum velocity that is achievable at the instant of impacting the target can be reduced by 38 percent (Figure 1.1(a)) when the effects of ablation are accounted for, which translates to a reduction in the terminal kinetic energy by about 60 percent, thereby substantially limiting the destruction of the target. The mission flown in the illustration corresponds to that of a hypothetical slender hypersonic glide vehicle that is required to fly at a constant altitude of 40 km for the first 1,000 km and strike a target that is located at a distance of 1,500 km at maximum velocity. The dramatic ablation of the TPS also significantly alters the angle-of-attack ( $\alpha$ ) profile that is necessary to fly the maximum final velocity trajectory (Figure 1.1(b)). For instance, it can be seen that the magnitude of  $\alpha$  that is required at a velocity of 4.5 km/s has changed approximately from 7 deg to 20 deg. This would have consequence

in the design of the control actuators, which are now required to handle a 185 percent increase in the required magnitude of  $\alpha$  at 4.5 km/s. The capability introduced by the first contribution of the dissertation to gain these critical insights resulting from the explicit coupling between ablation and flight dynamics is a substantial advancement in the state-of-the-art in conceptual hypersonic mission design.



(a) Ablation of the TPS can significantly reduce the maximum achievable final velocity, an important consideration in missions involving slender hypersonic vehicles employed in military applications.

(b) Ablation of the TPS can significantly alter the angle-of-attack profile, which can in turn have consequences in the design of control actuators.

Figure 1.1. Illustration of the significance of explicitly capturing the coupling between the ablation of TPS and the flight dynamics of slender hypersonic vehicles used in military applications.

### 1.1.2 Advantage of Incorporating Rigid Body Dynamics Into Conceptual Mission Design

Another significant limitation of the state-of-the-art results from modeling the vehicle as a point-mass. This simplified model is unable to capture key insights that would otherwise be possible if the vehicle is modeled as a rigid body. For instance, the slender hypersonic vehicles of consideration in this dissertation are maneuvered by actuating the control surfaces, which can lead to an increased drag. The consequence



is again a substantially reduced terminal velocity. This is illustrated in Figure 1.2, wherein the terminal velocity of a similar slender hypersonic vehicle is maximized while it strikes a target that is located at a distance of 450 km. It can be seen that the terminal velocity is lower by 22 percent when the vehicle is modeled as a rigid body, which translates to a 39 percent reduction in the terminal kinetic energy. The other advantage of modeling the vehicle as a rigid body is the ability to automatically account for the controllability of the vehicle. As a result, it is no longer necessary to enforce bounds on  $\alpha$  to represent the vehicle's maneuvering capabilities, as is the case in the state-of-the-art.

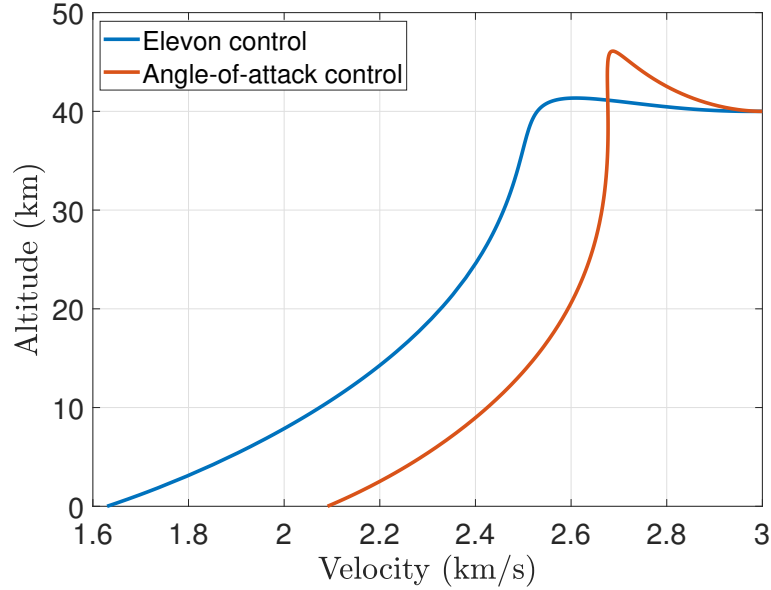
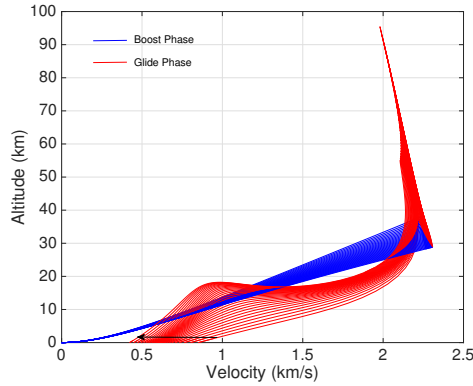


Figure 1.2. Illustration of reduction in terminal velocity resulting from modeling the vehicle as a rigid body.

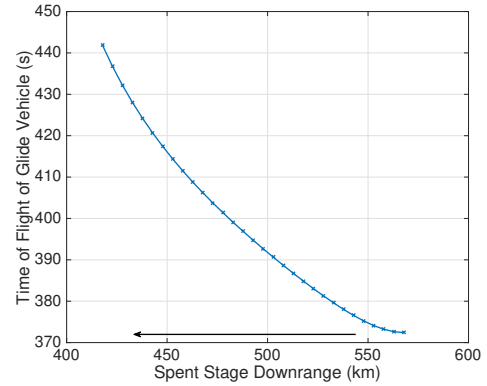
### 1.1.3 The Need for Employing Indirect Methods to Design highly Coupled Multi-Phase Trajectories

A typical military hypersonic mission consists of a boost phase, which is followed by a glide phase, leading to a multi-phase trajectory. In the state-of-the-art, such a

trajectory is optimized using direct methods because of the simplicity in setting up and solving the problem. However, the fundamental limitation of this approach is the inability to guarantee the optimality of the calculated trajectory. Furthermore, since the optimization is performed after the trajectory is discretized, this approach does not take advantage of every available information in the problem, thereby rendering it very difficult to solve problems where the flight phases are highly coupled, such as when constraints are imposed on the impact location of the spent boost stage. Such constraints may be introduced to prevent the booster from impacting an ally territory, and can have significant impact on the overall mission performance. For instance, enforcing the spent booster to impact at a distance of 420 km from the launch site instead of 570 km (a 26 percent reduction) results in a 50 percent reduction in the impact velocity (and a 75 percent reduction in the terminal kinetic energy) of the glide vehicle that is required to strike a target, located 600 km from the launch site, with maximum velocity and in minimum time. The booster impact constraint also increases the flight time of the glide vehicle by 19 percent, which in turn leads to



(a) Moving the impact location of the spent booster closer to the launch site substantially reduces the impact velocity of the glide vehicle.



(b) Moving the impact location of the spent booster closer to the launch site substantially increases the flight time of the glide vehicle.

Figure 1.3. Illustration of the influence of impact constraints of the spent boost stage on mission performance.

an increased warning time, and therefore, a reduction in the element of surprise on the adversary. In addition to enabling the capability to gain such insights, the third contribution of the dissertation advances the state-of-the-art by demonstrating that it is even possible to employ indirect methods to reliably solve for such multi-phase trajectories involving highly coupled flight phases. Since the indirect framework is built on a strong foundation of the calculus of variations, the calculated trajectories are guaranteed to be at least locally optimal.

#### **1.1.4 Unified Framework for Increased Fidelity of Conceptual Hypersonic Mission Design**

Although each contribution of the dissertation is an advancement in the state-of-the-art by itself, it would be highly beneficial if they are integrated into a unified design framework. Such a framework would enable the conceptual design of hypersonic missions involving multiple phases of flight, wherein the coupling between each flight phase, the vehicle geometry, mass distribution, maneuverability, aerothermal effects, and the resulting TPS ablation can be simultaneously analyzed.

### **1.2 Summary**

The consequence of the research presented in this dissertation is a new capability to generate high quality solutions for all phases of hypersonic flight, while simultaneously capturing the complex coupling associated with aerothermodynamic heating, the resulting ablative shape change, and rigid body dynamics, which are completely ignored in the state-of-the-art conceptual design approach. Such in-depth analysis during this design phase reduces design iterations in subsequent phases because of the availability of a base-point design that is more representative of the vehicle's performance, maneuverability, and the aerothermal environment that it encounters. Additionally, the capability that is developed can also be leveraged to optimize the

characteristics of hypothetical TPS materials, vehicle geometry, mass distribution, and control effector configuration specific to a given class of hypersonic missions.

The other notable accomplishment of this dissertation is the exclusive use of indirect methods of trajectory optimization in the three contributions. The ability to employ indirect methods to solve for optimal trajectories that are comprised of multiple phases of flight while also accounting for the effects of ablation of the TPS and rigid body dynamics is a substantial advancement in the state-of-the-art.



## 2. LITERATURE REVIEW

### 2.1 The State-of-the-Art Conceptual hypersonic Mission Design Process

Traditionally, conceptual hypersonic mission design is a large iterative root-solving process that is constructed with individual disciplinary models and analyses [4]. Due to the complexity of these disciplinary models, the analyses are performed using tools developed by the disciplinary experts and independent of the overall design process. While several multidisciplinary design optimization (MDO) tools [5–11] have been developed that attempt to efficiently construct the coupling between the individual disciplines, they employ the domain-specific tools which are in turn developed with the aim of achieving higher fidelity or capturing wider range of solutions, thereby making the design process highly computationally intensive. Moreover, since each disciplinary analysis involves its own set of design variables, the overall design process is segregated into a sequential iterative process (Figure 2.1) that typically involves vehicle shape design, followed by aerodynamic performance characterization (which involves the generation of large look-up tables) and trajectory design. Furthermore, high-fidelity aerothermal analysis is performed on certain critical points along the trajectory.

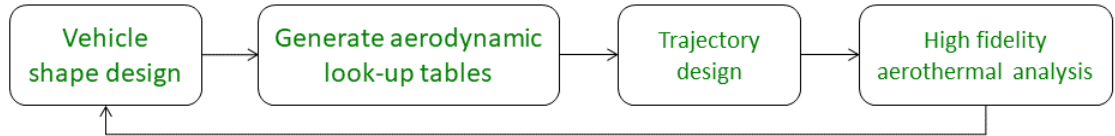


Figure 2.1. Illustration of the sequential iterative conceptual design approach.

This design methodology is very time-consuming because each iteration involves the generation of aerodynamic look-up tables using high-fidelity tools. Additionally, the flight dynamics model neglects the effects of TPS ablation, thereby resulting in trajectories that are not representative of the aerothermal environment that would be encountered. Furthermore, the vehicle is assumed to be a point-mass, which ignores the maneuvering capabilities of the vehicle. These limitations in the current design approach lead to a large number of design iterations. Also, multi-phase trajectory design is limited in scope in the state-of-the-art because of the employment of direct methods, which are typically unreliable for solving for optimal trajectories involving highly coupled flight phases. The rest of this chapter discusses the prior work that has attempted to address these limitations.

## **2.2 Prior Work Related to Capturing the Coupling Between Ablative Shape Change and Trajectory**

During conceptual hypersonic mission design, vehicles and trajectories are simultaneously constructed to provide adequate performance that satisfies mission requirements. Slender hypersonic systems that support emerging military applications often experience extreme heating environments that result in substantial shape change due to ablation of the TPS. This dramatic in-flight shape change also results in significant change in aerodynamic and mission performance. Due to the complex chemical reactions associated with ablation, the in-flight shape change of slender hypersonic systems is traditionally ignored during early conceptual design.

There exists some literature that describes conceptual aerothermal and ablation analysis. Doman and Blake [12] presented a method to provide estimates of mass properties and aerodynamic forces and moments of a reentry vehicle that ablates due to aerodynamic heating. This method requires the knowledge of vehicle shape before and after the flight, and also the actual trajectory that it flies. From this knowledge, surface recession is modeled as a function that maps the coordinates of points on the

outer mold line (OML) to a particular location along the trajectory. These points are used to generate a three-dimensional grid that can be used in aerodynamic prediction codes to obtain the aerodynamic coefficients. However, this model is only valid for a particular vehicle shape, TPS material, and trajectory for which the data were obtained. If any of these parameters are changed, the model for the dynamics of the OML has to be reconstructed. Other current ablation analysis techniques for conceptual design [13, 14] completely ignore shape change. They are only used to predict the mass loss rate of the TPS material, which can be used for TPS sizing. However, the reference trajectory used by these analyses is obtained by neglecting the effects of ablative shape change altogether, and hence, the predicted mass loss rates are not representative of the actual trajectory that would be flown.

There also exists considerable literature that describes higher fidelity ablation models [15–21]. Some of these models are specific to the mechanism of char removal, such as spallation [22] and intumescence [23]. These models employ finite difference methods and have been incorporated into a family of program packages [24–33]. While they generate better estimates of surface recession, they are computationally intensive. As a result, they are not used in conceptual design, but instead appear in subsequent phases. Moreover, these analyses are performed using freestream conditions corresponding to select trajectory points calculated during conceptual design, where ablative shape change is traditionally ignored. With advances in computing power, it has become possible to calculate the surface recession over the entire trajectory and not just select trajectory points. For instance, Hassan et. al. [34] calculated the surface recession on an axisymmetric nose tip of a slender vehicle over a given trajectory that was obtained independently (through propagation of flight dynamic equations for a fixed geometry and aerodynamic coefficients, from flight test data, etc.). Although there have been studies that involve generating trajectories in tandem with ablative shape change, they are limited to axisymmetric vehicles and use the higher fidelity programs. As a result, the calculation of such trajectories is time consuming. Moreover, there is no optimization of the trajectory involved. Instead,



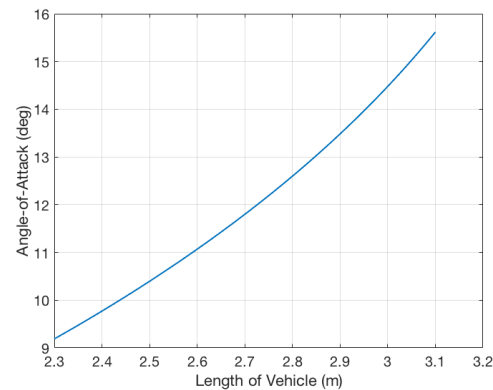
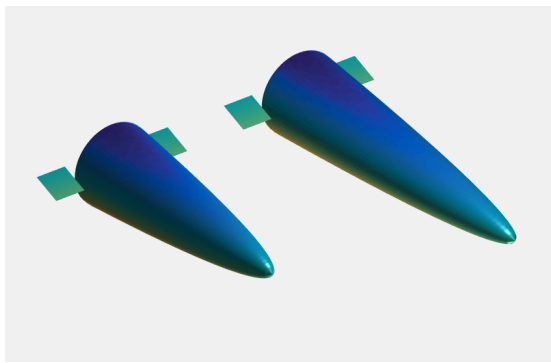
the governing equations are propagated forward in time. Such an approach has been applied to construct the entry trajectory of Mars Pathfinder [35] and a slender hypersonic vehicle used in missile applications [36].

Although these analyses provide substantial insights into the coupling between surface recession and flight dynamics, they are computationally intensive and are used only in advanced design phases, for instance, after the vehicle geometry has been established in conceptual design. However, this geometry will have been established without the knowledge of this coupling. If the high-fidelity analyses are not favorable, then the designers need to go back to conceptual design and alter the geometry and trajectory accordingly (again without the knowledge of the coupling). This can lead to several time consuming design iterations. Therefore, it would be beneficial to develop a methodology that enables the rapid generation of optimal trajectories and vehicle geometries during conceptual design that account for this coupling. This results in the use of a more representative design solution for subsequent high fidelity analyses, thereby reducing the number of design iterations and saving time. However, since conceptual design involves the generation of several design concepts, a trade-off between analysis fidelity and computational speed is imminent. Nevertheless, such an analysis in conceptual design, even if of lower fidelity, is a substantial advancement in the state-of-the-art.

The first contribution of this dissertation described in Chapter 6 incorporates an ablation model into the flight dynamics model at a conceptual level. This integrated model is used in the indirect trajectory optimization framework. As a result, the control history is derived explicitly from the information contained in the coupling between ablative shape change and the flight dynamics.

### 2.3 Prior Work Related to Incorporating Rigid Body Dynamics Into Conceptual Mission Design

When a hypersonic vehicle is protected by an ablative TPS, its mass distribution continuously evolves throughout the trajectory. For instance, the center of mass constantly shifts, and the moment of inertia varies. This can have consequences in the controllability and the stability of the vehicle. This is illustrated in Figure 2.2, which shows the change in trim angle-of-attack ( $\alpha$ ) of an elliptic-parabolic vehicle, as its length changes (because of ablation) while the base ellipse and the control surface deflections are held constant. The vehicle becomes more stable, but less maneuverable, as it ablates.



(a) Initial (right) and final (left) vehicle geometries. (b) Plot of trim angle-of-attack corresponding to 20 deg. elevon deflection as the vehicle geometry evolves.

Figure 2.2. Illustration of variation of trim angle-of-attack with evolution of vehicle geometry.

Such analysis requires the vehicle to be modeled as a rigid body. However, traditional conceptual design analyses involve a point-mass 2-DOF or 3-DOF flight dynamics model [37–41] because the emphasis is usually on translational motion. As a result, they do not provide direct insight into the rigid body motion. For instance, it is not straightforward to determine whether the maneuverability of the vehicle is

sufficient to fly the calculated trajectory. It would therefore be beneficial to incorporate rigid body dynamics into conceptual mission design. This would also enable the simultaneous design of the trajectory, the configuration of the control surfaces (such as its location on the vehicle, geometry, etc.), and the required actuation force.

However, most of the literature available for rigid body analysis during conceptual design is confined to modeling aerothermoelastic effects and flight control system design [42–52]. Since they involve finite difference methods to solve for the aerothermal effects, they are not suited for trajectory optimization. This may be mitigated by using surrogate models in place of the finite difference models. For instance, Keshmiri et. al. [53] developed a 6-DOF model wherein the computational fluid dynamics (CFD) estimate of the aerodynamic coefficients was approximated by polynomial functions of angle-of-attack, side-slip angle, etc. This model was again predominantly developed for modeling and simulation purposes. This approach is not conducive for conceptual mission design because a higher fidelity analysis (CFD) is first required to be performed to develop the surrogate aerodynamic model, which defeats the purpose of conceptual design.

There is very limited literature that describes trajectory optimization with rigid body dynamics. Moreover, prior work involves major assumptions and does not use the indirect framework. For instance, Yokoyama et. al. [54] optimized the ascent trajectory of a space plane using rigid body dynamics by assuming: 1) the pitch rate to be zero at all times to address the numerical stiffness (which is in fact addressed in this dissertation) and 2) the vehicle to have the ability to achieve any angle-of-attack instantaneously. By definition, these assumptions reduce the rigid body to a point mass. Farooq and Limebeer [55] used acceleration demands in the body-fixed coordinates in the rigid body model as control variables. This approach contains no information about the control surface deflection angles. The optimizer outputs the time history of these control variables assuming that the vehicle’s autopilot solves the control allocation problem to generate the demanded acceleration corresponding to

the optimal trajectory. There is also no information about the drag penalty incurred by deflecting the control surfaces.

It is, therefore, very beneficial to design optimal trajectories with rigid body dynamics. It enables the concurrent design of the vehicle configuration that includes geometry, mass distribution, control surface geometry and location, etc. Creating this capability is also a significant advancement in the state-of-the-art because vehicle configuration and the trajectory are traditionally not simultaneously designed. Instead, they are designed in sequence and involves several time consuming design iterations. The second contribution of the dissertation explained in Chapter 7 describes the implementation of the rigid body flight dynamics model into conceptual hypersonic mission design. The optimal trajectories designed using this integrated framework are more representative of the vehicle's capabilities when compared to the current state-of-the-art. This approach is also conducive to implicitly capturing the aerodynamic trim conditions as the vehicle shape changes (for example, when the vehicle ablates).

## **2.4 Prior Work Related to the Design of Multi-Phase Trajectories**

The third contribution of the dissertation is the simplification of the design of hypersonic missions that involve multiple phases of flight. The trajectories of such multi-phase systems are governed by equations of motion that are piecewise continuous in time. For instance, the equations of motion of a two-stage launch vehicle have a discontinuity at the instance of stage separation because the parameters such as mass, aerodynamic coefficients, etc. change discretely. The performance index can also be unique for each phase of flight, thereby making it piecewise continuous as well. For example, during entry, descent, and landing (EDL), the trajectory might be optimized to minimize heat-load during the hypersonic phase and to minimize propellant consumption during powered descent to the surface. These systems can be viewed as autonomously switched hybrid systems [56], wherein the position and velocity states

form the continuous state variables, while the mode of operation (corresponding to before and after stage separation in a multi-stage launch vehicle) is the discrete state variable. A particular mode of operation is active when certain conditions on the continuous states and time are satisfied, making the system autonomously switched.

There is a wealth of literature that discusses the various approaches for the calculation of optimal trajectories of non-autonomously switched hybrid systems, wherein the mode sequence can be controlled. These approaches involve the computation of the optimal discrete state schedule through the pre-computation of optimality zones [57], relaxation techniques [58, 59], and the insertion of needle variations of the discrete state in a given discrete state sequence followed by the application of gradient methods [60].

For autonomously switched hybrid systems, optimal trajectories are in general computed using direct methods because of the ease of implementation and convergence. For example, direct collocation with sequential quadratic programming (SQP) was employed to determine the optimal start-up control of an evaporation system that was modeled as an interconnected hybrid system [61], to implement a model predictive control for the stabilization of wheeled mobile robots subject to wheel slippage [62], and to optimize the trajectory of boost-glide missiles with aeroheating considerations [63]. In another approach, optimal trajectories for multi-phase space missions were generated by dividing the problem into an outer and inner loop, wherein the outer loop optimized the discrete states using a genetic algorithm and the inner loop performed optimization on the continuous dynamics using nonlinear programming [64]. Also, pseudospectral methods were employed to design optimal multi-phase trajectories of hypersonic reconnaissance vehicles with temperature constraints [65].

Alternatively, indirect methods leverage the necessary conditions of optimality that result in a multi-point boundary value problem (MPBVP) in a system of differential-algebraic equations (DAEs), as described in [66] and [67]. In general, the calculation of solution from the necessary conditions of optimality is not straight-forward because

the associated numerical algorithms need to be initiated with a guess solution for all modes that is close to the actual solution, which is difficult to generate. The problem is exacerbated as the number of intermediate boundary conditions (switching instances) are increased. As a result, the solution approaches for optimal control problems for multi-phase aerospace systems traditionally avoid indirect methods. Nevertheless, there is some literature that discusses the indirect solution approach. In one such approach, the optimal control problem is transcribed into an equivalent problem that is parameterized by the switching instants [68]. The values of the derivatives of the cost functional based on the solution of a two-point boundary value problem (TP-BVP) in a system of DAEs are obtained. This method becomes exponentially more complex when the number of modes of operation increases because it necessitates the evaluation of every possible discrete state sequence. Another approach partially leverages indirect methods. The hybrid optimal control problem is divided into a two-step process, wherein the values of the continuous states at the switching manifolds are determined using gradient-based methods, and the trajectories that connect these states within each mode are computed using indirect methods [69]. However, a fully indirect approach has traditionally been ignored in the design of multi-phase trajectories.

The third contribution of the dissertation described in Chapter 8 simplifies the design of multi-phase trajectories within the indirect framework. A new methodology, named the relaxed autonomously switched hybrid system (RASHS) approach, is developed that fully leverages the indirect necessary conditions of optimality and addresses the associated challenges, in part, by relaxing the original problem using saturation functions to approximate the piecewise dynamics and cost functional as continuous equations. The new continuous equations of motion describe the motion of the vehicle for all phases of flight, such that the intermediate boundary conditions and the corresponding change in flight dynamics during the mode switchings are inherently satisfied. Moreover, the new continuous cost functional is also valid for all phases of flight. As a result, the multi-phase trajectory design problem is con-

verted into a single-phase problem. Therefore, the necessary conditions of optimality in the indirect framework result in a TPBVP wherein only the end-point boundary conditions need to be explicitly enforced.

## 2.5 Summary

This chapter described the state-of-the-art conceptual hypersonic mission design and the prior work that attempted to address the limitations of this design approach. The rest of this dissertation focuses on the individual contributions that addresses the limitations of the state-of-the-art by:

1. incorporating the effects of ablative shape change into mission design (Chapter 6),
2. incorporating rigid body dynamics into trajectory design (Chapter 7),
3. simplifying the design of multi-phase trajectories in the indirect framework (Chapter 8).

These contributions are combined into a unified conceptual hypersonic mission design framework (Chapter 9).

The primary purpose of mission design is the design of trajectories that are optimized to achieve the mission goals while satisfying constraints, and is explained in Chapter 5. These optimal trajectories are governed by the flight dynamics (explained in Chapter 3), which are in turn influenced by the aerodynamic forces and moments acting on the vehicle (explained in Chapter 4). In essence, Chapters 3 through 5 form the foundation for the contributions of this dissertation.

### 3. POINT-MASS FLIGHT DYNAMICS

This chapter describes the point-mass flight dynamics model used in this dissertation. The end-goal of this dissertation, which is to develop a mission design framework that combines all three contributions, incorporates a rigid body model. However, the contributions pertaining to the incorporation of ablative shape change into conceptual hypersonic mission design (Chapter 6) and the simplification of trajectory design of multi-phase systems (Chapter 8) are described using a point-mass model. The extension of this model to incorporate rigid body motion will be described in Chapter 7, which by itself is a contribution of this dissertation. Moreover, additional states will be introduced later in Chapter 6 to describe the evolution of the vehicle geometry resulting from the ablation of the thermal protection system. The present chapter will focus on the point-mass 3-DOF model, which will be the foundation upon which additional states will be introduced in subsequent chapters.

A spherically symmetric and rotating planet is assumed. The center of the planet is assumed to be inertial. The vehicle states are described by altitude,  $h$ , longitude,  $\theta$ , latitude,  $\phi$ , atmospheric-relative velocity,  $v$ , atmospheric-relative flight-path-angle,  $\gamma$ , and heading angle,  $\psi$ . The governing equations of motion are given as follows:

$$\begin{aligned} \frac{{}^i d\mathbf{r}}{dt} &= (\boldsymbol{\Omega} \times \mathbf{r}) + \mathbf{v} \\ {}^i \frac{d}{dt} ((\boldsymbol{\Omega} \times \mathbf{r}) + \mathbf{v}) &= \frac{\mathbf{F}}{m} \end{aligned} \quad (3.1)$$

where

$$\begin{aligned} \mathbf{r} &= (R + h) \left( \cos \phi \cos \theta \hat{\mathbf{X}}_G + \cos \phi \sin \theta \hat{\mathbf{Y}}_G + \sin \phi \hat{\mathbf{Z}}_G \right) \left( \right. \\ \mathbf{v} &= v \left( \cos \gamma \sin \psi \hat{\mathbf{e}}_E + \cos \gamma \cos \psi \hat{\mathbf{e}}_N + \sin \gamma \hat{\mathbf{e}}_Z \right) \end{aligned} \quad (3.2)$$

In Eq. (3.2),  $\mathbf{r}$  is the inertial position vector represented in the planet-centered planet-fixed coordinate frame, wherein  $\hat{\mathbf{X}}_G$ ,  $\hat{\mathbf{Y}}_G$  and  $\hat{\mathbf{Z}}_G$  are the unit vectors passing



through the 0 deg longitude, 90 deg longitude, and the geographical North pole, respectively, as illustrated in Figure 3.1(a). In this figure,  $\hat{\mathbf{X}}$ ,  $\hat{\mathbf{Y}}$  and  $\hat{\mathbf{Z}}$  are the inertial unit vectors and  $\boldsymbol{\Omega}$  is the angular velocity vector of the planet's rotation. Moreover,  $\mathbf{v}$  is the atmospheric relative velocity represented in the local horizon frame, wherein  $\hat{\mathbf{e}}_E$ ,  $\hat{\mathbf{e}}_N$ , and  $\hat{\mathbf{e}}_Z$  represent the unit vectors pointing East, North, and up (from the center of the planet) respectively, as shown in Figure 3.1(b). The superscript prefix  $i$  indicates an inertial time derivative.

The total force acting on the vehicle,  $\mathbf{F}$ , is given as:

$$\begin{aligned} \mathbf{F} = & (T \cos \alpha - D) \hat{\mathbf{x}}_W + (T \sin \alpha + L) \sin \sigma \hat{\mathbf{y}}_W \\ & + (T \sin \alpha + L) \cos \sigma \hat{\mathbf{z}}_W - \frac{\mu m}{(R + h)^2} \hat{\mathbf{e}}_Z \end{aligned} \quad (3.3)$$

where  $\hat{\mathbf{x}}_W$ ,  $\hat{\mathbf{y}}_W$  and  $\hat{\mathbf{z}}_W$  represent the unit vectors in the wind frame. Figure 3.1(c) illustrates the relationship between the local horizon and the wind frames. When the vehicle is flying East ( $\psi = 90$  deg) and at constant altitude ( $\gamma = 0$  deg),  $\hat{\mathbf{x}}_W$ ,  $\hat{\mathbf{y}}_W$  and  $\hat{\mathbf{z}}_W$  align with the local horizon unit vectors  $\hat{\mathbf{e}}_E$ ,  $\hat{\mathbf{e}}_N$  and  $\hat{\mathbf{e}}_Z$  respectively. Figure 3.1(d) illustrates the definition of  $\alpha$  and  $\sigma$ . The vehicle's roll, pitch and yaw axes are defined by the body-fixed unit vectors  $\hat{\mathbf{x}}_B$ ,  $\hat{\mathbf{y}}_B$  and  $\hat{\mathbf{z}}_B$  respectively.

Furthermore,  $T$  is the thrust force magnitude,  $\alpha$  is the angle-of-attack,  $\sigma$  is the bank angle,  $m$  is the instantaneous mass of the vehicle, and  $L$  and  $D$  are the lift and drag forces given by:

$$\begin{aligned} L &= \frac{1}{2} \rho_\infty v^2 C_L S \\ D &= \frac{1}{2} \rho_\infty v^2 C_D S \end{aligned} \quad (3.4)$$

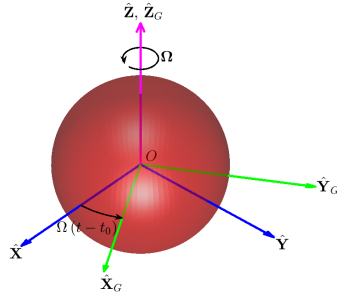
where  $C_L$  and  $C_D$  are the lift and drag coefficients, and  $S$  is the reference area. The derivation of  $C_L$  and  $C_D$  are explained in Chapter 4. Also,  $\rho_\infty$  is the freestream density of the stationary atmosphere. If the vehicle burns propellant, a new state  $m_F$  is introduced, which represents the mass of propellant consumed. The dynamics for  $m_F$  is given by:

$$\dot{m}_F = \dot{m}_{F,max} \frac{T}{T_{max}} \quad (3.5)$$

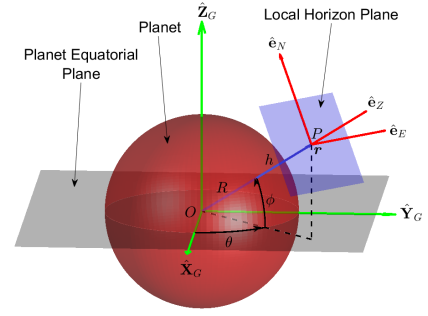
where  $T_{max}$  is the maximum thrust and  $\dot{m}_{F,max}$  is the corresponding maximum propellant flow rate. The instantaneous mass of the vehicle is then given by:

$$m = m_0 - m_F \quad (3.6)$$

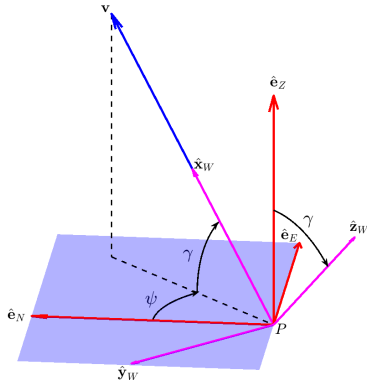
where  $m_0$  is the initial mass for a given flight segment.



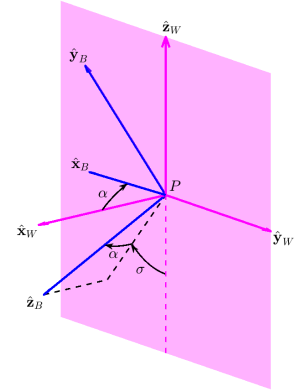
(a) Relationship between inertial and planet-centered planet-fixed frames.



(b) Relationship between planet-centered planet-fixed and local horizon frames.



(c) Relationship between local horizon and wind frames.



(d) Relationship between wind and body frames.

Figure 3.1. Relationship between coordinate frames.

The flight dynamics model explained in this chapter is used in trajectory optimization. The model is also modified accordingly to include additional states to represent vehicle geometry (Chapter 6) and rotational motion (Chapter 7). The next chapter describes the aerodynamics model that is used to derive  $C_L$  and  $C_D$ , which is in turn used in the flight dynamics model that was explained in this chapter.

## 4. AERODYNAMICS

### 4.1 Introduction

This chapter describes the aerodynamics model used in this dissertation. Since the class of missions relevant to this investigation involve flight predominantly in the atmosphere, the vehicle flight dynamics are predominantly influenced by the aerodynamic forces and moments. Traditionally, high fidelity aerodynamic analysis is performed to generate look-up tables, which are in turn used in the flight dynamics model. However, such tables cannot be used when the vehicle shape dynamically evolves along the trajectory because of ablation. As a result, it is necessary to employ a model that enables the rapid computation of the aerodynamic forces and moments for any given orientation of the vehicle with respect to the freestream. Consequently, the Modified Newtonian flow theory is primarily employed in conjunction with panel methods to calculate the steady aerodynamic force and moment coefficients. The effects of unsteady flow arising from the rotational motion of the vehicle relative to the freestream are incorporated using piston theory. The Modified Newtonian steady flow conditions are also used in the aerothermal analysis. The Modified Newtonian flow theory combined with piston theory facilitates a reasonable trade-off between accuracy and computational speed, which is necessary during conceptual mission design.

### 4.2 Steady Flow: Modified Newtonian Flow Theory

Newtonian flow theory [70] states that the collision of a fluid particle with the surface of a body is inelastic. The body is also assumed to be frictionless. As a result, the particle transfers all of its normal momentum to the body and retains its

tangential momentum, as illustrated in Figure 4.1(a). In this illustration,  $\mathbf{v}_\infty$  is the freestream vector or the relative wind vector. The direction of this vector is opposite to that of the atmospheric-relative velocity  $\mathbf{v}$  of the vehicle. The transfer of normal momentum results in a pressure force. The corresponding pressure coefficient is given by:

$$C_p = \frac{p - p_\infty}{\frac{1}{2}\rho_\infty v_\infty^2} = 2 \cos^2 \chi \quad (4.1)$$

The Modified Newtonian flow theory brings about a Mach number dependence on the estimated surface pressure based on the flow conditions downstream of the normal portion of the shock (Figure 4.1(b)). Behind the shock, the stagnation pressure  $p_0$  is given by:

$$p_0 = p_2 + \frac{1}{2}\rho_2 v_2^2 \quad (4.2)$$

Across the normal part of the shock, the velocity and density ratios are:

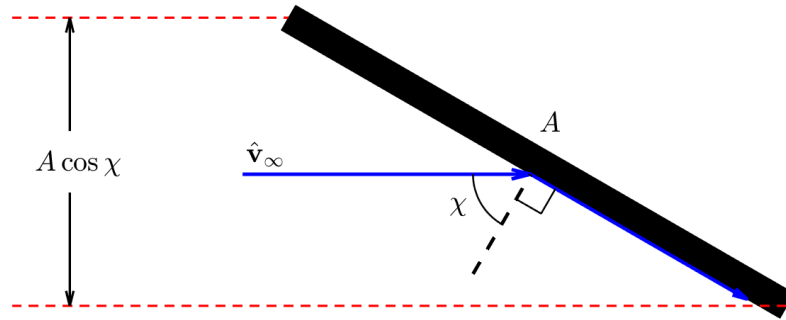
$$\frac{v_2}{v_\infty} = \frac{\rho_\infty}{\rho_2} = \epsilon \quad (4.3)$$

where  $\epsilon \ll 1$  at hypersonic conditions. The subscripts  $\infty$  and 2 refer to the flow conditions upstream and downstream of the normal portion of the shock. From conservation of momentum,

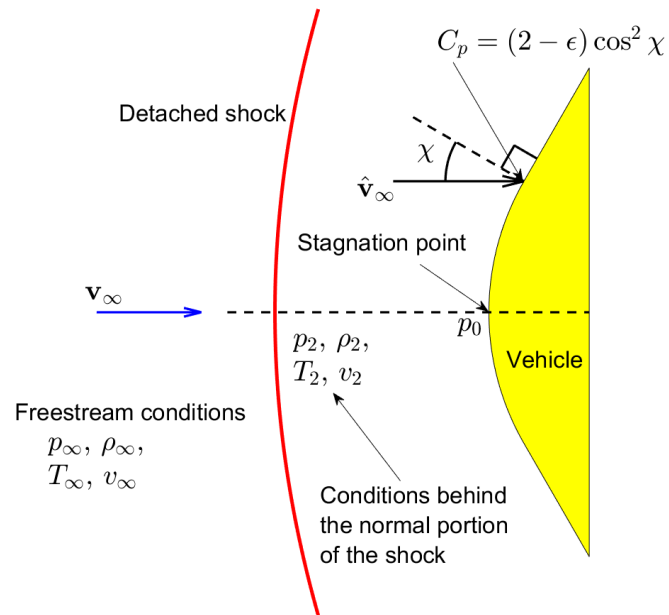
$$\begin{aligned} p_\infty + \rho_\infty v_\infty^2 &= p_2 + \rho_2 v_2^2 \\ p_2 &= p_\infty + \rho_\infty v_\infty^2 (1 - \epsilon) \end{aligned} \quad (4.4)$$

From Eqs. (4.2) and (4.4),

$$\begin{aligned} p_0 &= p_\infty + \frac{1}{2}\rho_\infty v_\infty^2 (2 - \epsilon) \\ C_{p,0} &= \frac{p_0 - p_\infty}{\frac{1}{2}\rho_\infty v_\infty^2} = 2 - \epsilon \end{aligned} \quad (4.5)$$



(a) Transfer of normal momentum between fluid particle and surface (image modified from Anderson [71]).



(b) The quantities downstream of the shock are computed assuming a normal shock.

Figure 4.1. Illustration of Modified Newtonian flow.

Consequently, Lees [72] proposed the following modification to Eq. 4.1:

$$C_p = (2 - \epsilon) \cos^2 \chi \quad (4.6)$$

Therefore, the pressure corresponding to steady flow conditions at a given point on the vehicle is given by:

$$p_e = \begin{cases} p_\infty + \frac{1}{2} \rho_\infty v_\infty^2 (2 - \epsilon) \cos^2 \chi, & \text{if unshadowed} \\ p_\infty, & \text{if shadowed} \end{cases} \quad (4.7)$$

The density and temperature at the local point are calculated by assuming an isentropic expansion of the fluid from the stagnation point to the local pressure,  $p_e$ . The stagnation density and temperature are given by:

$$\begin{aligned} \rho_0 &= \rho_2 \left( \frac{p_0}{p_2} \right)^{\frac{1}{\gamma}} \\ T_0 &= T_2 \frac{p_0^{\frac{\gamma-1}{\gamma}}}{p_2} \end{aligned} \quad (4.8)$$

where  $\gamma$  is the ratio of the specific heats at constant pressure and volume ( $c_p/c_v$ ). Moreover:

$$p_2 = p_\infty + \rho_\infty v_\infty^2 (1 - \epsilon) \quad (4.9)$$

Consequently, the local density and temperature are given by:

$$\begin{aligned} \rho_e &= \rho_2 \frac{p_e^{\frac{1}{\gamma}}}{p_2} \\ T_e &= T_2 \left( \frac{p_e}{p_2} \right)^{\frac{\gamma-1}{\gamma}} \end{aligned} \quad (4.10)$$

The freestream conditions are derived from a cubic spline interpolation of the 1976 US Standard Atmosphere model [73]. The local flow conditions ( $p_e$ ,  $\rho_e$  and  $T_e$ ) are used as the boundary layer edge conditions in the aerothermal analysis. They are also used in the piston theory analysis to account for unsteady flow, which will be discussed in Section 4.3.

### 4.3 Unsteady Flow: Piston Theory

Piston theory [74] accounts for unsteady flow resulting from rotational motion of the vehicle relative to the freestream. This model is required to incorporate rigid body motion in Chapter 7. According to this theory, the pressure exerted at a point on the vehicle is assumed to be equal to the pressure on the face of a piston placed at that point, moving into a column of perfect gas due to the rotational motion of the vehicle. This is illustrated in Figure 4.2. In the illustration,  $\omega$  is the angular velocity of the vehicle.

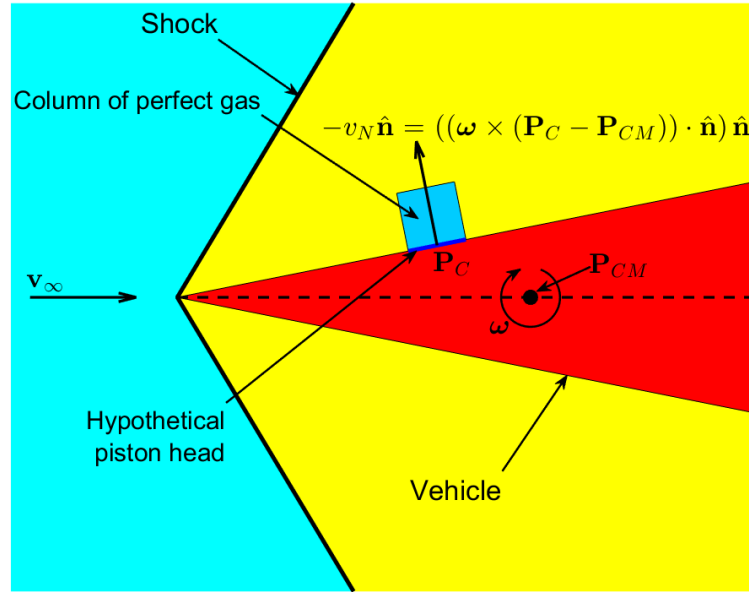


Figure 4.2. Illustration of unsteady flow analysis using piston theory.

The total pressure,  $p_t$ , on the face of the piston is given by:

$$\frac{p_t}{p_e} = \left( 1 + \frac{\gamma - 1}{2} \frac{v_N}{a_e} \right)^{\frac{2\gamma}{\gamma - 1}} \quad (4.11)$$

where the subscript  $e$  refers to the quantities corresponding to the steady flow conditions computed in Section 4.4.2. Additionally,  $a_e$  is the local speed of sound calculated



as  $\sqrt{\gamma R T_e}$ , where  $R$  is the specific gas constant, and  $v_N$  is the component of the velocity of the point of interest on the surface of the vehicle that is normal to the steady flow. The binomial expansion of Eq. (4.11) to first order results in:

$$\frac{p_t}{p_e} = 1 + \frac{2\gamma}{\gamma - 1} \frac{\gamma - 1}{2} \frac{v_n}{a_e} = 1 + \frac{\gamma v_N}{a_e} \quad (4.12)$$

Recognizing that  $p_e = \rho_e R T_e$  for a perfect gas and  $a_e^2 = \gamma R T_e$ , it can be shown that  $\gamma = \frac{a_e^2 \rho_e}{p_e}$ . Substituting this into Eq. (4.12) results in the basic result for first-order linear piston theory:

$$p_t = p_e + \rho_e a_e v_N \quad (4.13)$$

At a point  $\mathbf{P}_C$  on the vehicle that possesses an angular velocity vector  $\boldsymbol{\omega}$  with respect to its center of mass, the normal velocity  $v_N$  at  $\mathbf{P}_C$  is given by:

$$v_N = -(\boldsymbol{\omega} \times (\mathbf{P}_C - \mathbf{P}_{CM})) \cdot \hat{\mathbf{n}} \quad (4.14)$$

where  $\hat{\mathbf{n}}$  is the unit normal directed into the vehicle at the point of interest, and  $\mathbf{P}_{CM}$  is the center of mass of the vehicle with respect to the same reference point as that of  $\mathbf{P}_C$ . Consequently, the total pressure acting at  $\mathbf{P}_C$ , which is the sum of the pressure estimate  $p_e$  computed from steady flow conditions (from Modified Newtonian flow), and the quantity  $\rho_e a_e v_N$  that accounts for the unsteady flow, is given by:

$$p_t = p_e - ((\rho_e a_e \boldsymbol{\omega} \times (\mathbf{P}_C - \mathbf{P}_{CM})) \cdot \hat{\mathbf{n}}) \quad (4.15)$$

The total aerodynamic force acting on the vehicle and moment acting about the center of mass of the vehicle can be obtained by integrating this pressure  $p_t$  along the inward-pointing normal  $\hat{\mathbf{n}}$  at  $\mathbf{P}_C$  and the quantity  $(\mathbf{P}_C - \mathbf{P}_{CM}) \times p_t \hat{\mathbf{n}}$  respectively over the entire surface of the vehicle. That is:

$$\begin{aligned} \mathbf{F}_{AERO} &= \iint_A p_t \hat{\mathbf{n}} \, dA \\ \mathbf{M}_{AERO} &= \iint_A (\mathbf{P}_C - \mathbf{P}_{CM}) \times p_t \hat{\mathbf{n}} \, dA \end{aligned} \quad (4.16)$$

However, it is usually not possible to derive an analytical expression for these integrals. Therefore, panel methods are employed to evaluate the approximate values of these integrals, as explained in Section 4.4.

#### 4.4 Panel Methods

In panel methods [75], the vehicle geometry is approximated using flat plates. In this dissertation, the flat plates were represented by triangles and quadrilaterals. The aerodynamic force and moment (about the vehicle CM) are computed for each panel using the Modified Newtonian flow theory and piston theory. The force corresponding to a given panel is assumed to act at its centroid. Finally, the forces and moments corresponding to each panel are summed up to obtain the resultant force and moment vector acting on the entire vehicle.

The panel methods were uniquely developed and adopted into this dissertation in order to accommodate unsteady flow and geometry evolution resulting from TPS ablation. As a first step, the vehicle geometry is required to be approximated using flat plates. This is explained in the next section.

##### 4.4.1 Approximation of the Vehicle Geometry using Flat Panels

The first step in panel methods is to approximate the vehicle geometry using flat plates. In this dissertation, this task is accomplished by first deriving the analytical parametric representation of the surface that defines the geometry such that:

$$\mathbf{P} = \begin{bmatrix} x \\ y \\ z \end{bmatrix} = \mathbf{S}(c, d) \quad (4.17)$$

where  $c \in [c_L, c_U]$  and  $d \in [d_L, d_U]$  are the parameters that define the surface. Next, the domains of  $c$  and  $d$  are discretized into  $m$  and  $n$  samples such that the corresponding discretized values of  $c$  and  $d$  are given by:

$$\begin{aligned}
c_i &= c_L + \left( \frac{d_U - c_L}{m-1} \right) i, \text{ where } i = 0, 1, 2, \dots, m-1 \\
d_j &= d_L + \left( \frac{d_U - d_L}{n-1} \right) j, \text{ where } j = 0, 1, 2, \dots, n-1
\end{aligned} \tag{4.18}$$

The points on the surface corresponding to each combination of discretized  $c$  and  $d$  are given by:

$$\mathbf{P}(i, j) = \mathbf{S}(c_i, d_j) \tag{4.19}$$

Panels can be constructed such that adjacent points from Eq. (4.19) form their vertices. Therefore, the vertices of a given panel are  $\mathbf{P}(i, j)$ ,  $\mathbf{P}(i, j+1)$ ,  $\mathbf{P}(i+1, j+1)$  and  $\mathbf{P}(i+1, j)$ . All the panels can be constructed by varying  $i$  from 0 to  $m-2$ , and  $j$  from 0 to  $n-2$ .

In general, the vertices will be unique, resulting in a quadrilateral panel. It should be noted that some panels will have a repeated vertex. In such cases, one of the repeated vertices is dropped, resulting in a triangular panel. This is demonstrated using an example wherein a hemisphere is represented using flat panels. Let the hemisphere of interest be constructed from the portion of a unit sphere centered at the origin that is above the  $y-z$  plane in an  $x-y-z$  cartesian coordinate system. The parametric form of such a hemisphere is given by:

$$\begin{aligned}
\mathbf{P} &= \begin{bmatrix} x \\ y \\ z \end{bmatrix} = \begin{bmatrix} \cos(c) \\ \sin(c) \cos(d) \\ \sin(c) \sin(d) \end{bmatrix} \\
&\text{where } c \in \left[0, \frac{\pi}{2}\right], d \in [0, 2\pi]
\end{aligned} \tag{4.20}$$

Such a hemisphere is illustrated in Figure 4.3(a). Suppose the domain of  $c$  and  $d$  are discretized into  $m = 11$  and  $n = 11$  points each, the hemisphere can be represented by  $(m-1) \times (n-1) = 10 \times 10 = 100$  panels, as shown in Figure 4.3(b). It can immediately be seen that all panels comprised of the vertices  $\mathbf{P}(0, j)$ ,  $\mathbf{P}(0, j+1)$ ,  $\mathbf{P}(1, j+1)$  and  $\mathbf{P}(1, j)$  have a repeated vertex  $[1 \ 0 \ 0]^T$ . This vertex corresponds to

the points  $\mathbf{P}(0, j)$  and  $\mathbf{P}(0, j + 1)$ . One of these repeated vertices is dropped from each panel, resulting in 3 vertices, thereby making the corresponding panels triangular (marked magenta in Figure 4.3(b)). Other panels remain as quadrilaterals (marked cyan in Figure 4.3(b)).

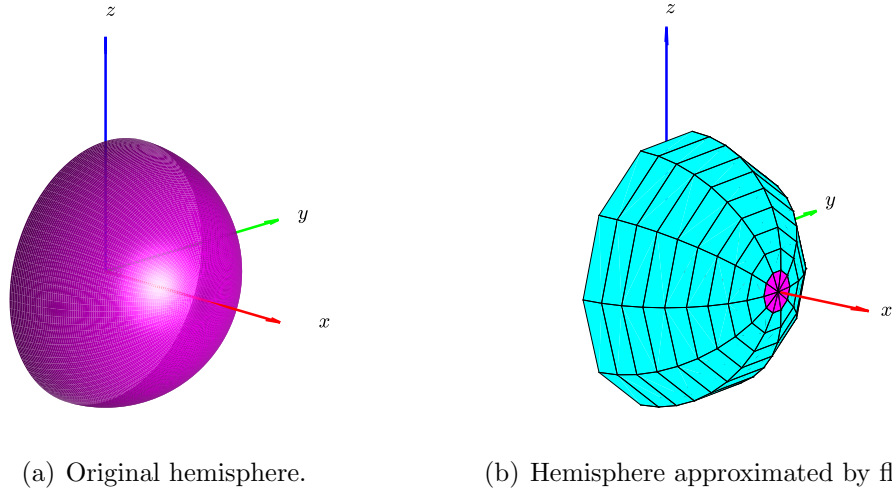


Figure 4.3. Representation of a smooth hemisphere using flat panels.

Once the panels are generated, the aerodynamic force and moment are calculated for each of them, as explained in Section 4.4.2.

#### 4.4.2 Computation of Aerodynamic Force and Moment for Each Panel

Following the generation of panels using the methodology explained in Section 4.4.1, the aerodynamic force and moment are computed for each of them. Figure 4.4 illustrates a triangular and a quadrilateral panel. Let the vertices of a given triangular panel be  $\mathbf{P}_1$ ,  $\mathbf{P}_2$ , and  $\mathbf{P}_3$  corresponding to  $W$ ,  $X$  and  $Y$  respectively. Furthermore, let the vertices of a given quadrilateral panel be  $\mathbf{P}_1$ ,  $\mathbf{P}_2$ ,  $\mathbf{P}_3$ , and  $\mathbf{P}_4$  corresponding to  $W$ ,  $X$ ,  $Y$  and  $Z$  respectively. The center of pressure of each panel is assumed to be located at its centroid.

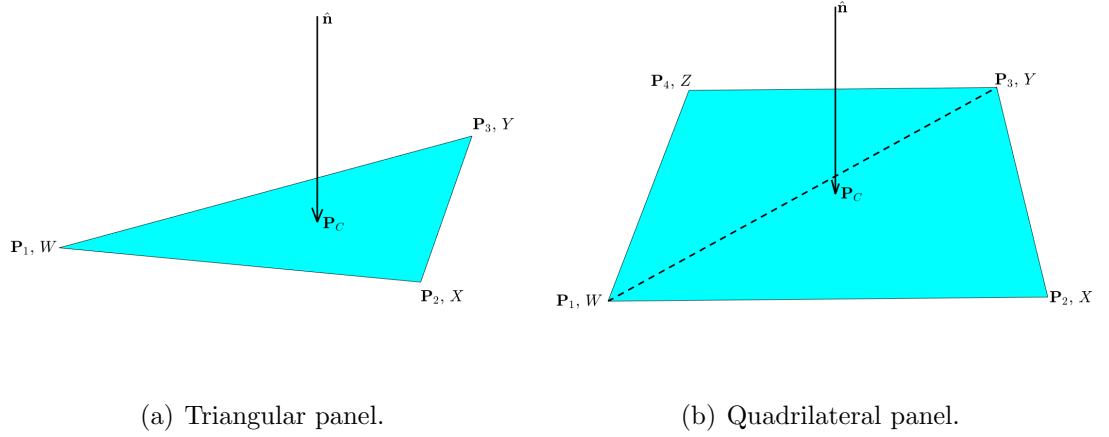


Figure 4.4. Illustration of triangular and quadrilateral panels along with centroid and unit inward-pointing normal vector.

The centroid of each panel is given by:

$$\mathbf{P}_C = \frac{\sum_{i=1}^n \mathbf{P}_i}{n} \quad (4.21)$$

where  $n = 3$  for a triangle and  $n = 4$  for a quadrilateral. The area of a triangular panel is given by:

$$\Delta A = \Delta WXY = \frac{1}{2} \sqrt{\begin{pmatrix} y_1 & z_1 & 1 \\ y_2 & z_2 & 1 \\ y_3 & z_3 & 1 \end{pmatrix}^2 + \begin{pmatrix} z_1 & x_1 & 1 \\ z_2 & x_2 & 1 \\ z_3 & x_3 & 1 \end{pmatrix}^2 + \begin{pmatrix} x_1 & y_1 & 1 \\ x_2 & y_2 & 1 \\ x_3 & y_3 & 1 \end{pmatrix}^2} \quad (4.22)$$

where  $x_i$ ,  $y_i$ , and  $z_i$  are the coordinates of each vertex of the triangle. That is:

$$\mathbf{P}_1 = \begin{bmatrix} x_1 & y_1 & z_1 \end{bmatrix}^T \quad (4.23a)$$

$$\mathbf{P}_2 = \begin{bmatrix} x_2 & y_2 & z_2 \end{bmatrix}^T \quad (4.23b)$$

$$\mathbf{P}_3 = \begin{bmatrix} x_3 & y_3 & z_3 \end{bmatrix}^T \quad (4.23c)$$

To calculate the area of a quadrilateral panel, it is first split into triangular sections. The area of these triangular sections are calculated using Eq. (4.22) and summed up to obtain the area of the quadrilateral panel. That is:

$$\Delta A = \Delta WXYZ = \Delta WXZ + \Delta ZXY \quad (4.24)$$

The unit normal for each panel is given by:

$$\hat{\mathbf{n}} = \frac{(\mathbf{P}_2 - \mathbf{P}_1) \times (\mathbf{P}_3 - \mathbf{P}_1)}{|(\mathbf{P}_2 - \mathbf{P}_1) \times (\mathbf{P}_3 - \mathbf{P}_1)|} \quad (4.25)$$

It should be noted that  $\hat{\mathbf{n}}$  is required to be inward-pointing. If Eq. (4.25) results in an outward-pointing unit normal, the negative of the computed vector is chosen as the unit normal. Suppose the angle between the inward-pointing unit normal of a given panel and the relative wind vector is  $\chi$ , it is clear that the panel is exposed to the wind when  $\chi \in (-\pi/2, \pi/2)$ . Consequently, the pressure corresponding to steady flow acting on the panel is:

$$p_e = \begin{cases} p_\infty + \frac{1}{2}\rho_\infty v_\infty^2 (2 - \epsilon) (\hat{\mathbf{v}}_\infty \cdot \hat{\mathbf{n}})^2, & \text{if } \hat{\mathbf{v}}_\infty \cdot \hat{\mathbf{n}} > 0 \\ p_\infty, & \text{otherwise} \end{cases} \quad (4.26)$$

where  $\hat{\mathbf{v}}_\infty$  is the unit relative wind vector. Accounting for unsteady flow arising from the rotational motion of the vehicle, the total pressure acting on the panel is given by:

$$p_t = p_e - \rho_e a_e ((\boldsymbol{\omega} \times (\mathbf{P}_C - \mathbf{P}_{CM})) \cdot \hat{\mathbf{n}}) \quad (4.27)$$

where  $\mathbf{P}_{CM}$  is the center of mass of the vehicle. The total force acting on the panel is given by:

$$d\mathbf{F} = p_t \Delta A \hat{\mathbf{n}} \quad (4.28)$$

This force is assumed to act at the centroid of the panel. Therefore, the moment acting on the panel about the center of mass of the vehicle is given by:

$$d\mathbf{M} = (\mathbf{P}_C - \mathbf{P}_{CM}) \times d\mathbf{F} \quad (4.29)$$

The total force acting on the vehicle and the moment acting about the center of mass of the vehicle is obtained by summing up the corresponding values for each panel:

$$\begin{aligned} \mathbf{F} &= \sum d\mathbf{F} \\ \mathbf{M} &= \sum d\mathbf{M} \end{aligned} \quad (4.30)$$

In essence, Eq. 4.30 approximates the integrals in Eq. 4.16. The approximate values converge to the corresponding exact values as the number of panels is increased. For certain geometries, it is possible to derive the analytical expression for the steady-state aerodynamic force and moment acting on the vehicle. These expressions were used to validate the results of aerodynamic force computation using panel methods, as discussed in Section 4.4.3.

#### 4.4.3 Validation of the Panel Methods

This section presents one of the validation cases of the panel methods. Validation was limited to steady-flow conditions, wherein the geometry does not exhibit rotational motion. The validation case presented in this section is that of a vehicle possessing a conical geometry subject to a steady flow. The cone has a half angle ( $\delta$ ) of 20 deg and a base radius ( $R_B$ ) of 0.5 m. The curved surface and the base of the cone are divided into 10,000 and 1,000 panels respectively. The original conical geometry and its approximation using panels are shown in Figure 4.5. The origin is at the cone's vertex. The angle-of-attack is varied between  $-18$  deg and  $18$  deg. The freestream conditions are shown in Table 4.1.

Since the side-slip angle is 0 deg, the force along the  $y$  axis, and moments about  $x$  and  $z$  axes are zero. It is therefore only required to calculate the force along  $x$  and  $z$  axes ( $F_x$  and  $F_z$ ) and moment about the  $y$  axis ( $M_y$ ). Moreover, the moment

Table 4.1. Freestream conditions for validation of panel methods.

Freestream condition	Value
Pressure ( $p_\infty$ )	1.172 kPa
Temperature ( $T_\infty$ )	226.65 K
Density ( $\rho_\infty$ )	0.018 kg/m <sup>3</sup>
Velocity ( $v_\infty$ )	4 km/s
Heat capacity ratio ( $c_p/c_v$ )	1.4

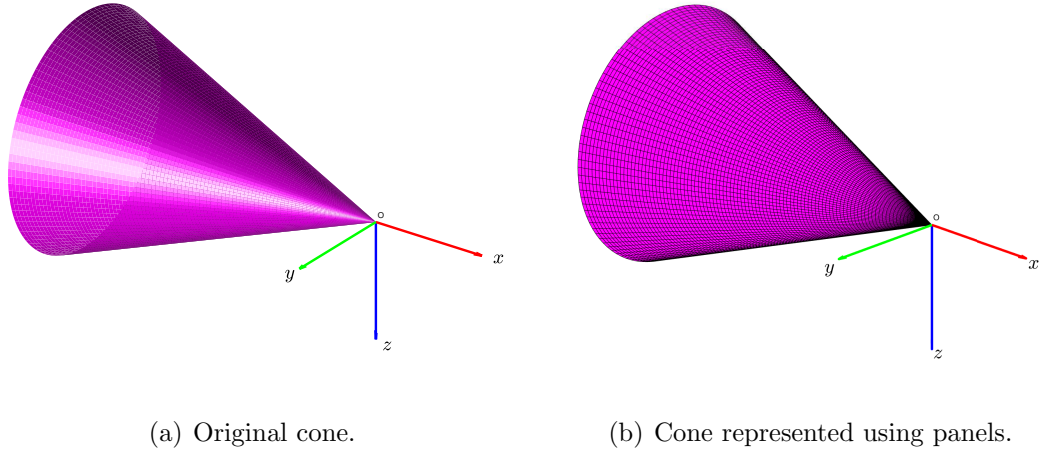


Figure 4.5. Illustration of the cone geometry used in validation of the panel method.

component  $M_y$  is computed about the origin (located at the vertex of the cone) and not the center of mass. This does not affect the validation because the moment about the center of mass can be readily calculated as:

$$\mathbf{M}_{AERO,CM} = \mathbf{M}_{AERO,O} - (\mathbf{P}_{CM} \times \mathbf{F}_{AERO}) \quad (4.31)$$

where  $\mathbf{M}_{AERO,CM}$  is the aerodynamic moment vector computed about the center of mass,  $\mathbf{M}_{AERO,O}$  is the aerodynamic moment computed about the origin, and  $\mathbf{F}_{AERO}$  is the aerodynamic force acting on the vehicle, which is also computed using panel



methods. If the computation of the force and moment about the origin are accurate, so will the computed moment about the center of mass.

It is possible to derive the analytical expression for  $F_x$ ,  $F_z$  and  $M_y$ . The parametric expression for the cone is given by:

$$\begin{aligned} \mathbf{P} &= \begin{bmatrix} -\frac{c}{\tan \delta} \\ c \cos(d) \\ c \sin(d) \end{bmatrix} \begin{pmatrix} \\ \\ \end{pmatrix} \\ c &\in [0, 0.5] \\ d &\in [0, 2\pi] \end{aligned} \quad (4.32)$$

The cartesian expression of the same cone is given by:

$$f = x^2 \tan^2 \delta - y^2 - z^2 = 0 \quad (4.33)$$

The inward-pointing normal at any point on the curved surface is given by:

$$\mathbf{n} = \nabla f = \begin{bmatrix} 2x \tan^2 \delta \\ -2y \\ -2z \end{bmatrix} \begin{pmatrix} \\ \\ \end{pmatrix} = \begin{bmatrix} -2c \tan \delta \\ -2c \cos(d) \\ -2c \sin(d) \end{bmatrix} \begin{pmatrix} \\ \\ \end{pmatrix} \quad (4.34)$$

Consequently, the inward-pointing unit normal is given by:

$$\hat{\mathbf{n}} = \begin{bmatrix} -\sin \delta \\ -\cos(d) \cos \delta \\ -\sin(d) \cos \delta \end{bmatrix} \begin{pmatrix} \\ \\ \end{pmatrix} \quad (4.35)$$

The relative wind unit vector is given by:

$$\mathbf{v}_\infty = \begin{bmatrix} \cos \alpha \\ 0 \\ \sin \alpha \end{bmatrix} \begin{pmatrix} \\ \\ \end{pmatrix} \quad (4.36)$$

The aerodynamic force acting on the curved surface of the cone is given by:

$$\begin{aligned}
\mathbf{F}_{CURVED} &= \int_{c=0}^{R_B} \int_{d=0}^{2\pi} \frac{c}{\sin \delta} \left( p_{\infty} + \frac{1}{2} \rho_{\infty} v_{\infty}^2 (2 - \epsilon) (\hat{\mathbf{v}}_{\infty} \cdot \hat{\mathbf{n}})^2 \right) \hat{\mathbf{n}} \, dd \, dc \\
&= \left[ \begin{pmatrix} \frac{1}{2} \rho_{\infty} v_{\infty}^2 (2 - \epsilon) \frac{\pi R_B^2}{2} (\sin^2 \alpha + 2 \sin^2 \delta - 3 \sin^2 \alpha \sin^2 \delta) \\ 0 \end{pmatrix} \begin{pmatrix} \pi R_B^2 p_e \end{pmatrix} \right] \begin{pmatrix} \\ \\ -\frac{1}{2} \rho_{\infty} v_{\infty}^2 (2 - \epsilon) \pi R_B^2 \cos \alpha \cos^2 \delta \sin \alpha \end{pmatrix} \begin{pmatrix} \\ \\ \end{pmatrix} \quad (4.37)
\end{aligned}$$

The aerodynamic moment acting on the curved surface about the origin is given by:

$$\begin{aligned}
\mathbf{M}_{CURVED} &= \int_{c=0}^{R_B} \int_{d=0}^{2\pi} \frac{c}{\sin \delta} \left[ \mathbf{P} \times \left( p_{\infty} + \frac{1}{2} \rho_{\infty} v_{\infty}^2 (2 - \epsilon) (\hat{\mathbf{v}}_{\infty} \cdot \hat{\mathbf{n}})^2 \right) \hat{\mathbf{n}} \right] \, dd \, dc \\
&= \left[ \begin{pmatrix} 0 \\ -\frac{1}{2} \rho_{\infty} v_{\infty}^2 (2 - \epsilon) \frac{2\pi R_B^3 \cos \alpha \cos \delta \sin \alpha}{3 \sin \delta} \\ 0 \end{pmatrix} \right] \begin{pmatrix} \\ \\ \end{pmatrix} \quad (4.38)
\end{aligned}$$

Since the base of the cone is always shadowed, the aerodynamic force and moment acting on that portion of the geometry can be readily computed as:

$$\begin{aligned}
\mathbf{F}_{BASE} &= \begin{bmatrix} \pi R_B^2 p_e \\ 0 \\ 0 \end{bmatrix} \begin{pmatrix} \\ \\ \end{pmatrix} \\
\mathbf{M}_{BASE} &= \mathbf{0}
\end{aligned} \quad (4.39)$$

The total aerodynamic force and moment acting on the vehicle are given by:

$$\begin{aligned}
\mathbf{F}_{AERO} &= \mathbf{F}_{CURVED} + \mathbf{F}_{BASE} \\
&= \begin{bmatrix} \left( \frac{1}{2} \rho_{\infty} v_{\infty}^2 (2 - \epsilon) \frac{\pi R_B^2}{2} (\sin^2 \alpha + 2 \sin^2 \delta - 3 \sin^2 \alpha \sin^2 \delta) \right) \\ 0 \\ \left( -\frac{1}{2} \rho_{\infty} v_{\infty}^2 (2 - \epsilon) \pi R_B^2 \cos \alpha \cos^2 \delta \sin \alpha \right) \end{bmatrix} \begin{pmatrix} \\ \\ \end{pmatrix} \\
\mathbf{M}_{AERO,O} &= \mathbf{M}_{CURVED} + \mathbf{M}_{BASE} \\
&= \begin{bmatrix} \left( 0 \right) \\ \left( -\frac{1}{2} \rho_{\infty} v_{\infty}^2 (2 - \epsilon) \frac{2\pi R_B^3 \cos \alpha \cos \delta \sin \alpha}{3 \sin \delta} \right) \\ \left( 0 \right) \end{bmatrix} \begin{pmatrix} \\ \\ \end{pmatrix} \quad (4.40)
\end{aligned}$$

Therefore:

$$\begin{aligned}
F_x &= \frac{1}{2} \rho_{\infty} v_{\infty}^2 (2 - \epsilon) \frac{\pi R_B^2}{2} (\sin^2 \alpha + 2 \sin^2 \delta - 3 \sin^2 \alpha \sin^2 \delta) \\
F_z &= -\frac{1}{2} \rho_{\infty} v_{\infty}^2 (2 - \epsilon) \pi R_B^2 \cos \alpha \cos^2 \delta \sin \alpha \\
M_y &= -\frac{1}{2} \rho_{\infty} v_{\infty}^2 (2 - \epsilon) \frac{2\pi R_B^3 \cos \alpha \cos \delta \sin \alpha}{3 \sin \delta} \quad (4.41)
\end{aligned}$$

The comparison of the estimates of the force and moment components computed using panel methods and the analytical expressions is illustrated in Figure 4.6. It can be seen that the panel methods approximate the analytical expressions very well. The accuracy will increase with the number of panels used to approximate the geometry. Therefore, panel methods can serve as an effective tool in computing the hypersonic aerodynamic force and moments using the Modified Newtonian flow theory when analytical solutions do not exist. This is especially true when the effects of ablative shape change are incorporated into mission design (Chapter 6), wherein the vehicle assumes an arbitrary shape as a result of ablation of the thermal protection system.

Upon the calculation of the aerodynamic force and moment, the lift, drag and moment coefficients need to be computed, as explained in Section 4.5.

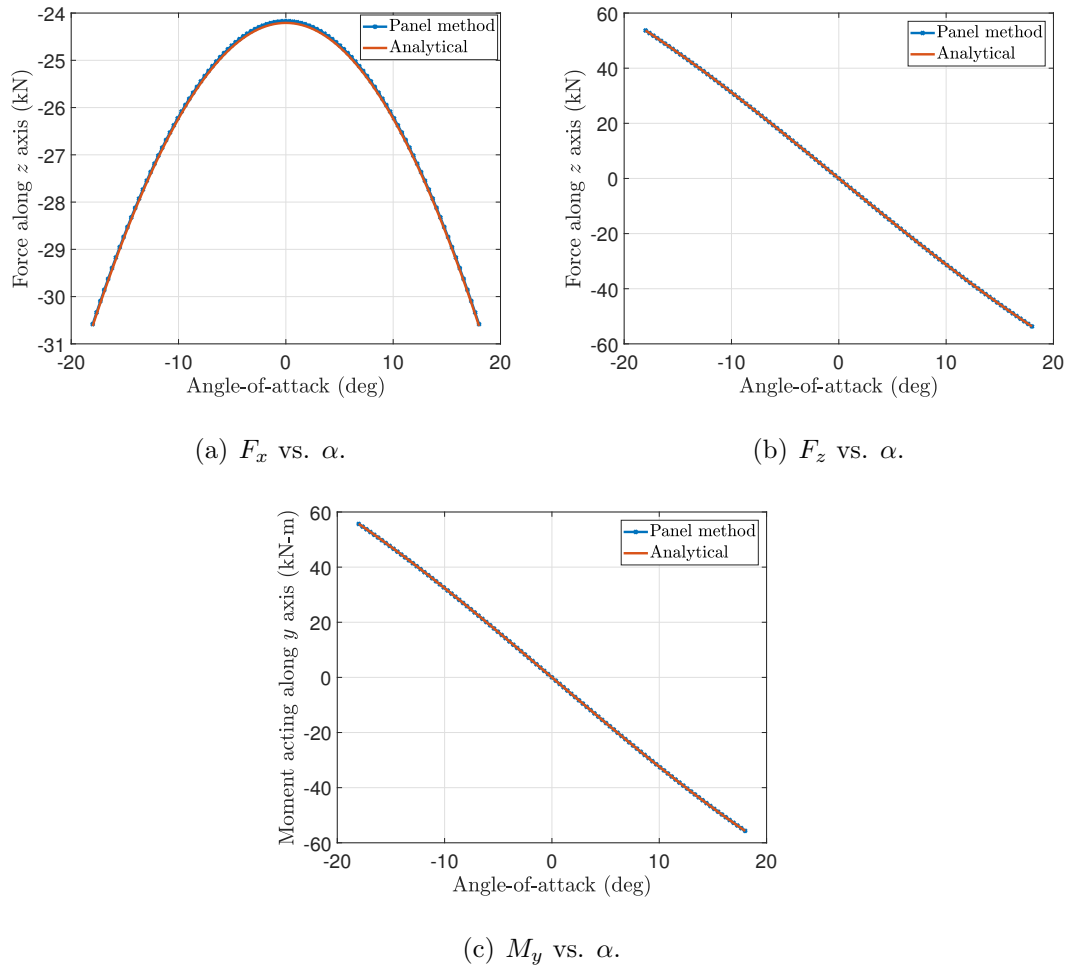


Figure 4.6. Illustration of validation of the panel methods.

#### 4.5 Computation of Lift, Drag and Moment Coefficients

The aerodynamic force and moments computed in the body frame are nondimensionalized to obtain the corresponding coefficients. Figure 4.7 shows the transformation from the wind frame to the body frame.

Assuming that the sideslip angle is 0 deg, the lift force is given by the projection of the aerodynamic force on the  $y$ - $z$  plane of the wind frame. The drag force is obtained by projecting the aerodynamic force onto the negative  $x$  axis of the wind frame. That is:

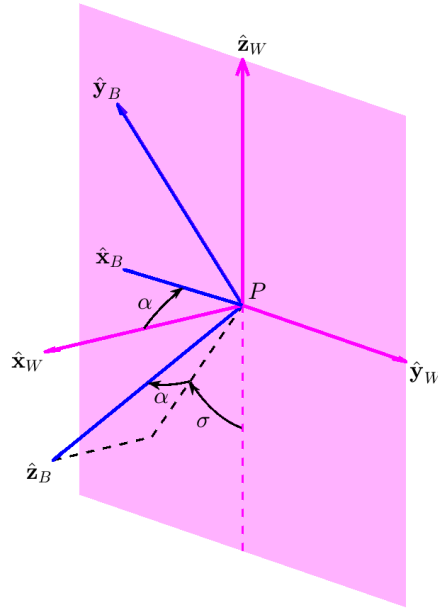


Figure 4.7. Relationship between wind and body frames.

$$\begin{aligned} L &= F_{x,B} \sin \alpha - F_{z,B} \cos \alpha \\ D &= -F_{x,B} \cos \alpha - F_{z,B} \sin \alpha \end{aligned} \quad (4.42)$$

where  $F_{x,B}$  and  $F_{z,B}$  are the aerodynamic force components in the body-fixed  $x$  and  $z$  axes respectively. The lift and drag coefficients are obtained by dividing the lift and drag forces by the dynamic pressure times the reference area:

$$\begin{aligned} C_L &= \frac{L}{\frac{1}{2} \rho_{\infty} v_{\infty}^2 S} \\ C_D &= \frac{D}{\frac{1}{2} \rho_{\infty} v_{\infty}^2 S} \end{aligned} \quad (4.43)$$

The aerodynamic moment coefficients are obtained by nondimensionalizing the aerodynamic moment components in the body frame as follows:

$$\begin{aligned}
CM_{x,B} &= \frac{M_{x,B}}{\frac{1}{2}\rho_\infty v_\infty^2 Sl} \\
CM_{y,B} &= \frac{M_{y,B}}{\frac{1}{2}\rho_\infty v_\infty^2 Sl} \\
CM_{z,B} &= \frac{M_{z,B}}{\frac{1}{2}\rho_\infty v_\infty^2 Sl}
\end{aligned} \tag{4.44}$$

If the side-slip angle is zero for a vehicle whose geometry is symmetric about the body-fixed  $x$ - $z$  frame,  $CM_x$  and  $CM_z$  will be zero.

It should be noted that this dissertation involves several examples wherein the ascent trajectories of launch vehicles and boost-glide trajectories of weapon systems are optimized. Since the vehicles in these examples are stationary at the beginning, the initial portion of their trajectories is subsonic. However, the computation of the boundary layer edge conditions requires the freestream Mach number to be greater than one. As a result, a fictitious freestream Mach number  $\mathcal{M}_\infty$  is introduced such that it is equal to 1 when the vehicle is flying subsonic, and equal to  $M_\infty$  when it is flying supersonic and hypersonic. That is:

$$\mathcal{M}_\infty = \begin{cases} 1, & \text{if } M_\infty < 1 \\ M_\infty, & \text{otherwise} \end{cases} \tag{4.45}$$

However, this introduces a discontinuity in the derivative of  $\mathcal{M}_\infty$  (with respect to time and states) when  $M_\infty = 1$ . This will force the trajectory optimization problem into an MPBVP, which is difficult to solve. As a result, Eq. (4.45) is approximated as follows:

$$\mathcal{M}_\infty \approx \frac{1}{1 + e^{s(M_\infty - 1)}} + \frac{M_\infty}{1 + e^{-s(M_\infty - 1)}} \tag{4.46}$$

where  $s$  is a slope parameter. In essence, Eq. (4.46) makes the corner point at Mach one in Eq. (4.45) smooth, thereby removing the discontinuity in the derivative. An arbitrarily high value for  $s$  may be chosen to approximate Eq. (4.45) well.

It should be noted that  $\mathcal{M}_\infty$  is used exclusively for the computation of the edge conditions of the boundary layer and normalizing the aerodynamic forces. The actual

Mach number ( $M_\infty$ ) is used to re-dimensionalize these coefficients to compute the lift, drag and moment.

This approximation assumes that the vehicle remains in the subsonic regime only briefly, as is the case in launch and boost-glide trajectories. Moreover, this approximation over-predicts the aerodynamic force and moments, thereby providing a conservative trajectory solution resulting from the higher wave drag. This dissertation dispensed with the use of the fictitious Mach number in missions where the vehicle was not expected to operate in the subsonic regime, as is the case in hypersonic glide trajectory design. In the future, a more sophisticated model for subsonic regime may be incorporated.

## 4.6 Summary

The methodology explained in this Chapter enables the rapid evaluation of aerodynamic forces, moments and edge conditions for an arbitrary 3-D body. The edge conditions corresponding to steady flow will be used in the aerothermal analysis described in Chapter 6. The force and moment computations that account for unsteady flow conditions will be used in rigid body dynamics (Chapter 7). The computed aerodynamic coefficients are substituted into the flight dynamics model described in Chapter 3, which is in turn used in the indirect trajectory optimization framework, explained in Chapter 5.

## 5. TRAJECTORY OPTIMIZATION USING INDIRECT METHODS

### 5.1 Introduction

The fundamental task of mission design is the calculation of trajectories that satisfy the mission requirements while simultaneously satisfying several constraints. Such trajectories are often optimized to minimize a performance index or cost functional,  $J$ . This dissertation implements the indirect methods of trajectory optimization, as explained in the rest of this chapter.

A trajectory optimization problem may be posed as follows:

$$\begin{aligned}
 \text{Minimize } J &= \Phi(\mathbf{X}(t_f), t_f) + \int_{t_0}^{t_f} \mathcal{L}(\mathbf{X}, \mathbf{U}, t) dt \\
 \dot{\mathbf{X}} &= \mathbf{f}(\mathbf{X}, \mathbf{U}, t) \\
 t_0 &= 0 \\
 \Psi_0(\mathbf{X}(t_0), t_0) &= 0 \\
 \Psi_f(\mathbf{X}(t_f), t_f) &= 0 \\
 c_i(\mathbf{X}) &\in [c_i^-, c_i^+] \left( \begin{aligned} d_k(\mathbf{X}, \mathbf{U}) &\in [d_k^-, d_k^+] \\ i &= 1, \dots, p \\ k &= 1, \dots, q \end{aligned} \right.
 \end{aligned} \tag{5.1}$$

It is required to design an optimal trajectory that minimizes the cost functional  $J$ . This functional can be characterized by a terminal cost,  $\Phi$ , and a path cost,  $\mathcal{L}$ , the Lagrangian. In an aerospace problem, the terminal cost may be a quantity such as velocity that is required to be minimized at the terminal point of the trajectory. The



path cost is a quantity that is required to be minimized throughout the trajectory. For instance, it might be required to minimize the stagnation-point heat-rate along the trajectory of an EDL vehicle. The optimal trajectory is required to satisfy the flight dynamics,  $\mathbf{f}$ . The vehicle's motion is described by the state vector,  $\mathbf{X}$ . The vehicle may be controlled by several variables such as angle-of-attack, bank angle, etc., as described by the control vector,  $\mathbf{U}$ . The optimal trajectory is also required to satisfy certain conditions at the initial and terminal points, as defined by  $\Psi_0$  and  $\Psi_f$ . An example of such conditions may be that the vehicle's initial and terminal altitude are required to be certain values. The vehicle is also subject to path constraints that are required to be satisfied along the entire trajectory, as described by  $c$  and  $d$ . These constraints may be defined by lower and upper bounds. The constraint  $c$  is only a function of states. An example of such a constraint is that the vehicle is not allowed to climb above a certain altitude. The constraint  $d$  is a function of both control and states. An example of such a constraint would be that the g-load is required to be within a certain value to limit the structural loads. The g-load is a function of angle-of-attack (control), dynamic pressure (which in turn is a function of the state variables, altitude and velocity), vehicle geometry, etc. There exist a variety of techniques to determine the solution of the trajectory optimization problem defined by Eq. (5.1) [76]. As explained in the next section, the direct methods are widely employed to calculate optimal trajectories.

### 5.1.1 Direct Methods of Trajectory Optimization and Their Key Limitations

As mentioned, the direct methods are widely employed to perform trajectory optimization, particularly with the advent of modern computing technology [77–81]. This approach gained traction because of the simplicity in setting up the problem and the relative ease of convergence. These methods involve the discretization of the trajectory and treating the time, states, and control at each node as design variables.

The states at adjacent nodes are related by difference equations. The control variables between these nodes are assumed to be linear. In essence, a constrained parametric optimization is performed, wherein the difference equations, control relations and boundary conditions constitute the equality constraints, and the path constraints constitute the inequality constraints. This problem is solved using techniques such as SQP. There are several software packages that perform trajectory optimization using direct methods [82–84]. The state-of-the-art is GPOPS II [82], which employs an hp-adaptive version of the Legendre-Gauss-Radau orthogonal collocation method [85–88].

The fundamental shortcoming of direct methods is that the optimality of the solution is not guaranteed. The trajectory is discretized before optimization is performed. Since discretization results in loss of some information about the problem, the subsequent optimization process does not use all the information contained in the problem, potentially resulting in suboptimal results. Furthermore, the discretization in fact alters the original problem, and additional local minima that don't exist in the original problem might be introduced. The fundamental limitations of direct methods are addressed by the indirect framework, which is described in the next section.

### 5.1.2 The Need for Indirect Methods of Trajectory Optimization

Indirect methods avoid the limitations of direct methods by performing the optimization before discretization. Consequently, the optimization process takes advantage of every available information in the problem, thereby guaranteeing the solution to be at least locally optimal. This approach involves the determination of the extremum of the cost functional  $J$  using the calculus of variations [89,90], resulting in the first order necessary conditions of optimality [91,92]. These necessary conditions result in a boundary value problem in a system of DAEs. Consequently, the optimization problem is reduced to that of root solving, which is in turn solved numerically. Because of this key advantage, this dissertation employed indirect methods to per-

form trajectory optimization. The next section describes the necessary conditions of optimality in the indirect framework.

## 5.2 Indirect Methods - The Necessary Conditions of Optimality

### 5.2.1 Unconstrained Trajectory Optimization Problems

In the absence of path constraints, the optimization problem is typically posed as:

$$\begin{aligned}
 \text{Minimize } J &= \Phi(\mathbf{X}(t_f), t_f) + \int_{t_0}^{t_f} \mathcal{L}(\mathbf{X}, \mathbf{U}, t) dt \\
 \dot{\mathbf{X}} &= \mathbf{f}(\mathbf{X}, \mathbf{U}, t) \\
 t_0 &= 0 \\
 \Psi_0(\mathbf{X}(t_0), t_0) &= 0 \\
 \Psi_f(\mathbf{X}(t_f), t_f) &= 0
 \end{aligned} \tag{5.2}$$

The cost functional is augmented as follows:

$$\begin{aligned}
 J' &= \Phi(\mathbf{X}(t_f), t_f) + \int_{t_0}^{t_f} \left( \mathcal{L}(\mathbf{X}, \mathbf{U}, t) + \boldsymbol{\lambda}^T (\mathbf{f}(\mathbf{X}, \mathbf{U}, t) - \dot{\mathbf{X}}) \right) dt \\
 &= \Phi(\mathbf{X}(t_f), t_f) + \int_{t_0}^{t_f} \left( \mathbf{H}(\mathbf{X}, \mathbf{U}, \boldsymbol{\lambda}, t) - \boldsymbol{\lambda}^T \dot{\mathbf{X}} \right) dt
 \end{aligned} \tag{5.3}$$

where  $\mathbf{H} = \mathcal{L} + \boldsymbol{\lambda}^T \mathbf{f}$  is the Hamiltonian. An additional vector  $\boldsymbol{\lambda}$ , the co-state vector, is introduced to adjoin the equality constraint defined by the dynamics. However, it should be noted that this dissertation employs the method described in [93] and [94], wherein the equality constraints defined by the end-point boundary conditions are not adjoined to the cost functional. Following the construction of the augmented cost functional, its first order variation is calculated and set to zero:

$$\delta J' = 0 \tag{5.4}$$

The necessary conditions of optimality are obtained by setting each term in the variation in Eq. (5.4) to zero [91]:

$$\begin{aligned}
\dot{\boldsymbol{\lambda}} &= - \left( \frac{\partial \mathbf{H}}{\partial \mathbf{X}} \right)^T \\
\frac{\partial \mathbf{H}}{\partial \mathbf{U}} &= 0 \\
\dot{\mathbf{X}} &= \mathbf{f}(\mathbf{X}, \mathbf{U}, t) \\
t_0 &= 0 \\
\Psi_0(\mathbf{X}(t_0), t_0) &= 0 \\
\Psi_f(\mathbf{X}(t_f), t_f) &= 0 \\
\mathbf{H}(\mathbf{X}(t_f), \mathbf{U}(t_f), \boldsymbol{\lambda}(t_f), t_f) dt_f - \mathbf{H}(\mathbf{X}(t_0), \mathbf{U}(t_0), \boldsymbol{\lambda}(t_0), t_0) \\
&\quad - \boldsymbol{\lambda}^T(t_f) d\mathbf{X}(t_f) + \boldsymbol{\lambda}^T(t_0) d\mathbf{X}(t_0) + d\Phi(\mathbf{X}(t_f), t_f) = 0
\end{aligned} \tag{5.5}$$

Eq. (5.5), called the Euler-Lagrange equations, shows that the control history is explicitly derived from the Hamiltonian, which in turn contains the physics of the problem. As a result, all of the optimality information is used in deriving the necessary conditions of optimality. The necessary conditions represent a TPBVP in a system of DAEs. For almost every problem of interest, this system does not have an analytical solution, and hence, is required to be solved numerically. The numerical solution approach will be explained in Section 5.3. The next section explains the incorporation of the path constraints into the optimization problem.

### 5.2.2 Constrained Trajectory Optimization Problems

Traditionally, in the indirect framework, constrained trajectory optimization problems are handled by introducing additional Lagrange multipliers [91]. The trajectory is in turn divided into multiple arcs depending on whether or not the constraint is active. This approach is explained in Appendix A. The challenge of this approach is that the necessary conditions of optimality result in an MPBVP, which is difficult to solve because the numerical solvers are required to be supplied with an initial guess

for every arc. Moreover, the guess is required to be close to the actual solution to guarantee convergence. It is therefore beneficial to reduce the MPBVP to a TPBVP, which is much easier to handle.

Graichen et al. [95] developed a methodology that reduces the necessary conditions of optimality of constrained trajectory optimization problems to a TPBVP. In this methodology, each inequality constraint in Eq. (5.1) is equated to a saturation function, resulting in additional sets of differential and algebraic equations. The saturation functions are chosen such that they asymptote to the upper and lower bounds defined by the corresponding original inequality path constraint. The additional differential equations implicitly account for the interior boundary conditions that result in the traditional necessary conditions of optimality, thereby reducing it to a TPBVP. The path constraints can be categorized into those that are functions of states only, and others that are functions of both states and control. The former results in additional states and controls, while the latter results in additional controls only, as demonstrated in the next two subsections.

### **Inequality Path Constraints that are Functions of States Only**

In the original optimal control problem in Eq. (5.1), each inequality state constraint  $c_i$  is equated to an appropriate saturation function so that:

$$c_i(\mathbf{X}) = \psi_i(\xi_{i,1}) \text{ where } i = 1, \dots, p \quad (5.6)$$

The variables  $\xi_{i,1}$  are added as states and Eq. (5.6) is differentiated until the control  $\mathbf{U}$  appears explicitly. New states,  $\xi_{i,j+1}$ , are added to replace the derivatives  $\dot{\xi}_{i,j}$ . Assuming the control appears at the  $r_i^{th}$  derivative of a given constraint  $c_i$ , the corresponding final derivative of  $\xi_{i,1}$ , that is,  $\dot{\xi}_{i,r_i}$  is set equal to a new control variable  $u_i$ . Consequently, the augmented dynamic system of equations is constructed as given below:

$$\begin{aligned}
\dot{\xi}_{i,j} &= \xi_{i,j+1} \\
\dot{\xi}_{i,r_i} &= u_i \\
\dot{\mathbf{X}} &= \mathbf{f}(\mathbf{X}, \mathbf{U}, t)
\end{aligned} \tag{5.7}$$

where  $i = 1, \dots, p$  and  $j = 1, \dots, r_i - 1$

### Inequality Path Constraints that are Functions of States and Control

Inequality path constraints that are functions of states and control are easier to handle. Similar to the path constraints that are functions of states only, the mixed state-control constraints are also directly substituted by additional saturation functions:

$$d_k(\mathbf{X}, \mathbf{U}) = \phi_k(w_k) \tag{5.8}$$

where  $w_i$  are the additional unconstrained control variables. Since control  $\mathbf{U}$  already appears in Eq. (5.8), no successive total time derivatives are necessary. Consequently, no additional state variables are introduced.

The saturation functions  $\psi$  and  $\phi$  whose upper and lower bounds are finite may be represented by appropriate sigmoid functions that saturate at these bounds. For instance, the constraint  $c_i$  with finite lower and upper bounds  $c_i^-$  and  $c_i^+$  respectively may be represented by the following sigmoid function:

$$\psi_i = c_i^- + \frac{c_i^+ - c_i^-}{1 + e^{-s \cdot \xi_{i,1}}} \tag{5.9}$$

where  $s$  represents the steepness of the transition from the lower to the upper bound. Figure 5.1 illustrates such a sigmoid functions whose bounds are 10 and 20, with  $s = 1$ .

If one of the bounds of the constraints is infinity, an appropriate one-sided saturation function such as an exponential function may be constructed. The saturation

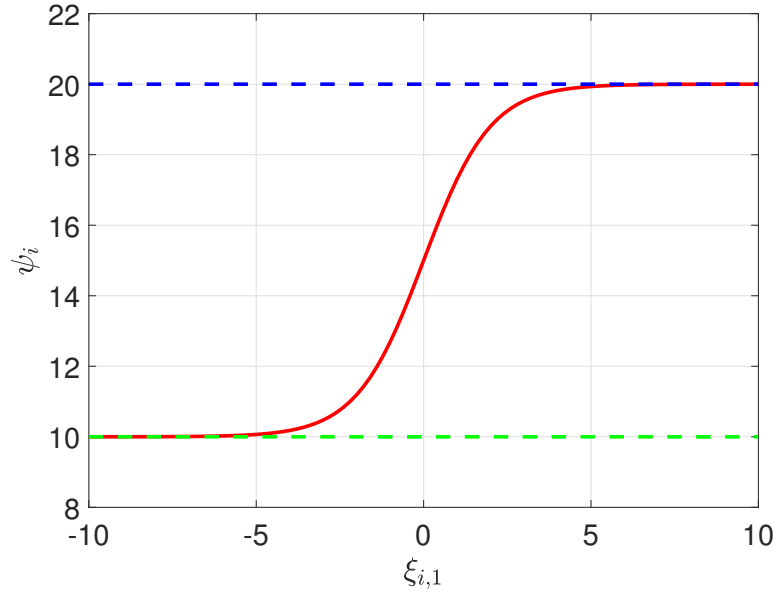


Figure 5.1. Illustration of a sigmoid function.

function corresponding to a constraint whose lower bound is negative infinity may be given by:

$$\psi_i = -e^{s \cdot \xi_{i,1}} + c_i^+ \quad (5.10)$$

On the other hand, if the upper bound is infinity, the saturation function may be given by:

$$\psi_i = e^{s \cdot \xi_{i,1}} + c_i^- \quad (5.11)$$

As before,  $s$  represents the steepness of the transition of the saturation function. Figure 5.2 illustrates a saturation function corresponding to a constraint whose lower bound is negative infinity and the upper bound is 20.

Following the generation of additional states and control variables, a new state vector  $\mathbf{X}'$  is constructing by augmenting the original state vector  $\mathbf{X}$  with the new state variables,  $\xi_{i,j}$ . That is:

$$\mathbf{X}' = \begin{bmatrix} \mathbf{X} \\ \xi_{1,1} \\ \vdots \\ \xi_{p,r} \end{bmatrix} \begin{pmatrix} \\ \\ \\ \end{pmatrix} \quad (5.12)$$

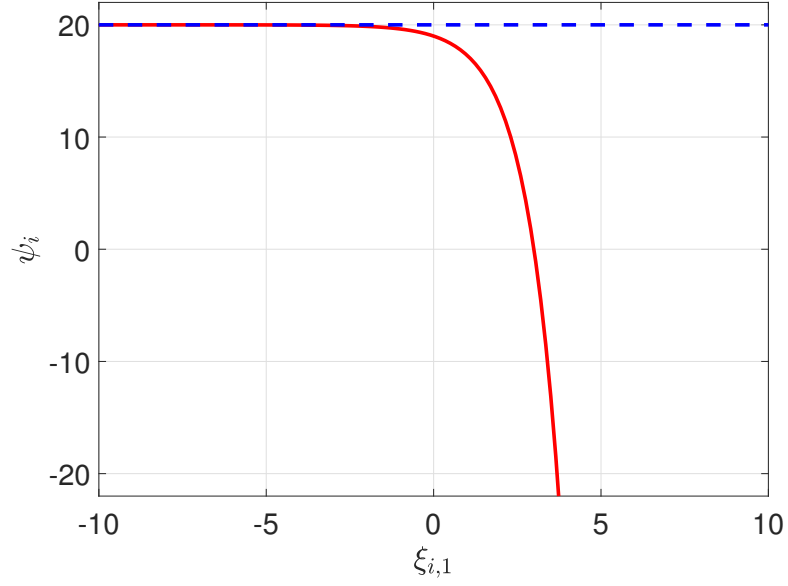


Figure 5.2. Illustration of an exponential function.

Consequently, the new dynamic system can be defined as:

$$\dot{\mathbf{X}}' = \mathcal{F}(\mathbf{X}', \mathbf{U}, u_i, w_i, t) \quad (5.13)$$

The inequality path constraints are now implicitly built into  $\mathcal{F}$ , thereby reducing the original problem to an unconstrained optimization problem. However, the Lagrangian  $\mathcal{L}$  should be augmented by the new control variables such that:

$$\mathcal{L}' = \mathcal{L} + \epsilon \left( \sum_{i=1}^p u_i^2 + \sum_{k=1}^q w_k^2 \right) \quad (5.14)$$



This step is crucial because when the trajectory hits the path constraints, the magnitude of the corresponding new control variables  $u_i$  and  $w_i$  become infinity. This will pose numerical issues while solving the necessary conditions of optimality. To prevent this, the Lagrangian  $\mathcal{L}$  is augmented as described by Eq. (5.14). This essentially turns the original problem into a weighted objective problem to minimize both the original cost functional and the magnitude of the new control variables. The weighting factor  $\epsilon$  defines how much priority is given to minimizing the magnitude of the new control variables. A very small  $\epsilon$  results in very little priority. Consequently, the optimal trajectory will get very close to the constraint boundary without actually hitting it, thus, preventing the magnitude of the new control variables from going to infinity. The smaller the value of  $\epsilon$ , the closer the weighted cost functional is to the original cost functional, and closer is the optimal solution to that of the original problem. Consequently, for practical purposes, the trajectory may be interpreted to ride the constraint boundary.

To derive the necessary conditions of optimality corresponding to  $\mathcal{F}$  and  $\mathcal{L}'$ , a new Hamiltonian  $\mathbf{H}'$  is defined as:

$$\mathbf{H}' = \mathcal{L} + \boldsymbol{\lambda}^T \mathbf{F} + \epsilon \left( \sum_{i=1}^p u_i^2 + \sum_{k=1}^q v_k^2 \right) \left( + \sum_{i=1}^p \left( \mu_i \left( \frac{d^{r(i)} c_i}{dt^{r(i)}} - \frac{d^{r(i)} \psi_i}{dt^{r(i)}} \right) + \sum_{k=1}^q \left( \nu_k (d_k - \phi_k) \right) \right) \quad (5.15)$$

where  $\mu_i$  and  $\nu_k$  are additional Lagrange multipliers. The last two summation terms in Eq. (5.15) force the inequality path constraints to be equal to the corresponding saturation functions. Since the new problem is unconstrained, the necessary conditions of optimality can be easily obtained from Eq. (5.5) as:

$$\begin{aligned}
\dot{\mathbf{X}} &= \mathbf{f}(\mathbf{X}, \mathbf{U}, t) \\
\dot{\xi}_{i,j} &= \xi_{i,j+1} \\
\dot{\xi}_{i,r_i} &= u_i \\
\dot{\lambda} &= - \left( \frac{\partial \mathbf{H}'}{\partial \mathbf{X}'} \right)^T \\
c_i(\mathbf{X})|_{t_0} &= \psi_i(\xi_{i,1})|_{t_0} \\
\frac{dc_i(\mathbf{X})}{dt}|_{t_0} &= \frac{\psi_i(\xi_{i,1})}{dt}|_{t_0} \\
&\vdots \\
\frac{d^{r(i)-1}c_i(\mathbf{X})}{dt^{r(i)-1}}|_{t_0} &= \frac{d^{r(i)-1}\psi_i(\xi_{i,1})}{dt^{r(i)-1}}|_{t_0} \\
\frac{\partial \mathbf{H}'}{\partial \mathbf{U}} &= \mathbf{0} \\
\frac{\partial \mathbf{H}'}{\partial u_i} &= 0 \\
\frac{\partial \mathbf{H}'}{\partial w_i} &= 0 \\
\frac{\partial \mathbf{H}'}{\partial \mu_i} &= 0 \\
\frac{\partial \mathbf{H}'}{\partial \nu_i} &= 0 \\
\Psi_0(\mathbf{X}(t_0), t_0) &= 0 \\
\Psi_f(\mathbf{X}(t_f), t_f) &= 0 \\
\mathbf{H}'(t_f)dt_f - \mathbf{H}'(t_0)dt_0 - \boldsymbol{\lambda}^T(t_f)d\mathbf{X}'(t_f) + \boldsymbol{\lambda}^T(t_0)d\mathbf{X}'(t_0) + d\Phi &= 0 \\
\text{where} \\
i &= 1, \dots, p \\
j &= 1, \dots, r_i - 1 \\
k &= 1, \dots, q
\end{aligned} \tag{5.16}$$

In essence, the necessary conditions of optimality remain a TPBVP despite the inequality path constraints. Solving this system of DAEs results in a trajectory that is guaranteed to be locally optimal and satisfy the path constraints. Although the

TPBVP is easier to handle, analytical solutions do not exist for complex aerospace problems. As a result, it is required to be solved numerically, as explained in the next section.

### 5.3 Numerical Solution to the Two-Point Boundary Value Problem

The TPBVP that defines the necessary conditions of optimality seldom has an analytical solution for aerospace problems. As a result, it is required to employ numerical techniques to calculate the solution. These can be categorized as initial value methods (IVM) and finite difference methods [96,97].

#### 5.3.1 Initial Value Methods

The IVMs involve solving a series of initial value problems (IVPs). One of the commonly used IVMs is single shooting, wherein the differential equations are propagated in the forward direction using the initial conditions defined by the initial boundary conditions. The free initial boundary conditions are guessed. The error in the terminal boundary condition is computed, and the sensitivity of the terminal values to perturbations in the initial conditions are derived from the state transition matrix. Using this sensitivity information, a correction is estimated in the free initial boundary conditions. Since the sensitivity is derived from the linearized system, the correction will not be fully accurate. Therefore, the process is repeated until the error in the terminal boundary conditions satisfy a certain tolerance.

Another IVM that is widely used is multiple shooting. It is similar to single shooting, except that the trajectory is divided into multiple arcs. Consequently, additional boundary conditions need to be introduced to ensure the continuity of the states and co-states. The differential equations are propagated in each arc with some guessed initial conditions. The sensitivity of states and co-states with respect to these initial conditions are calculated for each arc. Using this information, corrections are iteratively applied to each initial condition until the errors in the terminal and

interior boundary conditions satisfy a certain tolerance. Since the linear sensitivity information is calculated for a shorter arc in multiple shooting, the errors in the corrections are lower. Therefore, the region of convergence of the initial guess is increased, and the solution may be obtained in fewer iterations.

Although IVMs usually have reasonable convergence characteristics, they are computationally intensive. As a result, this dissertation employs finite difference methods, and existing software packages that employ these methods are utilized, as explained in the next section.

### 5.3.2 Finite Difference Methods

In finite difference methods, the independent variable, time, is discretized into nodes. It is required to compute the state vectors corresponding to each node, as illustrated in Figure 5.3.

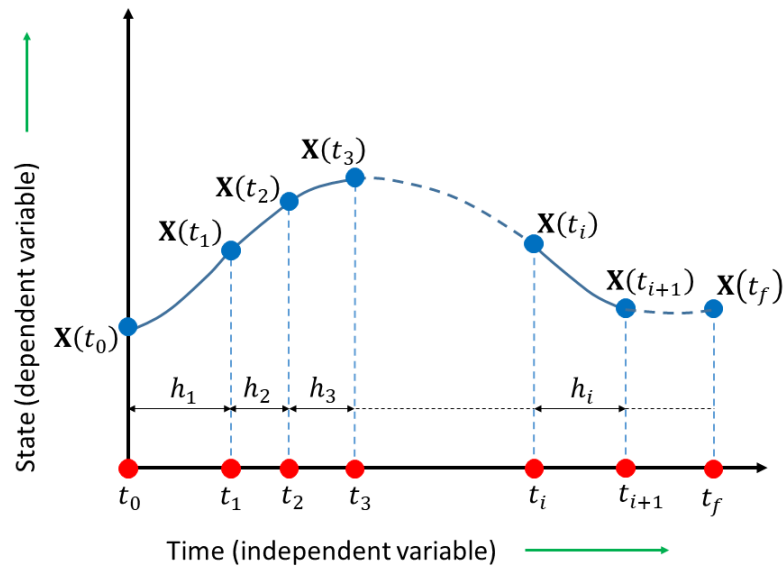


Figure 5.3. Illustration of finite difference methods to solve the TPBVP.

In Figure 5.3,  $h_i$  is the distance between the  $i^{th}$  and  $(i + 1)^{th}$  node. It is required to properly space the nodes by carefully choosing  $h_i$  (a process known as mesh refinement) to limit the error (called the residue) in the computed trajectory to less than a certain value. The state vectors at any given node are related to those at the adjacent nodes through difference equations. Suppose it is required to solve the following differential equation:

$$\dot{\mathbf{X}} = \mathbf{f}(\mathbf{X}, t) \quad (5.17)$$

subject to the end-point boundary conditions:

$$\Psi(\mathbf{X}(t_0), \mathbf{X}(t_f)) \quad (5.18)$$

wherein  $\Psi$  encompasses both initial and terminal boundary conditions. The states at a given node  $i$  are related to those at  $i + 1$  as follows [97]:

$$\begin{aligned} \mathbf{X}(t_{i+1}) = & \mathbf{X}(t_i) + \frac{h_i}{6} (\mathbf{f}(\mathbf{X}(t_i), t_i) + \mathbf{f}(\mathbf{X}(t_{i+1}), t_{i+1})) \\ & + \frac{2h_i}{3} \mathbf{f}\left(\frac{\mathbf{X}(t_i) + \mathbf{X}(t_{i+1})}{2} - \frac{h_i}{8} (\mathbf{f}(\mathbf{X}(t_{i+1}), t_{i+1}) - \mathbf{f}(\mathbf{X}(t_i), t_i)), t_i + \frac{h_i}{2}\right) \end{aligned} \quad (5.19)$$

Specifically, this equation represents the fourth order Lobatto IIIA collocation method. For a given mesh, Eqs. (5.18) and (5.19) together constitute a system of nonlinear algebraic equations. The unknown variables are the state variables corresponding to each node, which may be solved using a Newton-Raphson iteration [98]. If the final time  $t_f$  is unknown, the time  $t$  may be normalized as:

$$\tau = \frac{t}{t_f} \quad (5.20)$$

where  $\tau$  is the nondimensional time that varies between 0 and 1. The system dynamics are accordingly modified as:

$$\dot{\mathbf{X}} = t_f \mathbf{f}(\mathbf{X}, \tau) \quad (5.21)$$

Since  $t_f$  becomes an additional unknown that is required to be solved along with the states, an additional boundary condition is necessary. This is available in the necessary conditions of optimality, which are in fact a system of DAEs. The algebraic equations from which the control variables are calculated are solved simultaneously with Eqs. (5.18) and (5.19).

Suppose  $\mathbf{S}$  is the computed trajectory for a given mesh, the residual  $\mathbf{r}(t)$  in the differential equations is given by:

$$\mathbf{r}(t) = \frac{d\mathbf{S}(t)}{dt} - \mathbf{f}(\mathbf{S}(t), t) \quad (5.22)$$

The residual in the boundary conditions is simply  $\Psi(\mathbf{S}(t_0), \mathbf{S}(t_f))$ . The number of nodes and their positions are altered until the norms of the residuals are below a certain threshold.

The finite difference approach has been implemented in MATLAB's *bvp4c* [99,100], which implements a three-stage Labatto IIIA formula. The solution is c-1 continuous and accurate to fourth order. Mesh refinement is performed based on the size of the residuals.

The finite difference method has to be initiated with a guess solution. For many aerospace problems, the TPBVP that constitutes the necessary conditions of optimality is highly nonlinear. The problems posed by nonlinear TPBVPs are summarized in [101]. Consequently, the solution is extremely sensitive to the initial guess. The algorithm often fails to converge if the guess is not close to the actual solution, thereby making the initial guess generation very challenging. To tackle this challenge, a continuation scheme is employed, which is described in the next section.

### 5.3.3 The Continuation Method

In the continuation method, instead of solving the original problem of interest right away, a much simpler problem that will result in a very short trajectory is solved. If this problem is simple enough, a converged solution can be obtained even with a bad

initial guess. The problem is then evolved in steps to the problem of interest, wherein the solution in a given step is obtained by supplying the solution from the previous step as the guess. If the steps are small enough, the solution from the previous step will be close to that of the present step, thereby increasing the chance of convergence. This is illustrated in Figure 5.4. Ref. [4] demonstrated the robustness of this scheme for hypersonic trajectory design problems. Alternatively, there are other systematic methods to solve the necessary conditions of optimality. For instance, an indirect swarming method can be employed that combines the analytical necessary conditions of optimality with the particle swarm algorithm [102]. This dissertation employs continuation because of the associated simplicity.

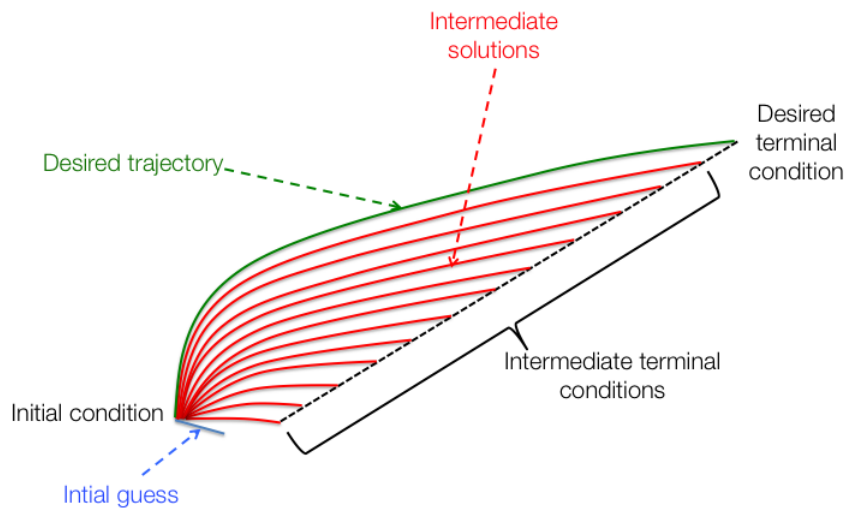


Figure 5.4. Illustration of the continuation process.

Thus far, the discussion of trajectory optimization assumed that the trajectory consists of a single flight phase. However, several aerospace vehicles fly trajectories that are composed of multiple phases, such as a multi-stage launch vehicle. Such trajectories are governed by equations of motion and cost functionals that are piece-

wise continuous. As a result, in the indirect framework, the necessary conditions of optimality result in an MPBVP, as explained in the next section.

#### 5.4 Necessary Conditions of Optimality for Multi-Phase Systems

Suppose an aerospace vehicle flies a trajectory that consists of  $n$  flight phases, and let the governing equations of motion in a flight segment  $i$  be given by:

$$\begin{aligned} \dot{\mathbf{X}} &= \mathbf{f}_i(\mathbf{X}, \mathbf{U}, t), \quad t \in [t_{i-1}, t_i] \\ \text{where } i &= 1, 2, \dots, n \end{aligned} \quad (5.23)$$

The following piecewise continuous cost functional is required to be minimized:

$$J = \Phi(\mathbf{X}_f, t_f) + \sum_{i=1}^n \int_{t_{i-1}}^{t_i} \mathcal{L}_i(\mathbf{X}, \mathbf{U}, t) dt \quad (5.24)$$

where  $t_n = t_f$ . The optimal trajectory should satisfy the end-point boundary conditions given by:

$$\begin{aligned} \Psi_0(\mathbf{X}_0, t_0) &= \mathbf{0} \\ \Psi_f(\mathbf{X}_f, t_f) &= \mathbf{0} \end{aligned} \quad (5.25)$$

The optimal trajectory should also satisfy the interior point boundary conditions given by:

$$\begin{aligned} \Psi_i(\mathbf{X}_i, t_i) &= \mathbf{0} \\ \text{where } i &= 1, 2, \dots, n-1 \end{aligned} \quad (5.26)$$

The necessary conditions of optimality are given by the following MPBVP in a system of DAEs [91]:



$$\begin{aligned}
\dot{\boldsymbol{\lambda}} &= - \left( \frac{\partial \mathbf{H}_i}{\partial \mathbf{X}} \right)^T, \quad t \in [t_{i-1}, t_i] \\
\dot{\mathbf{X}} &= \mathbf{f}_i(\mathbf{X}, \mathbf{U}, t), \quad t \in [t_{i-1}, t_i] \\
\frac{\partial \mathbf{H}_i}{\partial \mathbf{U}} &= \mathbf{0} \quad [t_{i-1}, t_i] \\
\Psi_0(\mathbf{X}_0, t_0) &= \mathbf{0} \\
\Psi_f(\mathbf{X}_f, t_f) &= \mathbf{0} \\
\mathbf{H}_{n,t_f} dt_f - \mathbf{H}_{1,t_0} dt_0 - \boldsymbol{\lambda}_f^T d\mathbf{X}_f + \boldsymbol{\lambda}_0^T d\mathbf{X}_0 + d\Phi_f &= 0 \\
\Psi_i(\mathbf{X}_i, t_i) &= \mathbf{0}, \quad i \neq n \\
\boldsymbol{\lambda}_i^{T-} &= \boldsymbol{\lambda}_i^{T+} + \Pi^T \frac{\partial \Psi_i}{\partial \mathbf{X}_i}, \quad i \neq n \\
\mathbf{H}_i^- &= \mathbf{H}_i^+ - \Pi^T \frac{\partial \Psi_i}{\partial t_i}, \quad i \neq n \\
\text{where } i &= 1, 2, \dots, n \\
\mathbf{H}_i &= \mathcal{L}_i + \boldsymbol{\lambda}^T \mathbf{f}_i
\end{aligned} \tag{5.27}$$

As discussed before, MPBVPs are more difficult to solve than TPBVPs. The third contribution of this dissertation (Chapter 8) simplifies the design of optimal trajectories of multi-phase systems by reducing this MPBVP to a TPBVP.

## 5.5 Summary

The indirect trajectory optimization methodology explained in this chapter serves as the foundation for the three contributions of the doctoral dissertation, namely: 1) integration of ablative shape change into conceptual hypersonic mission design, 2) incorporation of rigid body dynamics into trajectory design, and 3) simplification of trajectory optimization of multi-phase systems. The next chapter describes the first contribution of the dissertation: integration of ablative shape change into conceptual hypersonic mission design.

## 6. INTEGRATION OF ABLATIVE SHAPE CHANGE INTO CONCEPTUAL HYPERSONIC MISSION DESIGN

### 6.1 Introduction

This chapter describes the first contribution of the doctoral dissertation: integrating the effects of ablative shape change into conceptual hypersonic mission design. This contribution deals with hypersonic vehicles with an ablative TPS. The geometry of such vehicles evolves during flight. This contribution enables the design of optimal trajectories that account for the coupling between the evolution of vehicle geometry and flight dynamics. Ablation is modeled by correlating the surface recession of a set of points on the TPS to the corresponding local heat-rate through the heat of ablation. The following section describes the heat-rate model that was used for this purpose.

### 6.2 3-Dimensional Heat-Rate Model

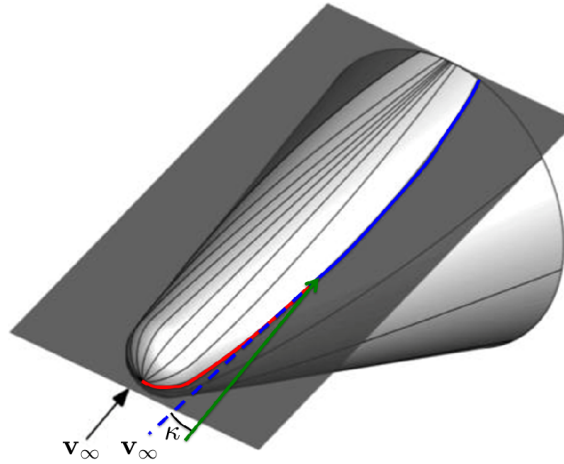
Hypersonic flow involves extremes in flow conditions that pose several computational challenges in predicting aerothermodynamic effects, as explained by Gnoffo [103]. These challenges are dependent on the desired level of fidelity of the predicted results. In the conceptual design phase, it is important to strike a balance between analysis fidelity and computational speed. Consequently, a rapid methodology that utilizes axisymmetric heat-rate solutions for 3-D bodies was employed.

Brykina et al. [104] showed that the heat-rate about a 3-D body can be obtained from 3-D thin viscous shock layer equations. These equations showed that the heat flux depends on: 1) the inclination of the surface of the body with respect to the freestream flow ( $\kappa$ ) and 2) the ratio of the Reynolds number to the mean

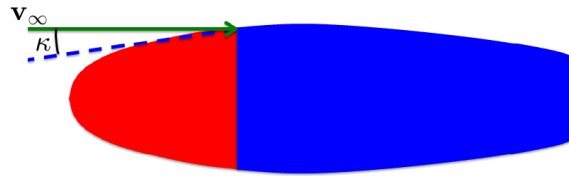
surface curvature ( $Re/H$ ). If the distributions in  $\kappa$  and  $Re/H$  between two bodies are matched, then the heat-rate distributions about these bodies are approximately equal. Consequently, following the approach of Brykina and Scott [105], the 3-D body is transformed into a series of axisymmetric bodies (called equivalent axisymmetric bodies, EABs) based on the distribution in  $\kappa$ . The heat-rate distribution is computed for these EABs using axisymmetric solutions. The computed heat-rates are mapped back to the original 3-D body by matching  $Re/H$  of the EABs and the 3-D body. This essentially means that the axisymmetric heat-rate prediction is multiplied by the factor  $\sqrt{(H_{3D}/H_{EAB})}$ , where  $H_{3D}$  is the mean curvature of the point of interest on the 3-D body, and  $H_{EAB}$  is the mean curvature at the corresponding location on the EAB. The next section explains the procedure to generate the EABs.

### 6.2.1 Generation of Equivalent Axisymmetric Body

The 3-D body is transformed into a series of axisymmetric bodies (EABs) using meridians. The meridians are defined by lines of intersection of the surface of the 3-D body and a plane that is parallel to the freestream vector and passing through the geometric (or Newtonian) stagnation point. Different meridians are obtained by rotating the plane about the freestream vector (Figure 6.1(a)). From the meridian, a 2-dimensional curve is constructed such that at a given distance along curve, the surface inclination angle ( $\kappa$ ) with respect to the freestream vector is the same as that along the meridian from the stagnation point. From this 2-D curve, the body of revolution is generated with the freestream vector as the axis of symmetry. This body of revolution is called the equivalent axisymmetric body, as shown in Figure 6.1(b). The heat-rate computed for these EABs, described in Section 6.2.2, is mapped back to the 3-D body.



(a) Generation of meridians. Original source: Bopp et al. [106].



(b) Equivalent axisymmetric body generated from the meridian.

Figure 6.1. Illustration of generation of meridians and corresponding equivalent axisymmetric bodies.

### 6.2.2 Axisymmetric Heating Analysis

The heat-rate distribution about the EAB is computed using axisymmetric solutions. The edge conditions for the EAB ( $p_e$ ,  $\rho_e$  and  $T_e$ ) are calculated based on the methodology explained in Chapter 4.

From the computed edge conditions, the heat-rate distribution is determined using an integral boundary layer approach for axisymmetric bodies developed by Zoby [107]. The heat-rate expression is:

$$\dot{q}_w = \frac{0.22}{Re_{\theta,e}} \left( \frac{\mu^*}{\mu_e} \right) \left( \frac{\mu^*}{\mu_e} \right) \left( \rho_e v_e (h_{aw} - h_w) Pr_w^{-0.6} \right) \quad (6.1)$$

where  $\mu$  is the dynamic viscosity,  $h$  is the enthalpy,  $Pr$  is the Prandtl number, and  $Re_{\theta,e}$  is the momentum thickness Reynolds number. The subscripts  $e$ ,  $w$  and  $aw$  denote conditions at the edge, wall, and adiabatic wall, respectively. The superscript  $*$  denotes quantities associated with Eckert's reference enthalpy [108], given by:

$$h^* = h_e + 0.5 (h_w - h_e) + 0.22 (h_r - h_e) \quad (6.2)$$

The recovery stagnation enthalpy used in Eq. (6.2) is computed for laminar flow as:

$$h_r = h_e + 0.5 \sqrt{Pr} v_e^2 \quad (6.3)$$

The reference temperature  $T^*$  is computed based on the reference enthalpy from Eq. (6.2) as:

$$T^* = h^* / c_p \quad (6.4)$$

The reference pressure  $p^*$  is equal to the local edge pressure  $p_e$ , and the reference density  $\rho^*$  is computed from the perfect gas equation of state:

$$\rho^* = \frac{P^*}{RT^*} \quad (6.5)$$

The reference viscosity is computed from the reference temperature using Sutherland's law:

$$\mu^* = \mu_{ref} \left( \frac{T^*}{T_{ref}} \right)^{\frac{3}{2}} \left( \frac{T_{ref} + S}{T^* + S} \right) \left( \right) \quad (6.6)$$

The momentum boundary layer thickness used in the definition of  $Re_{\theta,e}$  is given by [106]:

$$\theta = \frac{0.664}{1 + 0.09\sqrt{\beta}} \frac{\sqrt{\int_0^s \rho^* \mu^* v_e r^2 ds}}{\rho_e v_e r} \quad (6.7)$$

where  $r$  is the radius of the EAB at a given location on the axis of symmetry and  $s$  is the streamwise distance from the stagnation point. The nonzero pressure gradient across the boundary layer is taken into account through the pressure gradient parameter given by:

$$\beta = \frac{2\xi}{v_e} \left[ \left( \frac{dv_e}{ds} \right) / \left( \frac{d\xi}{ds} \right) \right] \left( \quad (6.8)$$

where  $\xi$  is a streamwise coordinate defined by the Lees-Dorodnitsyn transformation [109] as:

$$\xi = \int_0^x \rho_e \mu_e v_e dx \quad (6.9)$$

where  $x$  is the coordinate along the axis of symmetry from the stagnation point. The momentum thickness Reynold's number is given by:

$$Re_{\theta,e} = \frac{\rho_e v_e \theta_e}{\mu_e} \quad (6.10)$$

It is important to note that the integral in Eq. (6.7) becomes undefined at the stagnation point because  $v_e$ ,  $r$ , and  $s$  become zero. Therefore, in the region of the stagnation point, this integral is approximated as:

$$\int_0^{s_\epsilon} \rho^* \mu^* v_e r^2 ds \approx \frac{1}{4} (\rho^* \mu^*)_0 (v_e)_\epsilon r_\epsilon^2 s_\epsilon \quad (6.11)$$

where  $s_\epsilon$  is the small streamwise distance from the stagnation point. This approximate expression was derived by Hamilton et al. [110] based on two assumptions. The first assumption is that  $\rho^*$  and  $\mu^*$  are approximately constant inside  $s_\epsilon$ , and therefore,  $(\rho\mu)^*$  is approximately equal to its stagnation point value. The second assumption is that  $v_e$  and  $r$  are approximately linear in the region around the stagnation point.

In this dissertation, the value of  $s_\epsilon$  was chosen such that the corresponding distance along the axis of symmetry from the stagnation point is one-hundredth of the length of the axisymmetric body. A more systematic approach to choose the value of  $s_\epsilon$  remains to be investigated.

Since Eq. (6.1) becomes indeterminate at the stagnation point, the stagnation heat-rate is instead computed using Tauber's equation [111], given by:

$$\dot{q}_{w,0} = 1.83 \times 10^{-4} \left( \frac{\rho_\infty}{R_N} \right)^{0.5} v_\infty^3 \left( 1 - \frac{h_w}{h_0} \right) \left( \quad \right) \quad (6.12)$$

where  $R_N$  is the nose radius and  $h_0$  is the edge enthalpy at the stagnation point.

In summary, the heat-rate computation begins at a small distance away from the stagnation point and a quadratic curve fit is performed from this location to the stagnation point such that its slope with respect to the streamwise distance at the stagnation point is equal to zero. Once the heat-rate is computed using this approach, it is mapped back to the original 3-D body by matching  $Re/H$  as follows:

$$\dot{q}_{3D} = \sqrt{\frac{H_{3D}}{H_{EAB}}} \dot{q}_{EAB} \quad (6.13)$$

This method is henceforth termed the Newtonian Boundary Layer (BL) method. Validation was performed on this method, and the results of validation are presented in the next section.

### 6.2.3 Validation of Heat-Rate Model

The Newtonian BL method was validated using the results presented by Bopp et al. [106]. These results were obtained using the following methodologies:

1. The Newtonian BL method explained in this chapter.
2. Solution of the Navier-Stokes equations.
3. Data acquired from experiments.

Two cases are presented for validation that involve a sphere-cone geometry. In case 1, the geometry is exposed to an axisymmetric flow, while in case 2, it is exposed to a non-axisymmetric flow. The flow conditions for the test cases are shown in Table 6.1.

Table 6.1. Flow condition for each case.

<b>Case number</b>	$v_\infty$ , m/s	$\rho_\infty$ , kg/m <sup>3</sup>	$T_\infty$ , K	$\alpha$ , deg	$M_\infty$	$Re_\infty$ , m <sup>-1</sup>	$\gamma_\infty$	$T_w$ , K
1	1460	$9.75 \times 10^{-3}$	47.22	0	10.6	$3.94 \times 10^6$	1.4	300
2	943	$3.22 \times 10^{-2}$	62.87	20	6	$7.23 \times 10^6$	1.4	300

### Case 1

Case 1 involves a 15 deg sphere-cone geometry with a nose radius of 2.794 cm. The total length of the sphere-cone geometry is 48.87 cm. The freestream is thermochemically frozen with  $\gamma = 1.4$  and the wall is isothermal at 300 K. For this case, the generation of EABs is not necessary because the sphere-cone geometry flying at 0 deg angle-of-attack is already axisymmetric with respect to the flow. This case serves as a validation of the approach that uses the Modified Newtonian pressure distribution to compute the heat flux using Eq. 6.1. Figure 6.2 illustrates the results of validation. The result from experiments does not have data for the stagnation point. It can be seen that the results from this dissertation closely match those obtained by Bopp et al. [106] for the Newtonian BL approach. However, in either cases, the Newtonian BL method shows considerable error in the frustum portion of the geometry, when compared to the Navier-Stokes and experimental results. This is because the modified Newtonian flow theory predicts a constant pressure throughout the frustum region, which is not the case in reality. As a result, this approach over-predicts heating in the frustum. This error is tolerable during conceptual design because despite the over-



prediction, heating in the frustum region is low enough that the ablation is minimal. Consequently, the impact on shape change is also low.

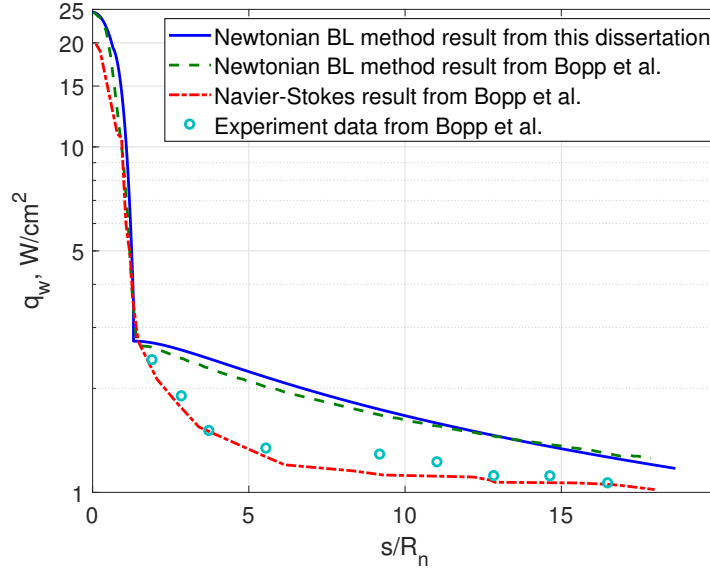


Figure 6.2. Case 1 - Heating along axisymmetric 15 deg. sphere-cone and comparison with results presented by Bopp et al. [106].

## Case 2

Case 2 involves a 15 deg sphere-cone geometry with nose radius 2.54 cm. The total length of the geometry is 24.8488 cm. The geometry is exposed to the flow at 20 deg angle-of-attack. The flow is thermochemically frozen with  $\gamma = 1.4$ , and the wall is isothermal at 300 K. This case is used to validate the EAB method to calculate heat flux. The windward centerline heating is shown in Figure 6.3. Two meridians originating from the stagnation point and traveling along the centerline were utilized to calculate the centerline heat-rate distribution. One meridian was along the upper surface and the other along the lower surface. Experimental data was not available for this case. It can be seen that the result from this dissertation reasonably agrees with that presented by Bopp et al. [106] for the majority of the geometry. However, the

Newtonian BL approach over-predicts the heat-rate at the sphere-cone junction because its inherent assumption cannot capture the overexpansion-recompression effect at this region.

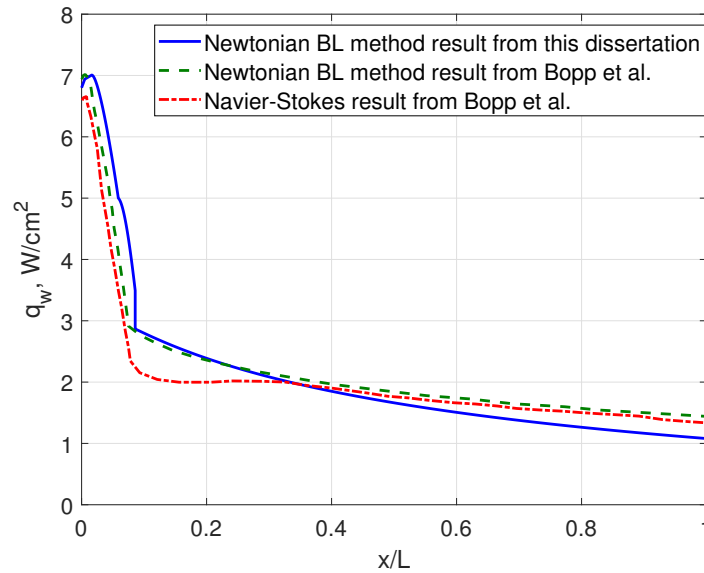


Figure 6.3. Case 2 - Centerline heating distribution on 15 deg. sphere-cone at 20 deg. angle-of-attack and comparison with results presented by Bopp et al. [106].

It should be noted that the accuracy of the heat-rate model with the Newtonian BL approach is low for blunt sphere-cone vehicle configurations used in planetary entry probes. For such vehicles, a large subsonic region covers the entire forebody, and there is a rapid expansion around the shoulder of the frustum. This results in increased heat-rate at the shoulder. Since the assumptions inherent in Modified Newtonian flow theory cannot account for these expansion regions, the heat-rate calculated based on this model will have considerable error. However, this contribution of the dissertation focuses on hypersonic missions involving slender vehicles used in military applications. Therefore, the heat-rate calculated for such vehicles based on this model is reasonably accurate. However, it should be noted that as the vehicle ablates and becomes blunt, the accuracy in the calculated heat flux reduces. The magnitude of the error remains

to be investigated and is beyond the scope of this dissertation. The heat-rate predicted using the methodology explained in Section 6.2 is used in modeling the ablation of the TPS, as explained in Section 6.3.

### 6.3 Ablation of Thermal Protection System

This section explains the ablation model that was used in this dissertation. Ablation is modeled as a correlation between the surface recession of specific points on the thermal protection system to the local heat-rate, through an empirical parameter called the Heat of Ablation. The vehicle geometry at any instant is constructed as a surface interpolation of those specific points using Non-Uniform Rational Basis Spline (NURBS) surfaces. The ablation model is also validated, and its results are presented.

#### 6.3.1 Modeling Ablation using Heat of Ablation

As stated, the ablation model used in this dissertation is based on the Heat of Ablation ( $Q_*$ ), which is a parameter that relates the heat-rate at a given point on the body to the corresponding surface recession rate. The advantage of this approach is the computation speed, which becomes crucial in conceptual design when the number of parameters that define an arbitrary 3-D shape becomes large. The parameter  $Q_*$  was defined during early experiments to correlate arc jet ablation data [112]. The ablation of the materials used in these experiments were only attributed to vaporization and transpiration. Based on these experiments, an analytical formulation was devised to predict ablation. This resulted in the formulation of the following surface energy equation [112]:

$$\dot{q}_{conv} - \dot{q}_{rerad} = \dot{q}_{cond} + \dot{q}_{vap} + \dot{q}_{trans} \quad (6.14)$$

where  $\dot{q}_{conv}$  is the net convective heat-rate entering the TPS in the absence of ablation,  $\dot{q}_{rerad}$  is the re-radiated heat-rate from the TPS surface,  $\dot{q}_{cond}$  is the net heat-rate

conducted into the TPS,  $\dot{q}_{vap}$  is the rate at which heat is absorbed in the vaporization of the TPS, and  $\dot{q}_{trans}$  is the rate at which heat is absorbed due to transpiration of the products of ablation into the boundary layer. Moreover:

$$\begin{aligned}\dot{q}_{conv} &= \dot{q}_{cw} \left( \frac{h_r - h_w}{h_r} \right) \left( \right. \\ \dot{q}_{rerad} &= \sigma \epsilon T_w^4 \\ \dot{q}_{vap} &= \rho_{TPS} \dot{s} h_v \\ \dot{q}_{trans} &= \rho_{TPS} \dot{s} \eta (h_r - h_w)\end{aligned}\tag{6.15}$$

where  $\dot{q}_{cw}$  is the cold-wall heat-rate,  $\sigma$  is the Stefan-Boltzmann constant,  $\epsilon$  is the emissivity,  $h_v$  is the heat of vaporization, and  $\eta$  is the transpiration coefficient.

In addition, the ablation model assumes that steady-state conditions hold true, as a result of which the heat-rate conducted into the TPS can be given by:

$$\dot{q}_{cond} = \rho_{TPS} \dot{s} c_p (T_w - T_0)\tag{6.16}$$

where  $T_0$  is the initial temperature of the TPS. Substituting Eqs. (6.15) and (6.16) into Eq. (6.14) and rearranging the terms yields:

$$\frac{\dot{q}_{cw} \left( \frac{h_r - h_w}{h_r} \right) \left( \right. \sigma \epsilon T_w^4}{\rho_{TPS} \dot{s}} = c_p (T_w - T_0) + h_v + \eta (h_r - h_w)\tag{6.17}$$

In Eq. (6.17), the right hand side is the Heat of Ablation,  $Q_*$ . It can be seen that the surface recession  $\dot{s}$  varies linearly with the total heat-rate entering the TPS. Through arc jet experiments, the values of surface recession are obtained for different heat-rates, and a linear fit is performed on this data to obtain  $Q_*$ . The surface recession is consequently given as:

$$\dot{s} = \frac{\dot{q}_{cw} \left( \frac{h_r - h_w}{h_r} \right) \left( \right. \sigma \epsilon T_w^4}{\rho_{TPS} Q_*}\tag{6.18}$$

Furthermore,  $\dot{q}_{cond}$  is precisely  $\dot{q}_w$ , the heat-rate that is estimated using the model described in Section 6.2. The re-radiated heat-rate,  $\dot{q}_{rerad}$  is neglected in this disser-

tation. This over-estimates the surface recession, resulting in a conservative ablation model. Therefore, the expression for surface recession can be simplified as:

$$\dot{s} = \frac{\dot{q}_w}{\rho_{\text{TPS}} Q_*} \quad (6.19)$$

Although the description of the ablation process assumed only vaporization and transpiration, it should be noted that  $Q_*$  can be experimentally obtained for any material by measuring the surface recession for different values of heat-rate and performing a linear fit between the two. Consequently,  $Q_*$  will have accounted for all the physical and chemical processes involved in ablation, with the assumption that the ablation has reached steady-state, resulting in a constant wall temperature. Despite the simplicity of this ablation model, incorporating it into conceptual mission design is a substantial advancement in the state-of-the-art because presently, the coupling between trajectory and ablative shape evolution is ignored altogether during this design phase. This simplified model was validated using a finite difference solver, as explained in the next section.

### 6.3.2 Validation of the Ablation Model

The scope of validation of the ablation model used in this dissertation was low because of limited data available in the public domain. Validation was performed for axisymmetric bodies subject to axisymmetric flow. The estimates of surface recession were compared with those of ABAXI [113,114], a software that is used to analyze the transient response of an ablating axisymmetric body using finite difference methods. ABAXI solves for the surface recession at constant freestream conditions (velocity, density, pressure, and temperature).

For the validation, the geometry was a hemisphere of radius 0.76 cm. The freestream Mach number, pressure, and temperature were set at 2.5, 0.1 atm and 289 K, respectively. The TPS was assumed to be Teflon-Astroquartz with a  $Q_*$  of 13.96 MJ/kg [115]. For axisymmetric flow, the shape change will be axisymmet-

ric as well. As a result, the geometry was modeled as a body of revolution. The two-dimensional curve from which the 3-D body was generated was represented by 8 points defined in a cartesian coordinate system, as shown in Table 6.2. In this coordinate system, the freestream direction is  $(1, 0)$ .

Table 6.2. Points constituting the 2-D curve representing the initial hemisphere.

Point	Coordinates (cm)
$\mathbf{P}_1$	(0, 0)
$\mathbf{P}_2$	(0.019, 0.169)
$\mathbf{P}_3$	(0.075, 0.330)
$\mathbf{P}_4$	(0.166, 0.474)
$\mathbf{P}_5$	(0.286, 0.594)
$\mathbf{P}_6$	(0.432, 0.685)
$\mathbf{P}_7$	(0.591, 0.741)
$\mathbf{P}_8$	(0.760, 0.760)

The 2-D curve was constructed by performing a quadratic spline fit on the instantaneous location of these points such that tangency was maintained at each of them. The heat-rate was calculated at each of these points (except  $\mathbf{P}_1$ ) from Eq. (6.1). Since  $\mathbf{P}_1$  will always remain the stagnation point, the corresponding heat-rate was calculated using Eq. (6.12). The surface recession corresponding to each point was subsequently calculated using Eq. (6.19), and the direction of the recession was assumed to be along the inward-pointing normal at that point. Consequently, the dynamics for the motion of a point  $\mathbf{P}_i$  was calculated as:

$$\dot{\mathbf{P}}_i = \dot{s}_i \hat{\mathbf{n}}_i \quad (6.20)$$

The simulation was run for 8 seconds and was compared with that of ABAXI. The results of validation are illustrated in Figure 6.4. It can be seen that the ablation predicted by the model used in this dissertation closely matches that of ABAXI. It

is important to note that ABAXI accounts for varying surface temperature, while the ablation model used in this research currently assumes an isothermal wall. It is known that Teflon-Astroquartz starts ablating when the surface temperature reaches about 850 K. Using this knowledge, the isothermal wall temperature was set at a higher value (1000 K) so that the heat-rate is slightly lower, and the over-prediction in surface recession resulting from the assumption that ablation is always at steady state is minimized.

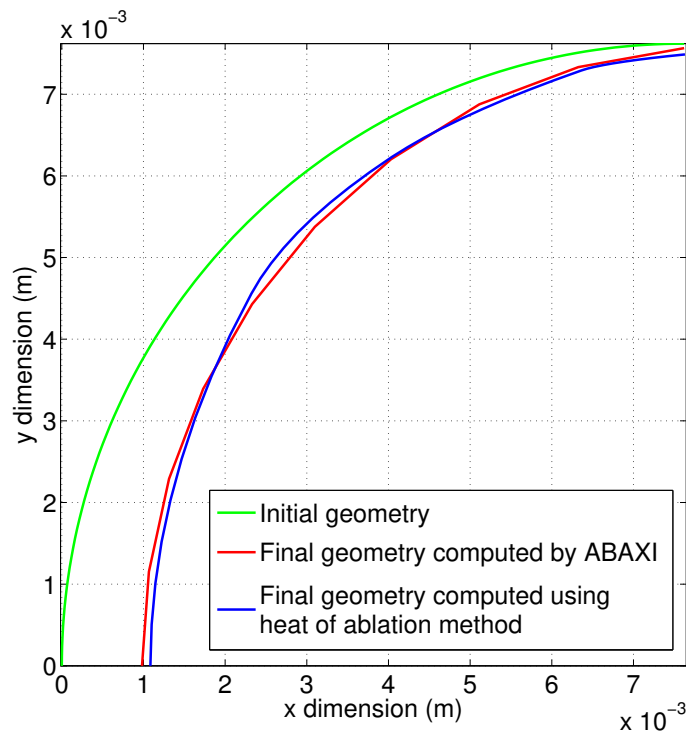


Figure 6.4. Validation of ablation model. Since the ablation is axisymmetric, only the top portion of the hemisphere as seen from the side is shown.

For the purpose of validation, both the flow and the initial geometry were assumed to be axisymmetric. As a result, the ablating vehicle remained axisymmetric as well. However, this will not hold true when the vehicle flies at a non-zero angle-of-attack or side-slip angle. Therefore, it is necessary to model ablation for an arbitrary

shape. To model arbitrary shape change resulting from non-axisymmetric ablation, a set of points that lie on the surface of the vehicle are tracked using Eq. (6.19). The coordinates of these points are defined with respect to a vehicle-fixed frame. A surface fit is performed on these points using Non-Uniform Rational Basis Spline (NURBS) surface. The fitted surface represents the instantaneous vehicle geometry. The points move at a rate  $\dot{s}$  along the direction of the instantaneous inward-pointing normal. Consequently, the fitted NURBS surface evolves with these tracked points. The procedure to perform the surface fit using NURBS is explained in Section 6.3.3.

### 6.3.3 Modeling Arbitrary Vehicle Geometry

The procedure to perform the surface fit is explained by Piegl and Tiller [116]. The general expression of a NURBS surface is given by:

$$\mathbf{P}_{k,l} = \mathbf{S}(c_k, d_l) = \sum_{i=0}^n \sum_{j=0}^m \left( N_{i,p}(c_k) N_{j,q}(d_l) \mathbf{W}_{i,j} \right) \quad (6.21)$$

where  $\mathbf{W}_{i,j}$  are the control points,  $\mathbf{P}_{k,l}$  are the points on the NURBS surface corresponding to the parameters  $c_k$  and  $d_l$ , and  $N_{i,p}$  and  $N_{j,q}$  are the  $p^{th}$  and  $q^{th}$  degree B-spline basis functions defined on the nonperiodic and nonuniform knot vectors  $\mathbf{C}$  and  $\mathbf{D}$  corresponding to the  $c$  and  $d$  directions respectively. Qualitatively, the control points influence the overall geometry of the surface. These points can be visualized as “strings of a puppet”, wherein the geometry of the surface can be manipulated by moving the control points. Moreover, the knot vectors define the region on the surface over which a given control point has influence.

In general, given the control points and the basis functions, any point on the surface corresponding to parameters  $c$  and  $d$  can be readily obtained from Eq. (6.21). However, since the NURBS surface represents the vehicle geometry, the points  $\mathbf{P}_{k,l}$  are already known, where  $k = 0, 1, 2, \dots, n$  and  $l = 0, 1, 2, \dots, m$ . In fact, they represent the points on the TPS whose recession resulting from ablation is tracked. It is instead required to determine the control points  $\mathbf{W}_{i,j}$ , the appropriate basis



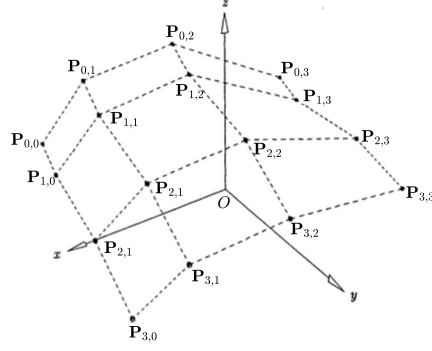


Figure 6.5. Illustration of NURBS surface interpolation (source: Piegl and Tiller [116], modified).

functions  $N_{i,p}$  and  $N_{j,q}$ , and the parameters  $c_k$  and  $d_l$  corresponding to each  $\mathbf{P}_{k,l}$  such that the resulting NURBS surface fits them. That is, given a set of  $(n+1) \times (m+1)$  points, it is required to construct a  $(p, q)^{th}$  degree NURBS surface interpolating these points. Figure 6.5 illustrates a set of points  $\mathbf{P}_{k,l}$  to be interpolated. In this illustration,  $n = m = 3$ .

The procedure to perform the interpolation is as follows:

- The parameter  $c_k$  corresponding to each  $\mathbf{P}_{k,l}$  are determined. The centripetal method is employed because it results in better results when the surface makes sharp turns. In this method, for each  $l$ , the value  $c_k^l$  is determined as:

$$\begin{aligned}
 c_0^l &= 0 \\
 c_n^l &= 1 \\
 c_k^l &= c_{k-1}^l + \frac{\sqrt{|\mathbf{P}_{k,l} - \mathbf{P}_{k-1,l}|}}{d_l}, \quad k = 1, 2, \dots, n-1
 \end{aligned} \tag{6.22}$$

where:

$$d_l = \sum_{k=1}^n \left( \sqrt{|\mathbf{P}_{k,l} - \mathbf{P}_{k-1,l}|} \right) \tag{6.23}$$

The parameter  $c_k$  is given by:

$$c_k = \frac{1}{m+1} \sum_{l=0}^m c_k^l, \quad k = 0, 1, 2, \dots, n \quad (6.24)$$

- Similarly, the parameter  $d_l$  corresponding to each  $\mathbf{P}_{k,l}$  is determined using the centripetal method as follows:

$$\begin{aligned} d_0^k &= 0 \\ d_m^k &= 1 \\ d_k &= \sum_{l=1}^m \left( \sqrt{|\mathbf{P}_{k,l} - \mathbf{P}_{k,l-1}|} \right) \\ d_l^k &= d_{l-1}^k + \frac{\sqrt{|\mathbf{P}_{k,l} - \mathbf{P}_{k,l-1}|}}{d_k}, \quad l = 1, 2, \dots, m-1 \\ d_l &= \frac{1}{n+1} \sum_{k=0}^n d_l^k, \quad l = 0, 1, 2, \dots, m \end{aligned} \quad (6.25)$$

- The knot vector  $\mathbf{C}$  corresponding to  $c$  direction is constructed. The length of  $\mathbf{C}$  is  $n+p+1$ . That is:

$$\mathbf{C} = \begin{bmatrix} \bar{c}_0 & \bar{c}_1 & \bar{c}_2 & \dots & \bar{c}_{n+p} \end{bmatrix}^T \quad (6.26)$$

The elements of  $\mathbf{C}$  are determined using the method of averaging as:

$$\begin{aligned} \bar{c}_0 &= \dots = \bar{c}_p = 0 \\ \bar{c}_{n+1} &= \dots = \bar{c}_{n+p+1} = 1 \\ \bar{c}_{j+p} &= \frac{1}{p} \sum_{i=j}^{j+p-1} \bar{c}_i \quad \text{where } j = 1, \dots, n-p \end{aligned} \quad (6.27)$$

- Similarly, the knot vector  $\mathbf{D}$  in the  $d$  direction with length  $m+q+1$  and elements  $\bar{d}_0, \dots, \bar{d}_{m+q}$  is constructed using the method of averaging:

$$\begin{aligned}
\bar{d}_0 &= \dots = \bar{d}_q = 0 \\
\bar{d}_{m+1} &= \dots = \bar{d}_{m+q+1} = 1 \\
\bar{d}_{j+q} &= \frac{1}{q} \sum_{i=j}^{j+q-1} \bar{d}_i \text{ where } j = 1, \dots, m-q
\end{aligned} \tag{6.28}$$

- The value of the basis function  $N_{i,p}$  on the knot vector  $\mathbf{C}$  for each  $c_k$  is evaluated through a recursive formula:

$$\begin{aligned}
N_{i,0}(c_k) &= \begin{cases} 1 & \text{if } \bar{c}_i \leq c_k \leq \bar{c}_{i+1} \\ 0 & \text{otherwise} \end{cases} \\
N_{i,p}(c_k) &= \frac{c_k - \bar{c}_i}{\bar{c}_{i+p} - \bar{c}_i} N_{i,p-1}(c_k) + \frac{\bar{c}_{i+p+1} - c_k}{\bar{c}_{i+p+1} - \bar{c}_{i+1}} N_{i+1,p-1}(c_k)
\end{aligned} \tag{6.29}$$

- Similarly, the value of the basis function  $N_{j,q}$  on the knot vector  $\mathbf{D}$  for each  $d_l$  is evaluated as:

$$\begin{aligned}
N_{j,0}(d_l) &= \begin{cases} 1 & \text{if } \bar{d}_j \leq d_l \leq \bar{d}_{j+1} \\ 0 & \text{otherwise} \end{cases} \\
N_{j,q}(d_l) &= \frac{d_l - \bar{d}_j}{\bar{d}_{j+q} - \bar{d}_j} N_{j,q-1}(d_l) + \frac{\bar{d}_{j+q+1} - d_l}{\bar{d}_{j+q+1} - \bar{d}_{j+1}} N_{j+1,q-1}(d_l)
\end{aligned} \tag{6.30}$$

- The values of  $\mathbf{P}_{k,l}(c_k, d_l)$ ,  $N_{i,p}(c_k)$  and  $N_{j,q}(d_l)$  are substituted into Eq. (6.21). This results in a system of linear algebraic equations in  $\mathbf{W}_{i,j}$ . Solving this system results in the values of the control points  $\mathbf{W}_{i,j}$ :

$$\mathbf{W} = \mathbf{N}^{-1} \mathbf{P} \tag{6.31}$$

where:

$$\begin{aligned}
\mathbf{W} &= \begin{bmatrix} \mathbf{W}_{0,0}^T & \dots & \mathbf{W}_{0,m}^T & \mathbf{W}_{1,0}^T & \dots & \mathbf{W}_{1,m}^T & \dots & \mathbf{W}_{n,m}^T \end{bmatrix}^T \\
\mathbf{P} &= \begin{bmatrix} \mathbf{P}_{0,0}^T & \dots & \mathbf{P}_{0,m}^T & \mathbf{P}_{1,0}^T & \dots & \mathbf{P}_{1,m}^T & \dots & \mathbf{P}_{n,m}^T \end{bmatrix}^T \\
\mathbf{N} &= \begin{bmatrix} N_{0,0}(c_0, d_0) & \dots & N_{0,m}(c_0, d_0) & N_{1,0}(c_0, d_0) & \dots & N_{1,m}(c_0, d_0) & \dots & N_{n,m}(c_0, d_0) \\ \vdots & \vdots & \vdots & \vdots & \vdots & \vdots & \vdots & \vdots \\ N_{0,0}(c_0, d_m) & \dots & N_{0,m}(c_0, d_m) & N_{1,0}(c_0, d_m) & \dots & N_{1,m}(c_0, d_m) & \dots & N_{n,m}(c_0, d_m) \\ N_{0,0}(c_1, d_0) & \dots & N_{0,m}(c_1, d_0) & N_{1,0}(c_1, d_0) & \dots & N_{1,m}(c_1, d_0) & \dots & N_{n,m}(c_1, d_0) \\ \vdots & \vdots & \vdots & \vdots & \vdots & \vdots & \vdots & \vdots \\ N_{0,0}(c_1, d_m) & \dots & N_{0,m}(c_1, d_m) & N_{1,0}(c_1, d_m) & \dots & N_{1,m}(c_1, d_m) & \dots & N_{n,m}(c_1, d_m) \\ \vdots & \vdots & \vdots & \vdots & \vdots & \vdots & \vdots & \vdots \\ N_{0,0}(c_n, d_m) & \dots & N_{0,m}(c_n, d_m) & N_{1,0}(c_n, d_m) & \dots & N_{1,m}(c_n, d_m) & \dots & N_{n,m}(c_n, d_m) \end{bmatrix} \begin{pmatrix} \\ \\ \\ \\ \\ \\ \\ \end{pmatrix} \\
&\quad \text{where } N_{i,j}(c_k, d_l) = N_{i,p}(c_k) N_{j,q}(d_l)
\end{aligned} \tag{6.32}$$

These control points  $\mathbf{W}_{i,j}$ , the parameters  $c_k$  and  $d_l$ , and the knot vectors  $\mathbf{C}$  and  $\mathbf{D}$  together define the NURBS surface that interpolates the points  $\mathbf{P}_{k,l}$ .

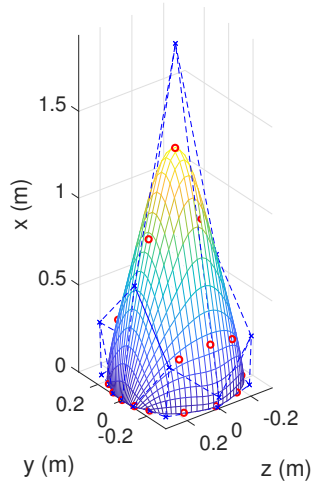


Figure 6.6. Example NURBS surface interpolation.

Table 6.3. Points over which the NURBS surface interpolation is performed (units in meters).

Point	Coordinates	Point	Coordinates
$\mathbf{P}_{1,1}$	$(0, -0.1667, 0.2887)$	$\mathbf{P}_{3,4}$	$(0.3333, 0.2887, 0)$
$\mathbf{P}_{1,2}$	$(0, -0.0863, 0.322)$	$\mathbf{P}_{3,5}$	$(0, 0.3333, 0)$
$\mathbf{P}_{1,3}$	$(0, 0, 0.3333)$	$\mathbf{P}_{4,1}$	$(0, -0.2887, -0.1667)$
$\mathbf{P}_{1,4}$	$(0, 0.0863, 0.322)$	$\mathbf{P}_{4,2}$	$(0.2887, -0.25, -0.1667)$
$\mathbf{P}_{1,5}$	$(0, 0.1667, 0.2887)$	$\mathbf{P}_{4,3}$	$(0.866, 0, -0.1667)$
$\mathbf{P}_{2,1}$	$(0, -0.2887, 0.1667)$	$\mathbf{P}_{4,4}$	$(0.2887, 0.25, -0.1667)$
$\mathbf{P}_{2,2}$	$(0.2887, -0.25, 0.1667)$	$\mathbf{P}_{4,5}$	$(0, 0.2887, -0.1667)$
$\mathbf{P}_{2,3}$	$(0.866, 0, 0.1667)$	$\mathbf{P}_{5,1}$	$(0, -0.1667, -0.2887)$
$\mathbf{P}_{2,4}$	$(0.2887, 0.25, 0.1667)$	$\mathbf{P}_{5,2}$	$(0, -0.0863, -0.322)$
$\mathbf{P}_{2,5}$	$(0, 0.2887, 0.1667)$	$\mathbf{P}_{5,3}$	$(0, 0, -0.3333)$
$\mathbf{P}_{3,1}$	$(0, -0.3333, 0)$	$\mathbf{P}_{5,4}$	$(0, 0.0863, -0.322)$
$\mathbf{P}_{3,2}$	$(0.3333, -0.2887, 0)$	$\mathbf{P}_{5,5}$	$(0, 0.1667, -0.2887)$
$\mathbf{P}_{3,3}$	$(1.3333, 0, 0)$		

Figure 6.6 illustrates an example wherein NURBS surface interpolation is performed on a set of points defined in Table 6.3. In the illustration, the red circles on the NURBS surface are the points on which the interpolation is performed, and the blue x's are the control points corresponding to the resulting surface.

Using this methodology, a NURBS surface interpolation is performed on a set of points on the TPS, whose movement resulting from recession is tracked. The interpolated surface represents the vehicle geometry at any given instant. The next section describes how the ablation model is integrated into the flight dynamics model.

#### 6.4 Integration of Ablation Model into Equations of Motion

The ablation model is integrated into the flight dynamics model by treating the coordinates of the points  $\mathbf{P}_{k,l}$  that define the geometry as state variables. In a given time step, a NURBS surface interpolation is performed on  $\mathbf{P}_{k,l}$ . This surface represents the instantaneous geometry of the vehicle. It should be noted that this surface is not closed. In order to generate a closed surface, the aft section of the vehicle is simply assumed to be a plane bearing the shape defined by the edge of the NURBS surface. Mathematically, this plane is expressed as:

$$\mathbf{S}_{AFT}(c, d) = \begin{bmatrix} 0 \\ S_{y_B}(c, d) \\ S_{z_B}(c, d) \end{bmatrix} \quad (6.33)$$

where  $S_{y_B}$  and  $S_{z_B}$  are the  $y$  and  $z$  components along the edge of the computed NURBS surface in the body-fixed frame. The ablation model assumes that the points that lie on this edge are restricted to move only along the  $y-z$  plane of the body frame, with the  $x$  axis being the vehicle's roll axis.

The aerodynamic force coefficients (and moment coefficients if treated as a rigid body) are computed using the model described in Chapter 4. The heat-rate is calculated at each  $\mathbf{P}_{k,l}$ , using the procedure explained in Section 6.2. The coordinates of the stagnation point required in the 3D heat-rate model are computed by noting that the stagnation normal vector is parallel to the freestream. The normal vector on the NURBS surface corresponding to parameters  $c$  and  $d$  is given by:

$$\mathbf{n}(c, d) = \mathbf{S}_c(c, d) \times \mathbf{S}_d(c, d) \quad (6.34)$$

where:

$$\begin{aligned} \mathbf{S}_c(c, d) &= \sum_{i=0}^n N'_{i,p}(c) N_{j,q}(d) \mathbf{W}_{i,j} \\ \mathbf{S}_d(c, d) &= \sum_{i=0}^n N_{i,p}(c) N'_{j,q}(d) \mathbf{W}_{i,j} \end{aligned} \quad (6.35)$$

and:

$$\begin{aligned} N'_{i,p}(c) &= \frac{p}{\bar{c}_{i+p} - \bar{c}_i} N_{i,p-1}(c) - \frac{p}{\bar{c}_{i+p+1} - \bar{c}_{i+1}} N_{i+1,p-1}(d) \\ N'_{j,q}(d) &= \frac{q}{\bar{d}_{j+q} - \bar{d}_j} N_{j,q-1}(d) - \frac{q}{\bar{d}_{j+q+1} - \bar{d}_{j+1}} N_{j+1,q-1}(d) \end{aligned} \quad (6.36)$$

The parameters  $c$  and  $d$  corresponding to the stagnation point are obtained by solving the following equation:

$$\mathbf{n}(c, d) \cdot \mathbf{v}_\infty - |\mathbf{n}(c, d)| |\mathbf{v}_\infty| = 0 \quad (6.37)$$

The mean curvature at a given point on the surface, required for the computation of the heat-rate, is given by:

$$H = -\frac{\nabla \cdot \hat{\mathbf{n}}}{2} \quad (6.38)$$

Following the computation of the heat-rate at each  $\mathbf{P}_{k,l}$ , the corresponding surface recession is computed using the model described in Section 6.3. The direction of the surface recession is assumed to be along the local inward-pointing normal. That is:

$$\dot{\mathbf{P}}_{k,l} = \dot{s}_{k,l} \hat{\mathbf{n}}_{k,l} \quad (6.39)$$

Also, since the points that lie on the circumference of the base of the vehicle geometry are assumed to move along the body-fixed  $y - z$  plane, the corresponding dynamic equations are given by:

$$\begin{aligned} \dot{\mathbf{P}}_{(k=0,n),l} &= \left( \dot{s}_{(k=0,n),l} \hat{\mathbf{n}}_{(k=0,n),l} \cdot \hat{\mathbf{y}}_B \right) \hat{\mathbf{y}}_B + \left( \dot{s}_{(k=0,n),l} \hat{\mathbf{n}}_{(k=0,n),l} \cdot \hat{\mathbf{z}}_B \right) \hat{\mathbf{z}}_B \\ \dot{\mathbf{P}}_{(k \neq 0,n),(l=0,m)} &= \left( \dot{s}_{(k \neq 0,n),(l=0,m)} \hat{\mathbf{n}}_{(k \neq 0,n),(l=0,m)} \cdot \hat{\mathbf{y}}_B \right) \hat{\mathbf{y}}_B \\ &\quad + \left( \dot{s}_{(k \neq 0,n),(l=0,m)} \hat{\mathbf{n}}_{(k \neq 0,n),(l=0,m)} \cdot \hat{\mathbf{z}}_B \right) \hat{\mathbf{z}}_B \end{aligned} \quad (6.40)$$

These dynamic equations are appended to those in the flight dynamics model described in Chapter 3. The instantaneous mass of the vehicle may be computed by assuming a uniform density (that is equal to  $\rho_{TPS}$ ) as:

$$m = \iiint_V \left( \rho_{TPS} dV = \rho \iiint_V dV \right) \quad (6.41)$$

where  $V$  is the volume enclosed by the NURBS surface.

While working with NURBS, it is easier to compute the volume using the Gauss Divergence Theorem [117] and evaluating the resultant surface integral numerically. The Gauss Divergence Theorem states that:

$$\iiint_V \left( \nabla \cdot \mathbf{G} dV = \iint_A \left( \mathbf{G} \cdot \hat{\mathbf{n}} dA \right) \right) \quad (6.42)$$

where  $\mathbf{G}$  is a vector field. If  $\mathbf{G} = [S_x \ 0 \ 0]^T$ , and  $S_x$  is the  $x$  component of  $\mathbf{S}(c, d)$  in the body frame, then:

$$\iiint_V \left( \nabla \cdot \mathbf{G} dV = \iiint_V \left( \nabla \cdot [S_x \ 0 \ 0]^T dV = \iiint_V dV = V_{NURBS} \right) \right) \quad (6.43)$$

Therefore, evaluating the surface integral in Eq. 6.42 with  $\mathbf{G} = [S_x \ 0 \ 0]^T$  gives the volume enclosed by the geometry. That is:

$$V = \int_{c=0}^1 \int_{d=0}^1 [S_x \ 0 \ 0]^T \cdot (\mathbf{S}_c \times \mathbf{S}_d) dc dd \quad (6.44)$$

The mass of the vehicle is readily computed as:

$$m = \rho_{TPS} V_{NURBS} \quad (6.45)$$

A more realistic vehicle may be considered to be composed of  $n$  subsystems, each of which may be modeled as enclosing a volume  $V_i$  with uniform density  $\rho_i$  embedded inside the TPS, as illustrated in Figure 6.7. The mass of such a vehicle can be calculated as:

$$m = \rho_{TPS} V_{NURBS} + \sum_{i=1}^n \left( \rho_i - \rho_{TPS} \right) V_i \quad (6.46)$$



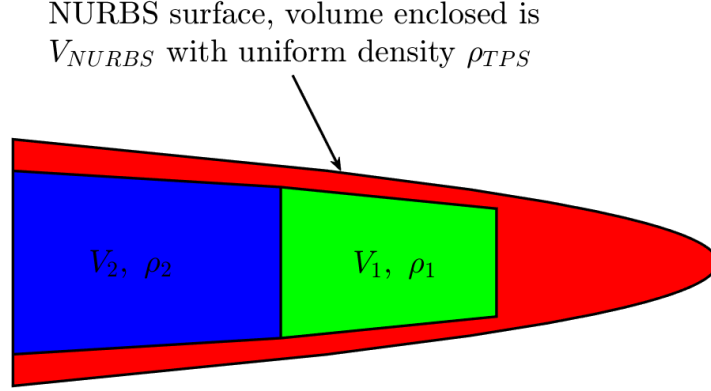


Figure 6.7. Vehicle composed of two additional volumes with different densities.

The calculated instantaneous vehicle mass  $m$  is substituted into the integrated flight dynamics model, which is summarized as:

$$\begin{aligned}
 \dot{\mathbf{P}}_{(k=0,n),l} &= \left( \dot{s}_{(k=0,n),l} \hat{\mathbf{n}}_{(k=0,n),l} \cdot \hat{\mathbf{y}}_B \right) \hat{\mathbf{y}}_B + \left( \dot{s}_{(k=0,n),l} \hat{\mathbf{n}}_{(k=0,n),l} \cdot \hat{\mathbf{z}}_B \right) \hat{\mathbf{z}}_B \\
 \dot{\mathbf{P}}_{(k \neq 0,n),(l=0,m)} &= \left( \dot{s}_{(k \neq 0,n),(l=0,m)} \hat{\mathbf{n}}_{(k \neq 0,n),(l=0,m)} \cdot \hat{\mathbf{y}}_B \right) \hat{\mathbf{y}}_B \\
 &\quad + \left( \dot{s}_{(k \neq 0,n),(l=0,m)} \hat{\mathbf{n}}_{(k \neq 0,n),(l=0,m)} \cdot \hat{\mathbf{z}}_B \right) \hat{\mathbf{z}}_B \\
 \frac{d\mathbf{r}}{dt} &= (\boldsymbol{\Omega} \times \mathbf{r}) + \mathbf{v} \\
 \frac{d}{dt} ((\boldsymbol{\Omega} \times \mathbf{r}) + \mathbf{v}) &= \frac{\mathbf{F}}{m}
 \end{aligned} \tag{6.47}$$

In essence, Eq. (6.47) integrates the effects of ablative shape change into the flight dynamics model. This integrated model is used in simulations and trajectory optimization, as presented in the next section.

## 6.5 Results

This section presents the results of simulations and mission design that utilize the integrated flight dynamics and ablation model.

### 6.5.1 Propagation of Equations of Motion

In this example, the equations of motion given in Eq. (6.47) are propagated in the Earth's atmosphere to demonstrate the difference in trajectories when ablation is accounted for and when it is neglected. Only 2-DOF motion is considered, wherein the vehicle is constrained to fly along the equator. As a result, the state variables can be reduced to atmospheric-relative velocity, atmospheric-relative flight-path-angle, altitude, longitude, and the coordinates of the points that define the geometry of the vehicle. Further, the Earth was assumed to be non-rotating ( $\boldsymbol{\Omega} = \mathbf{0}$ ). The coordinates of the points that define the initial vehicle geometry are given by Table 6.4. The initial conditions for the other states are given in Table 6.5.

Table 6.4. Points defining initial geometry (units in meters).

Point	Coordinates	Point	Coordinates
$\mathbf{P}_{1,1}$	(0, -0.1667, 0.2887)	$\mathbf{P}_{3,4}$	(0.3333, 0.2887, 0)
$\mathbf{P}_{1,2}$	(0, -0.0863, 0.322)	$\mathbf{P}_{3,5}$	(0, 0.3333, 0)
$\mathbf{P}_{1,3}$	(0, 0, 0.3333)	$\mathbf{P}_{4,1}$	(0, -0.2887, -0.1667)
$\mathbf{P}_{1,4}$	(0, 0.0863, 0.322)	$\mathbf{P}_{4,2}$	(0.2887, -0.25, -0.1667)
$\mathbf{P}_{1,5}$	(0, 0.1667, 0.2887)	$\mathbf{P}_{4,3}$	(0.866, 0, -0.1667)
$\mathbf{P}_{2,1}$	(0, -0.2887, 0.1667)	$\mathbf{P}_{4,4}$	(0.2887, 0.25, -0.1667)
$\mathbf{P}_{2,2}$	(0.2887, -0.25, 0.1667)	$\mathbf{P}_{4,5}$	(0, 0.2887, -0.1667)
$\mathbf{P}_{2,3}$	(0.866, 0, 0.1667)	$\mathbf{P}_{5,1}$	(0, -0.1667, -0.2887)
$\mathbf{P}_{2,4}$	(0.2887, 0.25, 0.1667)	$\mathbf{P}_{5,2}$	(0, -0.0863, -0.322)
$\mathbf{P}_{2,5}$	(0, 0.2887, 0.1667)	$\mathbf{P}_{5,3}$	(0, 0, -0.3333)
$\mathbf{P}_{3,1}$	(0, -0.3333, 0)	$\mathbf{P}_{5,4}$	(0, 0.0863, -0.322)
$\mathbf{P}_{3,2}$	(0.3333, -0.2887, 0)	$\mathbf{P}_{5,5}$	(0, 0.1667, -0.2887)
$\mathbf{P}_{3,3}$	(1.3333, 0, 0)		

The vehicle possesses a uniform density of 800 kg/m<sup>3</sup>, which is also the density of the generic TPS. It flies at a constant angle of attack of 10 deg. The heat of ablation

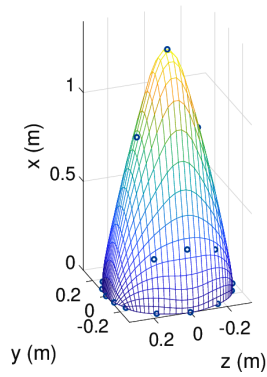
Table 6.5. Initial vehicle states for the propagation of the equations of motion.

State	Value
Atmospheric-relative velocity ( $v$ )	4,000 m/s
Atmospheric-relative flight-path-angle ( $\gamma$ )	0 deg.
Altitude ( $h$ )	50 km
Longitude ( $\theta$ )	0 deg

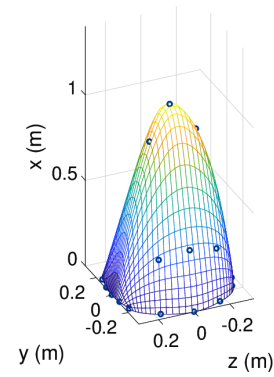
of the TPS is assumed to be 2.23 MJ/kg. The wall temperature is assumed to be constant at 1,000 K.

For comparison, these initial conditions are propagated again without the ablation model. Figure 6.8(a) illustrates the initial geometry of the vehicle. Figure 6.8(b) illustrates the geometry when it impacts the surface. It can be seen that the ablation is non-axisymmetric. The portion of the vehicle exposed to the flow ablates more, resulting in the geometry to evolve into a non-axisymmetric one. This alters the aerodynamic and mass characteristics. The evolution of vehicle mass is shown in Figure 6.8(c). Consequently, the trajectory that is flown is also altered. This can be seen in Figures 6.8(d) and 6.8(e), which compare the trajectories of the ablating and non-ablating vehicle. It can be seen that the shape of the ablating vehicle initially evolves such that the lift characteristics are improved. This, coupled with the lowered mass, results in the ablating vehicle to initially stay higher than the non-ablating vehicle. However, as the vehicle ablates more, it experiences much higher drag deceleration resulting from a blunted nose and reduction in mass. Therefore, the difference between the final downrange of the ablating and the non-ablating vehicle is about 225 km.

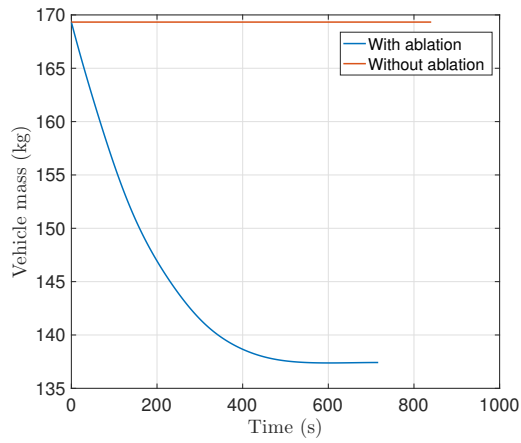
Although this analysis provides insights into the coupling between the shape evolution and the flown trajectory, it would be desirable to design optimal trajectories that account for this coupling. The next example presents an optimized trajectory of an ablating hypersonic vehicle.



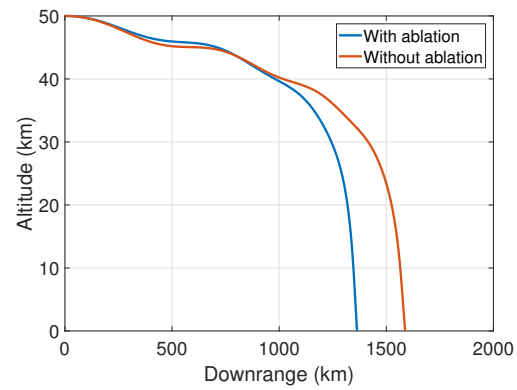
(a) Initial vehicle geometry.



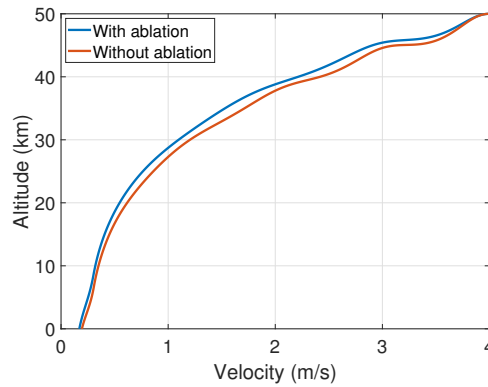
(b) Final vehicle geometry.



(c) Mass vs. Time.



(d) Altitude vs. Downrange.



(e) Altitude vs. Velocity.

Figure 6.8. Comparison of trajectories and vehicle geometry with and without ablation. The initial vehicle geometry and states are defined in Tables 6.4 and 6.5 respectively. The downrange is seen to be reduced by about 14 percent when ablation is accounted for.

### 6.5.2 Trajectory Optimization of a Hypersonic Vehicle Subject to Non-Axisymmetric Ablation

In this example, the trajectory of a hypothetical ablating hypersonic glide weapon system is optimized to minimize time, thereby reducing the warning time for the adversary. The trajectory represents the glide phase of a boost-glide weapon system. The conditions at booster separation are the initial conditions of this trajectory that is required to be optimized and are summarized in Table 6.6. The glide vehicle is required to impact a target that is located at 1.3476 deg longitude on the equator. Its geometry at booster separation is non-axisymmetric, and the corresponding coordinates of the tracked points on the TPS are shown in Table 6.7. Moreover, the vehicle is free to assume any geometry, velocity and flight-path-angle at impact. It also possesses a uniform density of  $800 \text{ kg/m}^3$ , which is also the density of the TPS. The heat of ablation of the TPS is  $2.23 \text{ MJ/kg}$ . As before, the vehicle is constrained to fly along the equator and is maneuvered by varying the angle-of-attack. The velocity and the altitude states are scaled by the corresponding desired initial values,  $3.8 \text{ km/s}$  and  $90 \text{ km}$ , respectively.

Table 6.6. Initial conditions for the glide trajectory.

State	Value
Atmospheric-relative velocity ( $v$ )	$3.8 \text{ km/s}$
Atmospheric-relative flight-path-angle ( $\gamma$ )	$-29.16 \text{ deg.}$
Altitude ( $h$ )	$90 \text{ km}$
Longitude ( $\theta$ )	$0 \text{ deg}$

Noting that this problem involves 79 state equations, the number of differential equations in the necessary conditions of optimality is 158, thereby making the solution process very computationally intensive. As a result, the solution methodology that was employed is different from the traditional continuation method explained in Chapter 5. Since the propagation of the state and co-state dynamics using a Runge-

Table 6.7. Points defining initial geometry (units in meters).

Point	Coordinates	Point	Coordinates
$\mathbf{P}_{1,1}$	$(0, -0.1667, 0.2887)$	$\mathbf{P}_{3,4}$	$(0.3338, 0.2913, 0)$
$\mathbf{P}_{1,2}$	$(0, -0.0863, 0.322)$	$\mathbf{P}_{3,5}$	$(0, 0.3333, 0)$
$\mathbf{P}_{1,3}$	$(0, 0, 0.3333)$	$\mathbf{P}_{4,1}$	$(0, -0.2887, -0.1667)$
$\mathbf{P}_{1,4}$	$(0, 0.0863, 0.322)$	$\mathbf{P}_{4,2}$	$(0.2896, -0.2541, -0.1693)$
$\mathbf{P}_{1,5}$	$(0, 0.1667, 0.2887)$	$\mathbf{P}_{4,3}$	$(0.868, 0, -0.1751)$
$\mathbf{P}_{2,1}$	$(0, -0.2887, 0.1667)$	$\mathbf{P}_{4,4}$	$(0.2896, 0.2541, -0.1693)$
$\mathbf{P}_{2,2}$	$(0.2898, -0.2549, 0.1698)$	$\mathbf{P}_{4,5}$	$(0, 0.2887, -0.1667)$
$\mathbf{P}_{2,3}$	$(0.8714, 0, 0.1906)$	$\mathbf{P}_{5,1}$	$(0, -0.1667, -0.2887)$
$\mathbf{P}_{2,4}$	$(0.2898, 0.2549, 0.1698)$	$\mathbf{P}_{5,2}$	$(0, -0.0863, -0.322)$
$\mathbf{P}_{2,5}$	$(0, 0.2887, 0.1667)$	$\mathbf{P}_{5,3}$	$(0, 0, -0.3333)$
$\mathbf{P}_{3,1}$	$(0, -0.3333, 0)$	$\mathbf{P}_{5,4}$	$(0, 0.0863, -0.322)$
$\mathbf{P}_{3,2}$	$(0.3338, -0.2913, 0)$	$\mathbf{P}_{5,5}$	$(0, 0.1667, -0.2887)$
$\mathbf{P}_{3,3}$	$(1.4549, 0, 0)$		

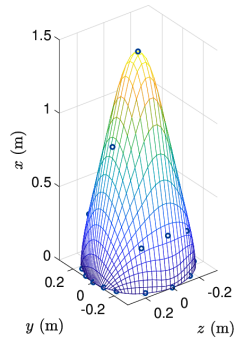
Kutta formulation is much faster, the majority of the solution is obtained using this method. The state and co-state dynamics are reverse-propagated using the Dormand-Prince method [118] from the desired impact location to 0 deg longitude. For this reverse propagation, the values for the velocity and flight-path-angle at the impact location were assumed to be 1 km/s and  $-40$  deg, respectively. Noting that these values in fact correspond to the free final values in the original optimization problem, their corresponding co-states at impact location are 0. Moreover, since the final geometry is not fixed, the co-states corresponding to the tracked points are also required to be 0 at impact. Finally, since the final longitude and altitude are fixed, their co-states are free to assume any final value. Hence, for the reverse-propagation, the longitude co-state at impact location was assumed to be an arbitrary value of  $-5,000$ . The

altitude co-state at impact was derived accordingly by solving the boundary condition on the Hamiltonian,  $\mathbf{H}(t_f) = 0$ .

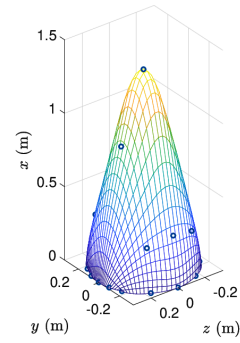
Since arbitrary values were assumed for the free co-states corresponding to the terminal point (impact location) of the trajectory, the values of the states at booster separation are not guaranteed to be equal to the desired values, except longitude because the reverse-propagation was stopped when its value reached 0 deg. However, this reverse-propagated solution is a valid locally optimal solution corresponding to these values of the initial states. As a result, this solution can be used as a seed in the continuation process with the finite difference method. Since every initial state is fixed, the finite difference method is not required to enforce conditions on the initial co-states. However, since the final geometry, velocity and flight-path-angle are free, their corresponding co-states are explicitly constrained to be 0.

Continuation was employed by varying the values of the states corresponding to booster separation to the desired values in 100 iterations. The solution of the reverse-propagation was used as the guess for the first iteration. It may be noted that this guess is in fact the solution of this initial problem. The solution of the final iteration is the desired solution of the original optimization problem.

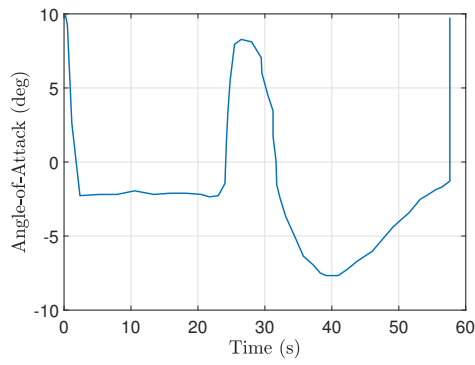
Figures 6.9(a) and 6.9(b) illustrate the initial and the final geometry of the vehicle respectively. Figure 6.9(c) illustrates the optimal control history. It can be seen that initially, the angle-of-attack is negative. This angle-of-attack also results in zero lift and minimum drag as the vehicle is non-axisymmetric. In general, attempting to maneuver the vehicle during this phase will be ineffective because the dynamic pressure is very low at this altitude. Any significant maneuver at this stage will only result in an increase in the overall drag loss, which translates to longer flight time. As the vehicle descends to a lower altitude and encounters more dynamic pressure, it increases the angle-of-attack to shallow the descent, thereby avoiding undershooting the target. Towards the end of the trajectory, it dives again, indicated by the negative angle-of-attack. This maneuver steepens the descent towards the end of the trajectory, thereby reducing the amount of time spent in the lower part of the atmosphere, which



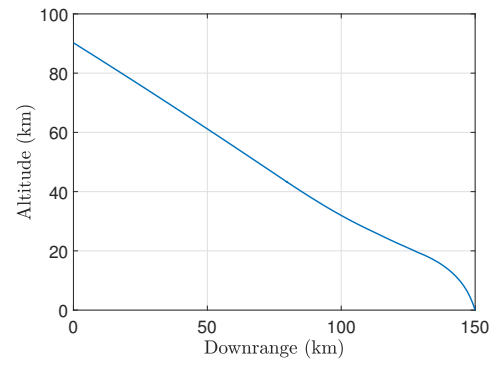
(a) Initial vehicle geometry.



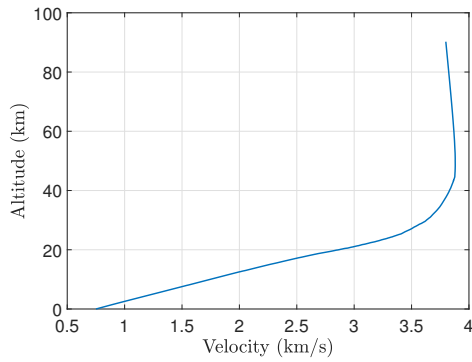
(b) Final vehicle geometry.



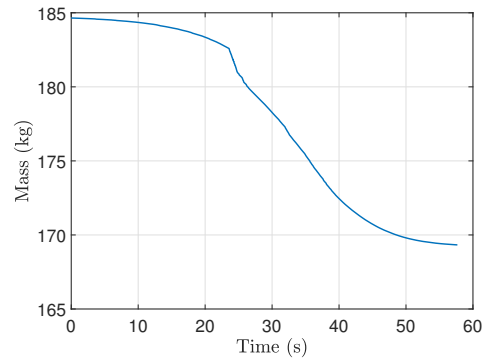
(c) Angle-of-attack vs. time.



(d) Altitude vs. downrange.



(e) Altitude vs. velocity.



(f) Mass vs. time.

Figure 6.9. Trajectory optimization of a hypersonic glide vehicle subject to non-axisymmetric ablation to minimize TOF. The states and glide vehicle geometry at booster separation are defined in Tables 6.6 and 6.7 respectively.



translates to reduced drag loss and flight time. Figures 6.9(d) and 6.9(e) show the resultant optimal trajectory. It can be seen that the impact velocity is 751 m/s. Since the vehicle ablates, it loses mass, as shown in Figure 6.9(f). It is interesting to observe an increase in mass loss rate when the angle-of-attack is increased at about 24 seconds. This is counter-intuitive as one would expect a reduction in mass loss rate because the peak heat-rate on the geometry is reduced. However, increasing the angle-of-attack also increases the incidence angle of the exposed surface with respect to the freestream, resulting in higher edge pressure and corresponding heat-rate. Therefore, although the peak heat-rate (which occurs at the stagnation point) is reduced, the local heat-rate throughout the surface area exposed to the flow is increased, resulting in an overall increase in ablation and the resultant mass loss rate.

As stated, this example involved 79 states, making the problem computationally intensive. This limited the scope of design analyses. However, this challenge may be mitigated by taking advantage of advances in parallel computing technology, and is a key area of future work of this dissertation. Nevertheless, substantial insights can be gained by assuming only axisymmetric ablation because the bulk of the surface recession occurs at the nose. This simplifying assumption enables more complex conceptual mission analysis. For instance, the effects of ablative shape change can be analyzed for constrained trajectory optimization problems, as described in the next section.

### **6.5.3 Trajectory Optimization of an Axisymmetrically Ablating Hypersonic Vehicle Subject to Inequality Constraint on Altitude**

In this example, the trajectory of an axisymmetrically ablating hypersonic glide vehicle is optimized to maximize the velocity at target impact to increase the destruction capability. Again, only planar motion is considered. The assumption of axisymmetric ablation is reasonable if the vehicle executes periodic roll maneuvers to even out the ablation around the vehicle, thereby resulting in an overall averaged

axisymmetric geometry. Consequently, the geometry is modeled as a body of revolution. The 2-D shape that generates the 3-D axisymmetric vehicle is discretized into 2 nodes: one at the nose, and the other at the base of the vehicle. Thus, the node at the nose represents the instantaneous length of the vehicle, and the one at the base represents the base radius. The 2-D shape is represented by a quadratic curve that joins these two nodes. At the nose, the curve is perpendicular to the roll axis ( $\hat{\mathbf{x}}_B$ ) of the vehicle. The initial length and radius of the vehicle are assumed to be 1.2 m and 0.2 m respectively. Also, ablation at the base of the vehicle is neglected. The heat-rate at the nose of the vehicle is calculated using Eq. (6.12), assuming a wall temperature of 1,000 K. The TPS properties are defined by a  $Q_*$  of 6.2 MJ/kg and a  $\rho_{TPS}$  of 977.78 kg/m<sup>3</sup>. The mass distribution of the vehicle is assumed to be such that its initial mass is 250 kg. The length of the vehicle becomes a state and is combined with the other states,  $v$ ,  $\gamma$ ,  $h$  and  $\theta$ .

As before, the glide vehicle is assumed to be a part of the boost-glide weapon system, and only the glide trajectory is optimized with the objective of maximizing the velocity when it impacts the target, which is located at 6.2882 deg longitude on the equator. The vehicle is constrained to fly below a parabolic altitude profile given by:

$$h < 1000 \left( \frac{75}{0.0706^2} \theta^2 - \frac{152}{0.0706} \theta + 96 \right) \quad (6.48)$$

In essence, the upper limit on the altitude is 96km at 0 deg longitude. This gradually lowers to 20 km at 4.0424 deg longitude and again smoothly rises back to 96 km at 8.0848 deg longitude. This profile for the altitude constraint is chosen because it is assumed that the adversary has established an early warning radar at 4.0424 deg longitude. It is beneficial to minimize the visibility to the radar by remaining below the horizon, and consequently, below the radar's line-of-sight (LOS), for the majority of the trajectory. By adhering to this altitude constraint, the vehicle attempts to minimize its visibility to the radar by remaining below its LOS.

The post-boost conditions serve as the initial conditions for the optimization problem. However, the post-boost flight-path-angle is free to be optimized. The initial and final conditions of the glide trajectory are summarized in Table 6.8. As before, the vehicle is controlled by varying the angle-of-attack.

The velocity and altitude are scaled by their respective initial values, 4 km/s and 60 km, resulting in  $V$  and  $\bar{h}$ . The altitude constraint introduces two additional generic states,  $\xi_1$  and  $\xi_2$ , and one generic control variable,  $u_1$ . The optimal solution is obtained in three continuation steps. The first step involves iteratively varying the final conditions on altitude and longitude. The initial guess for the first iteration is generated by propagating the differential equations in the necessary conditions of optimality from Eq. (5.16) for 0.1 s using Dormand-Prince method, with the following initial conditions:

$$\begin{aligned}
 \mathbf{X}^T &= [V \quad \gamma \quad \bar{h} \quad \theta \quad l_V \quad \xi_1 \quad \xi_2]^T \\
 &= [1 \quad -0.35 \quad 1 \quad 0 \quad 1.2 \quad 0.1 \quad 0.1] \left( \begin{array}{c} \\ \\ \\ \\ \\ \end{array} \right. \\
 \boldsymbol{\lambda}^T &= \left( \begin{array}{c} \lambda_V \quad \lambda_\gamma \quad \lambda_{\bar{h}} \quad \lambda_\theta \quad \lambda_{l_V} \quad \lambda_{\xi_1} \quad \lambda_{\xi_2} \end{array} \right)^T \\
 &= [-0.1 \quad 0 \quad -0.1 \quad -0.1 \quad 0.1 \quad 0.1 \quad 0.1] \left( \begin{array}{c} \\ \\ \\ \\ \\ \end{array} \right.
 \end{aligned} \tag{6.49}$$

Table 6.8. Initial and terminal constraints.

State	Initial Condition	Final Condition
Velocity ( $v$ )	4 km/s	Free
Flight-path-angle ( $\gamma$ )	Free	Free
Altitude ( $h$ )	60 km	0 km
Downrange ( $\theta$ )	0 deg	6.2882 deg
Vehicle length ( $l_V$ )	1.2 m	Free

For the initial guess propagation, the value of  $\epsilon$ , the weighting factor for the generic control variable introduced by the altitude constraint, is set to 1. The final boundary conditions on altitude and longitude for the problem in the first iteration are set to

the corresponding values in the propagated initial guess. These conditions are varied in 200 iterations to 0 km and 0.1797 deg, respectively. In the second continuation step, the final condition on longitude is varied in 200 iterations to the desired value of 6.2882 deg. The evolution of the problem in the continuation process was chosen as described to guide the solution below the altitude constraint, thereby avoiding infeasible intermediate problems. In the third and final continuation step, the value of  $\epsilon$  is changed in 1,000 iterations to  $10^{-8}$ . The solution of the final iteration in step 3 is the desired optimal solution.

The resultant optimal trajectory is illustrated in Figure 6.10. For comparison, another trajectory corresponding to the same mission is calculated by neglecting ablation. It can be seen that although the physical trajectories for the two cases are similar (Figure 6.10(a)), the control histories to follow them are very different (Figure 6.10(b)). This fact can be potentially important while designing the control surfaces because the ablating vehicle has a more aggressive control history, and it should be capable of achieving the higher angle-of-attack. The ablating vehicle also experiences more drag deceleration as it loses mass (Figure 6.10(d)) and its nose becomes blunt (Figure 6.10(c)). As a result, it has a reduced final velocity, which is more than 60 percent lower than that of the non-ablating vehicle (Figure 6.10(e)).

Thus far, the discussions involved designing optimal trajectories by assuming that the vehicle geometry and TPS properties are established. However, the integrated framework can also be used to perform conceptual design of new TPS materials, as discussed in the next section.

#### **6.5.4 Trade Studies for Designing New Thermal Protection System Materials**

A key capability gained in the integrated design framework discussed in this chapter is the ability to perform trade studies during conceptual design to determine the desired properties of new TPS materials. At the conceptual level, a TPS material

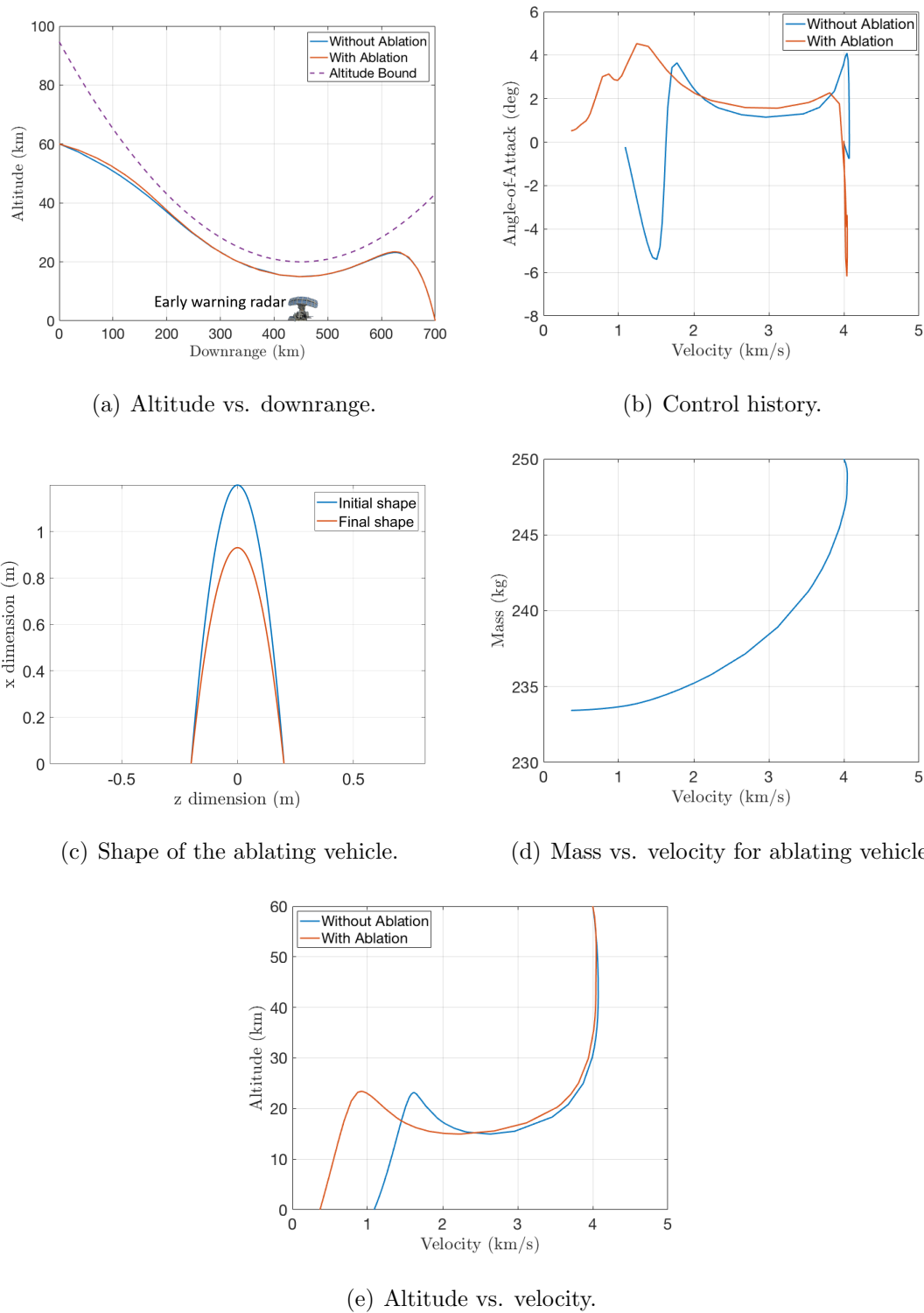


Figure 6.10. Comparison of maximum final velocity trajectories with altitude constraints, calculated with and without TPS ablation. The glide vehicle states and geometry at booster separation and the desired final states are defined in Table 6.8. The final velocity of the ablating vehicle is reduced by more than 60 percent.

may be characterized by its heat of ablation,  $Q_*$ , and density,  $\rho_{TPS}$ . It is typically required to determine the desired values for these parameters to meet certain mission requirements. In subsequent design phases, appropriate materials are synthesized to meet these parameters. In essence, this framework makes it possible to optimize the TPS properties specific to the intended mission by performing design trade studies.

For instance, consider a military mission wherein it is required to maximize the velocity at impact of a target that is located at a maximum distance of 450 km from booster burnout. In this example, the booster cut-off conditions are well established, and are summarized in Table 6.9.

The vehicle geometry is also established, and is assumed to be a circular paraboloid of length 4 m and base radius 0.5 m. The vehicle is also assumed to comprise of two subsystems, as described in Table 6.10.

Table 6.9. Conditions at booster burnout.

State	Value
Atmospheric-relative velocity ( $v$ )	4 km/s
Atmospheric-relative flight-path-angle ( $\gamma$ )	0 deg.
Altitude ( $h$ )	40 km
Downrange	0 km

Table 6.10. Properties of subsystems.

Subsystem number	Volume	Average density
1	0.553 m <sup>3</sup>	100 kg/m <sup>3</sup>
2	0.034 m <sup>3</sup>	17,000 kg/m <sup>3</sup>

The rest of the volume of the vehicle is filled with TPS material, whose influence on the mission is studied. Trade studies may be performed by varying  $Q_*$  while holding  $\rho_{TPS}$  constant (Figure 6.11), and vice versa (Figure 6.12). It can be seen that a low

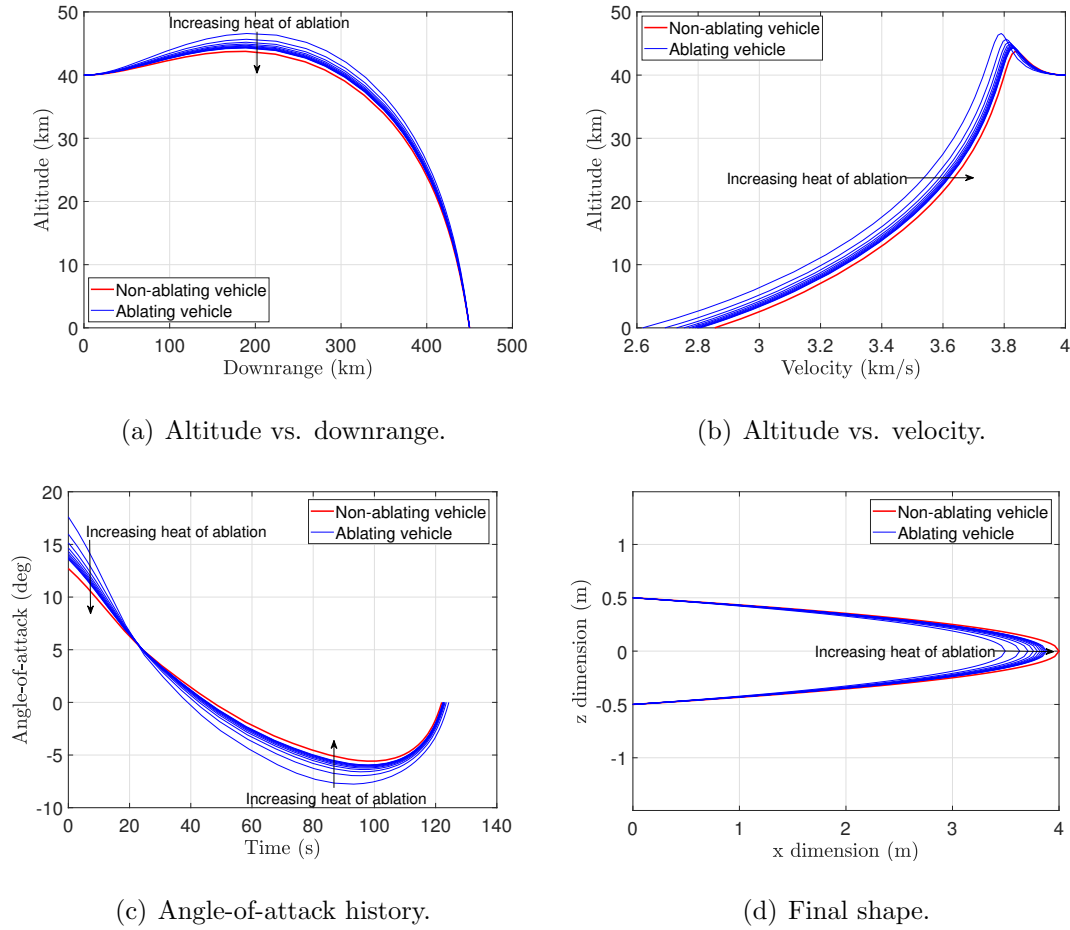


Figure 6.11. Influence of increasing the heat of ablation of the TPS on the trajectory.  $Q_*$  is varied from 2 MJ/kg to 10 MJ/kg, while  $\rho_{TPS}$  is held at 800 kg/m<sup>3</sup>.

$Q_*$  results in the vehicle climbing to a higher altitude initially to reduce ablation and the accompanying drag. As it nears the target, it performs a dive to rapidly traverse the denser portions of the atmosphere, thereby maximizing final velocity. However, the blunted vehicle and the aggressive maneuver eventually proves to be costly. On the flip side, a high  $Q_*$  enables the vehicle to fly lower without encountering severe ablation, thereby reducing the aggressiveness of the climb and preserving its velocity. From the mission stand-point, a very high  $Q_*$  is desired. However, such a TPS is required to have a very high heat capacity to prevent the conduction of heat into

the subsystems. On the other hand, a very low  $Q_*$  will result in excessive ablation and a degradation in the mission performance. In the worst case, the TPS may completely burn through and the subsystems will no longer be protected from the heating. Therefore, a trade-off is necessary between mission performance and the extent of protection against heating. This trade study enables the designer to make more informed design decisions.

Increasing the TPS density can also be seen to improve mission performance. The final velocity increases because the overall mass of the vehicle increases, resulting

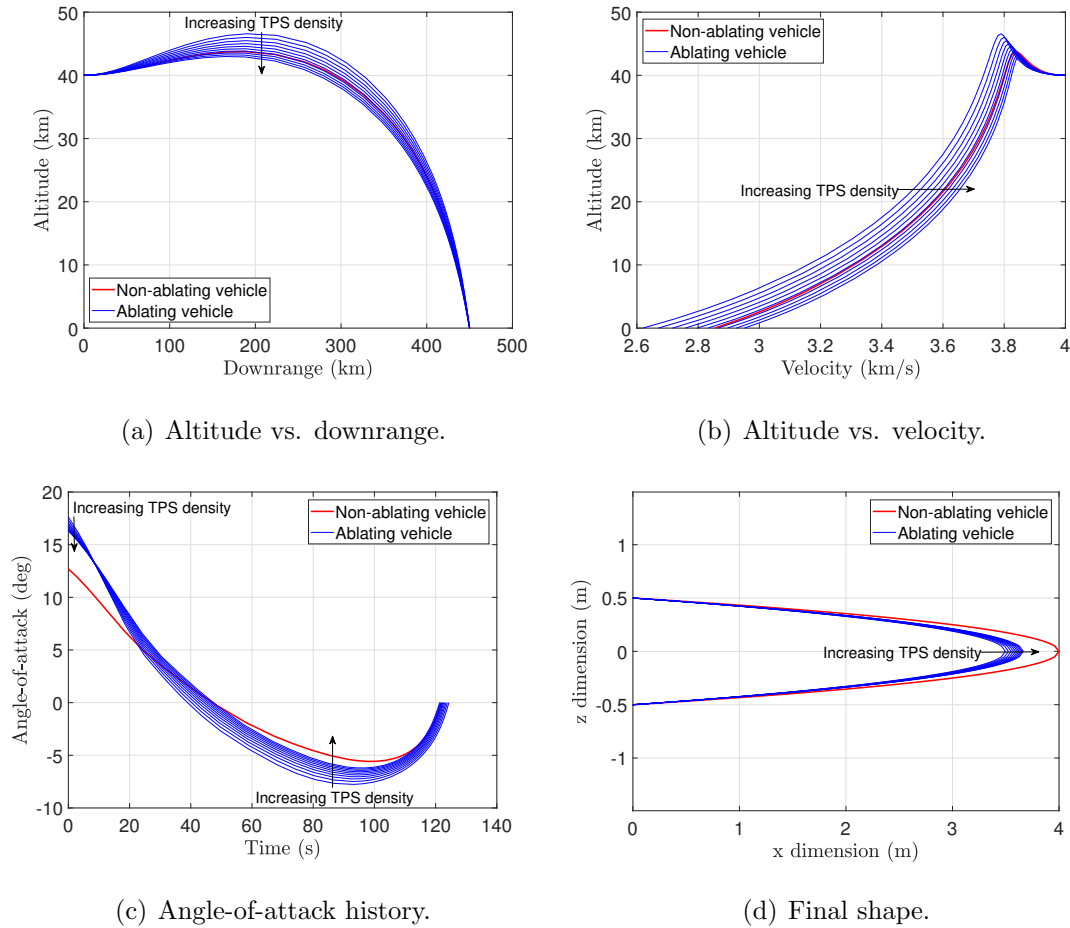


Figure 6.12. Influence of increasing the TPS density.  $\rho_{TPS}$  is varied from  $800 \text{ kg/m}^3$  to  $1,500 \text{ kg/m}^3$ , while  $Q_*$  is held at  $2 \text{ MJ/kg}$ .



in lower drag deceleration because of the increased ballistic coefficient. However, the increased mass results in the vehicle flying lower, thereby encountering higher dynamic pressure and associated structural load. Nevertheless, despite the lower trajectory, the ablation is less. In essence, if it is impractical to design a TPS with high  $Q_*$ , a high density TPS may instead be designed when it is desired to reduce ablation. Although a more favorable mission performance is achieved from an increased TPS density, the vehicle's mass is also increased, thereby requiring a more powerful booster during the boost phase, resulting in a trade-off.

In essence, by studying the effects of  $Q_*$  and  $\rho_{TPS}$  on the mission performance, suitable values can be defined for these parameters that provide the required balance between mission performance, TPS performance and practicality of the TPS design. Subsequent design phases will involve synthesizing materials that satisfy these parameters.

## 6.6 Summary

The results presented in this chapter demonstrate the advancement in the state-of-the-art in conceptual hypersonic mission design by capturing the explicit coupling between the flight dynamics and the evolution of vehicle geometry resulting from ablation of the TPS. Optimal trajectories that account for this coupling are more representative of the aerothermal environment encountered by the vehicle. The indirect framework for trajectory optimization enables the determination of the optimal control history explicitly from the information contained in this coupling. Moreover, the trajectories that were designed can be trusted to be at least locally optimal, unlike other direct trajectory optimization methods.

However, the scope of analysis using non-axisymmetric ablation model was limited because of the increased computational cost. Nevertheless, insights were gained just by forward-propagating the dynamic equations of the non-axisymmetric model. Furthermore, an optimal trajectory was developed using this model. The computational

challenges may be addressed by leveraging parallel computing, which is a logical next step beyond this dissertation.

By assuming axisymmetric ablation, it was possible to perform more in-depth mission design analysis that involved path constraints. More results involving such constraints were presented in [119], and can be found in Appendix B. This integrated framework with the assumption of axisymmetric ablation also provides the capability to perform trade studies to determine the desired TPS properties that satisfy mission requirements while providing the necessary protection from heating.

The key observations from the results presented in this chapter are the significant reduction in the maximum achievable final velocity (which is critical for slender hypersonic vehicles used in military applications) and the substantial variations in the angles-of-attack when TPS ablation is accounted for. However, it is not immediately clear whether the vehicle possesses the required maneuverability to achieve the resulting high angles-of-attack. To answer this, it is necessary to move away from point-mass dynamics and incorporate a rigid body model into the mission design framework, which is the focus of the second contribution of the dissertation and is discussed in Chapter 7.



## 7. INCORPORATION OF RIGID BODY DYNAMICS INTO TRAJECTORY DESIGN

### 7.1 Introduction

This chapter discusses the second contribution of the doctoral dissertation: incorporation of rigid body dynamics into the indirect trajectory optimization framework. Only pitch dynamics are incorporated, restricting the flight to be planar. Even this simplified dynamic system poses numerical challenges in the indirect framework, which are discussed. However, the incorporation of pitch dynamics alone provides substantial insight into the trajectory design problem for many hypersonic systems, particularly the ones with high  $L/D$  that enables them to extend their downrange. They can be maneuvered by modulating pitch through the actuation of elevons. The extent of this modulation depends on the mass distribution of the vehicle, and the location and the geometry of the elevons, as it will be seen in the results presented. This chapter extends the rigid body analysis to rocket-powered vehicles as well. Since the rate of propellant ejection is high for such vehicles, the effect of jet damping is required to be incorporated into the flight dynamics model, which is explained in the rigid body flight dynamics model described in the following section.

### 7.2 Flight Dynamics Model

The rigid body analysis incorporates planar motion with three degrees of freedom: two translational and one rotational. In essence, the vehicle is constrained to fly along the equator. Consequently, for the translational motion, the kinematic variables are altitude ( $h$ ) and longitude ( $\theta$ ), and the dynamic variables are atmospheric-relative velocity ( $v$ ) and atmospheric-relative flight-path-angle ( $\gamma$ ). These variables were also

used in the point-mass dynamics described in Chapter 3, and are illustrated again here in Figure 7.1. For the rotational motion, the kinematic variable is pitch angle ( $\Theta$ ) and the dynamic variable is pitch-rate ( $\omega$ ). Both  $\Theta$  and  $\omega$  are measured in the local horizon frame, as illustrated in Figure 7.2, which assumes a powered vehicle. The vehicle's pitch can be controlled by gimbaling the nozzle of the rocket motor ( $\delta_T$ ) and by actuating the control surface ( $\delta_C$ ). The thrust  $T$  is controlled by varying the propellant mass flow rate,  $\dot{m}$ .

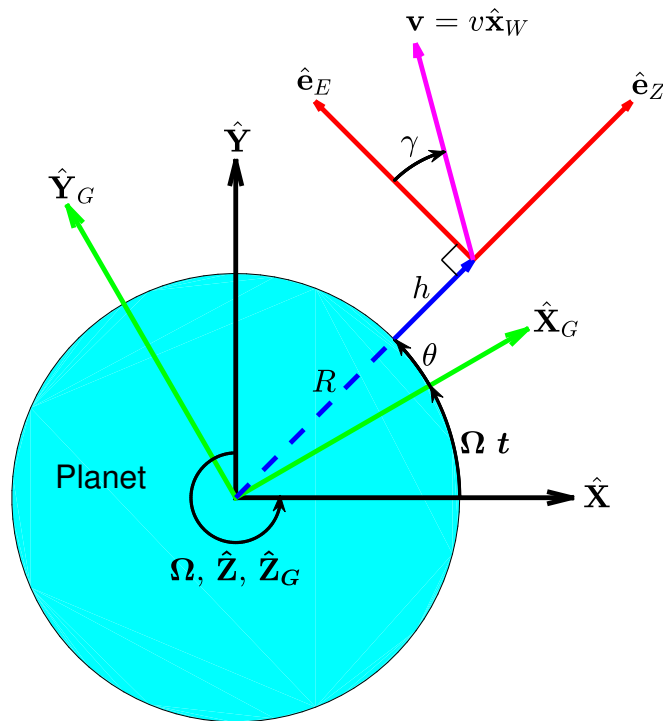


Figure 7.1. Illustration of translational state variables.

The dynamics for the translational state variables are directly derived from Chapter 3. This assumes that the dimensions of the vehicle are negligible when compared to those of the trajectory. As a result, the translational dynamics neglect the effect of shift in the center of mass as the vehicle burns propellant. However, the rotational



The dynamics for the pitch angle are given by:

$$\dot{\Theta} = \omega \quad (7.3)$$

The dynamics for the pitch rate are derived from the general rotational equations of motion [120] as:

$$\mathbf{M} = \frac{{}^i d\mathcal{H}_{CM}}{dt} \quad (7.4)$$

where the superscript prefix  $i$  represents an inertial time derivative. Furthermore,  $\mathcal{H}_{CM}$  is the inertial angular momentum vector about the center of mass of the vehicle, and is given by:

$$\mathcal{H}_{CM} = \bar{\bar{\mathbf{I}}}_{CM} \cdot {}^i \boldsymbol{\omega} \quad (7.5)$$

where  $\bar{\bar{\mathbf{I}}}_{CM}$  is the inertia tensor about the center of mass of the vehicle, and  ${}^i \boldsymbol{\omega}$  is the inertial angular velocity vector. In the 2-D case, Eq. (7.5) collapses to:

$$\mathcal{H}_{CM} = I_{y,CM} {}^i \omega \quad (7.6)$$

where:

$${}^i \omega = \omega - \dot{\theta} - \Omega \quad (7.7)$$

and  $I_{y,CM}$  is the moment of inertia about the pitch axis ( $\hat{\mathbf{y}}_B$ ). Consequently, Eq. (7.4) becomes:

$$M_y = I_{y,CM} (\dot{\omega} - \ddot{\theta}) + \dot{I}_{y,CM} (\omega - \dot{\theta} - \Omega) \quad (7.8)$$

The evolution of the pitch moment of inertia is the result of change in mass distribution as the vehicle burns propellant and the TPS ablates. The reduction in pitch moment of inertia caused by the consumption of propellants results in an increase in the magnitude of  ${}^i \omega$ . However, it should also be noted that vehicles with a propulsion system experience jet damping [121], wherein the ejected products of

combustion carry away some of the angular momentum, as illustrated in Figure 7.3. The resultant loss in the vehicle's angular momentum contributes to a reduction in  $^i\omega$ , thereby countering the effect of the decrease in pitch moment of inertia. As a result, the net change in  $\omega$  depends on the location of the nozzle with respect to the center of mass ( $r_T$ ), propellant flow rate, propellant density, and configuration of the propellant tanks.

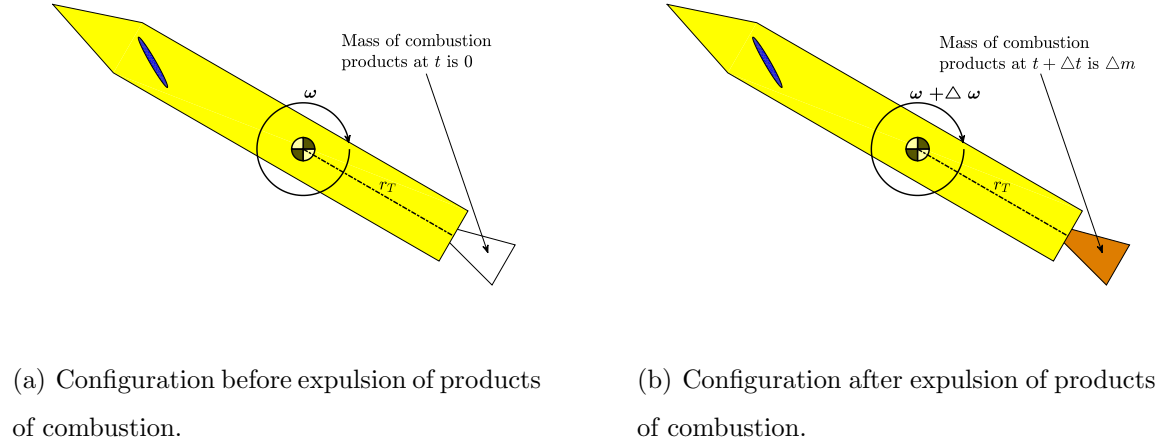


Figure 7.3. Illustration of loss in angular momentum in the products of combustion.

Nevertheless, since the propellant flow rate is significant, jet damping is required to be factored into the flight dynamics. At any given time interval,  $\Delta t$ , let the total mass of the propellant exiting the nozzle be  $\Delta m$ . By assuming this mass to be contained in a volume (the nozzle) that is very small when compared to the dimensions of the vehicle, the angular momentum about the center of mass possessed by it is:

$$\begin{aligned}\Delta \mathcal{H}_{F,CM} &= \Delta m r_T^2 {}^i\omega \\ &= \Delta m r_T^2 \left( \psi - \dot{\theta} - \Omega \right)\end{aligned}\tag{7.9}$$

It should be noted that since the motion is planar, the loss in angular momentum is only in the pitch axis ( $\hat{\mathbf{y}}_B$ ). Consequently, Eq. (7.9) represents the component of the angular momentum of  $\Delta m$  about the pitch axis. Since this mass is ejected during the time interval  $\Delta t$ , the average rate of change of angular momentum is:



$$\frac{\Delta \mathcal{H}_{F,CM}}{\Delta t} = \frac{\Delta m}{\Delta t} r_T^2 (\omega - \dot{\theta} - \Omega) \quad (7.10)$$

At the limit when  $\Delta t \rightarrow 0$ , the instantaneous rate of change (loss) of angular momentum resulting from the ejection of the products of combustion is:

$$\frac{d\mathcal{H}_{F,CM}}{dt} = \dot{m} r_T^2 (\omega - \dot{\theta} - \Omega) \quad (7.11)$$

Consequently, Eq. (7.8) needs to be modified as:

$$M_y = I_{y,CM} (\dot{\omega} - \ddot{\theta}) + \dot{I}_{y,CM} (\omega - \dot{\theta} - \Omega) + \dot{m} r_T^2 (\omega - \dot{\theta} - \Omega) \quad (7.12)$$

Therefore, the dynamics for the pitch rate is given by:

$$\dot{\omega} = \frac{M_y - \left( \dot{I}_{y,CM} + \dot{m} r_T^2 \right) (\omega - \dot{\theta} - \Omega)}{I_{y,CM}} + \ddot{\theta} \quad (7.13)$$

Figure 7.4 illustrates the pitch rate of a rocket stage tumbling in vacuum and in the absence of gravity sources. The stage is a hollow cylinder of length 5.68 m and radius 1 m. The inert mass is 2,000 kg, and the corresponding center of mass is located at 2.8 m from the base along the axis of the cylinder. The pitch moment of inertia of the inert structure about its center of mass is 300 kg-m<sup>2</sup>. The entire cylinder is assumed to be initially filled with propellant, whose density is 700 kg/m<sup>3</sup>. The nozzle is located at the base of the cylinder ( $r_T = 2.8$ m), and is not gimbaled. The engine operates with a propellant flow rate of 400 kg/s. The illustration compares the evolution of the pitch rate ( $\omega$ ) when the loss in angular momentum in the combustion products is accounted for and neglected. It can be seen that for this configuration of the booster, the difference is substantial. This demonstrates that depending on the configuration of the rocket, the loss in angular momentum in the combustion products cannot be neglected. In this particular case, the loss in angular momentum does not fully counter the effect of decrease in the pitch moment of inertia of the rest of the stage. As a result, the pitch rate still increases over time.

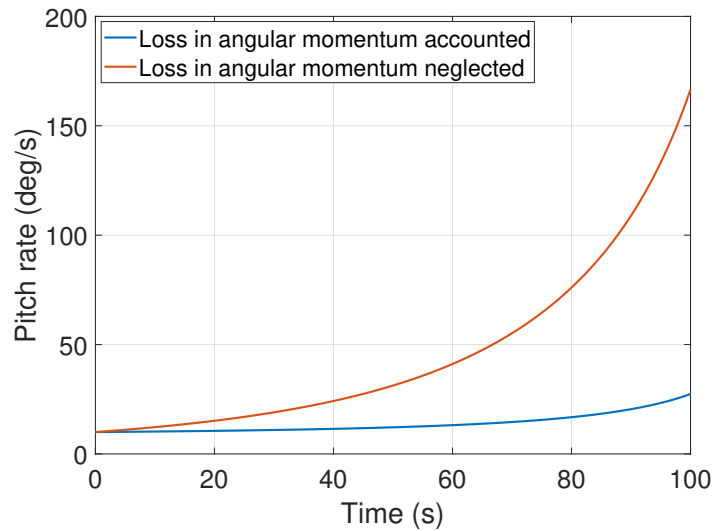


Figure 7.4. Comparison of variation in pitch rate evolution when the loss in angular momentum resulting from the ejection of combustion products is accounted for and neglected.

The 3-DOF rigid body equations of motion described in this section can in theory be applied in the indirect trajectory optimization framework. However, it poses some numerical issues, as discussed in the next section.

### 7.3 Numerical Stiffness

For aerodynamically stable configurations, the equations of motion described in Section 7.2 become numerically stiff (singularly perturbed [122, 123]) at hypersonic speeds. The stiffness is predominantly caused by the  $\dot{\omega}$  equation. When the vehicle is aerodynamically stable, any perturbation in the pitch angle from the trim value will result in a restoring aerodynamic moment, which will lead to an oscillation in the pitch angle. This oscillation is damped, as predicted by piston theory. The damping is high if the area of the control surfaces is high. Moreover, this oscillation corresponds to the short-period mode [124]. In traditional subsonic aircraft, this mode is heavily damped, in part, because of the larger wing area and lower restoring aerodynamic moment.

However, at hypersonic speeds, the oscillation is severely under-damped because the restoring moment is very high. The problem is exacerbated by the smaller area of the control surfaces. As a result, the deflection of the control surface from the trim condition induces a lightly damped, high frequency pitch oscillation about the new trim angle-of-attack. This oscillation is illustrated in Figure 7.6, corresponding to a hypothetical sphere-cone vehicle with quadrature arrangement of fins with elevons (Figure 7.5).

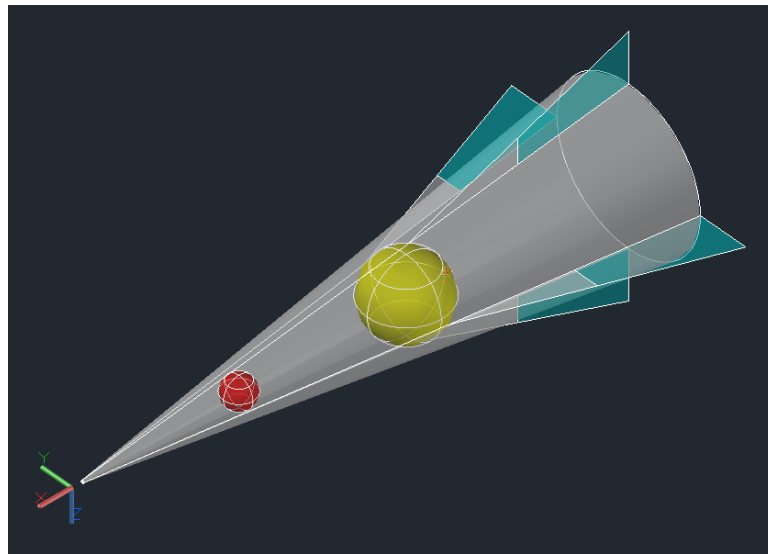


Figure 7.5. Hypothetical vehicle used in the illustration of numerical stiffness.

In the illustration, the freestream velocity and density are assumed to be fixed at Mach 1.5 and  $0.2 \text{ kg/m}^3$  respectively. Initially,  $\Theta$ ,  $\omega$ , and the control surface deflection are set to 0. In this flow condition,  $\Theta$  is also equal to the angle-of-attack,  $\alpha$ . After 5 seconds, the left and right control surfaces ( $\delta_L$  and  $\delta_R$ ) are deflected by the same amount,  $\delta_C$ , equal to  $-10 \text{ deg}$ . This results in oscillation in  $\Theta$ . As explained, this oscillation has a high frequency and is lightly damped. The frequency increases with higher Mach number, aerodynamic stability (e.g. when the center of mass is located further forward in the vehicle), and lower pitch moment of inertia. This high frequency oscillation results in numerical stiffness.

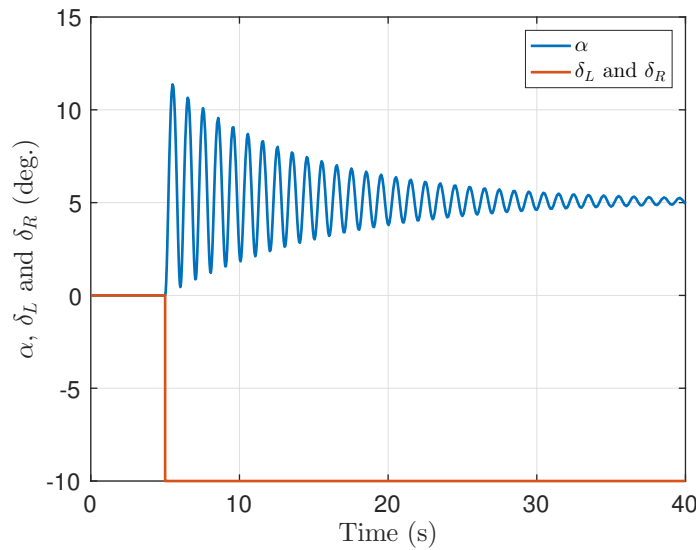


Figure 7.6. Illustration of numerical stiffness.

There is a bulk of literature that describes methodologies to solve IVPs involving stiff systems [122, 123, 125–127]. For solving BVPs, shooting methods may be used, which can take advantage of these stiff IVP methods. However, the corrections in the guessed free boundary conditions for each iteration will be very inaccurate because the terminal conditions are highly sensitive to perturbations in the initial conditions. Multiple shooting can in principle address this sensitivity issue. However, this will require a large number of intermediate arcs to limit the sensitivity of the boundary conditions to reasonable levels. If finite difference methods are used, they will require a highly refined mesh to guarantee stability of the solution, in accordance with the Nyquist criterion [122]. This results in a prohibitively large number of trajectory points, which in turn increases the computational load.

There exists considerable literature that describes several approaches to solve stiff BVPs [128–130]. However, these discussions are limited to scalar systems and simple higher dimensional systems. Adapting these algorithms for aerospace problems is a tedious process. Instead, this dissertation focuses on tackling the root of the issue by reducing the numerical stiffness of the differential equations, thereby allowing the use

of finite difference methods that have been used throughout this dissertation without any modifications. To reduce the numerical stiffness, pitch rate is fed back to the control surfaces (elevons) through a DC gain or a washout filter [124], depending on the vehicle configuration. Figure 7.7 illustrates the feedback loop with the washout filter.

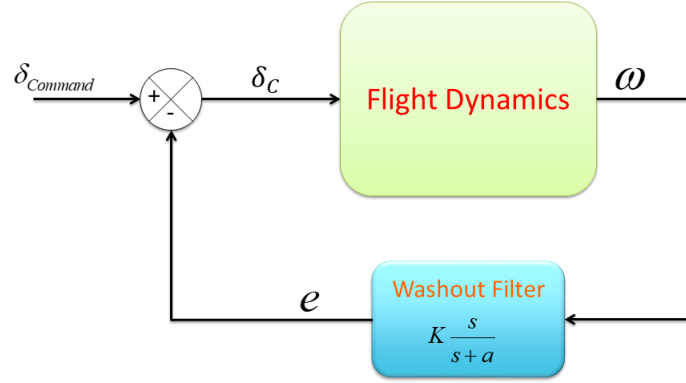


Figure 7.7. Washout filter added in the feedback path from the pitch rate to the elevon inputs.

The washout filter is essentially a high pass filter. Therefore, it allows the high frequency components of the pitch rate to pass through the feedback path, which then combine with the control surface command ( $\delta_{command}$ ) to generate  $\delta_C$  (the original control variable) that compensates the pitch oscillations. The structure of the washout filter is:

$$C(s) = K \frac{s}{s + a}, \text{ where } a > 0 \quad (7.14)$$

This introduces a new state,  $e$ , with the differential equation:

$$\dot{e} = \dot{\omega} - ae \quad (7.15)$$

This equation is added to the equations of motion defined in Section 7.2. Figure 7.8 illustrates the response of angle-of-attack after adding the washout filter.

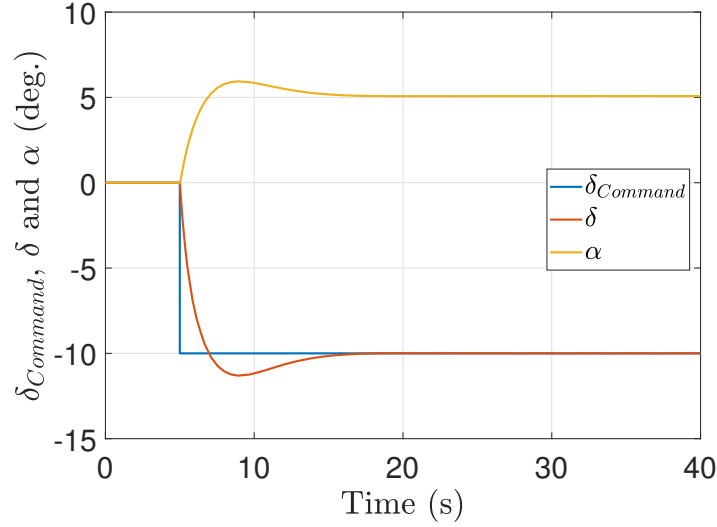


Figure 7.8. Damped oscillations in the presence of the washout filter, resulting in reduced numerical stiffness.

The washout filter damps the pitch rate oscillations, thereby reducing the numerical stiffness. This augmented system with pitch rate feedback is used as the system dynamics while performing trajectory optimization. While employing continuation, the gain of the filter may be iteratively brought to zero, essentially leading to the solution of the original problem without the washout filter. The design of the washout filter involved a certain amount of trial and error. A more systematic approach may be employed using root locus [131]. However, since this method is applied to a linearized system, considerable trial and error will still be involved because the original system is highly nonlinear. A reliable systematic method to design the washout filter remains to be investigated. The next section presents the results of trajectory optimization using the 3-DOF rigid body dynamics with the washout filter.

## 7.4 Results

This section presents optimal trajectories that were designed using the 3-DOF rigid body model. Two examples are presented: 1) a single-stage launch to circular orbit, and 2) glide trajectory of a slender hypersonic vehicle.

### 7.4.1 Single-Stage Launch to Circular Orbit

In this section, the launch trajectory of a single stage to orbit (SSTO) vehicle is optimized. It is desired to reach a circular equatorial orbit at an altitude of 150 km in minimum time. For the duration of the trajectory, the engines operate at a maximum thrust of 8.304 MN, and the vehicle is constrained to fly east along the equator of the Earth. The vehicle is maneuvered by gimbaling the nozzle between 3 deg and  $-3$  deg, which in turn modulates the pitch angle. At the launch pad, the vehicle is erect ( $\Theta = 90$  deg). When the vehicle achieves the target orbit, the pitch rate is required to be nullified. However, the pitch angle may assume any value. Accordingly, desired initial and final conditions on the states are summarized in Table 7.1.

Table 7.1. Initial and final conditions for the single-stage launch trajectory.

State	Initial Condition	Final Condition
Altitude ( $h$ )	0 km	150 km
Longitude ( $\theta$ )	0 deg	Free
Atmospheric-relative velocity ( $v$ )	0.7338 m/s	7.338 km/s
Atmospheric-relative flight-path-angle ( $\gamma$ )	90 deg	0 deg
Pitch ( $\Theta$ )	90 deg	free
Pitch rate ( $\omega$ )	0 deg/s	0 deg/s

In Table 7.1, the desired final value for  $v$  is calculated by subtracting the velocity of the atmosphere at 150 km altitude from the corresponding circular orbital speed, as shown in Eq. (7.16).

$$v(t_f) = \sqrt{\left(\frac{\mu}{R + h(t_f)} - (R + h(t_f))\right) \Omega} \quad (7.16)$$

where  $h(t_f) = 150 \text{ km}$

The vehicle configuration is illustrated in Figure 7.9. The aerodynamic coefficients are calculated using the methodology explained in Chapter 4. The vehicle is propelled by a liquid motor that burns RP-1 [132] and liquid oxygen (LOx [133], the oxidizer), with an LOx-RP-1 ratio of 2.56, corresponding to an engine like the RD-180 [134]. The engine is also assumed to possess an  $I_{sp}$  of 480 s. It should be noted that SSTO is not presently possible because the launch mass and dimensions of the vehicle become very large, as evidenced by the Tsiolkowski rocket equation [121]. As a result, an unrealistic value for  $I_{sp}$  was used in this example to make the engine more efficient while also producing a large amount of thrust, thereby requiring less propellant at launch and consequently limiting the dimensions and mass of the vehicle to reasonable levels. Nevertheless, this example serves to demonstrate the incorporation of rigid body dynamics into propulsive vehicles. A multi-stage launch example will be shown later in Chapter 9. For the SSTO vehicle, the total propellant flow rate corresponding to maximum thrust is 1,763.1 kg/s. The density of RP-1 is 900 ks/m<sup>3</sup> and that of LOx is 1,141 ks/m<sup>3</sup>. The propellants are stored in cylindrical tanks of radius 1.7 m. The launch vehicle is mated with a payload, which is modeled as a solid cylinder of mass 100 kg, radius 0.5 m and height 2 m. The mass and inertia of the inert structure are 17.081 tons and 26,589 kg-m<sup>2</sup>, respectively. The center of mass of the inert structure is located 28.7 m from the base of the fuselage along the roll axis. Since the vehicle is always accelerating, it is assumed that the propellants settle back in their tanks and assume the shape of a cylinder. At any given instant, the center of mass of the fuel and the oxidizer is the geometric center of the cylinder that they form. The height of these cylinders corresponding to a time  $t$  is given by:

$$h_i = \frac{m_{0,i} - \dot{m}_i t}{\pi r_i^2 \rho_i} \quad (7.17)$$



where  $h_i$ ,  $m_{0,i}$ ,  $\dot{m}_i$ , and  $\rho_i$  are the height, initial mass, mass flow rate, and density of the propellant (calculated separately for RP-1 and LOx). The center of mass is located at  $h_i/2$  from the base of the cylinder along its axis. Their moments of inertia about their pitch axes and their respective centers of mass are given by:

$$I_{i,CM} = \frac{m_i}{12} (3r_i^2 + h_i^2) \quad (7.18)$$

Since the payload is modeled as a uniform solid cylinder, its center of mass and inertia can be similarly calculated. With the knowledge of the center of mass of each component of the vehicle (inert, RP-1, LOx and payload), the center of mass of the vehicle can be readily calculated as:

$$\mathbf{r}_{CM} = \frac{m_{\text{INERT}}\mathbf{r}_{\text{INERT},CM} + m_{\text{RP-1}}\mathbf{r}_{\text{RP-1},CM} + m_{\text{LOx}}\mathbf{r}_{\text{LOx},CM} + m_{\text{PAY}}\mathbf{r}_{\text{PAY},CM}}{m_{\text{INERT}} + m_{\text{RP-1}} + m_{\text{LOx}} + m_{\text{PAY}}} \quad (7.19)$$

Since the vehicle is axisymmetric and only pitch motion is considered, the pitch moment of inertia of the vehicle about the instantaneous center of mass is readily calculated using the parallel axis theorem as:

$$\begin{aligned} I_{y,CM} = & I_{\text{INERT},CM} + m_{\text{INERT}}|\mathbf{r}_{\text{INERT},CM} - \mathbf{r}_{CM}|^2 \\ & + I_{\text{RP-1},CM} + m_{\text{RP-1}}|\mathbf{r}_{\text{RP-1},CM} - \mathbf{r}_{CM}|^2 \\ & + I_{\text{LOx},CM} + m_{\text{LOx}}|\mathbf{r}_{\text{LOx},CM} - \mathbf{r}_{CM}|^2 \\ & + I_{\text{PAY},CM} + m_{\text{PAY}}|\mathbf{r}_{\text{PAY},CM} - \mathbf{r}_{CM}|^2 \end{aligned} \quad (7.20)$$

These derived parameters are substituted into the 3-DOF rigid body dynamics explained in Section 7.2, which is in turn used to perform the trajectory optimization in the indirect framework. The velocity state is scaled by the desired final velocity (7.338 km/s), and the altitude is scaled by the desired final altitude (150 km).

The optimization is performed using continuation, which is implemented in five steps. The initial guess for the first iteration is obtained by propagating the differential equations in the TPBVP necessary conditions using the Dormand-Prince method [118] for 0.1 seconds, with the the following initial conditions:

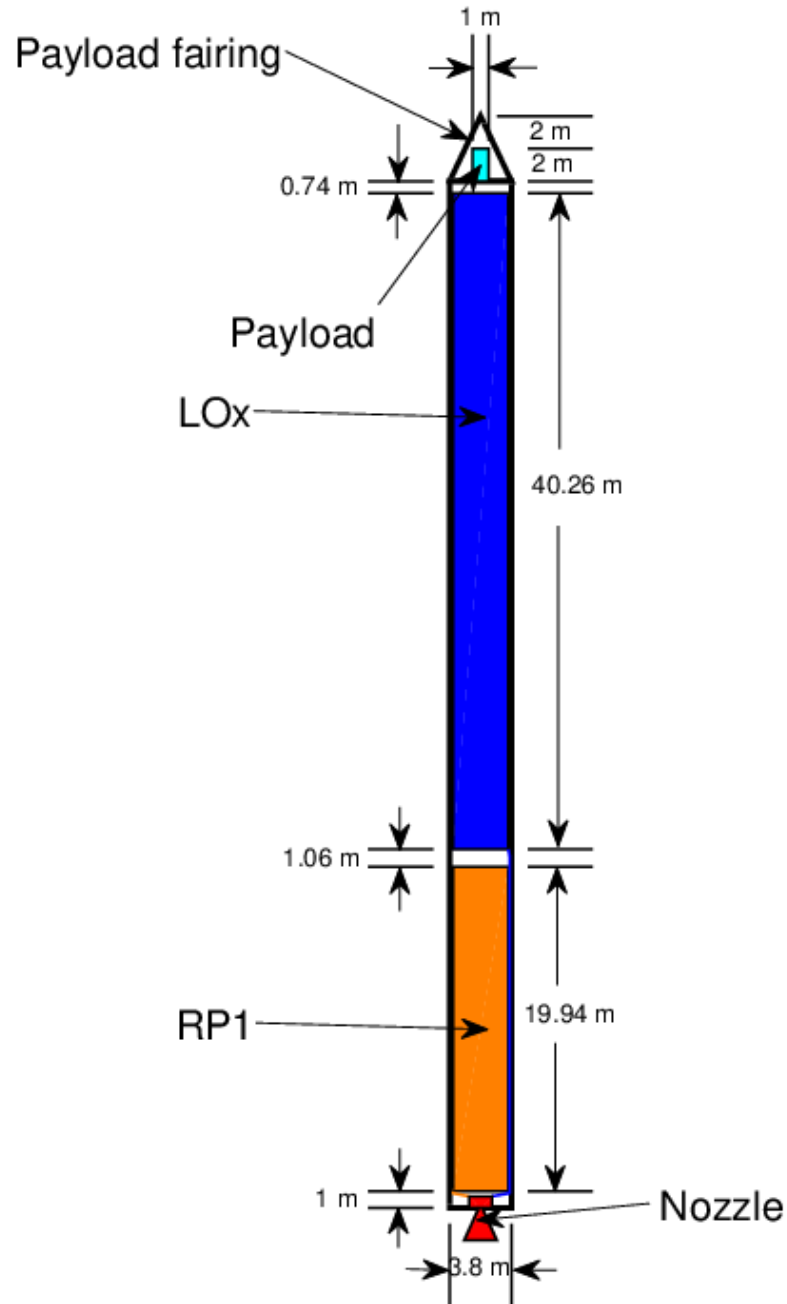


Figure 7.9. Launch vehicle geometry.

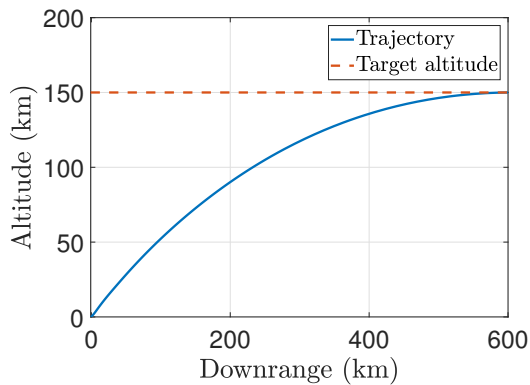
$$\begin{aligned}
 \mathbf{X}^T &= [V \quad \gamma \quad h \quad \theta \quad \Theta \quad \omega] = \begin{bmatrix} 0.0001 & \frac{\pi}{2} & 0 & 0 & \frac{\pi}{2} & 0 \end{bmatrix} \begin{pmatrix} \\ \\ \\ \\ \\ \end{pmatrix} \\
 \boldsymbol{\lambda}^T &= [\lambda_V \quad \lambda_\gamma \quad \lambda_h \quad \lambda_\theta \quad \lambda_\Theta \quad \lambda_\omega] = \begin{bmatrix} -1 & 0 & 1 & -1 & 1 & -1 \end{bmatrix} \begin{pmatrix} \\ \\ \\ \\ \\ \end{pmatrix}
 \end{aligned} \tag{7.21}$$

Initially, the atmospheric density is assumed to be exponential, bearing a surface density of  $1.225 \text{ kg/m}^3$  and a scale height of 1 km. Although this value for the scale height is unrealistic, it is conducive for the continuation process as the atmospheric effects quickly reduce along the ascent trajectory. The other freestream conditions are calculated from the cubic-spline fitted U.S. Standard Atmosphere (1976) model. Also, the value of the weighting factor  $\epsilon$  (because control is bounded) in the cost functional is initially set to 0.1.

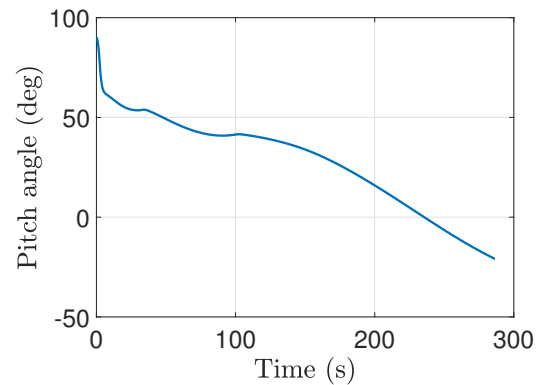
In the first continuation step, the final velocity and flight path angle are set free. For the first iteration in this step, the final boundary condition on altitude is set to the corresponding final value in the initial guess. It is then varied in 200 equal increments to the desired value of 150 km. In the second continuation step, the final boundary condition on  $\gamma$  is fixed. In the first iteration, it is set equal to the corresponding free final value of the solution of the last iteration in step 1. Furthermore, this solution is used as the initial guess for the first iteration in step 2. The final boundary condition on  $\gamma$  is then varied in 200 equal increments to the desired value of 0 deg. In the third continuation step, the final condition on  $v$  is also fixed. For the first iteration, it is set equal to the corresponding free value in the solution of the final iteration of step 2. As before, this solution is used as the initial guess for the first iteration in step 3. The final boundary condition on  $v$  is then changed in 200 equal increments to the desired final value of 7.338 km/s. In the fourth continuation step, the scale height is varied in 200 equal increments to the desired value of 8.5 km. In the final continuation step,  $\epsilon$  is varied in 200 equal decrements to 0.000001. After the continuation process, the exponential atmospheric density is replaced by the original cubic-spline fitted U.S. Standard Atmosphere (1976) density. The final problem in the continuation process is solved again with this atmospheric model, using the corresponding solution that was previously calculated as the initial guess. The resulting solution is the desired solution of the original problem.

Figure 7.10(a) illustrates the ascent trajectory. Since the desired orbit is prograde, the vehicle is required to pitch down towards east, as shown in Figure 7.10(b). Since

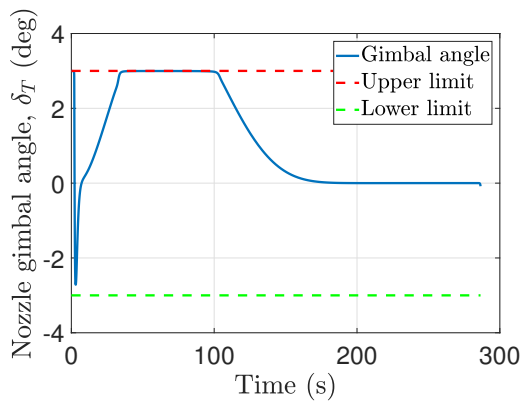
the vehicle is initially erect, the gimbal angle is required to be positive in order to generate the required moment to initiate the pitch motion in the desired direction. This is illustrated by the positive initial gimbal angle in Figure 7.10(c). This value quickly spikes to a negative value to limit the pitch rate. While traversing the lower atmosphere, the vehicle maintains a positive angle-of-attack to leverage the body lift along with thrust to climb to orbit (Figure 7.10(d)). Since the vehicle is aerodynamically unstable (as the center of mass is located generally towards the aft section of the vehicle), appropriate thrust vectoring that prevents the angle-of-attack from



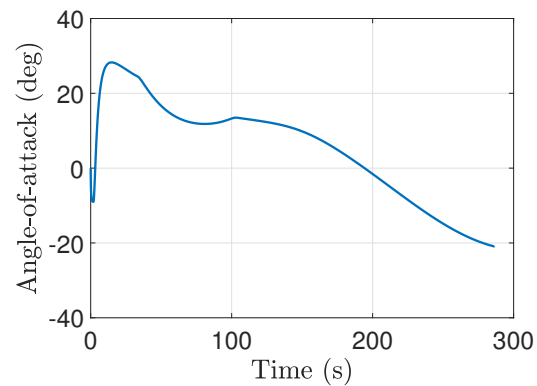
(a) Altitude vs. downrange.



(b) Pitch angle vs. time.



(c) Gimbal angle vs. time.



(d) Angle-of-attack vs. time.

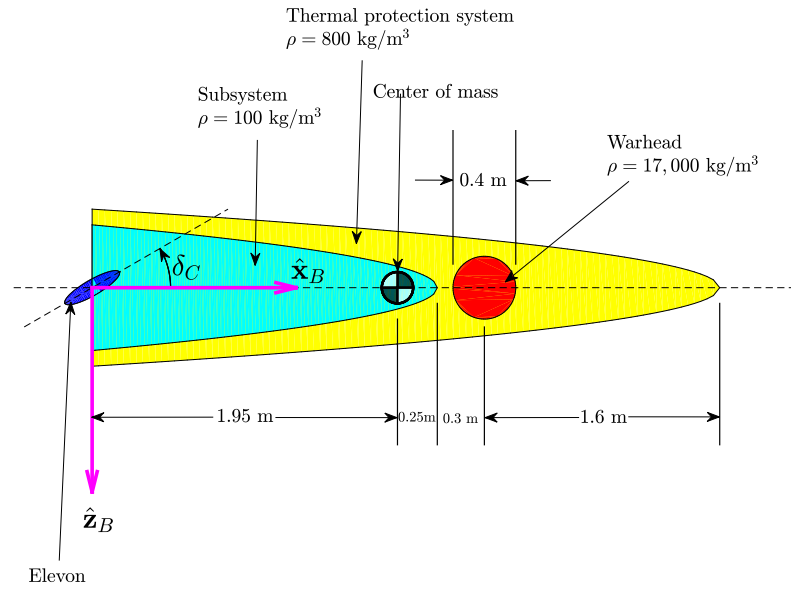
Figure 7.10. Minimum time single-stage ascent to circular equatorial orbit. The desired initial and final states are defined in Table 7.1, and the launch vehicle geometry is illustrated in Figure 7.9.

rising is observed. In fact, it can be seen that the gimbal angle saturates for about 1 minute. This means that for this configuration of the vehicle, the nozzle should be designed to facilitate more gimbaling. Alternatively, the geometry of the launch vehicle can be changed. The fuselage radius can be increased and stabilizing fins can be added to make the vehicle more aerodynamically stable, thereby containing the aggressiveness of thrust vectoring. This is the sort of design study that the rigid body analysis facilitates. As the vehicle climbs to higher altitudes, the dynamic pressure substantially reduces, thereby requiring less aggressive thrust vectoring. In fact, the gimbal angle can be seen to approach 0 deg.

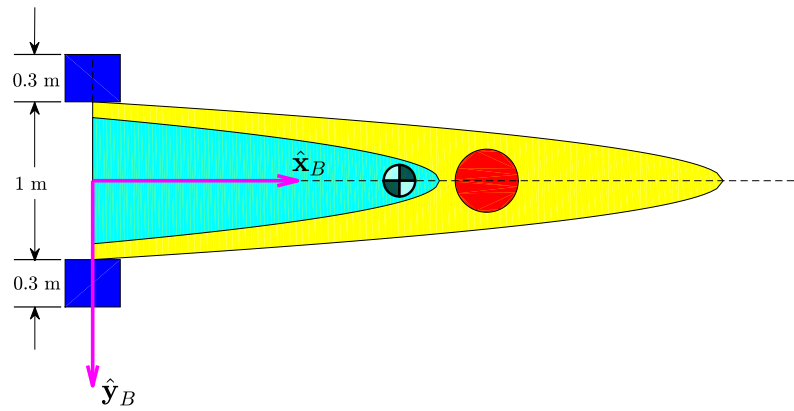
The next section describes an example wherein the glide trajectory of a slender hypersonic vehicle is optimized. Since the equations of motion are numerically stiff, a washout filter is employed.

#### 7.4.2 Glide Trajectory of a Slender Hypersonic Vehicle

In this example, the glide trajectory of a hypersonic weapon system is optimized to maximize the impact velocity at the target. The vehicle configuration is illustrated in Figure 7.11. The fuselage is an elliptic paraboloid of length 4 m and base radius 0.5 m. The aft section of the vehicle contains the subsystems (such as the flight computer). These systems are assumed to be contained in another elliptic paraboloid section bearing a uniform density of  $100 \text{ kg/m}^3$ , embedded in the fuselage. This section is 2.2 m long and possesses a base radius of 0.4 m. A warhead of radius 0.2 m and density  $17,000 \text{ kg/m}^3$  is positioned 2.5 m from the base of the fuselage along its roll axis. The rest of the fuselage is composed of TPS material of density  $800 \text{ kg/m}^3$ . The vehicle's pitch is varied by deflecting a pair of massless elevons located at the aft portion of the vehicle, as illustrated. Each elevon is 0.3 m long (Figure 7.11(b)) and possesses an elliptical cross section with a semi major axis of 0.2 m and a semi minor axis of 0.05 m (Figure 7.12). The elevons are actuated about an axis that passes through the center of the elliptical cross section.



(a) Side view.



(b) Top view.

Figure 7.11. Vehicle configuration.

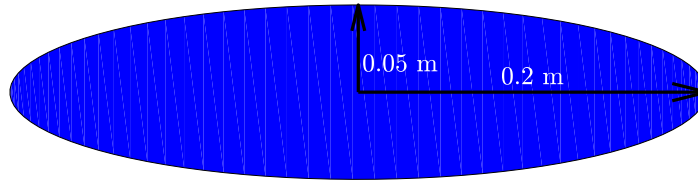


Figure 7.12. Elevon cross section.

Accordingly, the mass of the vehicle was calculated to be 1,413 kg. The center of mass was determined to be located at a distance of 1.95 m along the roll axis from the base of the fuselage. The pitch moment of inertia about the center of mass was calculated to be 1,133 kg-m<sup>2</sup>.

The vehicle is assumed to have been boosted to an altitude of 40 km and a velocity of 3 km/s. During the separation of the booster, the vehicle is assumed to be flying level ( $\gamma = 0$  deg). The pitch angle is 0 deg and the pitch rate is 0 deg/s. Moreover, the coordinates at separation are 0 deg latitude and longitude. The vehicle is constrained to fly along the equator. It is required to strike a target that is located at 4.0424 deg longitude on the equator. To address the numerical stiffness, a feedback from  $\omega$  to  $\delta_C$  is added. For this vehicle, a DC gain of 1 was sufficient in the feedback path. As a result, no additional states are introduced. Accordingly, the desired initial and final conditions are tabulated in Table 7.2.

The altitude and velocity states are scaled by their respective initial values. The continuation process involves just one step with 500 iterations. The initial guess for the first iteration is obtained by propagating the differential equations in the TPBVP

Table 7.2. Initial and final conditions for the glide trajectory.

State	Initial Condition	Final Condition
Altitude ( $h$ )	40 km	0 km
Longitude ( $\theta$ )	0 deg	4.0424 deg
Atmospheric-relative velocity ( $v$ )	3 km/s	free
Atmospheric-relative flight path angle ( $\gamma$ )	0 deg	free
Pitch ( $\Theta$ )	0 deg	free
Pitch rate ( $\omega$ )	0 deg/s	free

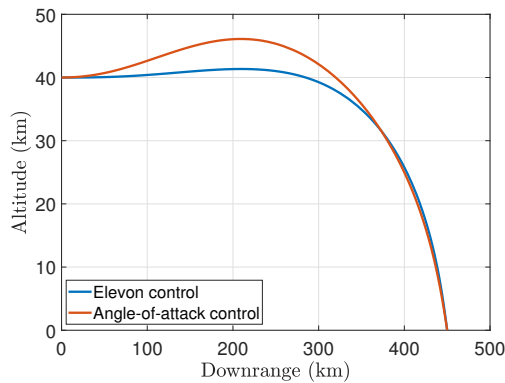
necessary conditions using the Dormand-Prince method for 0.1 seconds, with the the following initial conditions:

$$\begin{aligned} \mathbf{X}^T &= \begin{bmatrix} \gamma & h & \theta & \Theta & \omega \end{bmatrix} = \begin{bmatrix} 1 & 0 & 1 & 0 & 0 & 0 \end{bmatrix} \begin{pmatrix} \\ \\ \\ \\ \end{pmatrix} \\ \boldsymbol{\lambda}^T &= \begin{bmatrix} \lambda_V & \lambda_\gamma & \lambda_h & \lambda_\theta & \lambda_\Theta & \lambda_\omega \end{bmatrix} = \begin{bmatrix} 0.1 & 0 & 0.1 & -0.1 & 0.1 & -0.1 \end{bmatrix} \begin{pmatrix} \\ \\ \\ \\ \end{pmatrix} \end{aligned} \quad (7.22)$$

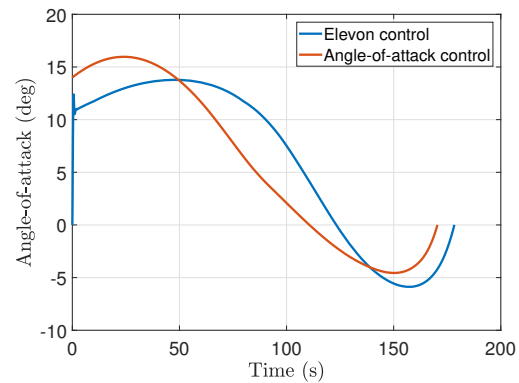
For the first iteration, the final boundary conditions on altitude and longitude are set to the corresponding final values in the initial guess. They are then varied in 500 equal increments to the corresponding desired values of 0 km and 4.0424 deg, respectively. The solution of the final iteration is the desired solution. For comparison, the same problem is solved again with the exception that the elevons are absent and the angle-of-attack is directly controlled. This is representative of the present state-of-the-art approach to conceptual trajectory optimization. Figure 7.13(a) compares the physical trajectories. The difference in the two solutions is immediately apparent. Since the objective is to maximize final velocity, it is beneficial to fly at a higher altitude to minimize drag until getting close to the target. Towards the end, a dive maneuver may be performed to quickly traverse the lower denser region of the atmosphere, thereby reducing drag loss. This is precisely what the vehicle does in both cases. However, the vehicle with elevon control does not climb as high as the one with  $\alpha$  control because the elevons are unable to generate the necessary pitch moment to



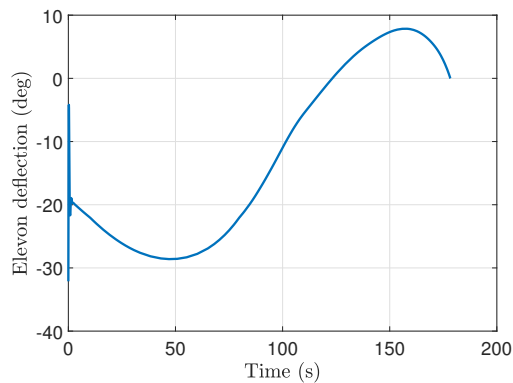
achieve the required  $\alpha$  (Figure 7.13(b)). The lower  $\alpha$  results in a lower lift force and climb performance. In fact, the initial deflection of the elevons (Figure 7.13(c)) results in a moment that is already close to the maximum that they are capable of generating. Any higher deflection will only result in a drop in moment and an increase in drag. Towards the end of the trajectory, the elevons are deflected in the opposite direction to initiate the dive towards the target. However, any deflection in



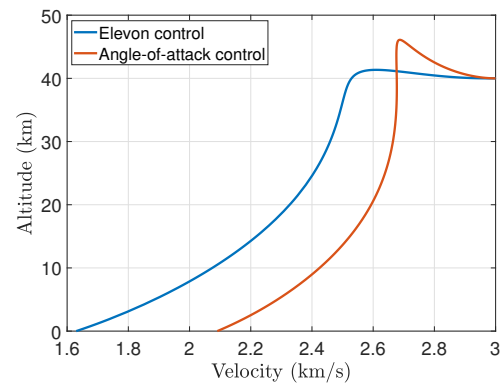
(a) Altitude vs. downrange.



(b) Angle-of-attack history.



(c) Elevon deflection history.



(d) Altitude vs. velocity.

Figure 7.13. Comparison of maximum final velocity trajectories of a hypothetical hypersonic glide vehicle calculated using rigid body and point-mass flight dynamics. The vehicle geometry and configuration at booster separation are illustrated in Figures 7.11 and 7.12. The vehicle states at booster separation and the desired final states are defined in Table 7.2.

the elevons results in a drag penalty. Consequently, the final velocity of the vehicle with elevon control is 1.630 km/s, 461 m/s (or 22 percent) lower than the vehicle with  $\alpha$  control (Figure 7.13(d)).

This example demonstrates how the optimal trajectories can be different when rigid body motion is accounted for. Trade studies can be performed by varying the geometry and configuration of the elevons and studying the corresponding family of optimal trajectories. For instance, increasing elevon span does not necessarily result in a higher final velocity (Figure 7.14, wherein the span is varied from 1.6 m to 2.1 m), but increasing the chord length does (Figure 7.14, wherein the chord length is varied from 0.4 m to 0.8 m). In either case, the reference trajectory is the solution corresponding to the vehicle with  $\alpha$  control. It can be seen that varying the configuration of the control surface does not alter the physical trajectory (altitude vs. downrange) much, although the final velocity changes significantly.

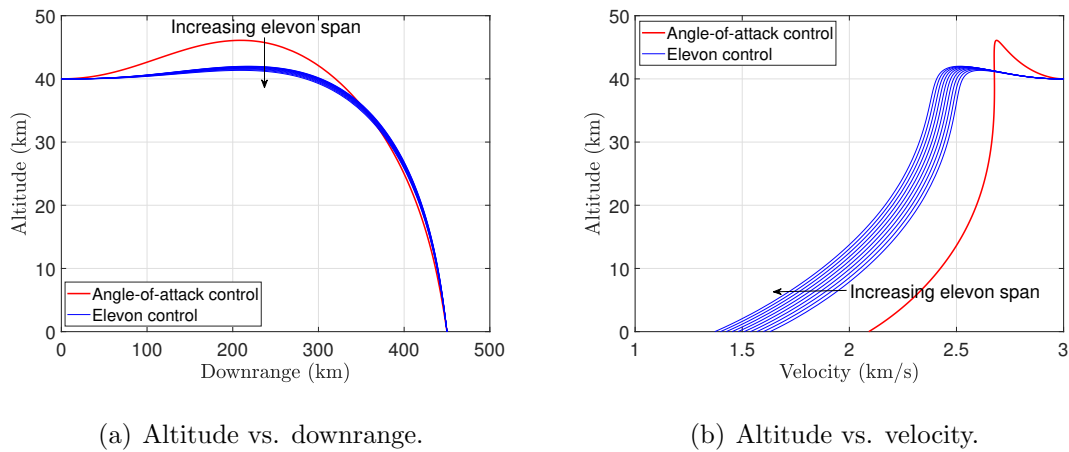


Figure 7.14. Increasing elevon span from 1.6 m to 2.1 m has a negative impact on mission performance.

Alternatively, the elevons can be made more effective by reducing the aerodynamic stability of the vehicle by moving its center of mass aft. This may be accomplished by altering its mass distribution by rearranging the components. For instance, the warhead may be moved closer to the base of the fuselage. With a reduced aerodynamic

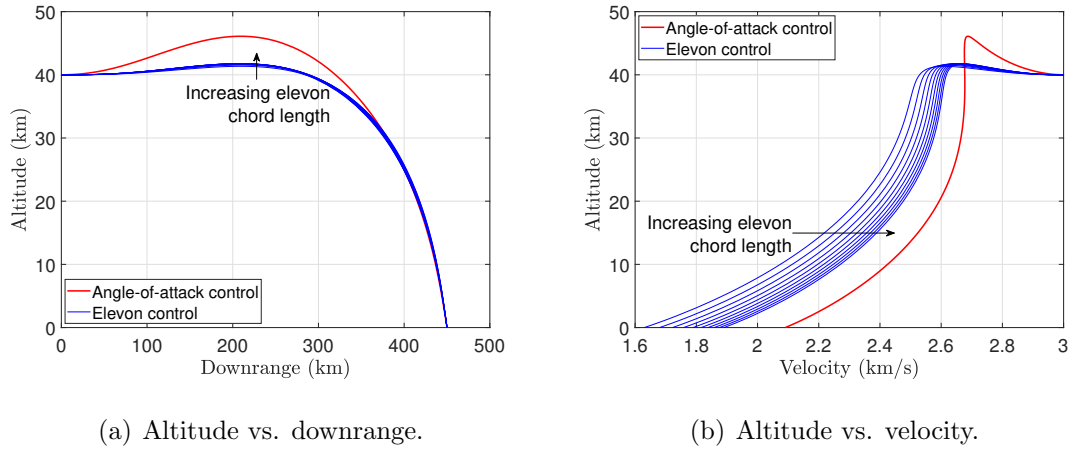


Figure 7.15. Increasing elevon chord length from 0.4 m to 0.8 m improves mission performance.

stability, a higher  $\alpha$  can be achieved from a given elevon deflection. Similar trade studies can be performed by studying the family of trajectories generated by varying the mass distribution of the vehicle. For instance the vehicle climbs higher and the final velocity increases (Figure 7.16) as the warhead is moved aft from 2.5 m to 2.37 m, measured from the base of the fuselage and along the roll axis. However, the

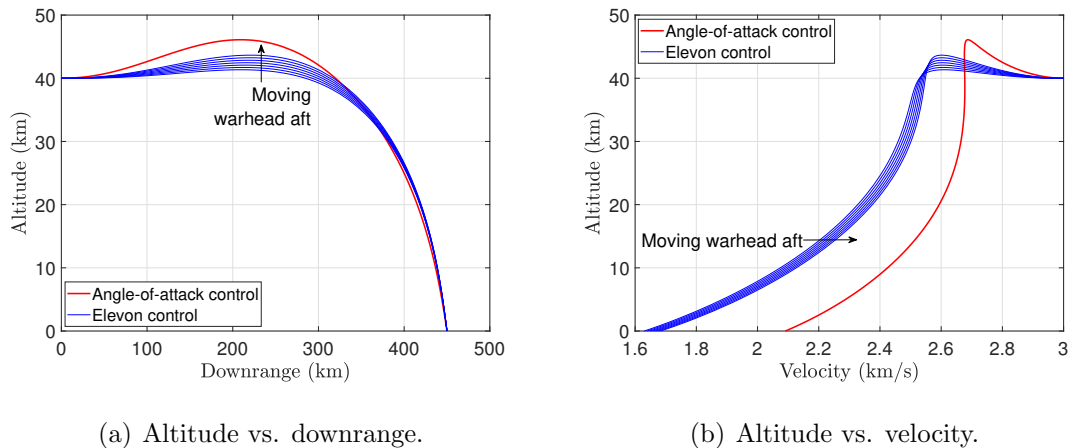


Figure 7.16. Moving the warhead back from 2.5 m to 2.37 m (measured from the base of the fuselage and along the roll axis) improves mission performance.

gain in the final velocity is less than that achieved by the modification of the elevon configuration.

These trade studies suggest that the impact velocity can be controlled by adjusting the elevon configuration, while the trajectory altitude can be controlled by adjusting the position of the warhead. The trajectory altitude is of significance from a heating and ablation standpoint as a higher altitude results in a milder aerothermal environment.

## 7.5 Summary

This chapter described the introduction of rigid body analysis into the trajectory optimization framework. The state-of-the-art trajectory design process employs a point-mass flight dynamics model that does not account for the maneuverability of the vehicle because the mass distribution and the configuration of the control effectors are neglected. This limitation is addressed by modeling the vehicle as a rigid body.

However, it was seen that for highly aerodynamically stable vehicles, the rigid body equations of motion were numerically stiff. The stiffness was reduced by introducing a washout filter along the feedback path from pitch rate to the elevon deflection control.

Although only the pitch dynamics were introduced, substantial insights could be gained just by analyzing the planar motion. For instance, it was seen in the single-stage launch example how the nozzle gimbal angle can saturate if the mass distribution is not ideal. Saturation of control in the reference is dangerous because if the vehicle does fly this trajectory in the real world, it will be unable to correct for perturbations in the states while flying the saturation portion of the trajectory. In essence, the closed loop control breaks down when the control saturates. Since the vehicle is already aerodynamically unstable, the angle-of-attack may increase to dangerous levels, which may lead to a structural failure.

Insights were also gained from designing hypersonic glide trajectories for a hypothetical boost-glide system using the rigid body model, wherein the the maximum

achievable final velocity was substantially reduced because of the increased drag resulting from the deflection of the elevons. The rigid body framework was also demonstrated to be useful for designing the configuration of the vehicle. For this purpose, trade studies were presented wherein the mission performance was observed to be enhanced by increasing the elevon chord length, decreasing the elevon span, and moving the warhead aft.

When this contribution is integrated with the ablation framework, further insights can be gained at a conceptual level. For instance, the trim angle-of-attack will not remain constant for an ablating vehicle for a given elevon deflection because the mass distribution continuously evolves. In the traditional framework, this may be modeled by imposing variable bounds on  $\alpha$ , which can be very cumbersome. However, the rigid body framework implicitly accounts for the bounds in  $\alpha$ .

Thus far, every analysis of glide vehicles assumed that they have already been boosted to hypersonic speeds. However, the true optimal hypersonic glide also depends on the boost trajectory. As a result, both phases should be optimized simultaneously, leading to a multi-phase trajectory optimization problem. This is the focus of the third contribution of the dissertation discussed in Chapter 8, wherein the design of optimal multi-phase trajectories is substantially simplified.

## 8. SIMPLIFICATION OF TRAJECTORY OPTIMIZATION OF MULTI-PHASE SYSTEMS

### 8.1 Introduction

This chapter describes the third contribution of the doctoral dissertation: simplification of the design of optimal trajectories for multi-phase aerospace systems using indirect methods. In such trajectories, a given phase is active when a set of conditions on the states and time are satisfied. The optimal control problem of such systems involves piecewise dynamics and cost functional. As seen in Section 5.4, the necessary conditions of optimality result in an MPBVP in a system of differential-algebraic equations, which need to be solved numerically. As in the TPBVP, the numerical solver needs to be supplied with an initial guess that is close to the actual solution, which is a difficult task. The issue of supplying a good initial guess for the TPBVP was addressed by the continuation method, wherein it was required to supply an initial guess only for the problem corresponding to the first iteration. Since this iteration involved a very short trajectory, convergence was easy even with a poor initial guess. However, this approach is not straight forward for an MPBVP primarily because it is required to guess the solution corresponding to all phases of flight, even for the initial iteration. It is difficult to define a trivial initial problem that encompasses all phases of flight. Moreover, Eq. (5.27) shows that depending on the switching conditions, the co-states and Hamiltonian may exhibit discontinuities at the phase boundaries. An estimate of these jumps also needs to be incorporated into the initial guess to guarantee convergence. However, given that the co-states do not have a physical meaning in general, this is a difficult task. As a result, it would be beneficial if the MPBVP can be reduced to a TPBVP, for which continuation can be employed more easily. This is accomplished by converting the piecewise dynamics and cost functional to  $c^1$

continuous quantities by employing saturation functions. Consequently, the interior boundary conditions that occur at the transitions of flight phases automatically get enforced as a consequence of propagating the new dynamical system. In essence, the numerical algorithm is only required to enforce the end-point boundary conditions, thereby reducing the original MPBVP to a TPBVP, which in turn is solved using continuation. This methodology, named the “Relaxed Autonomously Switched Hybrid System” (RASHS) approach, is explained in the section. It was also presented in [135, 136].

## 8.2 The Relaxed Autonomously Switched Hybrid System (RASHS) Approach

The foundational underpinning of the RASHS approach is the transformation of the system of piecewise continuous flight dynamic equations and the cost functional into a single continuous system. Suppose an aerospace system has  $m$  flight segments and is subject to the flight dynamic equations  $\mathbf{f}_k$  for a given segment  $k$ . Let the cost functional  $J$  associated with the segment  $k$  that is required to be minimized be  $J_k$ . The segment  $k$  is active when all  $n_k$  conditions  $g_{i,k} < 0$  associated with it are satisfied. That is:

$$\begin{aligned} \dot{\mathbf{X}} &= \mathbf{f}_k \\ J &= J_k \end{aligned} \quad \text{when } g_{i,k} < 0, \text{ where } i = 1, 2, \dots, n_k \quad (8.1)$$

where  $\mathbf{X}$  is the state vector. The piecewise dynamical equation in Eq. (8.1) can be expressed by a single equation that takes the following form:

$$\dot{\mathbf{X}} = \sum_{k=1}^m \xi_k \mathbf{f}_k \quad (8.2)$$

where,  $\xi_k$  is the switching function given by:

$$\xi_k = \begin{cases} 1 & \text{when } g_{i,k} < 0, \forall i \in \mathbb{N}, i \leq n_k \\ 0 & \text{otherwise} \end{cases} \quad (8.3)$$

Suppose  $[1 - u(g_{i,k})]$  is a unit step function that is equal to 1 when  $g_{i,k} < 0$  and 0 otherwise.  $\xi_k$  can then be represented using unit step functions as follows:

$$\xi_k = \prod_{i=1}^{n_k} [1 - u(g_{i,k})] \quad (8.4)$$

Eq. (8.4) tells that  $\xi_k = 1$  only when all the conditions  $g_{i,k}$  corresponding to segment  $k$  are satisfied. Consequently, Eq. (8.2) can be rewritten as:

$$\dot{\mathbf{X}} = \sum_{k=1}^m \prod_{i=1}^{n_k} [1 - u(g_{i,k})] \mathbf{f}_k \quad (8.5)$$

The unit step function  $[1 - u(g_{i,k})]$  can be approximated using a sigmoid function as:

$$[1 - u(g_{i,k})] \approx \frac{1}{1 + e^{s \cdot g_{i,k}}} \quad (8.6)$$

In Eq. (8.6),  $s$  is a measure of the slope at the transition point of the approximated “smooth” step. As  $s \rightarrow \infty$ , the sigmoid function approaches the original unit step function. Eq. (8.6) can be substituted into Eq. (8.5) so that:

$$\dot{\mathbf{X}} = \sum_{k=1}^m \prod_{i=1}^{n_k} \left[ \frac{1}{1 + e^{s \cdot g_{i,k}}} \right] \mathbf{f}_k \quad (8.7)$$

Eq. (8.7) is an approximation of the piecewise dynamics defined in Eq. (8.2). This equation results in a new dynamical system that is continuous and differentiable for all time. By following the same approach, the piecewise cost functional can be represented as a single continuous equation as:

$$J = \sum_{k=1}^m \prod_{i=1}^{n_k} \left[ \frac{1}{1 + e^{s \cdot g_{i,k}}} \right] J_k \quad (8.8)$$



Consequently, the trajectory optimization problem can be handled as a simpler TPBVP as opposed to an MPBVP.

It should be noted that Eqs. (8.7) and (8.8) do not force the flight phases to follow a certain sequence. However, in many aerospace applications, it is important that the flight phases follow a predetermined sequence. For instance, in a multi-stage launch mission, the first stage should be followed by the second stage, and so on. If the staging is time-switched, the discrete phase evolution is guaranteed to follow the predetermined sequence because time is monotonically increasing. However, it is not straight forward to guarantee the sequence for state-switched systems. For instance, consider an EDL mission with 3 phases: 1) hypersonic descent, 2) parachute descent, and 3) powered descent. Often, the parachute descent is triggered when the vehicle slows down to a certain velocity,  $v_P$ , and powered descent is triggered when the vehicle descends to a certain altitude,  $h_{PDI}$ . The values of  $v_P$  and  $h_{PDI}$  should be carefully chosen to guarantee that the flight phases follow the pre-determined sequence. Else, the vehicle might never slow down to  $v_P$  before descending to  $h_{PDI}$  and the parachute descent phase will never get triggered. Moreover, both hypersonic and powered descent phases will be active when the vehicle descends below  $h_{PDI}$ . The RASHS approach assumes that the designer has chosen the switching conditions carefully to ensure that the flight phases follow the desired sequence.

In order to explicitly enforce the phase sequence, additional protection conditions are required. For instance, to guarantee the occurrence of the parachute descent phase, an altitude protection might be added so that the hypersonic phase is active when the vehicle's velocity is above  $v_P$  and the altitude is above  $h_P$ , the parachute descent altitude. This can be viewed as an AND condition. The parachute descent phase would then be active when  $v < v_P$  or  $h < h_P$ , resulting in an OR condition. The formulation of the RASHS approach in this dissertation is compatible only with AND conditions, wherein a given phase of flight is active only when every associated condition is satisfied. Extension of the methodology for OR conditions, required

to explicitly enforce the phase sequence, is the next logical extension beyond this dissertation, and is explained in Appendix C.

The next section demonstrates the RASHS approach by applying it to the optimal control problem of multi-phase aerospace systems.

### 8.3 Results

This section demonstrates the RASHS approach by applying it to the following examples: 1) a multistage launch vehicle, 2) a multi-phase entry, descent, and landing (EDL) mission, and 3) a boost-glide weapon system. The RASHS framework can also be used to perform design trade studies of multi-phase systems, and are explained in this section.

#### 8.3.1 Atlas V 411 Launch to Circular Orbit

In this example, the launch trajectory of the Atlas-V launch vehicle in the 411 configuration [137] is optimized to minimize the time to reach a circular orbit. This in turn minimizes propellant usage. The optimization is performed using the RASHS approach, and the solution is compared with that obtained by solving the original MPBVP.

The launch trajectory consists of six phases:

1. **Booster Phase:** The solid rocket booster and the common core booster (first stage) engines operate at maximum thrust.
2. **Booster Cut-Off:** The solid rocket booster cuts off, but remains attached. The common core booster continues to fire at maximum thrust.
3. **Post Booster Jettison:** The solid rocket booster is jettisoned, and the common core booster continues to operate at maximum thrust.

4. **Throttle Down:** The common core booster throttles down to limit thrust acceleration to 5 g's.
5. **Ullage:** The common core booster cuts off and is jettisoned. The ullage motors fire for 10 seconds. The thrust is approximated to 0 N.
6. **Centaur Upper Stage:** The centaur upper stage (second stage) engine fires up and operates at maximum thrust until orbit is reached.

It should be noted that the thrust profile is known a priori. As a result, it is not treated as a control variable. The mission involves a launch from the equator at 0 deg longitude to an equatorial low-Earth circular orbit of altitude 150 km in minimum time. The launch vehicle is constrained to fly along the equator and is assumed to be a point-mass. As a result,  $\psi$  and  $\phi$  assume a constant value of 90 deg and 0 deg respectively, thereby collapsing the problem to a 2-DOF problem. The only control variable is  $\alpha$ , with  $\sigma$  bearing a constant value of 0 deg. The properties of the launch vehicle corresponding to each phase of flight are given in Table 8.1.

Table 8.1. Launch vehicle characteristics.

Phase	Time	Total Initial Mass	Propellant Flow Rate	Thrust
Booster phase	0 – 90 s	374,406 kg	1,682.6 kg/s	5.84 MN
Booster cut-off	90 – 94 s	222,969 kg	1,252.9 kg/s	4.152 MN
Post booster jettison	94 – 197.8 s	214,664 kg	1,252.9 kg/s	4.152 MN
Throttle down	197.8 – 235.6 s	84,649 kg	variable	variable
Ullage	235.6 – 245.6 s	24,676 kg	0 kg/s	0 N
Centaur upper stage	$\geq 245.6$ s	24,675 kg	22.48 kg/s	99,328 N

The launch vehicle is assumed to possess a constant drag coefficient ( $C_D$ ) of 0.5 and a reference area ( $S$ ) of 11.4 m<sup>2</sup>. The vehicle is assumed to produce no lift. The atmospheric surface density and scale height are assumed to be 1.225 kg/m<sup>3</sup> and 8.5 km, respectively. Suppose the equations of motion are labeled  $\mathbf{f}_1$  through  $\mathbf{f}_6$

corresponding to the 6 flight segments, and  $t_1$  through  $t_5$  are the times corresponding to each transition in phase of flight. The equations of motion can be represented using a single set of continuous differential equations using the RASHS approach as follows:

$$\dot{\mathbf{X}} = \left( \frac{1}{1 + e^{s(t-t_1)}} \right) \left( \mathbf{f}_1(\mathbf{X}, \mathbf{U}, t) + \left[ \sum_{i=1}^4 \left( \frac{1}{1 + e^{-s(t-t_i)}} \right) \left( \left( \frac{1}{1 + e^{s(t-t_{i+1}})} \right) \mathbf{f}_{i+1}(\mathbf{X}, \mathbf{U}, t) \right) \right] + \left( \left( \frac{1}{1 + e^{-s(t-t_5)}} \right) \mathbf{f}_6(\mathbf{X}, \mathbf{U}, t) \right) \right) \quad (8.9)$$

The initial and final conditions on the trajectory are given in Table 8.2. The initial value for  $v$  is set to 0.1 m/s instead of 0 m/s to avoid the singularity in the  $\dot{\gamma}$  equation. It should be noted that the initial  $\gamma$  is unconstrained. Since the equations of motion assume a point-mass model, constraining  $\gamma(t_0)$  to 90 deg would have negligible impact because the optimal  $\gamma$  would rapidly approach the corresponding unconstrained value immediately after launch as initial  $v$  is very small. The desired final value for  $v$  is calculated by subtracting the velocity of the atmosphere at 150 km altitude from the corresponding inertial circular speed, as shown in Eq. (8.10).

$$v(t_f) = \sqrt{\left( \frac{\mu}{R + h(t_f)} - (R + h(t_f)) \Omega^2 \right)} \quad (8.10)$$

where  $h(t_f) = 150$  km

Table 8.2. Initial and final conditions for the Atlas V launch trajectory.

State	Initial Condition	Final Condition
Atmospheric relative velocity ( $v$ )	0.1 m/s	7,338 m/s
Atmospheric relative flight path angle ( $\gamma$ )	free	0 deg
Altitude ( $h$ )	0 km	150 km
Longitude ( $\theta$ )	0 deg	free

The velocity and altitude states are scaled by their corresponding final values so that:

$$\begin{aligned} V &= \frac{v}{v(t_f)} \\ \hbar &= \frac{h}{h(t_f)} \end{aligned} \quad (8.11)$$

As a result, the new state vector is  $\mathbf{X} = [V \ \gamma \ \hbar \ \theta]^T$ . Additionally, the initial and final conditions on  $V$  become 0.1/7338 and 1, and those on  $\hbar$  become 0 and 1 respectively. Since the objective is to minimize the time to orbit, the cost functional is:

$$J = \int_a^b dt \quad (8.12)$$

The necessary conditions of optimality are derived using Eq. (5.5). The resultant TPBVP is solved using finite difference (implemented by Matlab's *bvp4c*) and continuation, as described in Section 5.3. The initial guess for the first iteration is obtained by propagating the differential equations in the TPBVP using the Dormand-Prince method [118] for 10 seconds, with the slope parameter in the sigmoid,  $s$ , equal to 4,000 and the following initial conditions:

$$\begin{bmatrix} \mathbf{X}^T & \boldsymbol{\lambda}^T \end{bmatrix}^T = \begin{bmatrix} V & \gamma & \hbar & \theta & \lambda_V & \lambda_\gamma & \lambda_\hbar & \lambda_\theta \end{bmatrix}^T = \begin{bmatrix} 0.1/7338 & \pi/4 & 0 & 0 & 1 & 0 & 0 & 0 \end{bmatrix}^T \quad (8.13)$$

The final boundary conditions on velocity and altitude are initially set to the corresponding final values from the propagation. The final condition on flight path angle is set to the desired value of 0 deg.

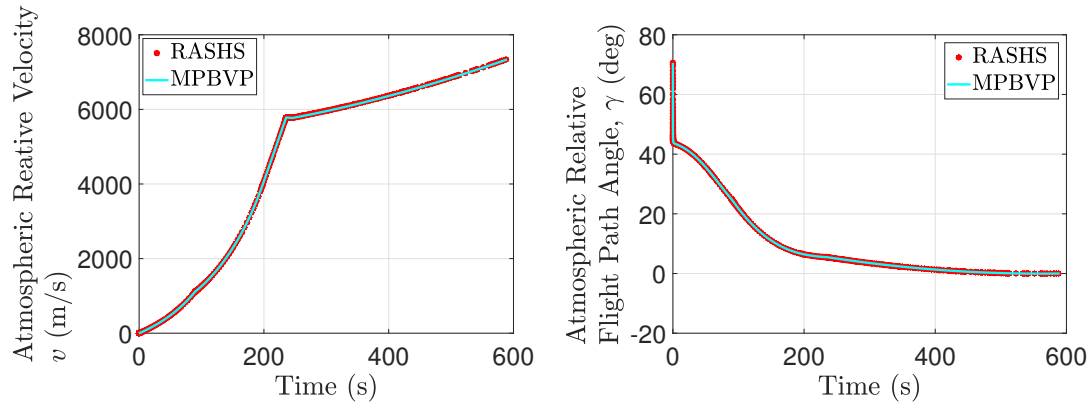
The continuation is implemented in three steps. In the first step, the final velocity and altitude are varied in 1,000 equal increments to the desired values of 7,338 m/s and 150 km respectively, with  $s = 4,000$ . In this step, the duration of the ullage phase is set to 0 s, resulting essentially in only five flight segments. In the second

step, the duration of the ullage phase is incremented to 10 s in 1,000 iterations. In the third and final step,  $s$  is varied in another 1,000 iterations to 60,000.

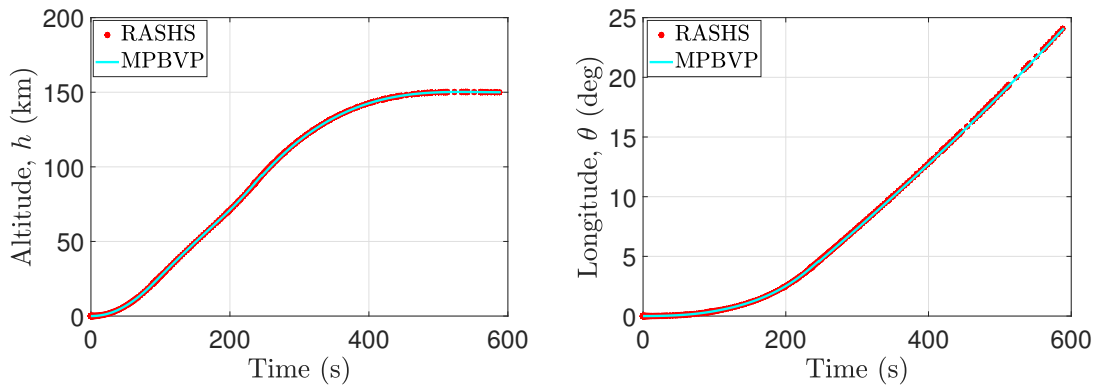
The solution of the final iteration in step 3 is the desired solution. The necessary conditions for the MPBVP are derived from Eq. (5.27). The solution obtained from the RASHS approach is used as the guess for this MPBVP and the solution is obtained using Matlab's *bvp4c*. This solution is compared with RASHS, and is observed to match very well. Since the solution of the necessary conditions of optimality is a local minimum that is influenced by the initial guess, the solution of the MPBVP might have been different if a different trajectory was supplied as the initial guess. Although the MPBVP solution was influenced by that of the RASHS approach, it is important to note that the goal of this comparison is to demonstrate that for a given local minimum, the two solutions match very well.

The time histories of the atmospheric relative velocity ( $v$ ) and the atmospheric relative flight path angle ( $\gamma$ ) calculated using the two methods are compared in Figures 8.1(a) and 8.1(b) respectively. The plots show that the final conditions on velocity ( $v(t_f) = 7,338$  m/s) and flight path angle ( $\gamma(t_f) = 0$  deg) are satisfied. A corner point can be observed in both plots at  $t = 90, 94$  s, 235.6 s and 245.6 s, corresponding to solid rocket booster cut-off, solid rocket booster jettison, common core booster cut off, and centaur upper stage engine activation, respectively. At these times, there is an abrupt change in mass and/or thrust. These points corresponding to the RASHS solution are actually smooth. Since the slopes of the sigmoid functions are large, they appear to be a corner and can be considered to be one for practical purposes. It can also be seen that the results from the two methods match very well. Therefore, it shows that the effects of smoothing in the RASHS solution do not result in significant deviations from the true solution as long as  $s$  in the sigmoid functions is large enough.

The time histories of altitude ( $h$ ) and longitude ( $\theta$ ) are shown in Figures 8.1(c) and 8.1(d) respectively. The final condition on altitude ( $h(t_f) = 150$  km) is observed to be satisfied. Since the  $\dot{h}$  and the  $\dot{\theta}$  don't have discontinuities, the corresponding



(a) Atmospheric relative velocity vs. time. (b) Atmospheric relative flight path angle vs. time.

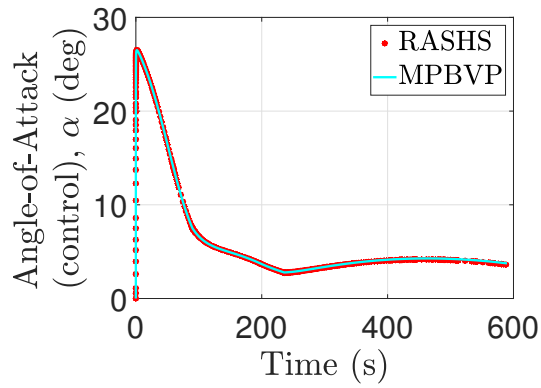


(c) Altitude vs. time. (d) Longitude vs. time.

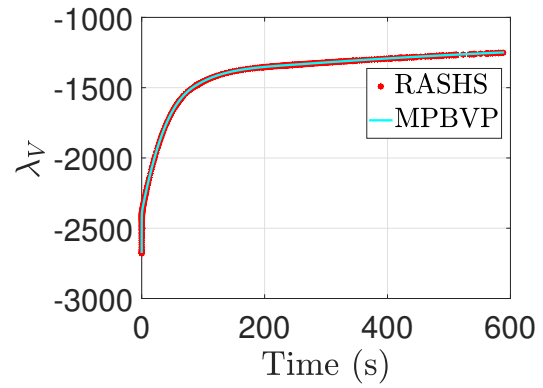
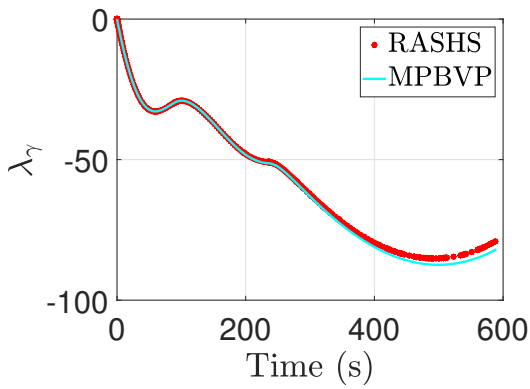
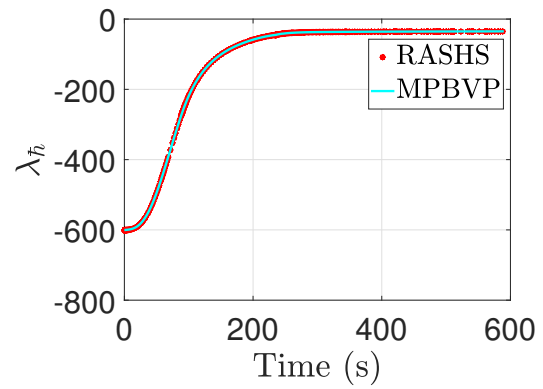
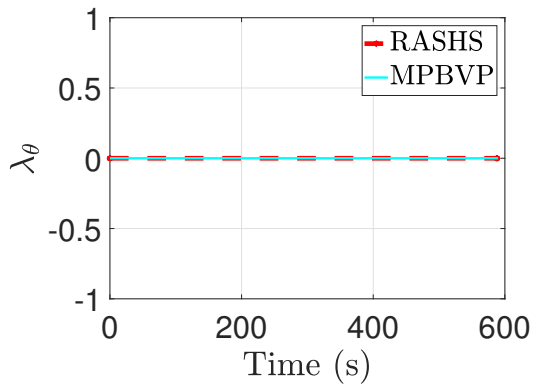
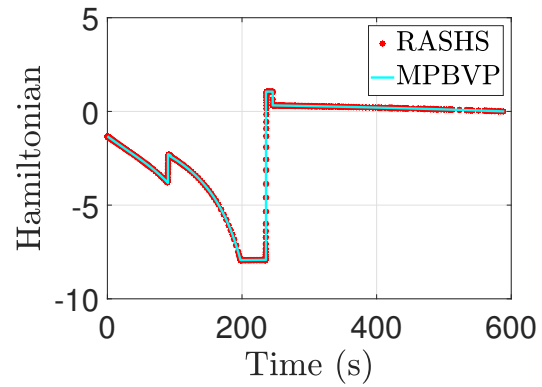
Figure 8.1. Minimum-time ascent trajectory of Atlas V 411 to equatorial circular orbit. The flight phases and the corresponding vehicle configuration are defined in Table 8.1, and the desired initial and final vehicle states are defined in Table 8.2.

plots of  $h$  and  $\theta$  are also smooth without any corner points. It can also be seen that the results from the two methods agree very well.

The control history is shown in Figure 8.2(a). The histories of the co-states are shown in Figures 8.2(b) through 8.2(e), and the history of the Hamiltonian is shown in Figure 8.2(f). The solutions obtained from the two methods agree very well in general. However, small deviations in the histories of control and  $\lambda_\gamma$  resulting from the smoothing effects of the sigmoid functions are observed. This also translates to



(a) Control history.

(b)  $\lambda_v$  vs. time.(c)  $\lambda_\gamma$  vs. time.(d)  $\lambda_h$  vs. time.(e)  $\lambda_\theta$  vs. time.

(f) Hamiltonian history.

Figure 8.2. Histories of control, co-states, and Hamiltonian.



a small difference in final time (588.04 s for RASHS and 588.82 s for the MPBVP). However, this deviation is small and can be safely neglected because the physical trajectories match very well. Since the discrete phase sequence is time-switched, the Hamiltonian is expected to jump at the phase boundaries. These jumps are observed to be the same in both methods. In the RASHS framework, these jumps were never enforced explicitly, nor were they guessed. They were simply a consequence of the transformed equations of motion and cost functional, thereby demonstrating the power of this framework. Finally, the boundary conditions on the co-states and the final condition on the Hamiltonian ( $\mathbf{H} = 0$ ) are also satisfied.

The next section demonstrates an example wherein each phase of flight is solely triggered by conditions on states. This results in discontinuities in certain co-states, which complicate the problem if it were to be treated as an MPBVP.

### 8.3.2 Mars Entry, Descent, and Landing

This section presents an example wherein a Mars entry, descent, and landing trajectory is optimized using the RASHS approach. The vehicle of interest is similar to that used in the Mars Science Laboratory mission [138–142].

The EDL trajectory consists of four phases. The first phase is hypersonic to low-supersonic. The total entry mass is 3,152 kg. The vehicle is trimmed at a non-zero angle-of-attack by means of a center of mass offset accomplished by ballasts with a mass of 150 kg. This results in a constant lift-to-drag ratio of 0.25 and a drag coefficient of 1.24. The reference area is 15.9 m<sup>2</sup>. The vehicle can be maneuvered by modulating the bank angle (the control variable). This phase ends when the vehicle slows down to 408 m/s, corresponding to about Mach 1.7. This triggers the parachute phase.

When the parachute phase is triggered, the vehicle jettisons the ballasts, reducing the mass to 3,002 kg and resulting in a trim angle-of-attack of 0 deg. Upon parachute deployment, the drag coefficient changes to 9.43. During this phase, the vehicle cannot

be maneuvered. When the vehicle slows down to 168 m/s, corresponding to about Mach 0.7, the heat shield is jettisoned.

The heat shield jettison marks the initiation of the third phase. The mass is reduced to 2,617 kg, while the drag coefficient remains at 9.43. When the vehicle descends to an altitude of 2 km, powered descent is initiated.

At powered descent initiation (fourth phase), the backshell along with the parachute is jettisoned, reducing the mass further to 2,268 kg. The drag coefficient changes to 0.31. In this phase of flight, the vehicle is assumed to be oriented such that the thrust vector is always retrograde, resulting in a 0 deg angle-of-attack and side-slip angle. The descent engines collectively have an  $I_{sp}$  of 210 s and a maximum mass flow rate of 12.3 kg/s, which in turn corresponds to a maximum thrust of 25.6 kN.

The vehicle's mass and aerodynamic characteristics corresponding to the beginning of each phase of flight are summarized in Table 8.3. The surface density and the scale height of the Martian atmosphere are assumed to be 0.025 kg/m<sup>3</sup> and 11.1 km respectively.

Table 8.3. EDL vehicle mass and aerodynamic properties.

Phase of flight	Mass	$L/D$	$C_D$	Control
Phase 1 (hypersonic to low supersonic)	3,152 kg	0.25	1.24	Bank angle
Phase 2 (parachute descent)	3,002 kg	0	9.43	No control
Phase 3 (parachute descent, heatshield jettison)	2,617 kg	0	9.43	No control
Phase 4 (powered descent)	2,268 kg	0	0.31	Retrograde thrust

The states  $h$ ,  $v$  and  $m_F$  are scaled by initial altitude ( $h(0) = 120$  km), initial atmospheric relative velocity ( $v(0) = 5.9$  km/s), and total propellant on board, equal to 387 kg, respectively. This results in the scaled variables  $\tilde{h}$ ,  $V$  and  $M_F$  such that:

$$\begin{aligned}
\hbar &= \frac{h}{h(0)} \\
V &= \frac{v}{v(0)} \\
M_F &= \frac{m_F}{387}
\end{aligned} \tag{8.14}$$

Thus, the state vector is  $\mathbf{X} = [\hbar \ \theta \ \phi \ V \ \gamma \ \psi \ M_F]^T$ . Since  $C_L$ ,  $C_D$ , and mass change discretely at the transitions between each phase of flight, the equations of motion are discontinuous in time. The desired initial and final conditions on the states are described in Table 8.4. A final velocity of 0.1 m/s is chosen to avoid singularity in the equations of motion.

Table 8.4. Initial and final conditions for the EDL trajectory.

State	Initial Condition	Final Condition
Altitude ( $h$ )	120 km	0 km
Longitude ( $\theta$ )	0 deg	16.027 deg
Latitude ( $\phi$ )	0 deg	1.1809 deg
Atmospheric relative velocity ( $v$ )	5.9 km/s	0.1 m/s
Atmospheric relative flight path angle ( $\gamma$ )	free	free
Atmospheric relative heading angle ( $\psi$ )	90 deg	free
Mass of propellant consumed ( $m_F$ )	0 kg	free

The stagnation-point heat load on the vehicle is minimized from entry interface to the beginning of powered descent, and the thrust is minimized as a surrogate for minimizing propellant used during powered descent. The stagnation-point heat-load  $Q$  corresponding to time  $\tau$  is obtained by integrating the stagnation-point heat-rate,  $\dot{q}$ , given by Sutton and Graves [143]. That is:

$$Q(\tau) = \int_0^\tau \dot{q} \, dt = \int_0^\tau k \sqrt{\left(\frac{\rho}{R_N}\right)} v^3 \, dt \tag{8.15}$$

where  $R_N$  is the geometric nose radius of the heat shield, and is assumed to be equal to 1.125 m. It is also assumed to be the same even after heat-shield jettison. Also,  $k$  is an empirical constant,  $\rho$  is the exponential atmospheric density, and  $v$  is the magnitude of the atmospheric-relative velocity.

Therefore, the cost functional to be minimized is posed as a weighted objective as follows:

$$J = K_1 \int_0^{t_{pdi}} \sqrt{\frac{\rho}{R_N}} v^3 dt + K_2 \int_{t_{pdi}}^{t_f} T^2 dt \quad (8.16)$$

where  $K_1$  and  $K_2$  are the weights. For this problem,  $K_1$  and  $K_2$  were chosen to be 1 and  $10^{-5}$  respectively. It was observed that these values brought the two integrals to roughly the same order of magnitude. Furthermore,  $t_{PDI}$  is the time corresponding to powered descent initiation at an altitude of 2 km, and  $t_f$  is the final time (touchdown time). Both  $t_{PDI}$  and  $t_f$  are not known a-priori and need to be determined as part of the optimization process. The Lagrangian,  $\mathcal{L}$ , is then given as:

$$\mathcal{L} = \begin{cases} K_1 \sqrt{\frac{\rho}{R_N}} v^3 & \text{when } t \leq t_{PDI} \\ K_2 T^2 & \text{otherwise} \end{cases} \quad (8.17)$$

It can be seen that  $\mathcal{L}$  is discontinuous at  $t_{PDI}$ . Since this problem has four flight segments, there are 5 boundaries, three of which are interior point boundaries.

Let  $v_P = 408$  m/s be the parachute deployment velocity,  $v_H = 168$  m/s be the heat shield jettison velocity, and  $h_{PDI} = 2$  km be the powered descent initiation altitude. Let the (scaled) equations of motion be represented by  $\mathbf{f}_1$  through  $\mathbf{f}_4$  during phases 1 through 4. The conditions under which  $\mathbf{f}_1$  through  $\mathbf{f}_4$  are “ON” are summarized in Table 8.5, along with the corresponding unit step multipliers.

Consequently, the equations of motion that represent all phases of flight are given as:

Table 8.5. “ON” conditions for each phase of flight.

Equations of Motion	“ON” Conditions	Unit Step Multiplier
$\mathbf{f}_1(\mathbf{X}, \sigma)$ (phase 1)	$v > v_P$	$u\left(V - \frac{v_P}{v(0)}\right)$
$\mathbf{f}_2(\mathbf{X})$ (phase 2)	$v < v_P$ $v > v_H$	$\left[1 - u\left(V - \frac{v_P}{v(0)}\right)\right] u\left(v - \frac{v_H}{v(0)}\right)$
$\mathbf{f}_3(\mathbf{X})$ (phase 3)	$v < v_H$ $h > h_{PDI}$	$\left[1 - u\left(v - \frac{v_H}{v(0)}\right)\right] u\left(h - \frac{h_{PDI}}{h(0)}\right)$
$\mathbf{f}_4(\mathbf{X}, T)$ (phase 4)	$h < h_{PDI}$	$1 - u\left(h - \frac{h_{PDI}}{h(0)}\right)$

$$\begin{aligned} \dot{\mathbf{X}} = & \left[ u\left(V - \frac{v_P}{v(0)}\right) \right] \mathbf{f}_1 + \left[ \left(1 - u\left(V - \frac{v_P}{v(0)}\right)\right) \cdot u\left(v - \frac{v_H}{v(0)}\right) \right] \mathbf{f}_2 \\ & + \left[ \left(1 - u\left(v - \frac{v_H}{v(0)}\right)\right) \cdot u\left(h - \frac{h_{PDI}}{h(0)}\right) \right] \mathbf{f}_3 + \left[ 1 - u\left(h - \frac{h_{PDI}}{h(0)}\right) \right] \mathbf{f}_4 \end{aligned} \quad (8.18)$$

The unit step functions in Eq. (8.18) can be replaced by equivalent sigmoid functions as shown in Eq. (8.19)

$$\begin{aligned} \dot{\mathbf{X}} = & \left[ \frac{1}{1 + e^{-s(V - \frac{v_P}{v(0)})}} \right] \mathbf{f}_1 + \left[ \left( \frac{1}{1 + e^{s(V - \frac{v_P}{v(0)})}} \right) \left( \frac{1}{1 + e^{-s(v - \frac{v_H}{v(0)})}} \right) \right] \mathbf{f}_2 \\ & + \left[ \left( \frac{1}{1 + e^{s(v - \frac{v_H}{v(0)})}} \right) \left( \frac{1}{1 + e^{-s(h - \frac{h_{PDI}}{h(0)})}} \right) \right] \mathbf{f}_3 + \left[ \frac{1}{1 + e^{s(h - \frac{h_{PDI}}{h(0)})}} \right] \mathbf{f}_4 \end{aligned} \quad (8.19)$$

Eq. (8.19) is a time-differentiable function that represents the equations of motion for all phases of flight and automatically accounts for the interior point conditions. Using the RASHS approach, the Lagrangian is also represented by a single smooth function. Recognizing that the first integral in Eq. (8.16) is nonzero when  $h > h_{PDI}$  and the second integral is nonzero when  $h < h_{PDI}$ , the cost functional can be represented by a smooth functional as shown in Eq. (8.20).

$$J = \int_0^{t_{PDI}} \left\{ \left[ \left( K_1 - \frac{1}{1 + e^{-s(\hbar - \frac{h_{PDI}}{h(0)})}} \right) \sqrt{\frac{\rho}{R_N}} v^3 \right] + \left[ \left( K_2 - \frac{1}{1 + e^{s(\hbar - \frac{h_{PDI}}{h(0)})}} \right) T^2 \right] \right\} dt \quad (8.20)$$

Using the smooth dynamics and cost functional, the necessary conditions of optimality are derived using Eq. (5.5). As before, the resultant TPBVP is solved using continuation, as described in Section 5.3. The guess for the initial iteration is obtained by propagating the differential equations in the TPBVP using the Dormand-Prince method for 0.1 seconds, with  $s = 500$  in Eqs. (8.19) and (8.20) and the following initial conditions:

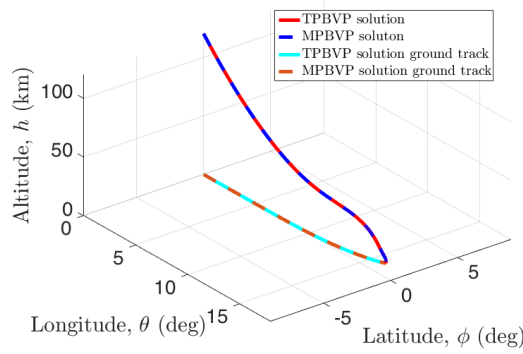
$$\begin{aligned} \begin{bmatrix} \mathbf{X}^T & \boldsymbol{\lambda}^T \end{bmatrix}^T &= [\hbar \ \theta \ \phi \ V \ \gamma \ \psi \ M_F \ \lambda_{\hbar} \ \lambda_{\theta} \ \lambda_{\phi} \ \lambda_V \ \lambda_{\gamma} \ \lambda_{\psi} \ \lambda_{M_F}]^T \\ &= [1 \ 0 \ 0 \ 1 \ 0 \ \pi/2 \ 0 \ 0 \ 1 \ -1 \ -1 \ 0 \ 0 \ 0] \end{aligned} \quad (8.21)$$

While propagating the guess, the  $L/D$  for the first phase is set to 0, making the trajectory purely ballistic. Also, the conditions on final velocity ( $v(t_f)$ ) and initial heading ( $\psi(0)$ ) are free. The continuation is implemented in five steps. In the first step, final altitude, latitude and longitude are varied in 1,000 iterations to the desired values of 0 km, 1.1809 deg, and 16.027 deg respectively. For the first iteration, these values are set to the corresponding final values resulting from the propagation of the initial guess. Consistent with the initial guess propagation, the initial heading and the final velocity are free, and consequently, the initial  $\lambda_{\psi}$  and the final  $\lambda_V$  are set to zero. The value of  $s$  in the sigmoid functions is set to 500. In the second step, the boundary condition on the final velocity is enforced, and is varied in 500 iterations to the desired value of 0.1 m/s. For the first iteration, this value is set to that corresponding to the solution of the last iteration of step 1. In step 3, the hypersonic  $L/D$  is varied in 500 iterations from 0 to 0.24. In step 4, the boundary condition on the initial heading is enforced, and is varied in 500 iterations from the value corresponding to the solution of the final iteration of step 3, to the desired value of 90 deg. In step 5, the value of  $s$  in the sigmoid functions is changed from 500 to 60,000 in 1,000 iterations.

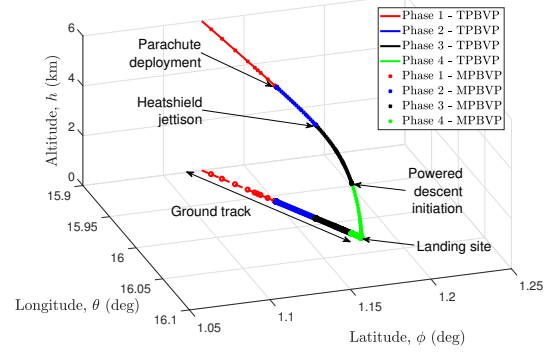
The solution of the final iteration in step 5 is the desired solution. As in the two-stage launch example, this solution is compared with that obtained from solving the MPBVP, which is in turn obtained by using the RASHS solution as the initial guess.

Figure 8.3(a) compares the physical trajectories from the two approaches. Figure 8.3(b) shows the same plot zoomed in to illustrate the parachute descent, heat shield jettison and powered descent. It can be seen that the vehicle states corresponding to the trajectory phase transition points (parachute deployment, heat shield jettison and powered descent initiation) in the two solutions are consistent with each other. Figure 8.3(c) compares the plots of altitude as a function of atmospheric relative velocity, and Figure 8.3(d) shows the same plot zoomed in. As before, the solutions from the two methods match. Additionally, a corner point can be observed at the moment of parachute deployment, which is caused by the discrete change in the drag coefficient. Although this corner point is actually smooth in the solution of the RASHS approach, the steep slopes of the sigmoid functions make it appear like a corner point, and the error associated with the smoothing is negligible for practical purposes. There is also a corner point at the moment of heat shield jettison and also powered descent initiation. However, this is not apparent because when the heat shield is jettisoned, the discrete change in ballistic coefficient is not as significant (it changes from 20.01 kg/m<sup>2</sup> to only 17.45 kg/m<sup>2</sup>). At powered descent initiation, the ballistic coefficient becomes high (453.6 kg/m<sup>2</sup>). This, coupled with the slow velocity, results in very low drag deceleration. The vehicle would essentially be in freefall, which is offset by the thrust from the descent engines. The initial thrust is not dramatically high (Figure 8.3(f)), and as a result, the corner is not apparent at powered descent initiation either.

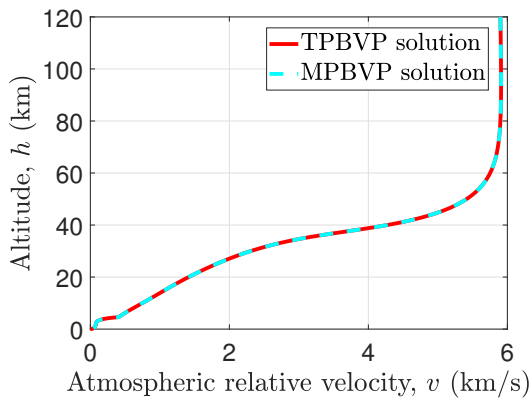
Figure 8.3(e) compares the bank angle control history that is calculated using the two methods. Once again, the results match very well. As expected, the vehicle banks left (positive value) to turn north-bound because the vehicle is flying East and the landing site is located North-East. The thrust profile during powered descent is shown in Figure 8.3(f) and is also determined to match very well.



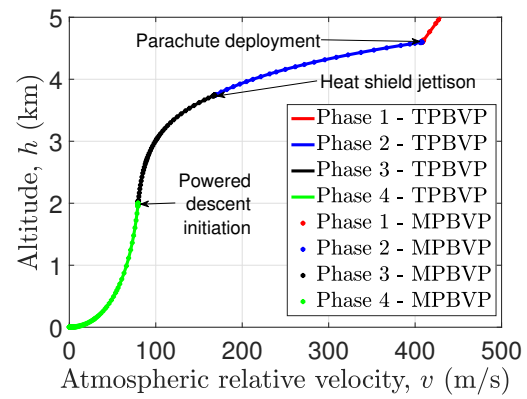
(a) Physical trajectory.



(b) Physical trajectory zoomed in.



(c) Altitude vs. atmospheric relative velocity.



(d) Altitude vs. atmospheric relative velocity, zoomed in.

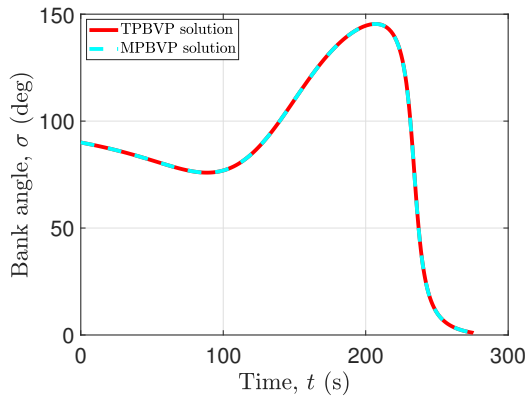
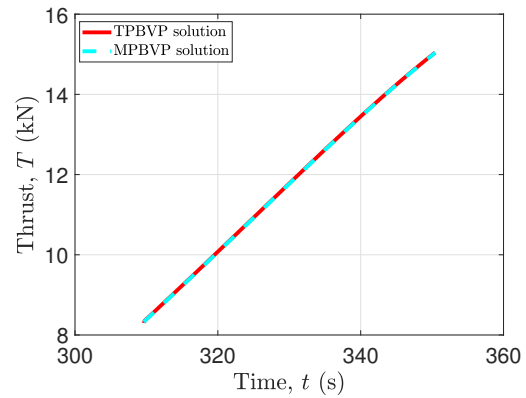
(e) Bank angle ( $\sigma$ ) vs. time.(f) Thrust ( $T$ ) vs. time.

Figure 8.3. Optimal Mars EDL trajectory of an MSL-like vehicle. The flight phases and the vehicle configuration are described in Table 8.3, and the desired initial and final vehicle states are defined in Table 8.4. The stagnation-point heat load is minimized until powered descent, and the thrust is minimized during powered descent.



The time histories of the states and co-states were compared and they matched as well, except for  $\lambda_\theta$  and  $\lambda_\phi$  (the co-states corresponding to longitude and latitude). The time histories of these co-states are shown in Figures 8.4(a) and 8.4(b). The deviations are the result of errors that are introduced because of the smoothing operation by the sigmoid functions. The deviations were observed to diminish as the slope of the sigmoid functions were increased, as expected. It is important to note that these are the co-states with free initial and final boundary conditions. Therefore, it may be inferred that the errors introduced because of the smoothing operation manifest in those co-states with free boundary conditions. However, this is the optimal result for the smoothed problem because the necessary conditions are satisfied.

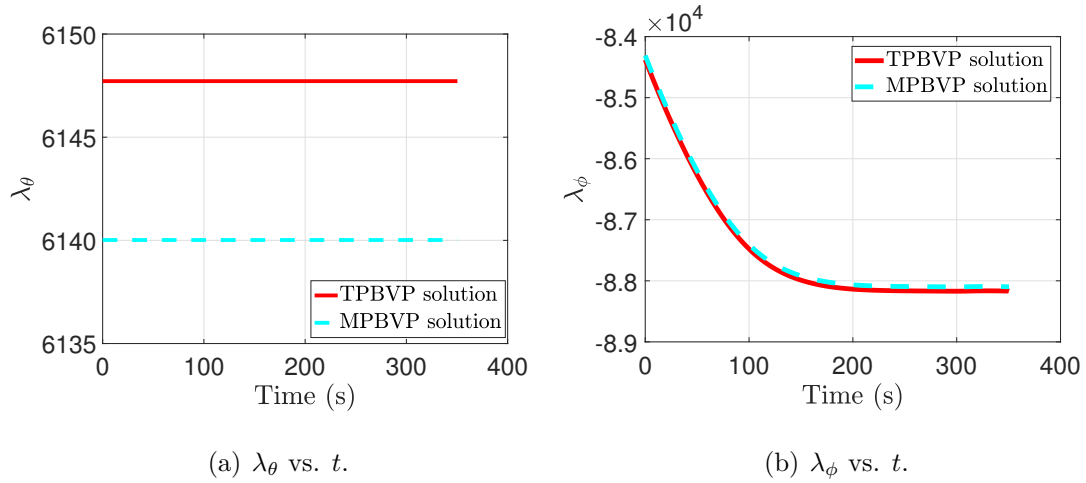


Figure 8.4. Longitude and latitude co-state histories.

Also of interest are the histories of  $\lambda_h$  and  $\lambda_V$ , the histories of co-states corresponding to non-dimensional altitude and velocity. Since the velocity is fixed at the instant of parachute deployment and heat shield jettison, the co-state corresponding to velocity is expected to jump at the times corresponding to these two events ( $t_P$  and  $t_H$ ) as predicted by Eq. (5.27). This is shown in Figure 8.5(a). Additionally, since the altitude is fixed at the instant of powered descent initiation, the co-state corresponding to altitude is also expected to jump at the corresponding time ( $t_{PDI}$ ).

This is shown in Figure 8.5(b). It can be seen that the jumps are very close to those predicted by solving the original MPBVP. In the RASHS approach, the jump is actually a smooth transition. The power of the RASHS approach is that these jumps are part of the smooth dynamics and are not explicitly enforced. As a result, the requirement for guessing these jumps is eliminated. Since the control histories match very well, the optimal result of the RASHS approach can be practically viewed as the optimal result of the original MPBVP as well.

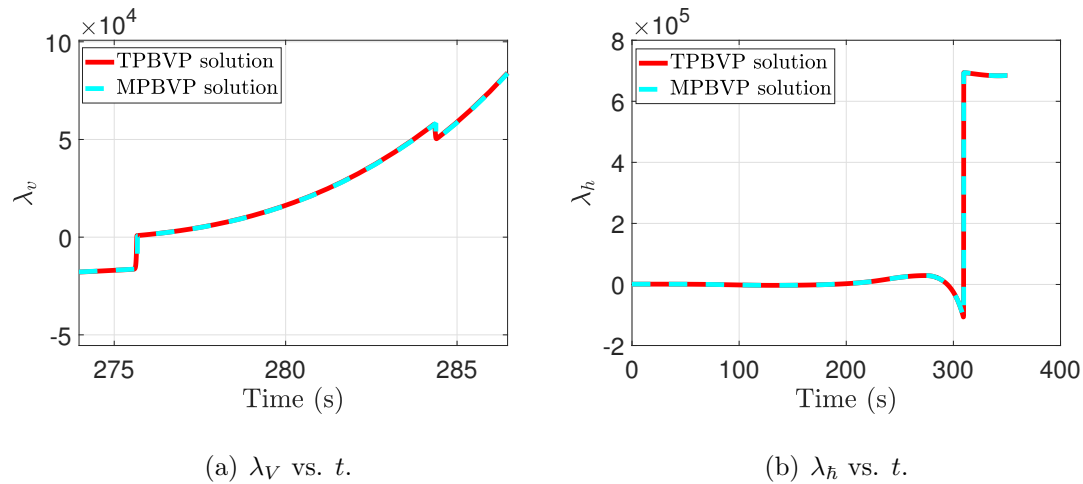


Figure 8.5. Velocity and altitude co-state histories.

The effectiveness of the RASHS approach was demonstrated using the launch and the EDL example. There are several aerospace systems that may be treated as multi-body systems, and RASHS can simplify the design of optimal trajectories for such systems, as demonstrated in the next section.

### 8.3.3 Multi-Body Example: Boost-Glide Weapon System

This section demonstrates the extension of the RASHS approach to multi-body systems by presenting an example wherein the trajectory of a hypothetical boost-glide weapon system is optimized to maximize the impact velocity and minimize the TOF of the glide vehicle, measured from launch. Constraints are imposed on the

location where the spent booster falls back to Earth. As a result, it is necessary to track the states of the spent booster, in addition to those of the glide vehicle, leading to a multi-body problem. Since the impact location of the booster depends on the conditions at booster burnout, the trajectories of the boost phase, glide vehicle, and the spent booster are coupled with one another.

The mission consists of the launch of a single stage boost-glide weapon system from 0 deg latitude and longitude to strike a target located at 2.6949 deg latitude and 4.0424 deg longitude. The spent booster is constrained to impact at 2.5440 deg latitude and 3.8171 deg longitude. It is required to minimize the time elapsed from the moment of launch to the instant when the glide vehicle impacts the target. It is also required to maximize the velocity at impact, leading to a weighted cost functional with weights 0.47 and 1:

$$J = -0.47 (v_2(t_f))^2 + \int_0^{t_f} dt \quad (8.22)$$

where  $v_2$  is the atmospheric-relative velocity of the glide vehicle and  $t_f$  corresponds to the time when it impacts the target. The chosen weights were found to scale the cost functional well. The desired initial and final values of the states of the booster and the glide vehicle are summarized in Table 8.6.

Table 8.6. End-point boundary conditions on states.

State	Initial value		Final value	
	Boost stage	Glide vehicle	Boost stage	Glide vehicle
Altitude	$h_1 = 0$ km	$h_2 = 0$ km	$h_1 = 0$ km	$h_2 = 0$ km
Longitude	$\theta_1 = 0$ deg	$\theta_2 = 0$ deg	$\theta_1 = 3.8041$ deg	$\theta_2 = 4.0424$ deg
Latitude	$\phi_1 = 0$ deg	$\phi_2 = 0$ deg	$\phi_1 = 1.7456$ deg	$\phi_2 = 2.6949$ deg
Velocity	$v_1 = 0.1$ m/s	$v_2 = 0.1$ m/s	free	free
Flight path angle	$\gamma_1 = 40$ deg	$\gamma_2 = 40$ deg	free	free
Heading angle	$\psi_1 = 0$ deg	$\psi_2 = 0$ deg	free	free

The dynamic state variables (velocity, flight path angle, and heading angle) correspond to the atmospheric-relative values. The rotation of the Earth is taken into account, and a stationary exponential atmosphere bearing a surface density of  $1.225 \text{ kg/m}^3$  and a scale height of 8.5 km is assumed. The booster and glide vehicle are considered to be point masses. The mass properties of the booster and glide vehicle are given in Table 8.7.

Table 8.7. Mass properties of the boost-glide system.

Stage	Empty mass	Fuel mass
Boost stage	5,000 kg	13,738 kg
Glide vehicle	2,316 kg	0 kg

Let the state vectors describing the motion of the booster and the glide vehicle be  $\mathbf{X}_1$  and  $\mathbf{X}_2$  respectively. The mission can be divided into three flight phases:

1. **Boost phase:** The booster operates at a constant thrust of 415.2 kN, corresponding to an  $I_{sp}$  of 277.27 seconds. The booster and the glide vehicle are linked together. Consequently,  $\mathbf{X}_1$  and  $\mathbf{X}_2$  are subject to the same dynamics  $\mathbf{f}$ . That is:

$$\begin{aligned}\dot{\mathbf{X}}_1 &= \mathbf{f}(\mathbf{X}_1, \alpha, \sigma, t) \\ \dot{\mathbf{X}}_2 &= \mathbf{f}(\mathbf{X}_1, \alpha, \sigma, t)\end{aligned}\tag{8.23}$$

During this phase, The vehicle is maneuvered by varying the angle-of-attack and bank angle. The lift and drag coefficients multiplied by the reference area are given by:

$$\begin{aligned}C_L S &= 0.1 \sin \alpha \\ C_D S &= 2 - 1.8 \cos \alpha\end{aligned}\tag{8.24}$$

The booster burnout and glide vehicle separation occurs at time  $t = t_b = 90$  s, and marks the end of this phase.

2. **Glide phase before booster impact:** The booster is subject to the dynamics  $\mathbf{f}_1$  until it impacts the Earth (altitude  $h_1 > 0$ ). The glide vehicle is subject to dynamics  $\mathbf{f}_2$ . That is:

$$\begin{aligned}\dot{\mathbf{X}}_1 &= \mathbf{f}_1(\mathbf{X}_1) \\ \dot{\mathbf{X}}_2 &= \mathbf{f}_2(\mathbf{X}_2, \alpha, \sigma)\end{aligned}\tag{8.25}$$

The booster follows a ballistic trajectory with  $(C_D S)_1 = 1$ . The glide vehicle is unpowered, and is maneuvered by varying the angle-of-attack and bank angle. Its lift and drag coefficients multiplied by the reference area are given by:

$$\begin{aligned}(C_L S)_2 &= 0.8 \sin \alpha \\ (C_D S)_2 &= 1.5 - 1.3 \cos \alpha\end{aligned}\tag{8.26}$$

3. **Glide phase post-booster impact:** The glide vehicle continues to be subject to the dynamics  $\mathbf{f}_2$  while the booster's states are frozen. That is:

$$\begin{aligned}\mathbf{X}_1 &= \mathbf{0} \\ \mathbf{X}_2 &= \mathbf{f}_2(\mathbf{X}_2, \alpha, \sigma)\end{aligned}\tag{8.27}$$

This phase lasts until the glide vehicle impacts the target, which also marks the end of the mission.

The “ON” conditions for  $\mathbf{f}$ ,  $\mathbf{f}_1$  and  $\mathbf{f}_2$  are summarized in Table 8.8.

Consequently, the equations of motion that represent all phases of flight are given as:

$$\dot{\mathbf{X}} = \begin{bmatrix} \dot{\mathbf{X}}_1 \\ \dot{\mathbf{X}}_2 \end{bmatrix} = \begin{bmatrix} [1 - u(t - t_b)] \mathbf{f} + [u(t - t_b) u(h_1)] \mathbf{f}_1 \\ [1 - u(t - t_b)] \mathbf{f} + u(t - t_b) \mathbf{f}_2 \end{bmatrix}\tag{8.28}$$

Table 8.8. “ON” conditions for each phase of flight.

Equations of Motion	“ON” Conditions	Unit Step Multiplier
$\mathbf{f}(\mathbf{X}_1, \alpha, \sigma, t)$	$t < t_b$	$1 - u(t - t_b)$
$\mathbf{f}_1(\mathbf{X}_1)$	$t > t_b$ $h_1 > 0$	$u(t - t_b) \cdot u(h_1)$
$\mathbf{f}_2(\mathbf{X}_2, \alpha, \sigma)$	$t > t_b$	$u(t - t_b)$

As before, the unit step functions are replaced by appropriate sigmoid functions, resulting in the following equations of motion that are continuous and differentiable for all time  $t$ :

$$\dot{\mathbf{X}} = \begin{bmatrix} \dot{\mathbf{X}}_1 \\ \dot{\mathbf{X}}_2 \end{bmatrix} = \begin{bmatrix} \left( \frac{1}{1+e^{s(t-t_b)}} \right) \mathbf{f} + \left( \frac{1}{1+e^{-s(t-t_b)}} \right) \left( \frac{1}{1+e^{-sh_1}} \right) \mathbf{f}_1 \\ \left( \frac{1}{1+e^{s(t-t_b)}} \right) \mathbf{f} + \left( \frac{1}{1+e^{-s(t-t_b)}} \right) \mathbf{f}_2 \end{bmatrix} \quad (8.29)$$

The velocity states ( $v_1$  and  $v_2$ ) are scaled by 4 km/s, and the altitude states ( $h_1$  and  $h_2$ ) are scaled by 40 km. The equations of motion defined by Eq. (8.29) and the cost functional defined by Eq. (8.22) are used in deriving the necessary conditions of optimality defined by Eq. (5.5). It is important to note that the consequence of Eq. (8.29) is that the trajectory of the spent booster will automatically terminate when it impacts the surface. As a result, the final boundary condition on its altitude ( $h_1 = 0$ ) is not required to be explicitly enforced, and can instead be left free. As before, the resultant TPBVP is solved using finite difference and continuation. The guess for the first continuation step is generated by propagating the differential equations defined by Eq. (8.29) using Dormand-Prince method for 10 seconds, with the slope  $s$  in the sigmoid functions set to 1,000 and the following initial conditions:

$$\begin{aligned}
\mathbf{X}_1^T &= \begin{bmatrix} h_1 & \theta_1 & \phi_1 & V_1 & \gamma_1 & \psi_1 \end{bmatrix} = \begin{bmatrix} 0 & 0 & 0 & \frac{0.1}{4000} & 0.7 & 0 \end{bmatrix} \left( \begin{array}{l} \times \\ \times \end{array} \right. \\
\mathbf{X}_2^T &= \begin{bmatrix} h_2 & \theta_2 & \phi_2 & V_2 & \gamma_2 & \psi_2 \end{bmatrix} = \begin{bmatrix} 0 & 0 & 0 & \frac{0.1}{4000} & 0.7 & 0 \end{bmatrix} \left( \begin{array}{l} \times \\ \times \end{array} \right. \\
\boldsymbol{\lambda}_1^T &= \begin{bmatrix} \lambda_{h_1} & \lambda_{\theta_1} & \lambda_{\phi_1} & \lambda_{V_1} & \lambda_{\gamma_1} & \lambda_{\psi_1} \end{bmatrix} = \begin{bmatrix} 0.01 & 0.1 & 0 & -1 & 0 & 0 \end{bmatrix} \left( \begin{array}{l} \times \\ \times \end{array} \right. \\
\boldsymbol{\lambda}_2^T &= \begin{bmatrix} \lambda_{h_2} & \lambda_{\theta_2} & \lambda_{\phi_2} & \lambda_{V_2} & \lambda_{\gamma_2} & \lambda_{\psi_2} \end{bmatrix} = \begin{bmatrix} 0.01 & 0.1 & 0 & -1 & 0 & 0 \end{bmatrix} \left( \begin{array}{l} \times \\ \times \end{array} \right.
\end{aligned} \tag{8.30}$$

The continuation is implemented in three steps. In the first step, final altitude, latitude and longitude of the glide vehicle are varied in 500 iterations to the desired values of 0 km, 2.6949 deg and 4.0424 deg respectively. For the first iteration in this set, these values are set to the corresponding final values resulting from the propagation of the initial guess. Consistent with the initial guess propagation, the value of  $s$  in the sigmoid functions is set to 1,000. Moreover, the final conditions on longitude and latitude of the booster are left free. Consequently, the final conditions on the corresponding co-states are set to 0. In the second continuation step, the boundary condition on the final latitude and longitude are fixed and varied in 1,000 iterations to the desired values of 1.7456 deg and 3.8041 deg respectively. For the first iteration, these values are set to those corresponding to the solution of the last iteration of step 1. Additionally, the corresponding co-states at final time are set free. In the third and final continuation step, the value of  $s$  in the sigmoid functions is changed from 1,000 to 60,000 in 1,000 iterations.

The solution of the final iteration in step 3 is the desired solution. As in the Atlas V 411 launch example, this solution is compared with that obtained by solving the MPBVP using finite difference, with the RASHS solution as the initial guess.

The trajectories of the boost stage and the glide vehicle are shown in Figure 8.6. Since the spent booster cannot be maneuvered, it follows a ballistic trajectory. Its impact location is dictated by the conditions at booster separation. Since the desired impact coordinates of the booster are out of plane with respect to the launch and glide vehicle target coordinates, the boost trajectory is required to be co-planar with the launch and booster impact coordinates. Following booster separation, the glide

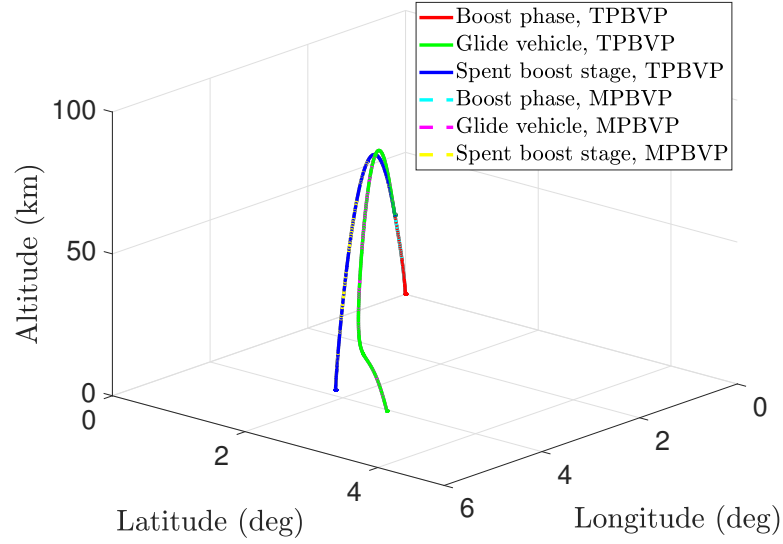


Figure 8.6. Maximum final velocity, minimum time boost-glide trajectory with constraints on the impact location of the spent booster. The desired initial and final states of the booster and the glide vehicle are defined in Table 8.6, and their properties are defined in Table 8.7.

vehicle banks to the left (counterclockwise), thereby turning north-bound towards the target. This is indicated by a positive angle-of-attack and bank angle following booster separation (Figure 8.7). The figures also show that the RASHS and MPBVP solutions match very well.

As predicted by Eq. (5.27), the Hamiltonian is discontinuous at the instant of booster burnout because this event is triggered by time ( $t_b = 90$  s), and is illustrated in Figure 8.8(a). Since the propagation of the states of the spent booster is stopped when it impacts the surface ( $h_1 = 0$ ),  $\lambda_{h_1}$  is expected to be discontinuous at the instant of booster impact. Figure 8.8(a) illustrates the history of  $\lambda_{h_1}$  predicted by RASHS and the original MPBVP. It can be seen that although the MPBVP solution has the expected discontinuity, the RASHS solution does not. In fact, the RASHS solution is never discontinuous. In the other examples, the transitions appeared to be discontinuous because the vehicle quickly traversed the vicinity of the boundary of the flight phase transition. In this example, however, the dynamics for the spent booster



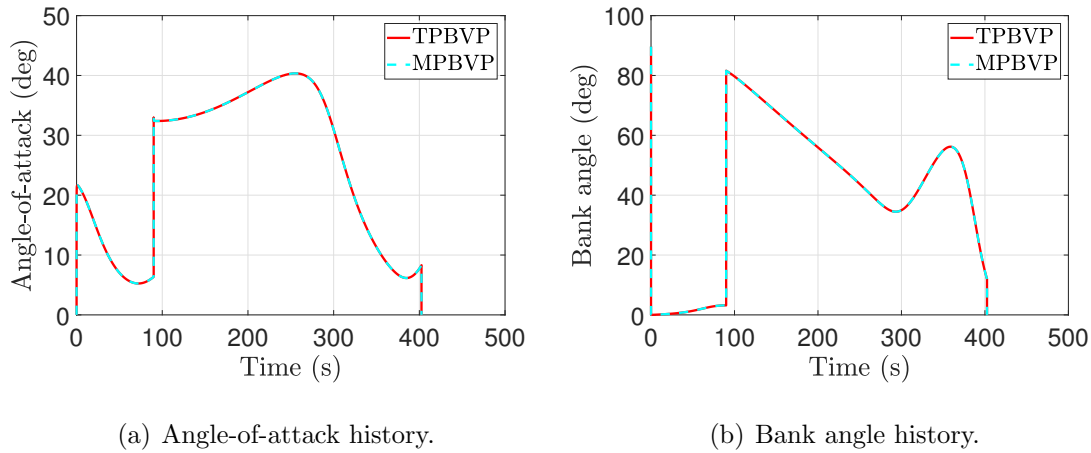


Figure 8.7. Control histories.

is  $\mathbf{0}$  below the surface. As a result, it remains at the vicinity of the phase boundary for the rest of the mission. Therefore, the apparent discontinuity in the RASHS solution is absent. In fact, almost all of the error resulting from the introduction of the sigmoid functions manifests in  $\lambda_{h_1}$ , while the rest of the states and co-states match very well. Therefore, this error is easily tolerable.

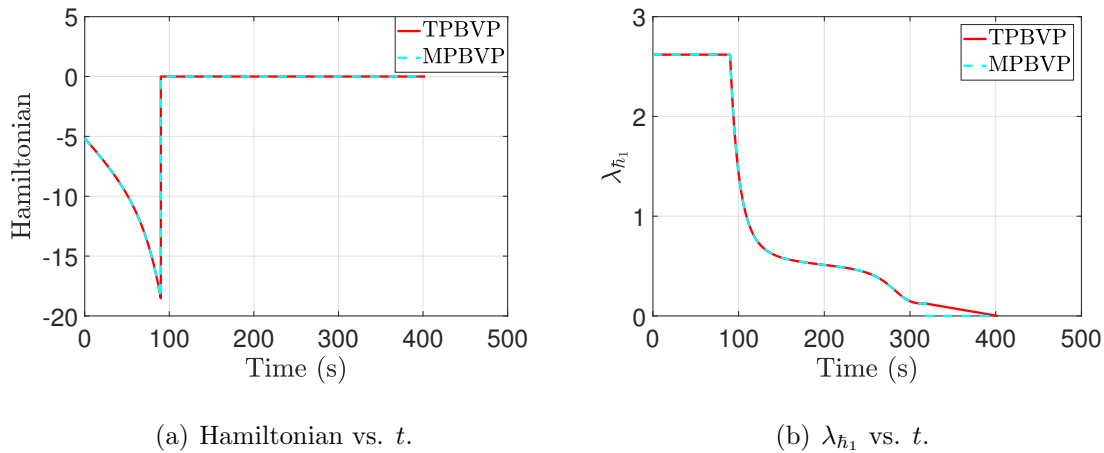


Figure 8.8. Histories of co-states and Hamiltonian.

The demonstrated simplification of missions of boost-glide systems with spent booster tracking enables easy trade studies during conceptual design of such systems, as described in the following section.

### **Trade Studies Using RASHS**

Since the RASHS approach reduces the MPBVPs to TPBVPs, it is possible to perform trade studies for conceptual mission design with relative ease. This section presents one such study for a boost-glide weapon system. For the purpose of the trade study, the same vehicle and cost functional from the previous example are used. It is required to study the effect of the variations in the impact coordinates of the spent booster on the rest of the mission. It is desired to have the spent booster impact as close to the launch site as possible so that the probability of it impacting unintended targets is minimized. Only planar motion is considered, and the target for the glide vehicle is located at a distance of 600 km from the launch site. The impact location of the spent booster is varied from 567.8 km to 417.8 km. Figure 8.9(a) shows the variation of the physical trajectory. Since the booster follows an uncontrolled ballistic trajectory after burnout, the states at booster separation are critical. The booster needs to be jettisoned at a shorter downrange distance if its impact distance is decreased. Since the burnout always occurs at 90 seconds and the booster cannot be throttled, the only way to accomplish this is by climbing to a higher altitude. In essence, the downrange is traded for altitude. However, the result is that the glide vehicle is required to fly a longer distance while unpowered. In order to avoid undershooting the target, it needs to maneuver more aggressively, thereby shallowing the descent. This is accomplished by increasing the angle-of-attack (Figure 8.9(b)). However, this maneuver results in increased drag, resulting in a lower impact velocity (Figure 8.9(c)). This also results in a longer time of flight for the glide vehicle (Figure 8.9(d)). This means that the adversary has more time to detect the vehicle

and intercept it. In essence, the impact location of the spent booster is traded for impact velocity and time of flight of the mission.

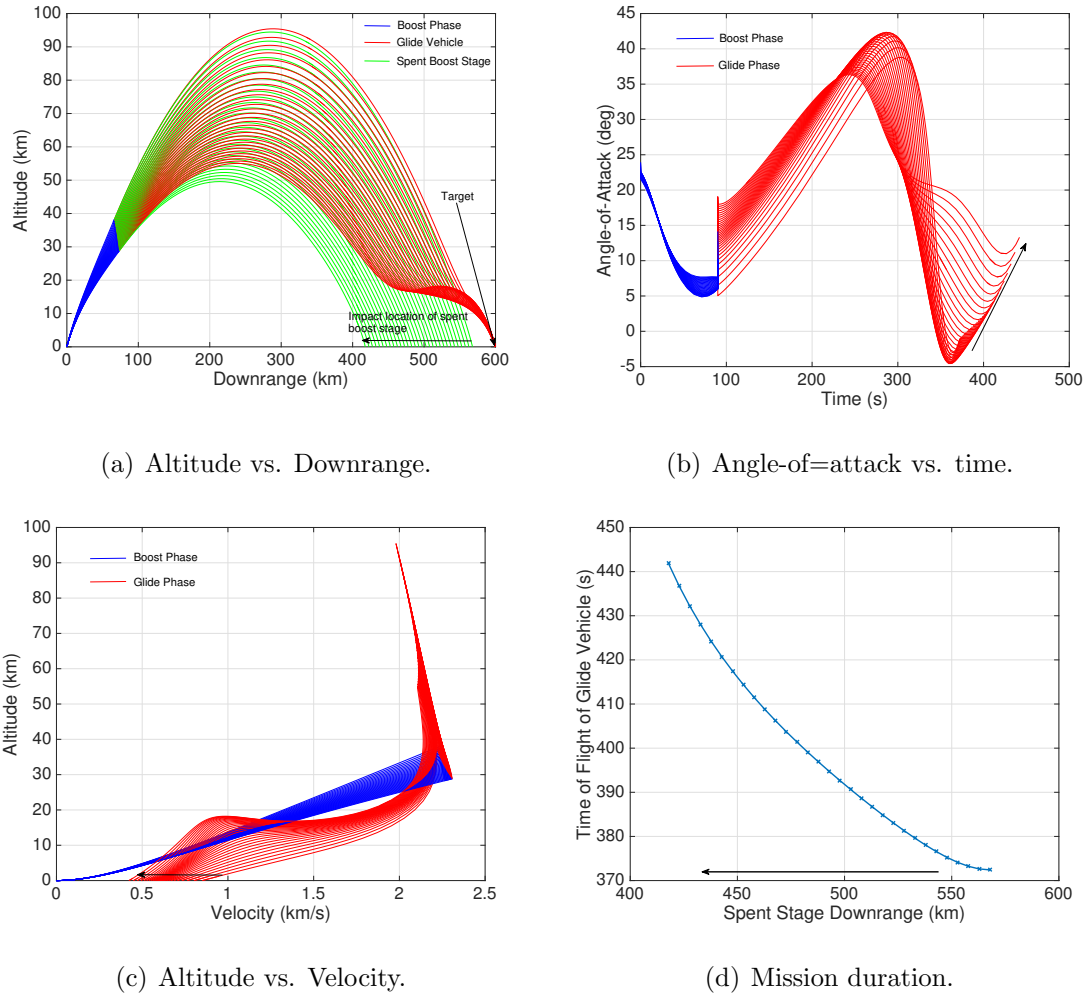


Figure 8.9. Mission trade study of a hypothetical boost-glide weapon system. Constraining the spent booster to impact closer to the launch site negatively impacts mission performance, wherein the impact velocity of the glide vehicle is reduced, and its TOF is increased.

## 8.4 Summary

This chapter described the Relaxed Autonomously Switched Hybrid System approach to simplify the design of optimal multi-phase trajectories. The necessary

conditions of optimality in the indirect framework traditionally result in an MPBVP in a system of DAEs. They involve interior-point boundary conditions, which define the transition of flight phases and ensure the continuity of the vehicle states, and are required to be explicitly enforced. Additionally, depending on the conditions that define the transition of flight phases, the co-states and the Hamiltonian may exhibit jumps. These make the generation of the initial guess more challenging.

The RASHS approach addresses this issue, in part, by reducing the problem to a TPBVP. This is accomplished by introducing smooth transitions at switching manifolds using sigmoid functions. Although the generation of an initial guess for the TPBVP is also difficult, it is mitigated by employing continuation. The TPBVP was demonstrated to be equivalent to the original MPBVP by comparing the solutions from the two methods.

The equivalence of the new TPBVP and the original MPBVP was illustrated using three examples: 1) multi-stage launch to circular orbit, 2) multi-phase entry, descent, and landing on Mars, and 3) a boost-glide weapon system. The third example involved the imposition of constraints on the impact location of the spent booster, thereby making the flight phases of the booster and the glide vehicle highly coupled. The RASHS approach demonstrated the ability to not just solve this type of a problem using indirect methods, but also perform design trade studies. Moving the impact location of the spent booster closer to the launch site was seen to have a negative influence on the mission performance, wherein the maximum achievable final velocity of the glide vehicle was reduced, and its TOF was increased. This multi-body mission design environment can also be extended to launch missions, such as those that require the spent stage to return to the launch site, as is the case with SpaceX's Falcon 9 launch vehicle [144].

Although RASHS serves as a powerful tool to design multi-phase trajectories, its effectiveness can be expanded by integrating it with more sophisticated flight dynamics model. The next chapter demonstrates this by combining the RASHS framework with the other two contributions of the dissertation.



## 9. UNIFIED CONCEPTUAL HYPERSONIC MISSION DESIGN FRAMEWORK

### 9.1 Introduction

In this chapter, the three contributions of the dissertation, namely 1) integration of ablative shape change into conceptual hypersonic mission design (Chapter 6), 2) incorporation of rigid body dynamics into trajectory design (Chapter 7), and 3) simplification of trajectory optimization of multi-phase systems (Chapter 8), are integrated into a single mission design framework. This enables the simultaneous design of multi-phase trajectories, basic aerothermal analysis and control effector design, which are traditionally performed independently of each other. Since this combined framework leverages the indirect optimization framework, the design solutions take advantage of the explicit coupling between these domains, thereby advancing the state-of-the-art in conceptual hypersonic mission design.

Three examples are presented to demonstrate the unified framework: 1) two-stage launch to circular orbit, 2) integration of ablative shape change with rigid body dynamics, and 3) rigid boost-glide weapon system trajectory with spent stage constraints.

### 9.2 Two-Stage Launch to Circular Orbit

This section presents an example wherein the ascent trajectory of a two-stage launch vehicle is optimized to minimize time. The example involves the same mission as described in Section 7.4.1, with the exception that a two-stage launch vehicle is used instead of a single-stage.

Since the mission involves two phases of flight, the RASHS approach can be leveraged. Furthermore, since rigid body motion is accounted for, this example serves to integrate the second and the third contribution of the dissertation, namely, incorporating rigid body dynamics into mission design, and simplifying the design of multi-phase trajectories.

The launch vehicle in this example is composed of three components: the first stage, the second stage, which also contains the payload fairing, and the payload (which is the same as in Section 7.4.1). The first stage is powered by an RD-180 engine (the one used on the Atlas V common core booster [137]), which combusts RP-1 with LOx with an oxidizer to fuel ratio of 2.56, producing a thrust of 4.152 MN. The mass flow rate corresponding to this thrust is 1,322.3 kg/s. The  $I_{sp}$  of the engine is 320.08 s. The inert mass of this stage is 33,103 kg. The center of mass of the inert structure is located 12.1 m along the roll axis from the base of its fuselage. The pitch moment of inertia of the inert structure about its center of mass is 298,750 kg-m<sup>2</sup>.

The second stage is powered by an RL10A engine (the one used on Centaur upper stage [145]), which combusts liquid hydrogen (LH2) [146] and LOx with an oxidizer to fuel ratio of 8, producing a thrust of 99.2 kN. The mass flow rate corresponding to this thrust is 22.04 kg/s. The  $I_{sp}$  of this engine is 459 s. The density of LH2 is 70.8 kg/m<sup>3</sup>. The mass of the inert structure of this stage is 8,850 kg, and its center of mass is located 6.30 m along the roll axis from its base. The pitch moment of inertia of the inert structure about its center of mass is 84,607 kg-m<sup>2</sup>.

Both engines operate at maximum thrust when their respective stages are active. Stage separation occurs at 175 s. The dimensions of the launch vehicle are illustrated in Figures 9.1 and 9.2. The radii of the launch vehicle and the propellant tanks are 1.9 m and 1.7 m, respectively.

The trajectory is solved using the same procedure as in Section 7.4.2, with the exception that the slope parameter for the RASHS framework is initially set to 1.

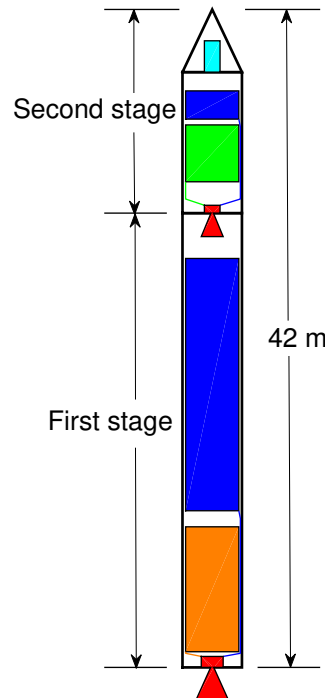
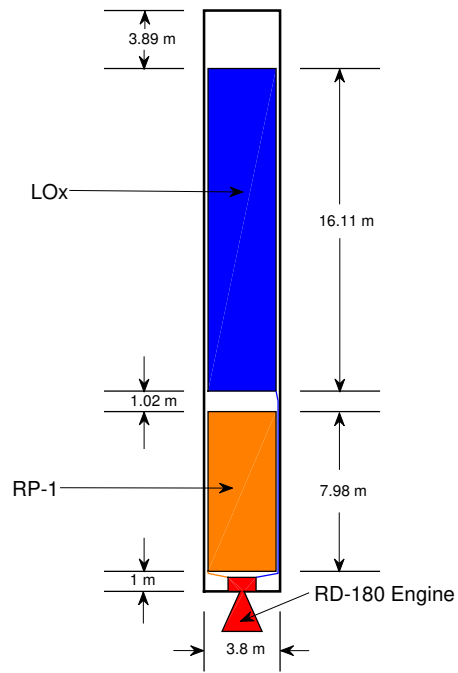


Figure 9.1. Illustration of the launch vehicle stack.

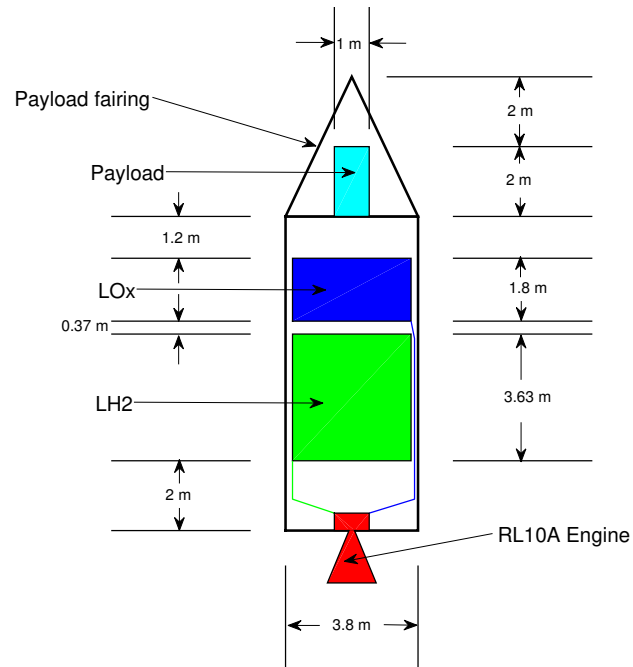
An additional continuation step is added at the end, wherein this slope parameter is varied in 1,000 equal increments to 60,000.

Figure 9.3(a) illustrates the optimized ascent trajectory. Since the second stage engine is not very powerful, it cannot be used for the climb portion of the trajectory. Instead, the first stage is predominantly used for lofting the vehicle to the orbital altitude, and the bulk of the tangential velocity is supplied by the second stage (Figure 9.4(d)). As before, since the target orbit is prograde, the vehicle pitches towards east (Figure 9.3(c)), and the corresponding thrust vectoring is shown in Figure 9.4(c). As before, the control saturates for a brief moment, which may be addressed by re-configuring the launch vehicle geometry or increasing the gimbal limits. It is also interesting to note that after stage separation, the pitch angle drops for a brief moment. The reason for this behavior is the low thrust-to-weight ratio of the second stage engine. The pitch angle drops to prevent the drop in the total velocity and to instead direct the effort towards increasing tangential velocity. As the





(a) Illustration of the first stage.



(b) Illustration of the second stage.

Figure 9.2. Illustration of each stage of the two-stage launch vehicle.

stage burns more propellant, the thrust-to-weight ratio increases, and then it becomes more economical to vector the thrust to balance the weight.

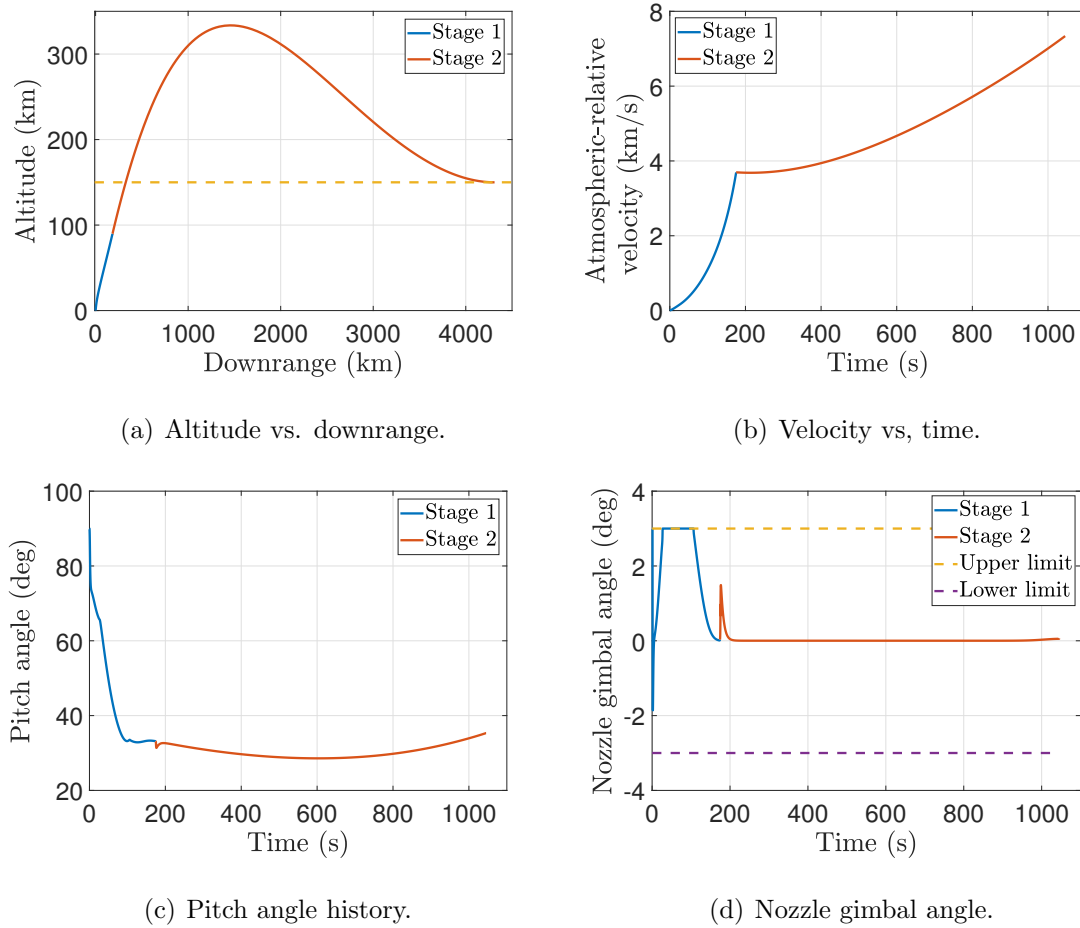


Figure 9.3. Illustration of the minimum time ascent trajectory of a two-stage launch vehicle to equatorial circular orbit. The vehicle configuration is illustrated in Figures 9.1 and 9.2, and the desired initial and final vehicle states are defined in Section 7.4.1, Table 7.1.

While this example demonstrated the effectiveness of the combined framework for launch missions, it can also be applied to glide missions. The next example combines the ablation and the rigid body frameworks and applies it to optimize the trajectory of a hypersonic glide weapon system.

### 9.3 Integration of Ablation With Rigid Body Dynamics

This section presents an example wherein the trajectory of an ablating hypersonic vehicle is optimized to maximize final velocity, while simultaneously accounting for rigid-body motion. The example involves the same mission and vehicle geometry as described in Section 7.4.2. However, in this case, the thermal protection system ablates axisymmetrically. Only the ablation of the nose of the vehicle is accounted for, and the overall geometry is constrained to be a circular paraboloid with a fixed base radius  $r_B$  of 0.5 m. Accordingly, only one extra state  $l_V$  is added to the 3-DOF rigid body equations of motion to represent the length of the vehicle.

The heat-rate at the nose of the vehicle is given by Sutton-Graves equation [143]. The nose radius that is required in the heat-rate equation is given by:

$$R_N = \frac{r_B^2}{2l_V} \quad (9.1)$$

Consequently, the dynamics for  $l_V$  is calculated as:

$$\dot{l}_V = -\frac{\dot{q}}{\rho_{TPS}Q_*} = -k\sqrt{2\rho_\infty l_V} \frac{v_\infty^3}{r_B \rho_{TPS}Q_*} \quad (9.2)$$

This equation is appended to the 3-DOF rigid body dynamics. Moreover, the heat of ablation  $Q_*$  is assumed to be 2.8628 MJ/kg. The mass, pitch moment of inertia about the center of mass, and the location of the center of mass itself become explicit functions of  $l_V$ , and are built into the equations of motion. Although the vehicle in this example is unpowered, there is still some loss in angular momentum, which is carried away by the ablation products. However, since the mass loss rate is not dramatic, the loss in angular momentum was observed to be very small. The pitch rate dynamics were fully dominated by the aerodynamic moments. As a result, the effect of loss in angular momentum was neglected.

It should also be noted that the translational dynamics is derived from Newton's second law as:

$$\mathbf{F} = m \, {}^i\dot{\mathbf{v}} + \dot{m} \, {}^i\mathbf{v} \quad (9.3)$$

Consequently,

$${}^i\dot{\mathbf{v}} = \frac{\mathbf{F} - \dot{m} \, {}^i\mathbf{v}}{m} \quad (9.4)$$

where  ${}^i\mathbf{v}$  is the inertial velocity vector. It can be seen that its dynamics is influenced by the rate of change of mass,  $\dot{m}$ . However, it was seen that the aerodynamic forces dominated this equation for the duration of the trajectory, and the contribution of  $\dot{m}$  was negligible in comparison. As a result, its contribution to the translational dynamics was neglected altogether, resulting in the following equation:

$${}^i\dot{\mathbf{v}} = \frac{\mathbf{F}}{m} \quad (9.5)$$

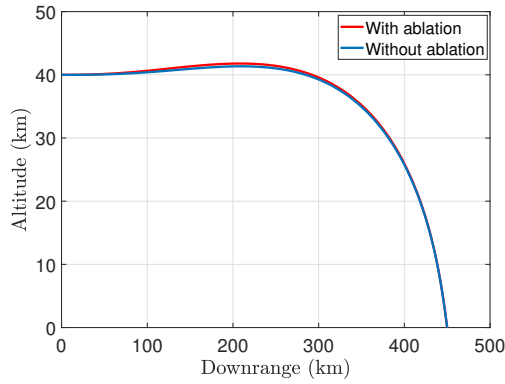
where the instantaneous value of  $m$  is used, which is a function of  $l_V$ . It should be noted that for all examples in this dissertation that involve a thrusting vehicle, Eq. (9.5) is still used despite a large  $\dot{m}$  corresponding to high propellant flow rate. However, the thrust that goes into  $\mathbf{F}$  is calculated as  $\dot{m}g_0I_{sp}$ , which is a consequence of the Tsiolkowski rocket equation [121]. This thrust equation is derived from the conservation of linear momentum of the vehicle-combustion product system, and the effect of  $\dot{m}$  is factored into it. As a result, even though Eq. (9.5) is used, it in fact represents Eq. (9.4) for this thrust equation.

The optimal trajectory is obtained by employing the same strategy for initial guess generation and continuation as in Section 7.4.2. The solution is compared with that of Section 7.4.2. It is interesting to note that the physical trajectories do not vary much (Figure 9.4(a)). This is because the solutions represent a minimum drag path as the objective is to maximize the final velocity. This path corresponds to the one wherein the vehicle encounters the least dynamic pressure. Since the dynamic pressure is only a function of velocity and altitude, the corresponding trajectory is largely unperturbed by the evolution of the geometry of the vehicle. However, the

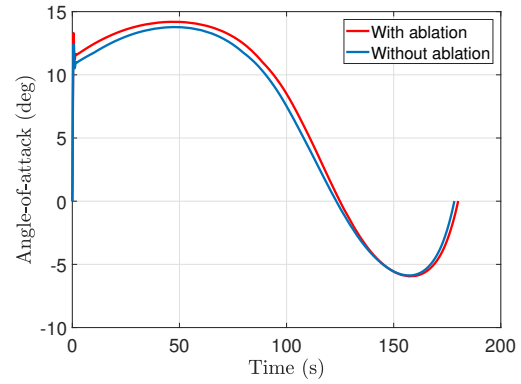
ablating vehicle's  $\alpha$  is increased throughout the mission (Figure 9.4(b)) to compensate for the degradation in its lift performance as its geometry evolves. Although the new  $\alpha$  differs only by a small margin, the elevon deflection required to achieve this is different (Figure 9.4(c)). It is seen to be higher in magnitude for the ablating vehicle because of the combined effect of the requirement to achieve a higher  $\alpha$  to compensate for the degraded lift performance, and the increase in aerodynamic stability as the shape evolves. The increased elevon deflection and the bluntness of the geometry caused by ablation results in a higher drag force along the minimum drag trajectory when compared to the non-ablating vehicle. This, combined with the reduction in mass, causes higher drag deceleration. As a consequence, the resulting final velocity is reduced (Figure 9.4(d)). The initial and the final geometries of the vehicle are shown in Figures 9.4(e) and 9.4(f) respectively. It can be seen that the ablation has caused the vehicle's length to reduce from 4 m to 3.815 m.

This example demonstrated the effectiveness of optimizing the trajectory of a rigid ablating hypersonic glide vehicle. Although only the ablation of the nose was accounted for, it is a reasonable approximation since bulk of the heat-rate occurs at this section of the geometry. In principle, the full non-axisymmetric model can be incorporated into this framework by simply adding the coordinates of the tracked points on the TPS as state variables in the 3-DOF rigid body model. However, this was not performed in this dissertation because of the associated high computational cost. Nevertheless, as stated before, this is an area to work on beyond this dissertation by leveraging advances in parallel computing technology.

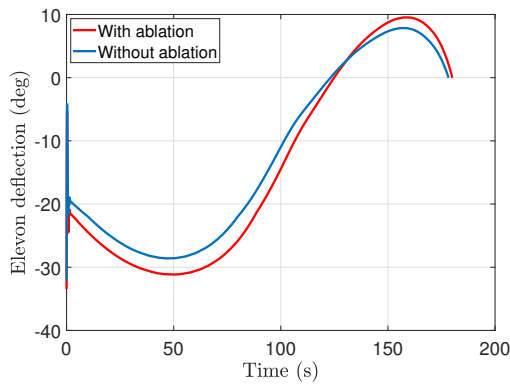
Additionally, this example assumed that the vehicle was already boosted to the required altitude and velocity. However, a truly optimal solution requires the simultaneous optimization of both the boost and the glide trajectory. The next section presents such an example, thereby combining all three contributions of the dissertation.



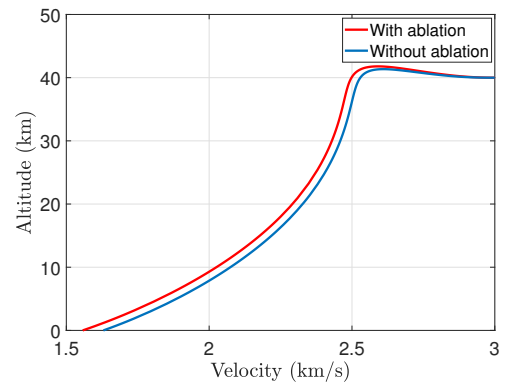
(a) Altitude vs. downrange.



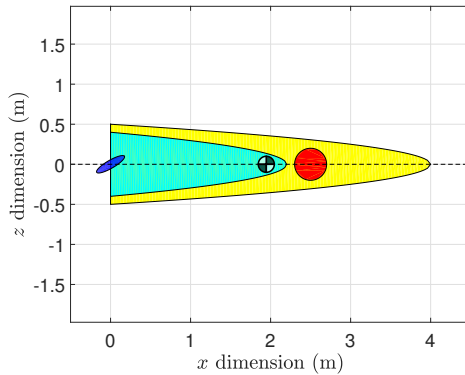
(b) Angle-of-attack history.



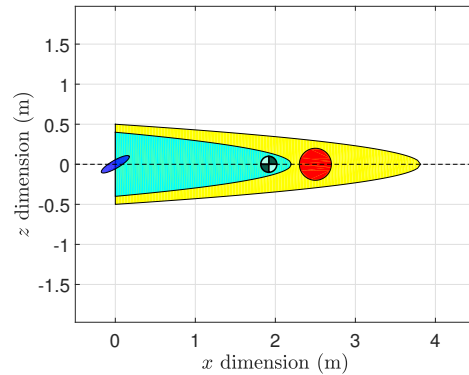
(c) Elevon deflection history.



(d) Altitude vs. velocity.



(e) Initial geometry.



(f) Final geometry.

Figure 9.4. Comparison of the maximum final velocity glide trajectories of a rigid hypothetical hypersonic glide vehicle, with and without an ablative TPS. The vehicle geometry and configuration at booster separation are illustrated in Section 7.4.2, Figures 7.11 and 7.12. The vehicle states at booster separation and the desired final states are defined in Section 7.4.2, Table 7.2.

#### 9.4 Rigid Boost-Glide Weapon System Trajectory with Spent Stage Constraints

In this example, the trajectory of a boost-glide weapon system is optimized to minimize the time of flight of the glide vehicle, measured from launch. The weapon system consists of a single-stage booster, with the glide vehicle stacked on top of it, as illustrated in Figure 9.5. The glide vehicle is the same as the one used in Section 9.3, and is protected by the same ablative TPS. As before, only the surface recession at the nose is accounted for. Moreover, after separation, the booster is constrained to impact at a specific coordinate. Also, both the booster and the glide vehicle are constrained to fly along the equator, and are subject to rigid body dynamics. As a result, this example demonstrates the integration of all three contributions of the dissertation into a single framework.

The booster is propelled by a solid rocket motor with a rod and tube propellant grain geometry [147]. This ensures a constant burn surface area for the duration of the burn, thereby maintaining the thrust at a constant value. The grain is comprised of Ammonium Perchlorate Composite Propellant (APCP) [148] that bears a density of  $1,721 \text{ kg/m}^3$ . Figure 9.6 illustrates the cross section of the booster to highlight the grain geometry.

A constant burn rate is assumed. Accordingly, the instantaneous radii of the rod ( $r_{\text{ROD}}$ ) and tube ( $r_{\text{TUBE}}$ ) sections of the grain are given by:

$$\begin{aligned} r_{\text{ROD}} &= r_{\text{ROD},0} - b_r t \\ r_{\text{TUBE}} &= r_{\text{TUBE},0} + b_r t \end{aligned} \tag{9.6}$$

where  $r_{\text{ROD},0}$  and  $r_{\text{TUBE},0}$  are the corresponding values at launch. The burn surface area is given by:

$$A_B = 2\pi (r_{\text{ROD}} + r_{\text{TUBE}}) h_{\text{GRAIN}} \tag{9.7}$$

where  $h_{\text{GRAIN}}$  is the grain height. The propellant flow rate and thrust are accordingly given as:

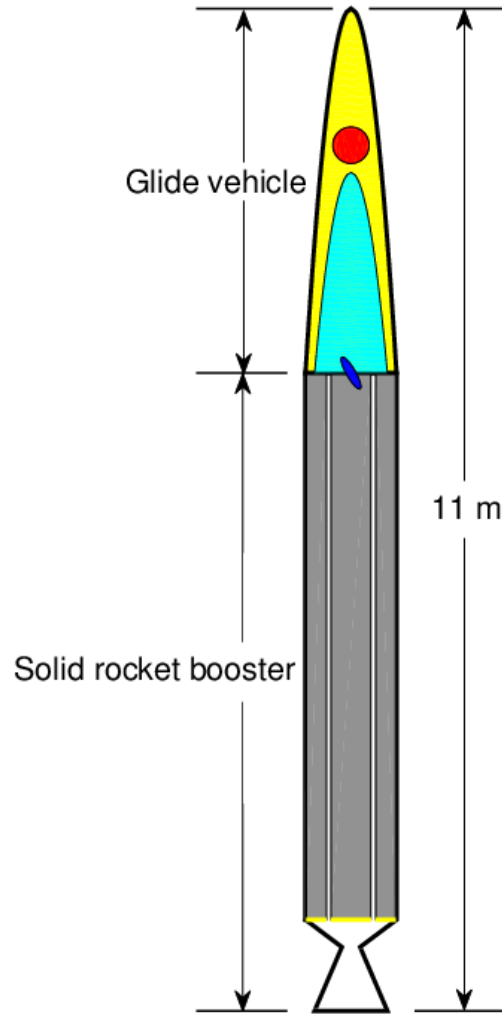


Figure 9.5. Illustration of the vehicle configuration at launch.

$$\begin{aligned}\dot{m} &= A_B \rho_{\text{APCP}} b_r \\ T &= \dot{m} g_0 I_{sp}\end{aligned}\tag{9.8}$$

In this example, it is assumed that the nozzle is designed to obtain an  $I_{sp}$  of 230 s, resulting in a constant burn rate of 3.3 mm/s. The initial radii of the rod and the tube section of the grain are 0.22 m and 0.27 m respectively. Figure 9.7 illustrates the booster geometry.



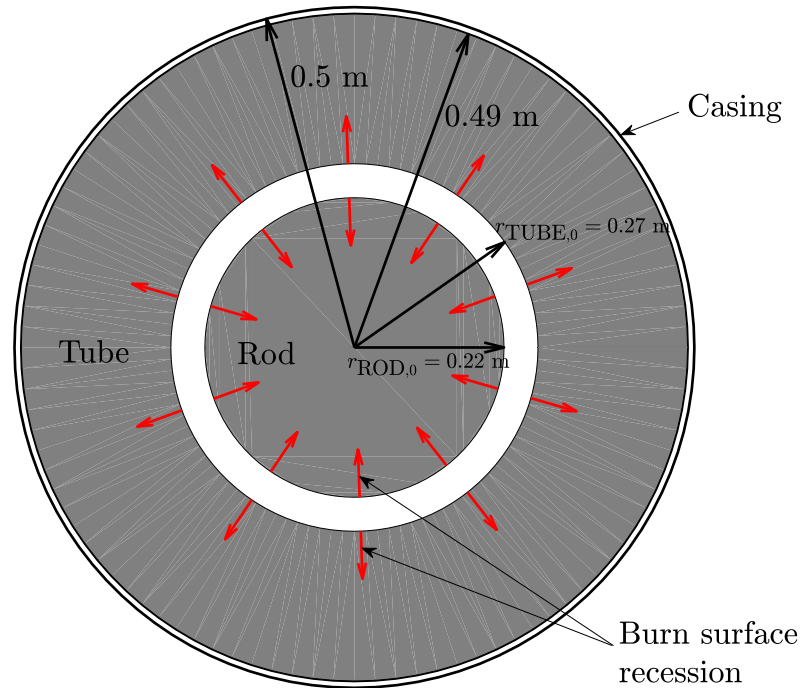


Figure 9.6. Booster cross section.

Accordingly, the thrust was calculated to be a constant value of 263 kN and the corresponding mass flow rate was calculated to be 117 kg/s. The booster burnout was calculated to occur at 60 s. The nozzle is assumed to be massless and is not affected aerodynamically. It can be gimbaled between 3 deg and  $-3$  deg. To calculate the mass, center of mass, and the corresponding pitch moment of inertia of the inert structure, the booster is modeled as a hollow cylinder with outer and inner radii 0.5 m and 0.49 m, respectively, and a density of 8,400 kg/m<sup>3</sup>. As a result, the center of mass is at the geometric center of the cylinder. The mass and pitch moment of inertia are 1,568 kg and 4,895 kg-m<sup>2</sup> respectively. During boost phase, the elevons of the glide vehicle are fixed at 0 deg deflection.

After burnout and separation, the booster is expected to tumble, resulting in upper and lower circular surfaces to be exposed to the flow. For the purpose of calculating the aerodynamic forces and moments, these surfaces are modeled as circular flat plates, thereby sealing the tubular structure of the spent booster. The aerodynamic

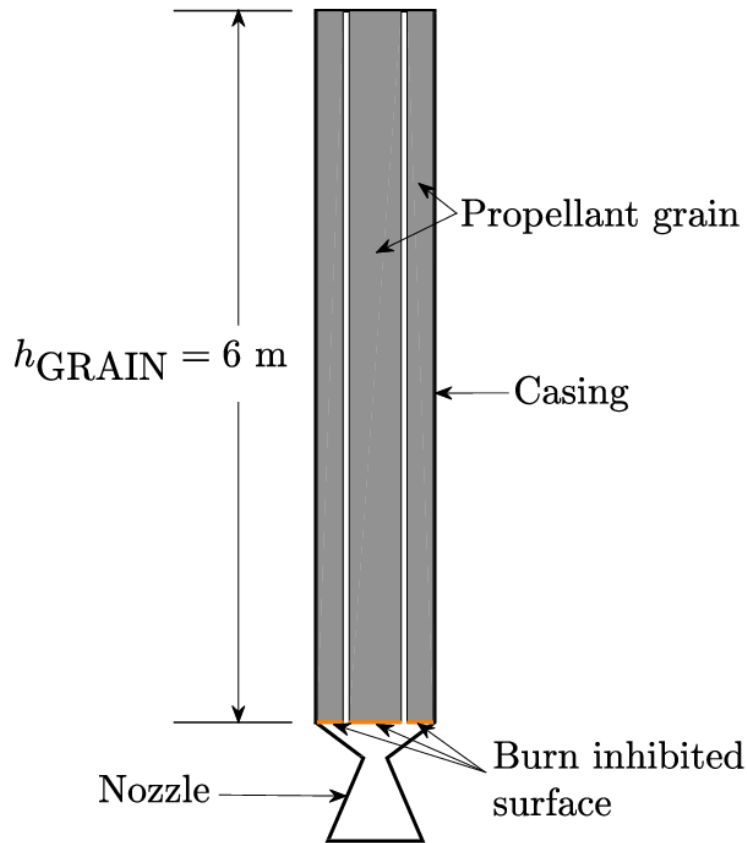


Figure 9.7. Booster configuration.

effects on the nozzle are continued to be ignored. The glide vehicle is controlled by deflecting the elevons between 20 deg and  $-20$  deg. The feedback from pitch rate to elevon deflection contains the same washout filter used in Section 7.4.2.

The mission consists of a launch from 0 deg longitude and latitude. The glide vehicle is required to strike a target located at 3.5933 deg longitude along the equator. The spent booster is required to impact at 0.5364 deg longitude on the equator. As stated before, it is required to minimize the time of flight of the glide vehicle, measured from launch. The desired initial and final conditions on the states and the booster are summarized in Tables 9.1 and 9.2 respectively. Like before, it should be noted that in the RASHS framework, the propagation of the states of the spent booster is stopped when it impacts the surface. Therefore, the final condition on its altitude

is left free. Furthermore, the velocity states are scaled by 2 km/s, and the altitude states are scaled by 60 km.

Table 9.1. Initial and final conditions on the booster states.

State	Initial Condition	Final Condition
Altitude ( $h_1$ )	0 km	Free
Longitude ( $\theta_1$ )	0 deg	0.5364 deg
Atmospheric relative velocity ( $v_1$ )	0.01 m/s	Free
Atmospheric relative flight path angle ( $\gamma_1$ )	90 deg	Free
Pitch angle ( $\Theta_1$ )	90 deg	Free
Pitch rate ( $\omega_1$ )	0 deg/s	Free

Table 9.2. Initial and final conditions of the glide vehicle states.

State	Initial Condition	Final Condition
Altitude ( $h_2$ )	0 km	Free
Longitude ( $\theta_2$ )	0 deg	3.5933 deg
Atmospheric relative velocity ( $v_2$ )	0.01 m/s	Free
Atmospheric relative flight path angle ( $\gamma_2$ )	90 deg	Free
Pitch angle ( $\Theta_2$ )	90 deg	Free
Pitch rate ( $\omega_2$ )	0 deg/s	Free
Fuselage length ( $l_V$ )	4 m	Free

The resultant TPBVP that represents the necessary conditions of optimality is solved by employing six continuation steps. The initial guess for the first iteration in step 1 is generated by propagating the state and co-state equations for 5 s using Dormand-Prince method, with the following initial guess:

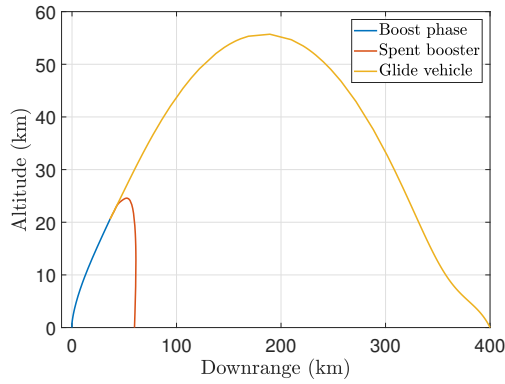
$$\begin{aligned}
\begin{bmatrix} V_1 & \gamma_1 & \hbar_1 & \theta_1 & \Theta_1 & \omega_1 \end{bmatrix}^T &= \begin{bmatrix} \frac{0.01}{2000} & \frac{\pi}{2} & 0 & 0 & \frac{\pi}{2} & 0 \end{bmatrix}^T \\
\begin{bmatrix} V_2 & \gamma_2 & \hbar_2 & \theta_2 & \Theta_2 & \omega_2 & l_V \end{bmatrix}^T &= \begin{bmatrix} \frac{0.01}{2000} & \frac{\pi}{2} & 0 & 0 & \frac{\pi}{2} & 0 & 4 \end{bmatrix}^T \\
\begin{bmatrix} \lambda_{V_1} & \lambda_{\gamma_1} & \lambda_{\hbar_1} & \lambda_{\theta_1} & \lambda_{\Theta_1} & \lambda_{\omega_1} \end{bmatrix}^T &= \begin{bmatrix} -0.1 & 0 & 0.1 & -0.1 & 0.1 & -0.1 \end{bmatrix}^T \\
\begin{bmatrix} \lambda_{V_2} & \lambda_{\gamma_2} & \lambda_{\hbar_2} & \lambda_{\theta_2} & \lambda_{\Theta_2} & \lambda_{\omega_2} & \lambda_{l_V} \end{bmatrix}^T &= \begin{bmatrix} -0.1 & 0 & 0.1 & -0.1 & 0.1 & -0.1 & -0.1 \end{bmatrix}^T
\end{aligned} \tag{9.9}$$

where the subscripts 1 and 2 reference the booster and the glide vehicle respectively. In the initial guess propagation, the slope parameter of the sigmoid in the RASHS framework is set to 1, and the value of  $\epsilon$  used as the weighting factor for the generic control variables (because the original control variables, the nozzle gimbal angle and the elevon deflection angle command, are bounded) is set to 0.1. The final boundary conditions on altitude and downrange of the glide vehicle are initially set to the corresponding final values of the propagated guess. They are then changed in 400 iterations to 30 km and 0.1797 deg respectively, noting that these are not the desired final values. During this step, the final boundary condition on the longitude of the booster is set free. In the second continuation step, the altitude of the glide vehicle is brought down to the desired value of 0 km in 400 iterations. In the third continuation step, the final boundary condition on the longitude of the glide vehicle is brought to the desired value of 3.5933 deg in 400 iterations. In the fourth continuation step, the final boundary condition on the longitude of the booster is fixed and is brought to the desired value of 0.5364 deg in 400 iterations. In the fifth continuation step, the slope parameter of the sigmoid function in the RASHS framework is changed to 10,000 in 1,000 iterations. In the sixth and final continuation step, the value of  $\epsilon$  is changed to 0.0001 in 1,000 iterations. The solution of the final iteration in this step is the desired solution of the optimization problem.

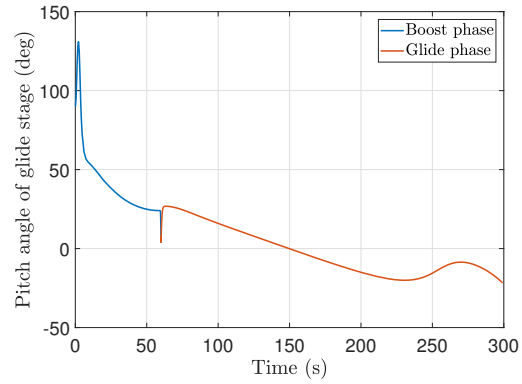
Figure 9.8(a) illustrates the time-optimal trajectory. It is desirable to have the burnout occur as close to the target as possible. This will ensure that the unpowered glide portion of the trajectory is short. It is also desirable to fly level at burnout so

that the ground speed of the glide vehicle just after separation is maximized, thereby minimizing the time-of-flight of the mission. However, the constraint on the impact location of the spent booster is required to be satisfied as well. In a purely ballistic flight, the booster would overshoot the constraint. To prevent this, the boost-glide stack performs two critical maneuvers. In the first one, the vehicle flies west away from the target just after launch and then pitches back towards it, as evidenced by the initial pitch maneuver to a value of about 131 deg (Figures 9.8(b) and 9.8(c)). In the second critical maneuver, the boost-glide stack abruptly pitches down just before booster separation. This imparts an angular velocity to the vehicle, which is carried over by the spent booster after separation. The spent booster tumbles until its pitch rate damps out, as predicted by piston theory, and settles at a pitch angle of  $-468$  deg (Figure 9.8(c)), which is essentially  $-108$  deg. This orientation is such that its body lift enables it to “glide” back to the designated impact location. Since the spent booster possesses a neutral aerodynamic stability because its center of mass is located at its geometric center at all times (discounting the nozzle) and the aerodynamic forces are predicted by assuming that it is a sealed cylinder, its pitch angle after pitch rate damping is maintained for the duration of the trajectory. The abrupt pitch motion is also carried over by the glide vehicle, as evidenced by the sharp decrease in its pitch angle at separation (Figure 9.8(b)). In addition to ensuring that the impact constraint on the spent booster is satisfied, the pitch rate that is required at separation is also optimized to minimize the time-of-flight of the glide vehicle.

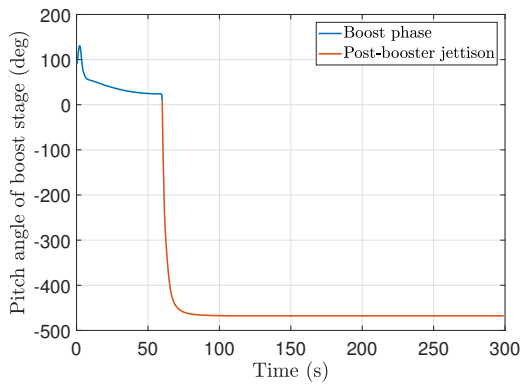
Figure 9.8(d) illustrates the history of the nozzle gimbal angle and the elevon deflection angle to accomplish all of this. The abrupt increase in the gimbal angle in the positive direction before booster separation results in the desired pitch rate at separation. This also causes an abrupt drop in the angle-of-attack of the boost-glide stack. When the glide vehicle eventually separates, it carries over this angle-of-attack. However, since the glide vehicle is aerodynamically stable, the high negative angle-of-attack (Figure 9.8(e)) that was carried over generates a high restoring aerodynamic moment that would cause the pitch angle to spring back up and adversely oscillate.



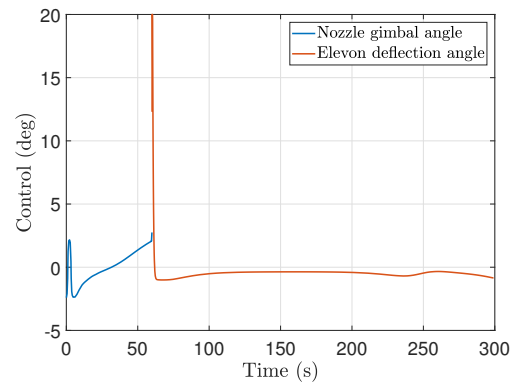
(a) Altitude vs. downrange.



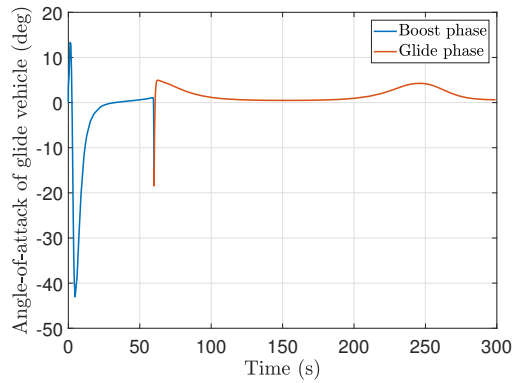
(b) Pitch angle of glide vehicle.



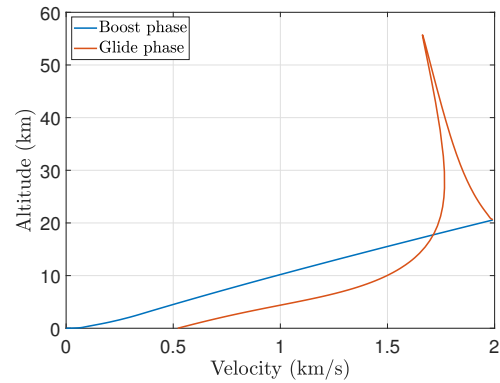
(c) Pitch angle of booster.



(d) Control histories.



(e) Angle-of-attack of glide vehicle.



(f) Altitude vs. velocity of glide vehicle.

Figure 9.8. Illustration of the minimum time trajectory of a hypothetical rigid boost glide weapon system with constraints on the impact location of the spent booster. The glide vehicle is protected by an ablative TPS, and its initial geometry is illustrated in Section 7.4.2, Figures 7.11 and 7.12. The boost-glide stack at launch is illustrated in Figure 9.5, and the booster configuration is illustrated in Figures 9.6 and 9.7. The desired initial and final states of the booster and the glide vehicle are defined in Tables 9.1 and 9.2 respectively.

This is countered by deflecting the elevons accordingly, as indicated by the spike in the positive direction just after separation. The glide vehicle largely flies with a small positive angle-of-attack after separation to avoid undershooting the target. It impacts the target with a velocity of 521 m/s (Figure 9.8(f)). For the duration of the trajectory, the TPS at the nose section of the glide vehicle ablates. The optimal trajectory accounts for the shape change as well. Figure 9.9 illustrates the glide vehicle geometry at launch and impact. Although the shape change is not dramatic, this example demonstrates the inclusion of its effect into the integrated conceptual mission design framework.

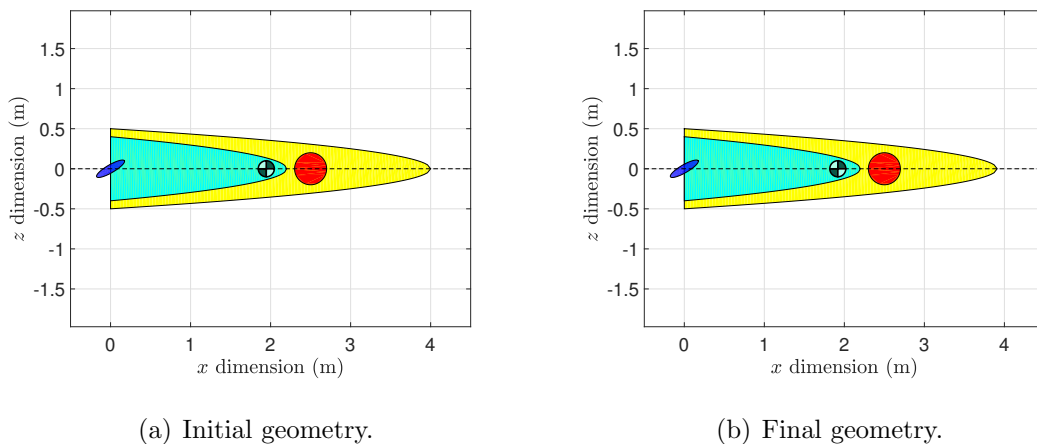


Figure 9.9. Illustration of initial and final geometry of the glide vehicle.

## 9.5 Summary

This chapter demonstrated the integration of the three contributions of the dissertation into a unified conceptual hypersonic mission design framework. The integrated framework serves as a powerful tool to perform higher fidelity conceptual design of complex hypersonic missions than previously possible, thereby substantially advancing the state-of-the-art. For instance, the final example involved the design an optimal trajectory of an ablating boost-glide rigid body weapon system, with constraints on

the impact location of the spent booster. The optimal solution of this example highlighted the complex coupling of the post-jettison trajectory of the booster with that of the boost phase and glide vehicle and the evolution of the glide vehicle geometry caused by ablation. The integration of the rigid body dynamics enabled the analysis of intricate details such as the optimal pitch rate at separation to ensure that the time of flight of the glide vehicle is minimized while simultaneously satisfying the impact constraint of the spent booster. Such an analysis would not have been possible even if the design was performed with the contributions of the dissertation independently without combining them.





## 10. SUMMARY AND FUTURE WORK

### 10.1 Summary of Contributions

The contributions of this dissertation substantially advanced the state-of-the-art in conceptual hypersonic mission design by:

1. incorporating the effects of ablative shape change into conceptual mission design,
2. incorporating rigid body dynamics into trajectory design, and
3. simplifying the design of multi-phase trajectories.

These contributions were largely applicable to slender hypersonic vehicles used in military applications, which are typically designed to fly at very high velocities in the hypersonic regime and impact the target with high kinetic energy. Additionally, these contributions were combined into a unified mission design framework.

The key knowledge gained from these contributions was that:

1. the maximum achievable terminal energy can be dramatically reduced when compared to the state-of-the art conceptual design process, and
2. the control history necessary to follow the maximum terminal energy trajectory can be altered significantly, which might in turn bear consequence on the design of the control actuators.

The other important accomplishment of this dissertation was the demonstration of the ability to even solve the highly coupled multi-phase trajectory optimization problems using indirect methods, while simultaneously accounting for the influence of TPS ablation and rigid body dynamics. These types of coupled problems have never

been solved before (without substantial simplifications to decouple the flight phases) using the state-of-the-art, which predominantly employs direct methods because of the ease of implementation, despite their inability to guarantee the optimality of the solution. As a result, the very ability to employ indirect methods to solve for optimal trajectories that are comprised of multiple phases of flight while also accounting for the effects of ablation of the TPS and rigid body dynamics is a substantial advancement in the state-of-the-art. Furthermore, since the indirect methods are built on a strong foundation of the calculus of variations, the calculated trajectories are guaranteed to be at least locally optimal.

The contributions of this dissertation were presented in several conferences and also resulted in a journal publication, which are listed in Appendix D, along with planned future publications and other publications not directly related to this dissertation. The summary of each contribution is provided below.

#### **10.1.1 Incorporation of Ablative Shape Change into Conceptual Hypersonic Mission Design**

This contribution integrated the effects of ablative shape change into conceptual mission design. This contribution deals with hypersonic vehicles with an ablative TPS, whose geometry evolves during flight. This contribution enables the design of optimal trajectories that account for the coupling between the evolution of vehicle geometry and the flight dynamics. Ablation was modeled by correlating the surface recession of a set of points on the TPS to the local heat-rate through the heat of ablation. The local heat-rate was calculated through a partially analytical technique that enables the use of axisymmetric solutions for arbitrary 3-D bodies. The coordinates of these tracked points were added as state variables in the flight dynamic equations. A NURBS surface interpolation was performed on these points to represent the instantaneous geometry.

An optimal trajectory was designed using this integrated model. The scope for extensive analysis was limited for the fully non-axisymmetric model because of associated computational cost. Instead, axisymmetric ablation was assumed to perform detailed conceptual mission design. The assumption of axisymmetric ablation is reasonable for slender vehicles used in this dissertation because bulk of the heat-rate occurs at the nose. Moreover, the vehicle may be assumed to perform periodic roll maneuvers, thereby allowing the geometry to remain axisymmetric.

The integrated axisymmetric ablation model enabled trade studies for the characterization of optimal properties of future TPS materials. The effect of the heat of ablation and the TPS density on mission performance was analyzed. In general, a higher  $Q_*$  and  $\rho_{TPS}$  is desirable from a mission perspective. However, a TPS with high  $Q_*$  ablates less and is therefore required to have a very high heat capacity to prevent the conduction of heat into the subsystems of the vehicle. Additionally, a high TPS density results in a heavier vehicle, thereby requiring a more powerful booster to boost it to hypersonic flight. Therefore, a trade-off between mission and TPS performance is necessary.

Although the optimal physical trajectories in some cases were observed to differ only by a small amount from those that neglected ablation, the control histories were more aggressive for the ablating vehicle. Since most cost functionals used in hypersonic missions can be translated to finding a path that minimizes/maximizes drag, the corresponding optimal path is largely independent of the shape evolution. This is because the minimum-drag path is dictated by the dynamic pressure, which is not an explicit function of the geometry. However, from a controls stand point, it is clear that shape evolution cannot be ignored.

### 10.1.2 Incorporation of Rigid Body Dynamics into Trajectory Design

This contribution incorporated rigid body dynamics into the indirect trajectory optimization framework. Only pitch dynamics were incorporated, thereby restricting

the flight to be planar. Even this simplified dynamic system was seen to pose numerical challenges in the indirect framework. These challenges were a consequence of the stiffness of the pitch rate dynamic equation because the time frame of the pitch motion is very small when compared to the translational states. The stiffness was addressed by feeding back pitch rate to the control input through a washout filter.

Despite accounting only for planar motion, substantial insights were gained during conceptual mission design. For instance, it enabled the direct study of the influence of vehicle mass distribution and control surface configuration on mission performance, which was not previously possible with point-mass dynamics. The rigid body analysis was also extended to vehicles with rocket propulsion, and jet damping was factored into the flight dynamics model. The optimal nozzle gimbal angle history provided insights into the design process. For instance, in the examples presented in this dissertation, the gimbal angle saturated, thereby suggesting the necessity to alter the vehicle geometry or the nozzle gimbal range.

### **10.1.3 Simplification of Trajectory Optimization of Multi-Phase Systems**

This contribution substantially simplified the design of optimal trajectories for multi-phase aerospace systems in the indirect framework. The optimal control problem of such systems involves piecewise dynamics and cost functional. Consequently, the necessary conditions of optimality result in an MPBVP in a system of DAEs, which is difficult to solve because the existing numerical approaches are required to be initiated with a guess that is close to the actual solution for all phases of flight. This problem was addressed by reducing the original MPBVP to a TPBVP by converting the piecewise dynamics and cost functional to  $c^1$  continuous using saturation functions. Consequently, the interior boundary conditions that occur at the transitions of flight phases were automatically enforced as a consequence of the new smooth equations of motion and cost functional. In essence, the numerical algorithm

was only required to enforce the end-point boundary conditions, thereby reducing the original MPBVP to a TPBVP. This novel methodology was named the “Relaxed Autonomously Switched Hybrid System” (RASHS) approach.

This approach enabled the easy design of a seven-phase ascent trajectory of the Atlas-V 411 launch vehicle, a four-phase Mars EDL trajectory of an MSL-like vehicle, and a two-phase boost-glide trajectory with a constraint on the impact location of the spent booster. The RASHS approach also enabled mission trade studies involving the boost-glide system.

#### **10.1.4 Unified Conceptual Hypersonic Mission Design Framework**

Although not officially listed as a contribution, this work integrated the stated three contributions into a single framework. Examples involved the design of a two-stage launch vehicle with rigid body dynamics, the design of a glide trajectory of an ablating hypersonic vehicle while accounting for rigid body dynamics, and the design of a boost-glide trajectory with constraints on the impact location of the spent booster, while accounting for rigid body motion and the ablation of the TPS of the glide vehicle.

This integrated framework enabled the design of optimal multi-phase trajectories that accounted for complex coupling between shape evolution and rigid body motion in a constrained multi-body environment. This was made possible not just by the individual contributions of the dissertation themselves, but by combining them into a single design framework, thereby greatly advancing the state-of-the-art in conceptual hypersonic mission design.

## **10.2 Future Work**

While the fidelity of conceptual hypersonic mission design was substantially improved by the contributions of this dissertation, certain aspects of propulsive hypersonic missions remain to be investigated. For instance, a more sophisticated propul-

sion model can be incorporated into orbital launch examples by accounting for atmospheric effects on the engine performance. Moreover, high-mass reentry missions often involve supersonic retropropulsion. The unified framework in this dissertation can benefit from higher fidelity retropropulsion models while designing such missions. In fact, optimal trajectories have been generated for human Mars entry missions using a high fidelity supersonic retropropulsion model [149]. This model may be integrated into the unified mission design framework. Moreover, several slender hypersonic vehicles are typically powered by scramjets. Trajectory optimization has been successfully performed using parametric scramjet cycle analysis in the indirect framework [150]. This work can also be integrated into the unified framework.

Additionally, a fictitious Mach number was employed when the vehicle operated in the subsonic regime, as was the case in the launch and boost-glide missions. A more sophisticated subsonic aerodynamic model may be implemented into the design framework to calculate more accurate trajectories. However, these trajectories are not expected to be altered by much as a result of this sophisticated model because the vehicle operates in the subsonic regime only for a brief period.

Also, the continuation process used in this dissertation involved a certain amount of trial and error. A more sophisticated method that adaptively predicts the next continuation step to guarantee convergence has been recently developed [151] and can be incorporated into the design framework presented in this dissertation.

Moreover, the mission design framework developed in this dissertation assumes a deterministic model for the vehicle and the atmospheric properties. However, there exists considerable uncertainty in planetary atmospheres. For instance, the uncertainty in the atmospheric properties of Mars makes heavy mass atmospheric entry that is typical of human-class missions challenging because the vehicles used in such missions are not maneuverable enough to counter the resultant perturbations from the optimal reference trajectory. Therefore, it is required to extend the mission design framework to design trajectories that are robust to these uncertainties. Prior work exists that enables the rapid design of robust trajectories within an indirect optimiza-

tion framework by utilizing an augmented cost functional to capture the worst case scenario associated with each dispersion [152]. This approach may be integrated into the unified mission design framework developed in this dissertation.

Furthermore, there exist hypersonic missions wherein the vehicle shape change is effected by processes other than ablation. For instance, heavy mass Mars entry vehicle concepts employ hypersonic inflatable aerodynamic decelerators (HIADs), which deform in-flight because of aerodynamic stress. For such systems, the vehicle shape may again be modeled by the same method explained in this dissertation with the difference that the movement of these points is governed by aerothermoelastic processes instead of ablation. Such processes have been modeled by solving the compressible Navier-Stokes equations with Menter's shear stress transport (SST) turbulence model [153]. However, such models are computationally intensive and hence, are not conducive for trajectory optimization during conceptual mission design. As a result, the unified design framework developed in this dissertation would benefit from simplified models that offer reasonable fidelity when designing missions involving inflatable decelerator systems.

The scope for improvement specific to each of the three contributions of this dissertation is presented below. These may also be incorporated into the unified framework to further advance the state-of-the-art in conceptual hypersonic mission design.

### **10.2.1 Incorporation of Ablative Shape Change into Conceptual Hypersonic Mission Design**

The 3-D heat-rate model incorporated in this dissertation is more accurate for slender hypersonic vehicles used in weapon systems. The accuracy of the predicted heat-rate reduces as the vehicle ablates and the geometry becomes blunt. The reduction in accuracy remains to be characterized systematically.



The heat of ablation is a data-correlation parameter. While it has a relatively constant value for teflon-like materials that were used for validation, it varies for other TPS materials. A variable  $Q_*$  model may be developed that is a function of the TPS wall temperature. Consequently, a variable wall temperature model needs to be implemented with the focus of having minimal impact on computational speed, while maintaining reasonable accuracy. Since the wall temperature also dictates the TPS thickness (in addition to the ablative surface recession rate), a more informed design decision about the TPS thickness can be made. This may be accomplished through a multidisciplinary design optimization, wherein both the trajectory and the TPS thickness can be simultaneously optimized to prevent burn-through resulting from excessive surface recession and conduction of heat into the subsystems resulting from excessive wall temperature.

Also, only 2-D trajectories were designed within the ablation framework. However, several military hypersonic missions involve the enforcement of complex interior-point constraints (such as avoiding flight over friendly territory). This would require the design of 3-D trajectories. To satisfy these constraints, the vehicle will be required to maneuver more, thereby remaining lower in the atmosphere to leverage the higher dynamic pressure. This will result in higher heating and resultant ablation. Consequently, the optimal trajectories are expected to differ even more from those of a non-ablating vehicle. However, just the generation of 2-D trajectories with non-axisymmetric ablation was seen to involve a substantial computational cost. This may be mitigated by leveraging advances in parallel computing technology and algorithms. In fact, constrained trajectory optimization using a 3-DOF point-mass flight dynamics model has been successfully performed by taking advantage of parallel computing on graphics processing units (GPUs) [154]. The ablation framework will greatly benefit from this work.

Finally, this dissertation assumed a calorically perfect gas that bears a constant specific heat ratio ( $\gamma$ ). However, hypersonic flow is associated with high enthalpy, leading to a calorically imperfect gas with a variable specific heat ratio resulting from

the excitation of the vibrational modes of the molecules. This will in turn alter the boundary layer edge conditions. Since the temperature distribution about the fuselage is non-uniform, the value of  $\gamma$  also varies locally, thereby leading to variations in the local edge pressure from those predicted by a calorically perfect gas model. This in turn alters the 3-D heat-rate distribution and aerodynamic force acting on the vehicle. This also leads to a shift in the center of pressure, thereby modifying the aerodynamic stability. Analytical models exist that predict the variation of the heat capacities and specific heat ratio as a function of temperature. However, this requires the knowledge of the wall temperature. Consequently, the calorically imperfect gas model may be implemented in conjunction with this variable wall temperature model. For the purpose of implementing such a higher fidelity aerothermal model, MINIVER (Miniature Version) aerothermal code [155–158], a NASA-developed tool that models post-shock and local flow properties at different angles of attack, might be employed.

### 10.2.2 Incorporation of Rigid Body Dynamics into Trajectory Design

The main scope for improvement in this contribution is its extension to 6-DOF flight dynamic model that enables the design of optimal 3-D trajectories that account for rigid body motion. The 6-DOF dynamics will result in numerical stiffness in the yaw motion as well. This can be addressed by a similar washout filter in the feedback path from yaw rate to the control inputs that are primarily responsible for yaw motion. The major challenge of incorporating 6-DOF dynamics in the indirect framework is that at each mesh point, the solution of a large number of control variables is required to be simultaneously calculated. Since the control equations are almost always transcendental, the solution requires the utilization of numerical methods, thereby resulting in a higher computational cost. This may be addressed by an approach wherein instead of explicitly solving for the optimal control law at every mesh point, the control variables themselves are added as states [159]. The corresponding dynamics may be obtained by taking a total time derivative of the

control equations. The corresponding boundary conditions are simply defined by these control equations themselves, which may be enforced either at the initial or the final time. The advantage of this approach is that it involves solving the control equations only at one of the end-points of the trajectory, as opposed to every mesh point.

Another area of improvement is the incorporation of a more sophisticated model for the control surfaces. Such a model would have the ability to capture complex phenomena associated with shock interactions, which is not possible in the current framework because of the inherent assumptions in the modified Newtonian flow theory.

Finally, the fidelity of conceptual mission design within the rigid body framework may be further improved by introducing structural vibration models. For instance, when the control surfaces are positioned in the aft portion of the vehicle, the resultant aerodynamic moment will induce cantilever-like deformations on the vehicle that can significantly alter the flight characteristics and control history, which are further exacerbated by the elevated aerodynamic forces inherent in hypersonic flight. This requires the inclusion of aeroelasticity models into the design framework. There is substantial literature on this subject for conceptual design from a control system design perspective [40, 42, 43, 45–47, 50, 51]. Further investigation may be performed to incorporate such a model for conceptual mission design.

### 10.2.3 Simplification of Trajectory Optimization of Multi-Phase Systems

The RASHS approach presented in this dissertation is not capable of enforcing conditions at the boundary of the flight phases that are not part of the switching conditions. For example, consider an EDL trajectory wherein the parachute deployment phase is triggered when the switching condition  $v < v_P$  is satisfied. At the phase transition,  $v$  is required to be equal to  $v_P$  and the states are required to be continuous. The RASHS approach implicitly ensures that these conditions are satisfied. However,

it is incapable of enforcing an additional constraint at parachute deployment, such as  $\gamma = -10$  deg. Incorporation of such a capability is a potential area of improvement in the RASHS framework.

Additionally, the RASHS approach assumes that the flight phases occur in a predetermined sequence, and the switching conditions are carefully chosen to guarantee this. In order to explicitly enforce the phase sequence, additional protection conditions are required, which can be viewed as a combination of AND and OR logics. The RASHS approach can be modified to incorporate these conditions and approximate them using saturation functions. Preliminary investigation has already been performed on this subject, and is explained in Appendix C.

## REFERENCES

## REFERENCES

- [1] Justin Bronk. Speed is the new stealth: The sr-72 challenges the future at mach 6. <https://rusi.org/commentary/speed-new-stealth-sr-72-challenges-future-mach-6>, November 2013. Online; retrieved 13 April 2018.
- [2] Neil G. Kacena. Stealth: An example of technology's role in the american way of war. Technical Report 19970908 012, Air War College, April 1995.
- [3] Carl von Clausewitz. *On War*. Princeton University Press, 1984.
- [4] Michael J. Grant. *Rapid Simultaneous Hypersonic Aerodynamic and Trajectory Optimization for Conceptual Design*. PhD thesis, Georgia Institute of Technology, 2012.
- [5] J. R. Olds. The suitability of selected multidisciplinary design and optimization techniques to conceptual aerospace vehicle design. pages 21–23, Cleveland, OH, September 1992. 4th AIAA/USAF/NASA/OAI Symposium on Multidisciplinary Analysis and Optimization.
- [6] R. D. Braun, R. W. Powell, R. A. Lepsch, D. O. Stanley, and I. M. Kroo. Comparison of two multidisciplinary optimization strategies for launchvehicle design. *Journal of Spacecraft and Rockets*, 32(3), 1995.
- [7] N. F. Brown and J. R. Olds. Evaluation of multidisciplinary optimization techniques applied to a reusable launch vehicle. *Journal of Spacecraft and Rockets*, 43(6), 2006.
- [8] R. E. Perez, H. H. T. Liu, and K. Behdinan. Evaluation of multidisciplinary optimization approaches for aircraft conceptual design. Albany, NY, August-September 2004. 10th AIAA/ISSMO Multidisciplinary Analysis and Optimization Conference.
- [9] Robert D. Braun. *Collaborative Optimization: An architecture for large-scale distributed design*. PhD thesis, Stanford University, Department of Aeronautics and Astronautics, May 1996.
- [10] J. Sobieszczanski-Sobieski, J. S. Agte, and R. R. Sandusky. Bi-level integrated system synthesis (bliss). Technical Report NASA-TM-1998-208715, National Aeronautics and Space Administration, 1998.
- [11] L. F. Rowell, R. D. Braun, J. R. Olds, and R. Unal. Multidisciplinary conceptual design optimization of space transportation systems. *Journal of Aircraft*, 36(1), 1999.
- [12] D. Doman and W. Blake. Ablation modeling for dynamic simulation of reentry vehicles. Reston, Va, 2006. American Institute of Aeronautics and Astronautics.

- [13] J. A. Dec and R. D. Braun. An approximate ablative thermal protection system sizing tool for entry system design. Reno, Nevada, 2006. 44th AIAA Aerospace Sciences Meeting and Exhibit.
- [14] L. Steg. Materials for re-entry heat protection of satellites. *ARS Journal*, 30:815–822, Sep. 1960.
- [15] Mark E. Ewing, Travis S. Laker, and David T. Walker. Numerical modeling of ablation heat transfer. Technical report, National Aeronautics and Space Administration.
- [16] R. M. Kendall, E. P. Bartlett, R. A. Rindal, and C. B. Moyer. An analysis of the coupled chemically reacting boundary layer and charring ablator, part i, summary report. Technical Report NASA CR-1060, National Aeronautics and Space Administration, June 1968.
- [17] C. B. Moyer and R. A. Rindal. An analysis of the coupled chemically reacting boundary layer and charring ablator, part ii, finite difference solution for the in-depth response of charring materials considering surface chemical and energy balance. Technical Report NASA CR-1061, National Aeronautics and Space Administration, June 1968.
- [18] E. P. Bartlett and R. M. Kendall. An analysis of the coupled chemically reacting boundary layer and charring ablator, part iii, nonsimilar solution of the multicomponent laminar boundary layer by an integral matrix method. Technical Report NASA CR-1062, National Aeronautics and Space Administration, June 1968.
- [19] E. P. Bartlett, R. M. Kendall, and R. A. Rindal. An analysis of the coupled chemically reacting boundary layer and charring ablator, part iv, a unified approximation for mixture transport properties for multicomponent boundary-layer applications. Technical Report NASA CR-1063, National Aeronautics and Space Administration, June 1968.
- [20] R. M. Kendall. An analysis of the coupled chemically reacting boundary layer and charring ablator, part v, a general approach to the thermochemical solution of mixed equilibrium-nonequilibrium, homogeneous or heterogeneous systems. Technical Report NASA CR-1064, National Aeronautics and Space Administration, June 1968.
- [21] R. A. Rindal. An analysis of the coupled chemically reacting boundary layer and charring ablator, part vi, an approach for characterizing charring ablator response with in-depth coking reactions. Technical Report NASA CR-1065, National Aeronautics and Space Administration, June 1968.
- [22] Richard D. Mathieu. Mechanical spallation of charring ablators in hyperthermal environments. *AIAA Journal*, 2(9):1621–1627, September 1964.
- [23] Gerald W. Russell and Forrest Strobel. Modeling approach for intumescent charring heatshield materials. *Journal of Spacecraft and Rockets*, 43(4):739–749, July-August 2006.
- [24] M. E. Ewing and T. S. Laker. Insulation thermal response and ablation code, itrac version 1.0, theory manual. Technical Report MAN000004, ATK Launch Systems Manual, Promontory, UT, March 2009.

- [25] M. E. Ewing, T. S. Laker, and P. H. Bauer. Insulation thermal response and ablation code, itrac version 1.0, theory manual. Technical Report MAN000005, ATK Launch Systems Manual, Promontory, UT, March 2009.
- [26] T. S. Laker and M. E. Ewing. Insulation thermal response and ablation code, itrac version 1.0, theory manual. Technical Report MAN000006, ATK Launch Systems Manual, Promontory, UT, March 2009.
- [27] C. B. Moyer and M. R. Wool. Users manual, aerotherm charring material thermal response and ablation program, version 3, volume 1, program description and sample problems. Technical Report AFRPL-TR-70-92, Air Force Rocket Propulsion Laboratory, Edwards AFB, CA, April 1970.
- [28] C. A. Powers and R. M. Kendall. Users manual, aerotherm chemical equilibrium (ace) computer program. Technical report, Aerotherm Corporation, Mountain View, CA, May 1969.
- [29] A. J. Amar, B. F. Blackwellz, and J. R. Edwards. One-dimensional ablation using a full newtons method and finite control volume procedure. 9th AIAA/ASME Joint Thermophysics and Heat Transfer Conference, June 2006.
- [30] Y.-K. Chen and Frank S. Milos. Ablation and thermal response program for spacecraft heatshield analysis. *Journal of Spacecraft and Rockets*, 36(3):475–483, May-June 1999.
- [31] Y.-K. Chen and Frank S. Milos. Two-dimensional implicit thermal response and ablation program for charring materials. *Journal of Spacecraft and Rockets*, 38(4):473–481, July-August 2001.
- [32] Y.-K. Chen and Frank S. Milos. Three-dimensional ablation and thermal response simulation system. 38th AIAA Thermophysics Conference, June 2005.
- [33] Frank S. Milos and Y.-K. Chen. Two-dimensional ablation, thermal response, and sizing program for pyrolyzing ablators. *Journal of Spacecraft and Rockets*, 46(6):1089–1099, November-December 2009.
- [34] Basil Hassan, David Kuntz, and Donald Potter. Coupled fluid/thermal prediction of ablating hypersonic vehicles. Reno, NV, January 1998. 36th AIAA Aerospace Sciences Meeting and Exhibit.
- [35] Y.-K. Chen, W. D. Henline, and M. E. Tauber. Mars pathfinder trajectory based heating and ablation calculations. *Journal of Spacecraft and Rockets*, 32(2):225–230, March-April 1995.
- [36] David W. Kuntz, Basil Hassan, and Donald L. Potter. Predictions of ablating hypersonic vehicles using an iterative coupled fluid/thermal approach. *Journal of Thermophysics and Heat Transfer*, 15(2):129–139, April-June 2001.
- [37] Michael J. Grant and Robert D. Braun. Rapid indirect trajectory optimization for conceptual design of hypersonic missions. *Journal of Spacecraft and Rockets*, 52:177–182, 2015.
- [38] Jiang Zhao, Rui Zhou, and Xuelian Jin. Reentry trajectory optimization for hypersonic vehicle satisfying complex constraints. *Chinese Journal of Aeronautics*, 26:1544–1553, Dec. 2013.



- [39] Timothy R. Jorris. *Common Aero Vehicle Autonomous Reentry Trajectory Optimization Satisfying Waypoint and No-Fly Zone Constraints*. PhD thesis, Air Force Institute of Technology, 2007.
- [40] Karl D. Bilimoria and David K. Schmidt. Integrated development of the equations of motion for elastic hypersonic flight vehicles. *Journal of Guidance, Control, and Dynamics*, 18(1):73–81, January-February 1995.
- [41] Takeshi Tsuchiya, Yoichi Takenaka, , and Hideyuki Taguchi. Multidisciplinary design optimization for hypersonic experimental vehicle. *AIAA Journal*, 45(7):1655–1662, July 2007.
- [42] N. J. Falkiewicz, C. E. S. Cesnik, M. A. Bolender, and D. B. Doman. Thermoelastic formulation of a hypersonic vehicle control surface for control-oriented simulation. Chicago, IL, August 2009. AIAA Guidance, Navigation, and Control Conference.
- [43] Jennifer Heeg, Michael G. Gilbert, and Anthony S. Pototzky. Active control of aerothermoelastic effects for a conceptual hypersonic aircraft. *Journal of Aircraft*, 30(4):200–208, 1993.
- [44] M. G. Gilbert, J. Heeg, A. S. Pototzky, C. V. Spain, D. L. Soistmann, and H. J. Dunn. The application of active controls technology to a generic hypersonic aircraft configuration. Technical Report NASA TM-101689, National Aeronautics and Space Administration, January 1990.
- [45] Michael Oppenheimer, Torstens Skujins, Michael Bolender, and David Doman. A flexible hypersonic vehicle model developed with piston theory. Hilton Head, SC, August 2007. AIAA Atmospheric Flight Mechanics Conference and Exhibit.
- [46] Frank R. Chavez and David K. Schmidt. Analytical aeropropulsive/aeroelastic hypersonic-vehicle model with dynamic analysis. *Journal of Guidance, Control, and Dynamics*, 17(6):1308–1319, November-December 1994.
- [47] Rick Lind. Linear parameter-varying modeling and control of structural dynamics with aerothermoelastic effects. *Journal of Guidance, Control, and Dynamics*, 25(4):733–739, July-August 2002.
- [48] Adam Culler, Trevor Williams, and Michael Bolender. Aerothermal modeling and dynamic analysis of a hypersonic vehicle. Hilton Head, SC, August 2007. AIAA Atmospheric Flight Mechanics Conference and Exhibit.
- [49] Baris Fidan, Maj Mirmirani, and Petros Ioannou. Flight dynamics and control of air-breathing hypersonic vehicles: Review and new directions. Norfolk, VA, December 2003. 12th AIAA International Space Planes and Hypersonic Systems and Technologies.
- [50] Trevor Williams, Michael Bolender, David Doman, and Oscar Morataya. An aerothermal flexible mode analysis of a hypersonic vehicle. Keystone, CO, August 2006. AIAA Atmospheric Flight Mechanics Conference and Exhibit.
- [51] Lisa Fiorentini, Andrea Serrani, Michael A. Bolender, and David B. Doman. Nonlinear robust adaptive control of flexible air-breathing hypersonic vehicles. *Journal of Guidance, Control, and Dynamics*, 32(2):402–417, March-April 2009.

- [52] Zongyi Guo Jun Zhou Jianguo Guo, Guoqing Wang. New adaptive sliding mode control for a generic hypersonic vehicle. Proceedings of the Institution of Mechanical Engineers, Part G: Journal of Aerospace Engineering, February 2017.
- [53] Shah Keshmiri, Maj Mirmirani, and Richard Colgren. Six-dof modeling and simulation of a generic hypersonic vehicle for conceptual design studies. Providence, RI, August 2004. AIAA Modeling and Simulation Technologies Conference and Exhibit.
- [54] Nobuhiro Yokoyama, Shinji Suzuki, Takeshi Tsuchiya, Hideyuki Taguchi, and Takeshi Kanda. Multidisciplinary design optimization of space plane considering rigid body characteristics. *Journal of Spacecraft and Rockets*, 44(1):121–131, January-February 2007.
- [55] Asif Farooq and David J. N. Limebeer. Trajectory optimization for air-to-surface missiles with imaging radars. *Journal of Guidance, Control, and Dynamics*, 25(5), 2002.
- [56] L. Tavernini. Differential automata and their discrete simulators. *Nonlinear Analysis, Theory, Methods and Applications*, 11(6):665–683, 1987.
- [57] P. Caines and M. Shaikh. Optimality zone algorithms for hybrid systems: Efficient algorithms for optimal location and control computation. pages 123–137. Hybrid Systems: Computation and Control, 2006.
- [58] S. C. Bengea and R. A. DeCarlo. Optimal control of switching systems. *Automatica*, 41(1):11–27, 2005.
- [59] P. Riedinger, J. Daafouz, and C. Iung. About solving hybrid optimal control problems. 17th IMACS World Congress, 2005.
- [60] M. Egerstedt, Y. Wardi, and H. Axelsson. Transition-time optimization for switched-mode dynamical systems. *IEEE Transactions on Automatic Control*, 51(1):110–115, 2006.
- [61] R. Iyer. Optimal start-up of an evaporation system modeled as an interconnected hybrid dynamical system. Master’s thesis, School of Electrical and Computer Engineering, Purdue University, West Lafayette, IN, May 2015.
- [62] S. Wei, M. Zefran, K. Uthaichana, and R. DeCarlo. Hybrid model predictive control for stabilization of wheeled mobile robots subject to wheel slippage. Roma, Italy, December 2007. IEEE International Conference on Robotics and Automation.
- [63] Yu Li, Naigang Cui, and Siyuan Rong. Trajectory optimization for hypersonic boostglide missile considering aeroheating. *Aircraft Engineering and Aerospace Technology*, 81(1):3–13, 2009.
- [64] C. M. Chilan and B. A. Conway. Automated design of multiphase space missions using hybrid optimal control. *Journal of Guidance, Control, and Dynamics*, 36(5):1410–1424, 2013.
- [65] Tadeusz J. Masternak. *Multi-Objective Trajectory Optimization of a Hypersonic Reconnaissance Vehicle with Temperature Constraints*. PhD thesis, Air Force Institute of Technology, December 2014.

- [66] M. Shaikh and P. Caines. On the hybrid optimal control problem: Theory and algorithms. *IEEE Transactions on Automatic Control*, 52(9):1587–1603, 2007.
- [67] M. Shaikh and P. Caines. Correction to "on the hybrid optimal control problem: Theory and algorithms". *IEEE Transactions on Automatic Control*, 54(6):1440, 2009.
- [68] X. Xu and P. Antsaklis. Optimal control of switched systems based on parameterization of the switching instants. *IEEE Transactions on Automatic Control*, 49(1):2–16, 2004.
- [69] B. Passenberg, M. Sobotka, O. Stursberg, M. Buss, and P. E. Caines. An algorithm for discrete state sequence and trajectory optimization for hybrid systems with partitioned state space. pages 4223–4229, Atlanta, GA, December 2010. 49th IEEE Conference on Decision and Control.
- [70] I. Newton. *Principia - Motte's Translation Revised*. University of California Press, 1946.
- [71] J. D. Anderson. *Hypersonic and High Temperature Gas Dynamics*. AIAA, 1989.
- [72] L. Lees. Laminar heat transfer over blunt-nosed bodies at hypersonic flight speeds. *Jet Propulsion*, pages 259–269, 1989.
- [73] NOAA, NASA, and USAF. U.s. standard atmosphere, 1976. Technical Report NOAA-S/T 76-1562, October 1976.
- [74] Holt Ashley and Garabed Zartarian. Piston theory - a new aerodynamic tool for the aeroelastician. *Journal of the Aeronautical Sciences*, 23(12):1109–1118, 7 1956.
- [75] Clever W. Bonner, E. and K Dunn. Aerodynamic preliminary analysis system ii: Part i theory. Technical report, NASA-CR-165627, April 1981.
- [76] John T. Betts. Survey of numerical methods for trajectory optimization. *Journal of Guidance, Control, and Dynamics*, 21(2):193–207, 1998.
- [77] Charles R. Hargraves and Stephen W. Paris. Direct trajectory optimization using nonlinear programming and collocation. *Journal of Guidance, Control, and Dynamics*, 10(4):338342, 1987.
- [78] Albert L. Herman and Bruce A. Conway. Direct optimization using collocation based on high-order gauss-lobatto quadrature rules. *Journal of Guidance, Control, and Dynamics*, 19(3):592599, 1996.
- [79] Robert Bibeau and David S. Rubenstein. Trajectory optimization for a fixed-trim reentry vehicle using direct collocation and nonlinear programming. AIAA Guidance, Navigation, and Control Conference and Exhibit, June 2000.
- [80] Michael J. Grant and Gavin F. Mendeck. Mars science laboratory entry optimization using particle swarm methodology. Hilton Head, SC, 2007. AIAA Atmospheric Flight Mechanics Conference and Exhibit.
- [81] John T. Betts. *Practical Methods for Optimal Control and Estimation Using Nonlinear Programming*. Society for Industrial and Applied Mathematics, second edition, 2010.

- [82] Michael A. Patterson and Anil V. Rao. Gpops- ii: A matlab software for solving multiple-phase optimal control problems using hpadaptive gaussian quadrature collocation methods and sparse nonlinear programming. *ACM Transactions on Mathematical Software*, 39(3):141, 2013.
- [83] I. Michael Ross. A beginners guide to dido: a matlab application package for solving optimal control problems. Technical report, 2007.
- [84] Philip E. Gill, Walter Murray, , and Michael A. Saunders. Snopt: An sqp algorithm for large-scale constrained optimization. *SIAM journal on optimization*, 12(4):9791006, 2002.
- [85] D. Garg, M. A. Patterson, W. W. Hager, A. V. Rao, and G. T. Huntington D. A. Benson. A unified framework for the numerical solution of optimal control problems using pseudospectral methods. *Automatica*, 46(11):1843–1851, November 2010.
- [86] D. Garg, W. W. Hager, and A. V. Rao. Pseudospectral methods for solving infinite-horizon optimal control problems. *Automatica*, 47(4):829–837, April 2011.
- [87] D. Garg, M. A. Patterson, C. L. Darby, C. Francolin, G. T Huntington, W. W. Hager, and A. V. Rao. Direct trajectory optimization and costate estimation of finite-horizon and infinite-horizon optimal control problems via a radau pseudospectral method. *Computational Optimization and Applications*, 49(2):335–358, June 2011.
- [88] M. A. Patterson and A. V. Rao. Exploiting sparsity in direct collocation pseudospectral methods for solving continuous-time optimal control problems. *Journal of Spacecraft and Rockets*, 49(2):364–377, March-April 2012.
- [89] Lev D. Elsgolc. *Calculus of Variations*. Dover Publications, Inc., 2007.
- [90] Iu. P. Petrov. *Variational Methods in Optimum Control Theory*. Academic Press Inc., 1968.
- [91] Arthur E. Bryson and Yu-Chi Ho. *Applied Optimal Control: Optimization, Estimation and Control*. Taylor and Francis, 1975.
- [92] David G. Hull. *Optimal Control Theory for Applications, Mechanical Engineering Series*. Springer, 2003.
- [93] James M. Longuski, Jose J. Guzman, and John E. Prussing. Optimal control with aerospace applications. chapter The Euler-Lagrange Theorem, pages 52–56. Springer, El Segundo, CA., 2014.
- [94] Magnus R. Hestenes. Calculus of variations and optimal control theory. chapter Classical Fixed Endpoint Problems, pages 87–92. John Wiley and Sons, Inc., New York, 1966.
- [95] Knut Graichen, Andreas Kugi, Nicolas Petit, and Francois Chaplais. Handling constraints in optimal control with saturation functions and system extension. *Systems and Control Letters*, 23(59):671–679, 2010.

- [96] Herbert B. Keller. *Numerical Methods for Two-Point Boundary-Value Problems*. Blaisdell, Waltham, MA., 1968.
- [97] Uri M. Ascher, Robert M. M. Mattheij, and Robert D. Russell. *Numerical Solution of Boundary Value Problems of Ordinary Differential Equations*. Prentice Hall, 1988.
- [98] Tjalling J. Ypma. Historical development of the newtonraphson method. *SIAM Rev.*, 37(4):531–551, 2002.
- [99] Jacek Kierzenka and Lawrence F. Shampine. A bvp solver based on residual control and the matlab pse. *ACM Transactions on Mathematical Software* 27, pages 299–316, 2001.
- [100] Lawrence F. Shampine, Jacek Kierzenka, and Mark W. Reichelt. Solving boundary value problems for ordinary differential equations in matlab with bvp4c. 2000.
- [101] Paul B. Bailey, Lawrence F. Shampine, and Paul Waltman. Nonlinear two point boundary value problems. New York, 1968. Academic.
- [102] Mauro Pontani and Bruce Conway. Optimal low-thrust orbital maneuvers via indirect swarming method. *Journal of Optimization Theory and Applications*, 162(1):272–292, 2014.
- [103] P. A. Gnoffo. Planetary-entry gas dynamics. *Annual Review of Fluid Mechanics*, 31:459–494, 1999.
- [104] I. G. Brykina, V. V. Rusakov, and V. G. Shcherbak. Axisymmetric analogy for three-dimensional viscous flow problems. *Fluid Dynamics*, 26:883–889, 1991.
- [105] I. G. Brykina and C. D Scott. An approximate axisymmetric viscous shock layer aeroheating method for three-dimensional bodies. Houston, Texas: Lyndon B. Johnson Space Center, 1998.
- [106] M. S. Bopp, S. M. Ruffin, R. D. Braun, I. G. Clark, and J. E. Theisinger. Multi-fidelity approach to estimate heating for three-dimensional hypersonic aeroshells. *Journal of Spacecraft and Rockets*, 50:754–762, Jul. 2013.
- [107] E. V. Zoby, J. N. Moss, and K. Sutton. Approximate convective-heating equations for hypersonic flows. *Journal of Spacecraft and Rockets*, 18:64–70, Jan. 1981.
- [108] E. R. G. Eckert. Engineering relations for friction and heat transfer to surfaces in high velocity flow. *Journal of the Aeronautical Sciences*, 22:585–587, 1955.
- [109] Lester Lees. Laminar heat transfer over blunt-nosed bodies at hypersonic flight speeds. *Jet Propulsion*, pages 259–269, April 1956.
- [110] H. H. Hamilton, K. J. Weilmuenster, and F. R. DeJarnette. Approximate method for computing laminar and turbulent convective heating on hypersonic vehicles using unstructured grids. June 2009.
- [111] Michael E. Tauber. A review of high-speed, convective, heat-transfer computation methods. Technical Report NASA-TP-2914, Ames Research Center, Moffett Field, CA., July 1989.

- [112] B. Laub. Tutorial on ablative tps. March 2007.
- [113] L. M. Howser and S. S. Tompkins. Computer program for the transient response of ablating axisymmetrix bodies influencing the effects of shape change. Technical Report NASA Technical Memorandum X-2375, National Aeronautics and Space Administration, Washington, D. C., October 1971.
- [114] S. S. Tompkins, J. N. Moss, C. M. Pittman, and L. M. Howser. Numerical analysis of the transient response of ablating axisymmetric bodies, including the effects of shape change. Technical Report NASA Technical Note D-6220, National Aeronautics and Space Administration, Washington, D. C., May 1971.
- [115] S. D. Williams and Donald M. Curry. Thermal protection materials: Thermo-physical property datar. Technical Report NASA-RP-1289, National Aeronautics and Space Administration, December 1992.
- [116] Les Piegl and Wayne Tiller. *The NURBS Book*. Springer, second edition, 1996.
- [117] Erwin Kreyszig. *Advanced Engineering Mathematics*. John Wiley and Sons, Inc., tenth edition, 2011.
- [118] John R. Dormand and P. J. Prince. A family of embedded runge-kutta formulae. *Journal of Computational and Applied Mathematics*, 6(1):19–26, November 1980.
- [119] Harish Saranathan and Michael J. Grant. Incorporation of ablative shape change into conceptual hypersonic mission design. San Diego, CA, January 2016. AIAA Atmospheric Flight Mechanics Conference, AIAA SciTech.
- [120] Donald T. Greenwood. *Principles of Dynamics*. Prentice Hall, Upper Saddle River, NJ., second edition, 1988.
- [121] William Tyrrell Thomson. *Introduction to Space Dynamics*. Dover Books on Aeronautical Engineering, 1986.
- [122] Uri M. Ascher and Linda R. Petzold. *Computer Methods for Ordinary Differential Equations and Differential-Algebraic Equations*. Philadelphia: Society for Industrial and Applied Mathematics, 1998.
- [123] Richard C. Aiken. *Stiff Computation*. Oxford University Press, 1985.
- [124] Brian L. Stevens and Frank L. Lewis. *Aircraft Control and Simulation*. John Wiley and Sons, Inc., second edition, 2003.
- [125] Lawrence F. Shampine. *Solving ODEs with MATLAB*. Cambridge University Press, Cambridge, 2003.
- [126] C. William Gear. *Numerical Initial Value Problems in Ordinary Differential Equations*. Prentice Hall, Englewood Cliffs, NJ., 1971.
- [127] Ernst Hairer and Gerhard Wanner. *Solving Ordinary Differential Equations II, Stiff and Differential-Algebraic Problems*. Springer-Verlag, Berlin, 1991.
- [128] Jacek Kierzenka and Lawrence F. Shampine. A fast adaptive numerical method for stiff two-point boundary value problems. *SIAM Journal on Scientific Computing*, 18(2):403–429, March 1997.

- [129] Joseph E. Flaherty and Jr. R. E. O'Malley. The numerical solution of boundary value problems for stiff differential equations. *Mathematics of Computation*, 31(137):66–93, January 1977.
- [130] P. Deuffhard. A modified newton method for the solution of ill-conditioned systems of nonlinear equations with application to multiple shooting. *Numerische Mathematik*, 22(4):289–315, August 1974.
- [131] Katsuhiko Ogata. *Modern Control Engineering*. Pearson Education, Inc., fifth edition, 2010.
- [132] Joseph W. Magee, Thomas J. Bruno, Daniel G. Friend, Marcia L. Huber, Arno Laesecke, Eric W. Lemmon, Mark O. McLinden, Richard A. Perkins, Jrg Baranski, and Jason A. Widegren. Thermophysical properties measurements and models for rocket propellant rp-1: Phase i. Technical Report NISTIR 6646, National Institute of Standards and Technology, February 2007.
- [133] D. L. Timrot and V. P. Borisoglebskii. The density of liquid oxygen on the saturation curve. *Soviet Physics JETP*, 11(6):1248–1250, December 1960.
- [134] Boris I. Katargin, Vladimir K. Chvanov, Felix J. Chelkis, Michael Popp, Lawrence G. Tanner, Robert C. vanGiessen, and Scott J. Connally. Rd-180 engine production and flight experience. 40th AIAA/ASME/SAE/ASEE Joint Propulsion Conference and Exhibit, July 2004.
- [135] Harish Saranathan and Michael J. Grant. Relaxed autonomously switched hybrid system approach to indirect multiphase aerospace trajectory optimization. *Journal of Spacecraft and Rockets*, 0(0):1–11, November 2017.
- [136] Harish Saranathan and Michael J. Grant. The relaxed autonomously switched hybrid system (rashes) approach to indirect multi-phase trajectory optimization for aerospace vehicles. Kissimmee, FL., January 2018. AIAA Atmospheric Flight Mechanics Conference.
- [137] United Launch Alliance. Atlas v launch services users guide. Technical report, Centennial, CO., March 2010.
- [138] David W. Way, Richard W. Powell, Allen Chen, Adam D. Steltzner, A. Miguel San Martin, P. Daniel Burkhart, and Gavin F. Mendeck. Mars science laboratory: Entry, descent, and landing system performance. IEEE Aerospace Conference, March 2007.
- [139] David W. Way, Jody L. Davis, and Jeremy D. Shidner. Assessment of the mars science laboratory entry, descent, and landing simulation. February 2013.
- [140] Matt Dawson, Gerry Brewster, Chris Conrad, Mike Kilwine, Blake Chenevert, and Olwen Morgan. Monopropellant hydrazine 700 lbf throttling terminal descent engine for mars science laboratory. Cincinnati, OH., July 2007. 43rd AIAA/ASME/SAE/ASEE Joint Propulsion Conference and Exhibit.
- [141] Richard P. Kornfeld, Ravi Prakash, Ann S. Devereaux, Martin E. Greco, Corey C. Harmon, and Devin M. Kipp. Verification and validation of the mars science laboratory/curiosity rover entry, descent, and landing system. *Journal of Spacecraft and Rockets*, 51(4):1251–1269, November 2014.

- [142] Sarag J. Saikia. Seven minutes of terror and “some science”. Cologne, Germany, 2015. 12th International Planetary Probe Workshop. [https://solarsystem.nasa.gov/docs/4\\_05\\_Seven\%20Minutes\%20of\%20Terror\%20and\%20Some\%20Science\\_S.\%20Saikia.pdf](https://solarsystem.nasa.gov/docs/4_05_Seven\%20Minutes\%20of\%20Terror\%20and\%20Some\%20Science_S.\%20Saikia.pdf), retrieved 12 March 2017.
- [143] K. Sutton and R. A. Graves. A general stagnation-point convective-heating equation for arbitrary gas mixtures. Technical Report NASA TR R-376, National Aeronautics and Space Administration, Washington, D. C., November 1971.
- [144] Space Exploration Technologies Corp. Falcon 9 launch vehicle payload user’s guide. [http://www.spacex.com/sites/spacex/files/falcon\\\_9\\\_users\\\_guide\\\_rev\\\_2.0.pdf](http://www.spacex.com/sites/spacex/files/falcon\_9\_users\_guide\_rev\_2.0.pdf). Online; retrieved 30 November 2017.
- [145] Thomas J. Rudman and Kurt L. Austad. The centaur upper stage vehicle. Liege, Belgium, December 2002. 4th International Conference on Launcher Technology.
- [146] Thomas Flynn. *Cryogenic Engineering*. CRC Press, second edition, November 2004.
- [147] H. Platzek. Preliminary solid rocket motor design techniques. Technical Report ADA063474, Naval Weapons Center, China Lake, CA, January 1979.
- [148] Clarke E. Hermance. A model of composite propellant combustion including surface heterogeneity and heat generation. *AIAA Journal*, 4(9):1629–1637, September 1966.
- [149] Maxwell H. Fagin. Payload mass improvements of supersonic retropropulsive flight for human class missions to mars. Master’s thesis, Purdue University, 2016.
- [150] Joseph Williams. Trajectory optimization using indirect methods and parametric scramjet cycle analysis. Master’s thesis, Purdue University, 2016.
- [151] Justin R. Mansell. Adaptive continuation strategies for indirect trajectory optimization. Master’s thesis, Purdue University, May 2017.
- [152] Michael J. Grant and Michael A. Bolender. Rapid, robust trajectory design using indirect optimization methods. Dallas, TX., June 2015. AIAA Atmospheric Flight Mechanics Conference, AIAA AVIATION Forum.
- [153] Jinghui Guo, Guiping Lin, Xueqin Bu, Shiming Fu, and Yanmeng Chao. Effect of static shape deformation on aerodynamics and aerothermodynamics of hypersonic inflatable aerodynamic decelerator. *Acta Astronautica*, 136:421–433, 2017.
- [154] Thomas Antony. Rapid indirect trajectory optimization on highly parallel computing architectures. Master’s thesis, Purdue University, 2014.
- [155] Kathryn E. Wurster. *MINIVER User’s Guide*. October 2000.
- [156] C. D. Engel and S. C. Praharaj. Miniver upgrade for the avid system. volume 1: Lanmin user’s manual. Technical Report NASA-CR-172212, NAS 1.26:172212, National Aeronautics and Space Administration, 1983.



- [157] C. D. Engel and C. P. Schmitz. Miniver upgrade for the avid system. volume 2: Lanmin input guide. Technical Report NASA-CR-172213, NAS 1.26:172213, National Aeronautics and Space Administration, 1983.
- [158] J. E. Pond and C. P. Schmitz. Miniver upgrade for the avid system. volume 3: Exits user's and input guide. Technical Report NASA-CR-172214, NAS 1.26:172214, National Aeronautics and Space Administration, 1983.
- [159] Thomas Antony and Michael J. Grant. Path constraint regularization in optimal control problems using saturation functions. Kissimmee, FL., January 2018. 2018 AIAA Atmospheric Flight Mechanics Conference, AIAA SciTech Forum.

## APPENDICES



## A. TRADITIONAL APPROACH TO INDIRECT CONSTRAINED TRAJECTORY OPTIMIZATION

Traditionally, path constraints are handled by introducing additional Lagrange multipliers [91]. Suppose the problem in Eq. 5.1 consists of equality constraints that are functions of control and the state variables, they can be posed as:

$$\mathbf{C}(\mathbf{X}, \mathbf{U}, t) = \mathbf{0} \quad (\text{A.1})$$

The Hamiltonian is adjoined as:

$$\mathbf{H} = \mathcal{L} + \boldsymbol{\lambda}^T \mathbf{f} + \boldsymbol{\mu}^T \mathbf{C} \quad (\text{A.2})$$

where  $\boldsymbol{\mu}$  is the vector of the additional Lagrange multipliers. This new augmented Hamiltonian is used in Eq. (5.5), which along with Eq. (A.3) forms the necessary conditions of optimality.

If a scalar equality constraint does not have explicit dependence on the control, it may be represented as:

$$C(\mathbf{X}, t) = 0 \quad (\text{A.3})$$

Successive total time derivatives of Eq. (A.3) are taken until control explicitly appears. Suppose this occurs at the  $q^{th}$  derivative, the Hamiltonian is augmented as:

$$\mathbf{H} = \mathcal{L} + \boldsymbol{\lambda}^T \mathbf{f} + \mu \frac{d^q C}{dt^q} \quad (\text{A.4})$$

where  $\mu$  is the Lagrange multiplier. As before, this new augmented Hamiltonian is substituted into Eq. (5.5), which along with the equation:

$$\frac{d^q C}{dt^q} = 0 \quad (\text{A.5})$$

forms the necessary conditions of optimality. Additionally, the following conditions need to be enforced at initial or final time:

$$\begin{bmatrix} C \\ \frac{dC}{dt} \\ \frac{d^2C}{dt^2} \\ \vdots \\ \frac{d^{(q-1)}C}{dt^{(q-1)}} \end{bmatrix} = \mathbf{0} \quad (\text{A.6})$$

Inequality path constraints are more difficult to handle. Suppose a scalar constraint is a function of states and control such that:

$$C(\mathbf{X}, \mathbf{U}, t) \leq 0 \quad (\text{A.7})$$

The Hamiltonian is augmented as before:

$$\mathbf{H} = \mathcal{L} + \boldsymbol{\lambda}^T \mathbf{f} + \mu C \quad (\text{A.8})$$

where

$$\mu \begin{cases} > 0, C = 0 \\ = 0, C < 0 \end{cases} \quad (\text{A.9})$$

The augmented Hamiltonian is substituted into Eq. (5.5) to obtain the necessary conditions of optimality. When  $C < 0$ ,  $\mu = 0$  and the control  $\mathbf{U}$  is simply obtained by solving the following equation:

$$\frac{\partial \mathbf{H}}{\partial \mathbf{U}} = 0 \quad (\text{A.10})$$

When  $C = 0$ ,  $\mathbf{U}$  and  $\mu$  are solved together from Eqs. (A.10) and (A.7).

Lastly, if the scalar inequality constraint is a function of states only, successive total time derivatives are taken until control explicitly appears, as in the equality constraints in states only. Assuming this occurs at the  $q^{th}$  derivative, the Hamiltonian is augmented as before:

$$\mathbf{H} = \mathcal{L} + \boldsymbol{\lambda}^T \mathbf{f} + \mu \frac{d^q C}{dt^q} \quad (\text{A.11})$$

where

$$\frac{d^q C}{dt^q} = 0 \text{ when } C = 0 \quad (\text{A.12})$$

and

$$\mu = 0 \text{ when } C < 0 \quad (\text{A.13})$$

Also,  $\mu$  is required to be non-negative if minimizing  $J$ . Eq. (5.5) with the augmented Hamiltonian and the equation  $C \leq 0$  constitutes a part of the necessary conditions of optimality. Since control appears only in the  $q^{th}$  derivative of  $C$ , in order for the control to be finite when the vehicle is flying along the boundary, the following tangency conditions need to be satisfied at the entry and exit of the boundary:

$$\begin{bmatrix} C \\ \frac{dC}{dt} \\ \frac{d^2 C}{dt^2} \\ \vdots \\ \frac{d^{(q-1)} C}{dt^{(q-1)}} \end{bmatrix} = \mathbf{0} \quad (\text{A.14})$$

This forms a set of interior boundary conditions and complete the necessary conditions of optimality. It can be seen that this results in an MPBVP, as opposed to a TPBVP. The number of interior boundary conditions increases with the number of path constraints, making the resultant MPBVP more challenging to solve. As a result, it is desirable to incorporate a methodology that would confine the necessary conditions of optimality to a TPBVP when inequality path constraints are introduced. Such a method is explained in Section 5.2.2.



## B. TRAJECTORY OPTIMIZATION OF AN AXISYMMETRICALLY ABLATING HYPERSONIC VEHICLE SUBJECT TO EQUALITY CONSTRAINT ON ALTITUDE

This example was presented in [119], and involves the optimization of the trajectory of an ablating hypersonic military glide vehicle that is subject to altitude constraints. Only planar motion is considered, and the Earth is assumed to be non-rotating. Consequently, the state variables that define the motion of the vehicle are velocity,  $v$ , flight-path-angle,  $\gamma$ , altitude,  $h$ , and downrange,  $\theta_S$ . The vehicle is controlled by varying the angle-of-attack. The axisymmetric ablation model and the vehicle geometry are the same as in Section 6.5.3. The TPS properties are defined by a  $Q_*$  of 8.5883 MJ/kg and a  $\rho_{TPS}$  of 1353.85 kg/m<sup>3</sup>, and the wall temperature is fixed at 1,000 K. Two cases corresponding to a high energy and a low energy post-boost condition are presented.

### Case 1: High Energy Post-Boost Condition

The post-boost conditions corresponding to this case are described in Table B.1. The vehicle is assumed to fly over an ally territory for the first 1,000 km. In this phase, it is constrained to fly at an altitude of 40 km because it is assumed that if the vehicle flies higher, the missile defense system of the ally will sense the vehicle as an intercontinental ballistic missile (ICBM) and trigger an alarm. On the other hand, if the vehicle flies lower, it might pose a hazard to the ally territory in the event that the vehicle's guidance system malfunctions. After the vehicle flies 1,000 km, it is assumed to have crossed over to hostile territory, at which point the altitude



constraint is lifted. The vehicle needs to fly a further 400 km to reach the target. The objective of the trajectory optimization problem is to maximize the velocity when the vehicle strikes the target.

There is no optimization involved in the first arc where the vehicle is constrained to fly at an altitude of 40 km. The trajectory representing this arc is obtained by simply numerically propagating the equations of motion with the initial conditions defined in Table B.1 until a downrange of 1,000 km is reached. The angle-of-attack for the first arc is calculated by solving the equation  $\dot{\gamma} = 0$ . The terminal conditions of this arc are used as the initial conditions for the second arc, where the trajectory optimization is performed. The initial and terminal conditions for the second arc are given in Table B.2.

Table B.1. Initial conditions for the trajectory arc with the altitude constraint.

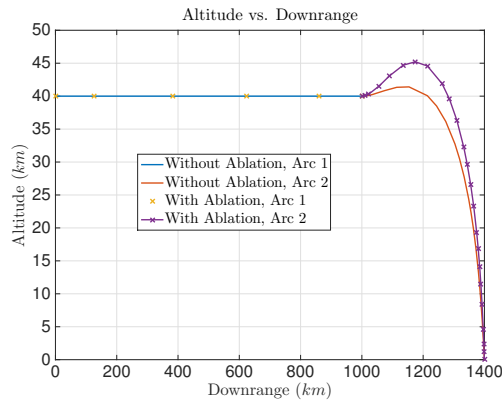
State Variable	Value
Velocity, $v$	6 km/s
Flight-path-angle, $\gamma$	0 deg
Altitude, $h$	40 deg
Downrange	0 km
Vehicle length, $l_V$	1.2 m

Table B.2. Initial and terminal conditions for the unconstrained trajectory arc.

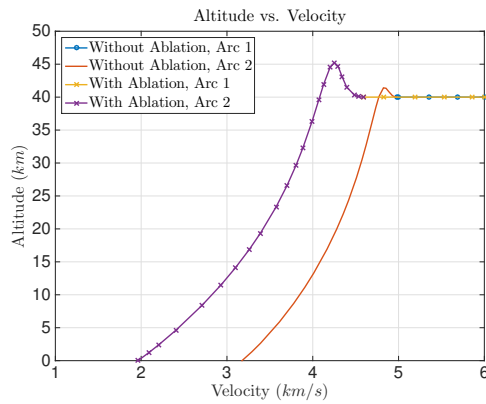
Variable	Initial Conditions	Terminal Conditions
Velocity, $v$	4.592 m/s	Free
Flight-path-angle, $\gamma$	0 deg	Free
Altitude, $h$	40 km	0 km
Downrange	1,000 km	1,400 km
Vehicle length, $l_V$	0.8576 m	Free

The results of trajectory optimization are illustrated in Figure B.1. For comparison, the optimal trajectory generated by neglecting ablative shape change is also shown. It can be seen that the optimal trajectory for the ablating vehicle is different (Figures B.1(a) and B.1(b)). Since the ablating vehicle experiences higher drag as its shape evolves, the velocity at the end of the first arc is lower. The lower velocity, coupled with higher drag coefficient (hence, lower lift-to-drag ratio) forces the vehicle to execute a loft maneuver. This enables the vehicle to climb to a higher altitude where it experiences less drag loss. Towards the end of the trajectory, it dives at a steeper angle towards the target. The loft and dive maneuvers are achieved by a more aggressive change in angle-of-attack, as seen in Figure B.1(e). The dive maneuver minimizes the time spent in the lower atmosphere where density is high, resulting in lower drag loss. Drag loss is also indirectly minimized because ablative shape change is minimized (Figure B.1(d)) as a consequence of a reduction in heat-load in the dive maneuver. The evolution in vehicle mass is shown in Figure B.1(c). A temporary reduction in mass loss rate can be observed at the initiation of the second arc. This is because the vehicle encounters less ablation as it climbs to a higher altitude while executing the loft maneuver. During this maneuver, the vehicle bleeds some speed without sacrificing the TPS.

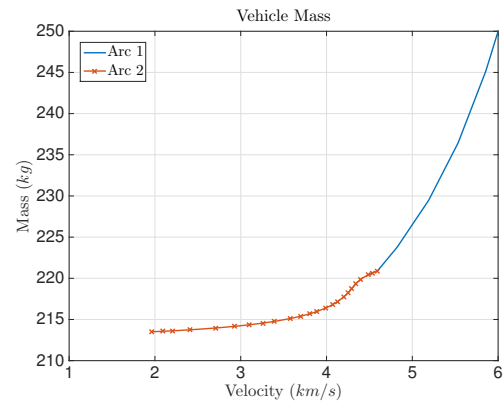
The next section presents a comparison of optimal trajectories of an ablating and a non-ablating vehicle flying a similar mission, but with a lower initial velocity and longer downrange to the target.



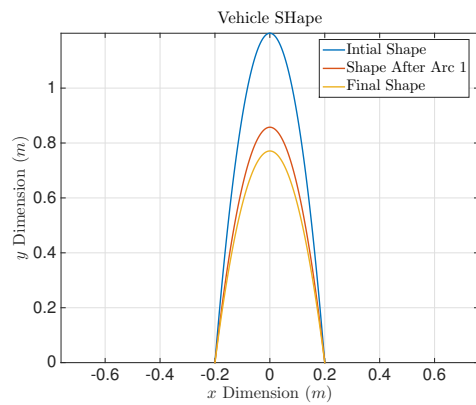
(a) Altitude vs. Downrange.



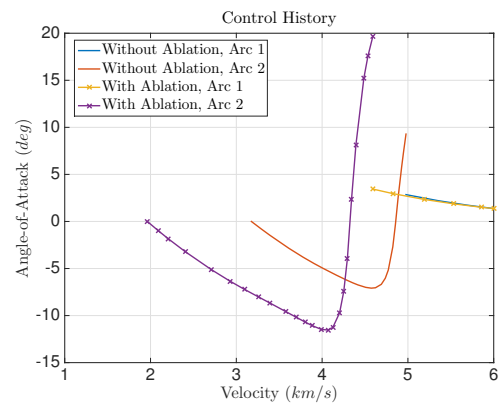
(b) Altitude vs. Velocity.



(c) Mass vs. Velocity for ablating vehicle.



(d) Shape of the ablating vehicle.



(e) Control History.

Figure B.1. Results of trajectory optimization of an axisymmetrically ablating hypersonic glide vehicle subject to equality constraint on altitude and high initial velocity.

## Case 2: Low Energy Post-Boost Condition

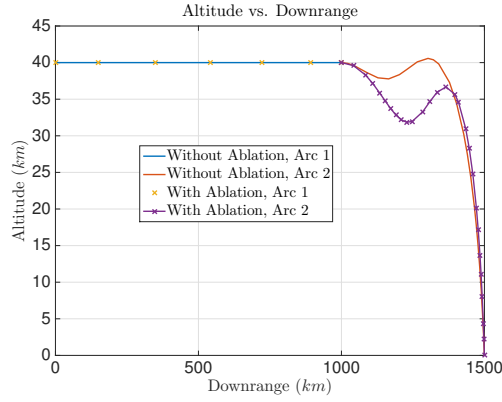
This example is similar to the previous one. The difference lies in the post-boost velocity and the target location, which is now 1,500 km away from the initiation of the glide phase. The post-boost conditions are summarized in Table B.3. The vehicle is protected by a TPS of lower performance, characterized by a heat of ablation  $Q_*$  of 6.2027 MJ/kg and a density  $\rho_{TPS}$  of 977.7778 kg/m<sup>3</sup>. As before, the vehicle is constrained to fly at an altitude of 40 km for the first 1,000 km. The initial conditions when the altitude constraint is removed are given in Table B.4. This table also summarizes the boundary conditions for the optimization that is performed on the second arc. The objective is again to maximize velocity on impact.

Table B.3. Initial conditions for the trajectory arc with the altitude constraint corresponding to case 2.

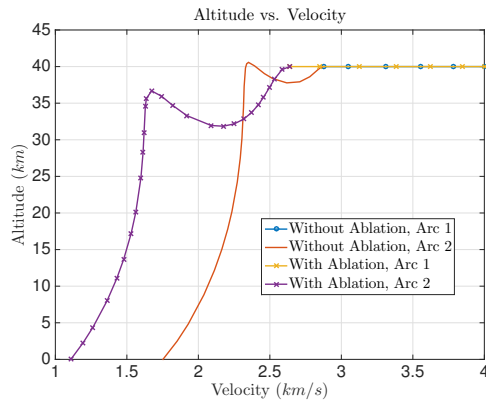
State Variable	Value
Velocity, $v$	4 km/s
Flight-path-angle, $\gamma$	0 deg
Altitude, $h$	40 deg
Downrange, $\theta_S$	0 km
Vehicle length, $L_{shape}$	1.2 m

Table B.4. Initial and terminal conditions for the unconstrained trajectory arc corresponding to case 2.

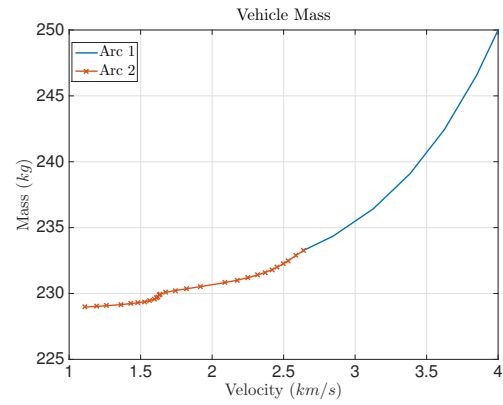
Variable	Initial Conditions	Terminal Conditions
Velocity, $v$	2.638 km/s	Free
Flight-path-angle, $\gamma$	0 deg	Free
Altitude, $h$	40 km	0 km
Downrange, $\theta_S$	1,000 km	1,500 km
Vehicle length, $L_{shape}$	0.9275 m	Free



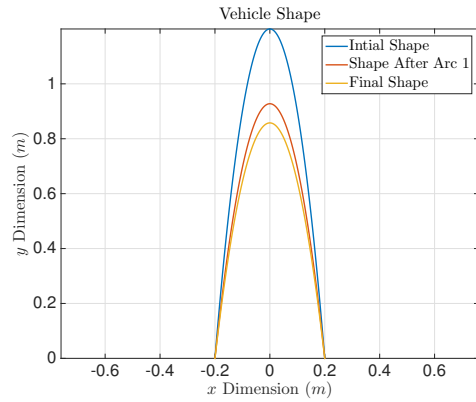
(a) Altitude vs. Downrange.



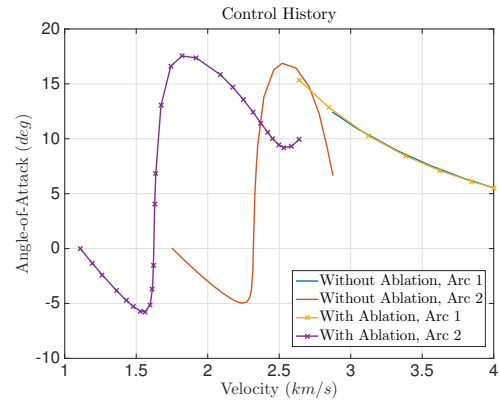
(b) Altitude vs. Velocity.



(c) Mass vs. Velocity for ablating vehicle.



(d) Shape of the ablating vehicle.



(e) Control History.

Figure B.2. Results of trajectory optimization of an axisymmetrically ablating hypersonic glide vehicle subject to equality constraint on altitude and low initial velocity.

Figure B.2 shows the results of the trajectory optimization. Like before, the optimal solution of the non-ablating vehicle is also shown for comparison. The trajectories are again seen to be different (Figures B.2(a) and B.2(b)). In either trajectory, the vehicles have insufficient velocity to perform a loft maneuver to minimize drag loss. As a result, they initially descend until the dynamic pressure is sufficient to perform the loft. Since the ablating vehicle loses more lift performance, it is forced to descend to a much lower altitude when compared to the non-ablating vehicle to take advantage of the increased dynamic pressure to execute the loft maneuver. After the loft, the vehicles dive towards the target to minimize ablation and drag loss by minimizing the time spent in the lower atmosphere, thereby maximizing final velocity. The control histories to perform the descent, loft and dive are illustrated in Figure B.2(e). The evolution of vehicle shape and mass are shown in Figures B.2(d) and B.2(c) respectively.



## C. POTENTIAL MODIFICATION TO RASHS TO ENABLE THE EXPLICIT ENFORCEMENT OF FLIGHT PHASE SEQUENCE

The RASHS approach described in Chapter 8 assumes that the flight phases occur in a predetermined sequence, and the switching conditions are carefully chosen to guarantee this. In order to explicitly enforce the phase sequence, additional protection conditions are required, which can be viewed as a combination of AND and OR logics. The RASHS approach can be modified to incorporate these conditions and approximate them using saturation functions. Preliminary investigation has been performed on this and is presented below.

Consider an EDL mission with 3 phases: 1) hypersonic descent, 2) parachute descent, and 3) powered descent. Often, the parachute descent is triggered when the vehicle slows down to a certain velocity,  $v_P$ , and powered descent is triggered when the vehicle descends to a certain altitude,  $h_{PDI}$ . The values of  $v_P$  and  $h_{PDI}$  should be carefully chosen to guarantee that the flight phases follow the pre-determined sequence. Else, the vehicle might never slow down to  $v_P$  before descending to  $h_{PDI}$  and the parachute descent phase will never get triggered. Moreover, both hypersonic and powered descent phases will be active when the vehicle descends below  $h_{PDI}$ . If the determination of  $v_P$  and  $h_{PDI}$  is not straightforward, the sequence of the flight phases can be explicitly enforced by introducing additional conditions defined by AND and OR logics. For instance, an additional protection can be introduced so that the parachute descent is triggered when either  $v < v_P$  or  $h < h_P$ , thereby guaranteeing its activation at some point during the EDL mission. Also, the hypersonic phase is active only when  $v > v_P$  and  $h_P > h_P$ , thereby ensuring that the parachute descent follows the hypersonic phase and not directly skipped to powered descent. Such a



condition will also ensure that only one phase is active at any given time. Following this, the powered descent phase is active simply when  $h < h_{PDI}$ . Logically, the switching conditions for hypersonic and parachute descent phases ( $\xi_1$  and  $\xi_2$ ) can be represented as follows:

$$\begin{aligned}\xi_1 &= (v > v_P) \text{ AND } (h > h_P) \\ \xi_2 &= [(v < v_P) \text{ OR } (h < h_P)] \text{ AND } (h > h_{PDI})\end{aligned}\tag{C.1}$$

For the powered descent phase, the switching function is simply given by:

$$\xi_3 = 1 - u(h - h_{PDI})\tag{C.2}$$

The AND and OR logical operations can be represented as follows:

$$\begin{aligned}\text{Suppose } A &= \begin{cases} 1 & \text{when } g_1 < 0 \\ 0 & \text{otherwise} \end{cases} \\ \text{and } B &= \begin{cases} 1 & \text{when } g_2 < 0 \\ 0 & \text{otherwise} \end{cases} \\ A \text{ AND } B &= A \cdot B\end{aligned}\tag{C.3}$$

$$A \text{ OR } B = \max[0, \min(A + B, 1)]$$

Using unit step functions,

$$A \text{ AND } B = [1 - u(g_1)] \cdot [1 - u(g_2)]$$

$$A \text{ OR } B = \max[0, \min(2 - u(g_1) - u(g_2), 1)]$$

The unit step functions can be represented using sigmoid functions and the minmax function can be represented by tanh, so that:

$$\begin{aligned}A \text{ AND } B &= \left( \frac{1}{1 + e^{s \cdot g_1}} \right) \cdot \left( \frac{1}{1 + e^{s \cdot g_2}} \right) \\ A \text{ OR } B &= \tanh \left( \zeta \cdot \left\{ \left( \frac{1}{1 + e^{s \cdot g_1}} \right) + \left( \frac{1}{1 + e^{s \cdot g_2}} \right) \right\} \right)\end{aligned}\tag{C.4}$$

where  $\zeta$  is a measure of the slope of the tanh function. Since the sigmoid functions are strictly positive, choosing  $\zeta > 0$  will ensure that Eq. (C.4) will always result in a value between 0 and 1.

Following Eq. (C.4), the switching condition for the hypersonic, parachute and powered descent phases ( $\xi_1$ ,  $\xi_2$  and  $\xi_3$ ) can be represented as follows:

$$\begin{aligned}\xi_1 &= \left( \frac{1}{1 + e^{-s \cdot (v - v_P)}} \right) \cdot \left( \frac{1}{1 + e^{-s \cdot (h - h_P)}} \right) \left( \right. \\ \xi_2 &= \left[ \tanh \left( \zeta \cdot \left\{ \left( \frac{1}{1 + e^{s \cdot (v - v_P)}} \right) + \left( \frac{1}{1 + e^{s \cdot (h - h_P)}} \right) \right\} \right) \right] \cdot \left[ \frac{1}{1 + e^{-s \cdot (h - h_{PDI})}} \right] \left( \right. \\ \xi_3 &= \frac{1}{1 + e^{s \cdot (h - h_{PDI})}}\end{aligned}\quad (C.5)$$

If the equations of motion for hypersonic, parachute and powered descent phases are given by  $\mathbf{f}_1$ ,  $\mathbf{f}_2$  and  $\mathbf{f}_3$  respectively, and the corresponding cost functionals are given by  $J_1$ ,  $J_2$  and  $J_3$  respectively, the approximated smooth equations of motion and cost functional are given as:

$$\begin{aligned}\dot{\mathbf{X}} &= \xi_1 \mathbf{f}_1 + \xi_2 \mathbf{f}_2 + \xi_3 \mathbf{f}_3 \\ J &= \xi_1 J_1 + \xi_2 J_2 + \xi_3 J_3\end{aligned}\quad (C.6)$$

In general, if a switching function associated with mode  $k$  is represented by a sum-of-product logical expression as follows:

$$\begin{aligned}\xi_k &= \sum_{i=1}^{a_k} \left( \prod_{j=1}^{b_{i,k}} A_{i,j,k} \right) \left( \right. \\ \text{where } A_{i,j,k} &= \begin{cases} 1 & \text{when } g_{i,j,k} < 0 \\ 0 & \text{otherwise} \end{cases}\end{aligned}\quad (C.7)$$

where the summation and the product represent OR and AND logics respectively,  $\xi_k$  can be approximated as follows:

$$\xi_k = \tanh \left( \zeta \cdot \sum_{i=1}^{a_k} \left( \prod_{j=1}^{b_{i,k}} \left( \frac{1}{1 + e^{s \cdot g_{i,j,k}}} \right) \right) \right) \left( \right. \quad (C.8)$$

For an aerospace system consisting of  $m$  flight segments, the smooth equations of motion and cost functional are given by:

$$\begin{aligned} \dot{\mathbf{X}} &= \sum_{k=1}^m \left\{ \tanh \left( \zeta \cdot \sum_{i=1}^{a_k} \left( \prod_{j=1}^{b_{i,k}} \left( \frac{1}{1 + e^{s \cdot g_{i,j,k}}} \right) \right) \right) \right\} \mathbf{f}_k \\ J &= \sum_{k=1}^m \left\{ \tanh \left( \zeta \cdot \sum_{i=1}^{a_k} \left( \prod_{j=1}^{b_{i,k}} \left( \frac{1}{1 + e^{s \cdot g_{i,j,k}}} \right) \right) \right) \right\} J_k \end{aligned} \quad (\text{C.9})$$

Trajectory optimization can then be performed using indirect methods with the transformed flight dynamic equations and cost functional given by Eq. (C.9).

## D. PUBLICATIONS RESULTING FROM THE DOCTORAL PROGRAM

### Publications from the Dissertation

#### Journal Publication

1. Saranathan, H. and Grant, M. J., “Relaxed Autonomously Switched Hybrid System Approach to Indirect Multiphase Aerospace Trajectory Optimization,” *Journal of Spacecraft and Rockets*, November 2017.  
(Ahead of print)

#### Conference Proceedings

1. Saranathan, H. and Grant, M. J., “The Relaxed Autonomously Switched Hybrid System (RASHS) Approach to Indirect Multi-Phase Trajectory Optimization for Aerospace Vehicles,” *2018 AIAA Atmospheric Flight Mechanics Conference, AIAA SciTech Forum*, AIAA 2018-0016, January 2018.  
(Won the 2018 AIAA SciTech Atmospheric Flight Mechanics Student Paper Competition)
2. Saranathan, H. and Grant, M. J., “Incorporation of Effects of Control Surfaces into Hypersonic Trajectory Optimization Framework,” *AIAA Atmospheric Flight Mechanics Conference, AIAA AVIATION Forum*, AIAA 2016-3245, May 2016.
3. Saranathan, H. and Grant, M. J., “Incorporation of Ablative Shape Change into Conceptual Hypersonic Mission Design,” *AIAA Atmospheric Flight Mechanics Conference, AIAA SciTech Forum*, AIAA 2016-0020, January 2016.

## Future Publications

1. Journal submission to JSR regarding the application of RASHS approach to multi-body systems.
2. Journal submission to JSR regarding the modification of RASHS to explicitly enforce the discrete phase sequence.
3. Journal submission to JSR regarding the incorporation of ablative shape change into conceptual hypersonic mission design.
4. Journal submission to JSR regarding the incorporation of rigid body model into the indirect trajectory optimization framework.
5. Journal submission to JSR regarding the integration of all the contributions of the dissertation into a unified conceptual hypersonic mission design framework.

## Other Publications and Presentations from the Doctoral Program

### Conference Proceedings

1. Saikia, S., Saranathan, H., Grant, M. J. and Longuski, J. M., “Trajectory Optimization Analysis of Rigid Deployable Aerodynamic Decelerator,” *AIAA/AAS Astrodynamics Specialist Conference, AIAA SPACE Forum*, AIAA 2014-4139, August 2014.

### Workshop Papers and Presentations

1. Sparapany, M., Antony, T., Saranathan, H., Klug, L., Libben, B., Shibata, E., Williams, J., Saikia, S. and Grant, M., “Enabling Mars Exploration Using inflatable Purdue Aerodynamic Decelerator with Deployable Entry Systems (iPAD-DLES) Technology,” *2016 NASA BIG Idea Forum*, Hampton, VA., April 2016.  
(**Finalists of the 2016 NASA BIG Idea Challenge**)

2. Saranathan, H., Saikia, S., Grant, M. J. and Longuski, J. M., "Trajectory Optimization with Adaptive Deployable Entry and Placement Technology Architecture," *11th International Planetary Probe Workshop*, June 2014.
3. Saikia, S., Saranathan, H., Grant, M. J. and Longuski, J. M., "Enabling Venus In Situ Missions Using Mechanically Deployed Aerodynamic Decelerator," *11th International Planetary Probe Workshop*, June 2014.
4. Saikia, S., Saranathan, H., Grant, M. J. and Longuski, J. M., "Assessment of Guided Aerocapture and Entry for Venus In Situ Missions Using Mechanically Deployed Aerodynamic Decelerator," *Workshop on Venus Exploration Targets*, April 2014.

VITA

## VITA

Harish Saranathan was born in Hosur, India, in 1990. He earned his Bachelor of Technology in Electronics and Communication Engineering from SASTRA University, Thanjavur, India, in May, 2012. His undergraduate project involved implementing searching and shortest path algorithms for swarm robotics.

He joined the Master of Science program in the School of Aeronautics and Astronautics at Purdue University, West Lafayette, Indiana, in August, 2012. He started working under the guidance of Prof. Michael J. Grant in the Rapid Design of Systems Laboratory (RDSL) beginning January, 2013, and worked on modeling shape change of slender hypersonic vehicles caused by the ablation of their thermal protection systems for conceptual design studies. During his Master's program, he also collaborated with other research groups on designing hypersonic missions, particularly those involving the Adaptive Deployable Entry and Placement Technology (ADEPT) architecture. He also co-authored the paper titled "Strategies For Mars Network Science Missions Via Innovative Aerocapture and EDL Architectures" that won second prize for outstanding oral presentation at the 10th International Planetary Probe Workshop. He earned his Master of Science in Aeronautics and Astronautics in May, 2014, and his project titled "Rapid Modeling of Shape Change of Ablating Slender Hypersonic Vehicles for Conceptual Mission Design" served as the foundation for his doctoral program.

Harish began his doctoral program at RDSL in May, 2014, and worked on increasing the fidelity of conceptual hypersonic mission design. He also expanded his research to guidance, navigation, and control (GN&C) systems design. Notably, he was part of a team that designed a Hypersonic Inflatable Aerodynamic Decelerator (HIAD) system for human Mars exploration, wherein he devised a modified form of the Apollo entry guidance algorithm for the HIAD system. The team was a finalist



at the NASA BIG Idea Challenge in 2016, and the work was presented at NASA Langley Research Center. Harish's doctoral work was also recognized by the American Institute of Aeronautics and Astronautics (AIAA), wherein he won the AIAA SciTech 2018 Atmospheric Flight Mechanics Conference Student Paper Competition for his paper titled "The Relaxed Autonomously Switched Hybrid System (RASHS) Approach to Indirect Multi-Phase Trajectory Optimization for Aerospace Vehicles." Harish also interned at the MathWorks, Inc. (Natick, MA) in summer 2017, wherein he worked on designing a 7 degree-of-freedom remote manipulator system for robotic space missions.

Harish's research interests include trajectory optimization, entry, descent, and landing (EDL) mission design, GN&C and robotics.